An Innovative Design of High-Temperature, Sensible Molten Salt Thermal Energy Storage Systems With Geopolymer Insulation

Youyang Zhao,[1] Thomas Viverito,[2] Ryan Bowers,[3] Chase Kimbal,[4] Tunahan Aytas,[5] and Elsa Olivetti[5]

1 National Renewable Energy Laboratory
2 Morgan Advanced Materials
3 Worley/Advisian
4 JT Thorpe & Son
5 Massachusetts Institute of Technology

NREL is a national laboratory of the U.S. Department of Energy
Office of Energy Efficiency & Renewable Energy
Operated by the Alliance for Sustainable Energy, LLC

This report is available at no cost from the National Renewable Energy Laboratory (NREL) at www.nrel.gov/publications.

Contract No. DE-AC36-08GO28308

Technical Report
NREL/TP-5700-88400
January 2024

An Innovative Design of High-Temperature, Sensible Molten Salt Thermal Energy Storage Systems With Geopolymer Insulation

Youyang Zhao,[1] Thomas Viverito,[2] Ryan Bowers,[3] Chase Kimbal,[4] Tunahan Aytas,[5] and Elsa Olivetti[5]

1 National Renewable Energy Laboratory
2 Morgan Advanced Materials
3 Worley/Advisian
4 JT Thorpe & Son
5 Massachusetts Institute of Technology

Suggested Citation
Zhao, Youyang, Thomas Viverito, Ryan Bowers, Chase Kimbal, Tunahan Aytas, and Elsa Olivetti. 2024. *An Innovative Design of Sensible Molten Salt Thermal Energy Storage Systems With Geopolymer Insulation*. Golden, CO: National Renewable Energy Laboratory. NREL/TP-5700-88400. https://www.nrel.gov/docs/fy24osti/88400.pdf.

NREL is a national laboratory of the U.S. Department of Energy
Office of Energy Efficiency & Renewable Energy
Operated by the Alliance for Sustainable Energy, LLC

This report is available at no cost from the National Renewable Energy Laboratory (NREL) at www.nrel.gov/publications.

Contract No. DE-AC36-08GO28308

Technical Report
NREL/TP-5700-88400
January 2024

National Renewable Energy Laboratory
15013 Denver West Parkway
Golden, CO 80401
303-275-3000 • www.nrel.gov

NOTICE

This work was authored in part by the National Renewable Energy Laboratory, operated by Alliance for Sustainable Energy, LLC, for the U.S. Department of Energy (DOE) under Contract No. DE-AC36-08GO28308. Funding was provided by the Office of Energy Efficiency and Renewable Energy Solar Energy Technologies Office. The views expressed herein do not necessarily represent the views of the DOE or the U.S. Government.

This report is available at no cost from the National Renewable Energy Laboratory (NREL) at www.nrel.gov/publications.

U.S. Department of Energy (DOE) reports produced after 1991 and a growing number of pre-1991 documents are available free via www.OSTI.gov.

Cover Photos by Dennis Schroeder: (clockwise, left to right) NREL 51934, NREL 45897, NREL 42160, NREL 45891, NREL 48097, NREL 46526.

NREL prints on paper that contains recycled content.

Final Technical Report

Project Title:	Molten Chloride Thermophysical Properties, Chemical Optimization, and Purification
Project Period:	4/1/2020–9/30/2023
Submission Date:	12/29/2023
Recipient:	National Renewable Energy Laboratory (NREL)
Address:	15013 Denver West Parkway Golden, CO 80401-3305
Website:	www.nrel.gov/csp
Award Number:	36332
Project Team:	Morgan Advanced Materials Massachusetts Institute of Technology Worley/Advisian J.T. Thorpe & Son, Inc.
Principal Investigator:	Youyang Zhao, Ph.D. Phone: (303) 275-4398 Email: Youyang.Zhao@nrel.gov
Business Contact:	Craig Turchi Phone: (303) 475-4668 Email: Craig.Turchi@nrel.gov
Technology Manager:	Shane Powers
Project Officer:	Christine Bing

This report is available at no cost from the National Renewable Energy Laboratory at www.nrel.gov/publications.

List of Acronyms

CapEx	capital expenditures
CCS	cold crush strength
CSP	concentrating solar power
CTE	coefficient of thermal expansion
DOE	U.S. Department of Energy
FE	finite element
FEA	finite-element analysis
GP	geopolymer
HTF	high-temperature fluid
IPA	isopropyl alcohol
LCOE	levelized cost of electricity
MIT	Massachusetts Institute of Technology
MOR	modulus of rupture
NREL	National Renewable Energy Laboratory
RFB	refractory firebricks
RTE	round-trip efficiency
SAM	System Advisor Model
TES	thermal energy storage
XCT	X-ray computed tomography
XRD	X-ray diffraction

This report is available at no cost from the National Renewable Energy Laboratory at www.nrel.gov/publications.

Executive Summary

Renewable energy technologies for power generation, such as photovoltaics and concentrating solar power (CSP), have emerged in recent decades and became more and more competitive. However, a major drawback for such renewable energy technologies alone is their intermittent nature, which requires an energy storage system to store excess renewable energy when it is abundant (e.g., during sunny daytime) and later discharge the stored energy when it is not (e.g., during cloudy time or at night). The implementation of an energy storage system resolves the difference when real-time supply from renewable sources does not meet the demand during the aforementioned intermittency. Various forms of energy storage are under development. One of the most cost-effective energy storage technologies is thermal energy storage (TES) with a high-energy-density heat transfer fluid (HTF) such as molten salts. In principle, the TES and HTF medium is heated by an energy source (e.g., by direct irradiation of sunlight through a solar receiver in CSP or by an electric heater powered by electricity generated by other renewable energy sources) to achieve the energy conversion to heat and thermal energy. The TES medium is then kept in a storage tank to maintain its thermal energy until discharged to a power cycle to generate electricity when needed.

Molten salt TES systems using solar salt (60 wt.% $NaNO_3$–40 wt.% KNO_3) as the TES medium and HTF have been implemented by the current CSP industry for Gen2 tower-based CSP technology. Gen3 CSP technology based on a ternary molten chloride salt (i.e., a Na-K-Mg chloride mixture) was also extensively investigated [1,2]. For molten nitrate salt TES systems, conventional metal storage tanks are usually designed based on other industries' codes (e.g., API 650) where the metal tank shell (made of stainless steel 347H for the hot tanks and carbon steel for the cold tanks) is directly exposed to molten nitrate salt at the hot and cold tanks' operation temperatures at ~565°C and ~290°C, respectively. These tanks only have external thermal insulation. For molten chloride salt TES systems that operate at ~500°C and ~720°C, metal storage tanks are internally insulated as well, first by a dense fire brick layer as the molten salt barrier and subsequently by a more thermally insulating porous fire brick layer to reduce the temperature to a level where the metal tank shell materials can be safely used [2]. Both designs have drawbacks. Tank floor failures have been reported for the nitrate salt TES tanks [3,4], which were suspected to be related to the thermal stresses and low-cycle thermal fatigue of the floor due to nonuniform temperature distribution during the first tank start-up and salt charging. Chloride salt TES tanks have only been investigated at a conceptual design stage with limited efforts on small-scale demonstration (<300 kg of storage capacity [5]). A well-identified risk of the chloride salt TES design is that, although the dense fire bricks have been confirmed to be thermally and chemically compatible with the molten chloride salt, the mortar joints' robustness at high temperatures has not been demonstrated [2]. Salt permeation through the salt barrier layer's mortar joints can lead to saturation of the porous fire brick layer underneath, causing a decrease in thermal insulation performance and even mechanical failure. Hence, the salt permeation resistance of the internal insulation is a major design consideration.

This project aims to mitigate the risks of the current molten salt TES tank designs. The goal is to create a more reliable and cost-effective TES system by (1) developing a new material solution for internal thermal insulation, and (2) designing a concrete-based tank structure to eliminate the metal-related issues (e.g., corrosion, thermomechanical failure). The project plans to make two major changes to the current TES tank design:

This report is available at no cost from the National Renewable Energy Laboratory at www.nrel.gov/publications.

- Firstly, the project aims to engineer a composite refractory insulation material that possesses sufficient thermal insulation properties without significantly sacrificing the resistance to salt permeation and mechanical strength, which is the major trade-off in traditional refractory insulation design. The primary objective is to perform materials design and optimization of the composite refractory to achieve the required thermal and mechanical properties as suitable internal insulation for molten salt TES.
- Secondly, the project aims to design a concrete-based TES system with conventional low-cost Portland cement serving as the primary tank structure and the aforementioned composite refractory as the internal thermal insulation and salt containment. The objective is to investigate the technical and economical feasibilities of concrete tanks for high-temperature molten salt storage applications.

The National Renewable Energy Laboratory, Morgan Advanced Materials (Morgan), and the Massachusetts Institute of Technology collaborated to design an aluminosilicate-based geopolymer material as the matrix of the composite refractory with cenospheres (an industrial byproduct from coal-firing power plants) and commercial lightweight aggregates as the major additive phases. This geopolymer material is referred to as "geopolymer insulation" throughout this report. Extensive materials characterization on the thermal and mechanical properties are performed on geopolymer insulation, which reveal impressive strength-to-weight ratio of 30,000 N·m/kg at about 720°C.[1] Molten salt immersion tests are conducted in molten nitrate salt at up to 550°C for more than 50 days and in molten chloride salt at up to 650°C for more than 27 days. The immersion test results indicate promising salt permeation resistance such that the geopolymer insulation maintains most of its thermal insulation performance when in contact with molten salts. Production trials in Morgan's manufacturing plant suggest cracking is a key issue during scaling-up, which can potentially be solved by further understanding the phase transitions and fine-tuning the additive content to counter volumetric shrinkage during high-temperature firing.

JT Thorpe and Worley/Advisian conceptually designed the insulation liner and concrete tank structure, respectively, of a full-scale storage system for both the nitrate and chloride salt TES. The designed thermal storage capacity is about 2,791 MWh-t for the nitrate salt TES, assuming a conventional carbon steel cold tank and a concrete hot tank with geopolymer internal insulation. The designed thermal storage capacity is about 2,400 MWh-t for the chloride salt TES, assuming two concrete hot tanks and two concrete cold tanks, both with geopolymer internal insulation. The cost estimate suggests that the economics for the designed nitrate salt TES system are more appealing at about $33/kWh-t (vs. $26.3/kWh-t for a reference conventional metal tank TES system designed by Worley/Advisian [6]).[2] For the molten chloride TES, on the other hand, due to its lower energy density, a two-pair design (i.e., two cold tanks and two hot tanks) is required to achieve a similar thermal storage capacity, which significantly impacts the system's affordability. Therefore, the economics for the designed chloride salt TES system are not appealing, unfortunately, at about $85/kWh-t.

[1] Commercial refractory fire bricks usually have a strength-to-weight ratio in the thousands of N·m/kg range.
[2] Note that the conventional design is based on 2020 U.S. dollars while the concrete structure and geopolymer insulation design is based on 2023 U.S. dollars.

This report is available at no cost from the National Renewable Energy Laboratory at www.nrel.gov/publications.

Table of Contents

This report is available at no cost from the National Renewable Energy Laboratory at www.nrel.gov/publications.

List of Figures

This report is available at no cost from the National Renewable Energy Laboratory at www.nrel.gov/publications.

This report is available at no cost from the National Renewable Energy Laboratory at www.nrel.gov/publications.

This report is available at no cost from the National Renewable Energy Laboratory at www.nrel.gov/publications.

This report is available at no cost from the National Renewable Energy Laboratory at www.nrel.gov/publications.

List of Tables

This report is available at no cost from the National Renewable Energy Laboratory at www.nrel.gov/publications.

1 Introduction

1.1 Background

The current generation of molten salt storage based on solar salt uses a pair of metal tanks (one cold tank and one hot tank) to contain the heat transfer fluid (HTF) and thermal energy storage (TES) medium. Carbon steel and an austenitic stainless steel (SS 347H) are used as the structural material for the cold tank and hot tank, respectively. The carbon steel and SS 347H shells are in direct contact with the molten nitrate salt at ~290°C and ~565°C, respectively. Several reports on the floor failure of the hot tank around the world have been noted, possibly due to thermal stresses and low-cycle fatigue of the SS 347H floor resulting from (1) repeated nonuniform temperature distribution of the floor during tank start-up and hot salt addition and (2) metallurgical susceptibility of SS 347H to cracking at the hot tank's operating temperature [7].

The next-generation molten salt storage based on a ternary chloride salt uses a similar design, but steel hot and cold tanks are internally insulated by refractory liners. The refractory aims to drop the temperature to a level at which more affordable stainless steel or carbon steel materials can be used in terms of corrosion resistance and mechanical strength; otherwise, the tanks are cost-prohibitive if only high-temperature alloys can be used, e.g., Ni-based superalloys.

Therefore, internal thermal insulation can theoretically benefit both types of molten salt TES. For current-generation nitrate salt TES, internal insulation could possibly serve as a buffer layer and add thermal mass to the floor and walls such that the heat transfer from the hot salt could be smoother, leading to less temperature inhomogeneity and thermal stresses. For the next-generation chloride salt TES, internal insulation is required to achieve economic viability by enabling the use of lower-cost tank structural materials. However, a few dilemmas remain in the design of internal insulation using conventional refractory materials.

- Dense refractory is shown to be robust against molten salt in terms of thermal stability, chemical compatibility, and mechanical strength. However, the weakest link of the dense refractory liner is the mortar joint, which is prone to salt permeation because it is usually made of less dense powders mixed with a liquid followed by curing. If the mortar joints allow salt permeation, it defeats the purpose of using the expensive dense refractory liner as a salt barrier.
- TES tanks are required to have low heat loss to preserve the thermal energy during the storage period (i.e., 8–10 hours every day). Gases typically are the best insulation material, as they have orders of magnitude lower thermal conductivity compared to liquids and solids. Hence, refractory designers incorporate a significant pore volume fraction in the refractory firebricks (RFBs). The manufacturing process usually produces open porosity that are interconnected and open to the environment. RFBs with open porosities work well with applications that insulate gases and solids because neither greatly impact the thermal insulation performance. But applications that require insulation of liquids are faced with a dilemma when using highly porous RFBs because the liquids can permeate and wet the porosities, leading to a significant increase in thermal conductivity. The increased thermal conductivity can lead to higher heat losses and overheating. The higher the initial thermal insulation performance of the RFBs (i.e., with higher volume fraction of open porosities), the higher the likelihood of liquid permeation into the RFBs because air or gas do not have

This report is available at no cost from the National Renewable Energy Laboratory at www.nrel.gov/publications.

any resistance against liquids displacing their volume. In addition, high-performance RFBs usually do not have high strength due to their high porosity (i.e., air or gas does not contribute to RFB strength).

In short, RFBs are believed to be cost-effective at providing thermal insulation to molten salts but only when a reliable salt permeation barrier is in place to protect the porosities in the RFBs. Unfortunately, a reliable and cost-effective salt permeation barrier design has not been demonstrated.

1.2 Project Overview

The multiyear project consisted of three stages of research. The first year was focused on the preliminary design of a viable thermal insulation concept and initial material screening for the thermal insulation. The second year was focused on extensive materials optimization, characterization, and analysis of the thermal insulation material before and after molten salt immersion testing. The third year was focused on scaling up the thermal insulation material with production trials in an industrial setting, conceptual design of the liner installation methods, concrete tank structure and foundation design, and costing for a full-scale TES system.

The outcomes and impacts are primarily twofold. First, the research and development of a new internal insulation material provides an alternative insulation design philosophy where salt permeation into insulation is no longer an extreme danger. Instead, it is carefully controlled to achieve a more reliable, self-containing, and self-healing salt containment. Second, the conceptual design and costing of an unconventional concrete-based TES structure opens new opportunities for TES construction methods. Specifically, concrete has been used for industrial-scale structures for decades (e.g., liquified natural gas tanks). This effort is one of the first to investigate the possibilities of using concrete for higher-temperature structures and transfer the existing knowledge base to the relatively new TES applications.

This report is available at no cost from the National Renewable Energy Laboratory at www.nrel.gov/publications.

2 Results and Discussion

2.1 Conceptual Design for Thermal Insulation

2.1.1 Design Inspiration and Strategy

Given the dilemmas explained in Section 1.1, this project is pursuing a different design philosophy for insulating and containing molten salt. The inspiration comes from the current industrial processes for aluminum smelting. The Hall–Héroult process for aluminum production has a containment need for a highly corrosive liquid electrolyte at high temperature (i.e., cryolite with dissolved alumina). And there is no compatible and cost-effective refractory insulation that can sustain the harsh operating conditions. Instead, the containment is achieved by a frozen layer of the molten electrolyte, which is compatible with the corrosive molten electrolyte itself. Figure 1 illustrates a simplified schematic of a typical Hall cell's sidewall design, which showcases the importance of a frozen electrolyte layer as the main containment. In order to achieve a frozen layer, the heat transfer needs to be carefully managed such that the molten electrolyte's temperature drops to its freezing point near the shell of the smelter. This design is viable because (1) the operating temperature of the aluminum smelting process (960°C–980°C) is not too far from the molten electrolyte's freezing temperature of about 960°C at the eutectic composition [8], (2) the smelter shell is cooled in a controlled fashion to achieve a relatively high heat flux and temperature gradient to freeze the electrolyte near the shell, and (3) the economics of the smelting process is not heavily impacted by heat loss.

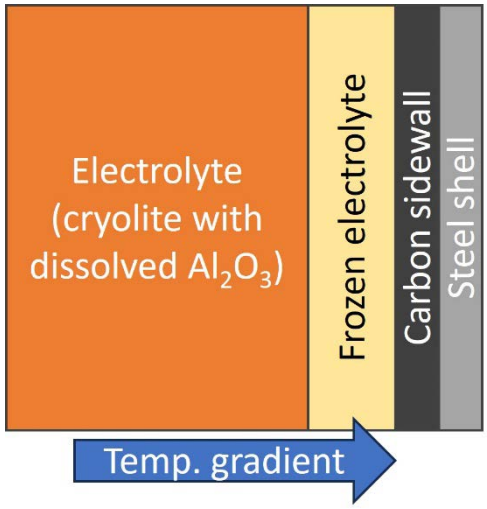

Figure 1. A simplified schematic of a typical Hall cell's sidewall design

Our molten salt containment and insulation concept is inspired by the idea of using the frozen material as self-containment of the same molten salt. The advantage of such a design for molten salt TES is that as long as the thermal profile across the containment is maintained, the self-containment is also self-healing. If a crack forms on the frozen salt layer, the leaked salt should freeze because the salt would leak into a region where the temperature is below its freezing point. This would repair the leakage without any external efforts. Another advantage is that frozen salt is certainly compatible with the same molten salt. However, such a design has challenges that are specific to TES applications. First, TES for concentrating solar power (CSP) applications need a

This report is available at no cost from the National Renewable Energy Laboratory at www.nrel.gov/publications.

large temperature difference (ΔT) of 200°C–250°C between the hot tank and cold tank to maximize the power generation efficiency. In addition, because a buffer must be kept between the salt's operating temperature and the salt's freezing temperature in the cold tank (i.e., at least 50°C above freezing) to avoid freeze risks, the hot tanks have to operate at 250°C–300°C above the freezing temperature for both nitrate and chloride TES systems in order to have the large ΔT. The 250°C–300°C temperature difference in the hot tank would require a significant heat flux (and hence heat loss) to achieve salt freezing for self-containment within a reasonable physical space. Figure 2 shows the calculated relationship between heat flux and insulation thickness, based on a simplified one-dimensional (1D) heat transfer scenario in Equation (1), for different thermal conductivities to achieve a 300°C temperature difference, where q is the heat flux, k is the thermal conductivity of the insulation, ΔT is the temperature difference, and Δx is the insulation thickness.

$$q = -k\frac{\Delta T}{\Delta x} \tag{1}$$

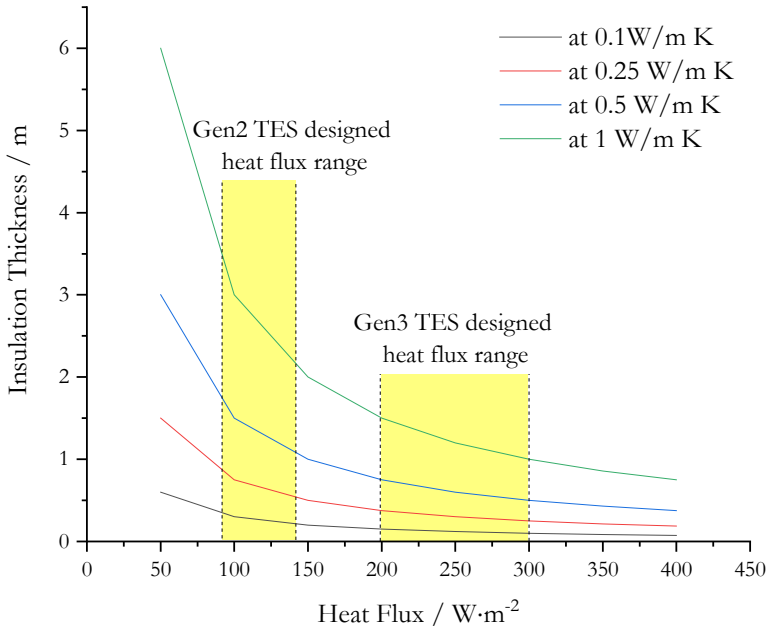

Figure 2. Relationship between heat flux and insulation thickness based on a simplified 1D heat transfer scenario for different thermal conductivities to achieve a 300°C temperature difference

It is clear that, for molten salt with thermal conductivity[3] of ~0.5 W/m·K (i.e., blue line in Figure 2), the required thickness to achieve a 300°C temperature difference is at least 1 m and 0.5 m for the designed heat flux ranges of the Gen2 nitrate salt TES and Gen3 chloride salt TES, respectively. The thickness range is calculated by assuming that the molten salt is a static layer without any convective heat transfer. In reality, maintaining a static 0.5–1 m layer of molten salt without convection near a vertical tank wall (or even near a horizontal floor) is almost impossible. Hence, a direct application of the insulation concept from the aluminum smelter is not viable for molten salt TES. The only alternative, mathematically based on Equation (1), is to significantly increase

[3] Thermal conductivity of about 0.5 W/m·K assumes no convective heat transfer.

This report is available at no cost from the National Renewable Energy Laboratory at www.nrel.gov/publications.

the heat flux to a level of >500 W/m^2 (beyond the x-axis of Figure 2). However, TES applications may not be able to afford such a high heat loss. Figure 2 also shows the challenges associated with thermal insulation design. Generally speaking, there is a practical limit on the thickness of a thermal insulation liner that can be produced or installed in real-world industrial applications. For example, a standard fire brick is about 9 in. or 22.8 cm in the longest dimension; refractory liner designers and installers have more confidence when the liner is less than 2–3 layers thick, giving a maximum liner thickness of less than 0.75 m. Thicker liners would lead to concerns of the liner's structural rigidity when used for large structures like TES tanks as well as concerns about the material and installation costs.

The internal thermal insulation design for molten salt TES tanks must balance constraints implied by multiple sets of properties. First, the balance between thermal insulation performance and salt permeation resistance must be carefully optimized because highly insulating materials are usually achieved by a high volume fraction of porosities, which are naturally less resistant to salt permeation (especially in the case of open porosities). Second, the balance between thermal insulation performance and mechanical strength/corrosion resistance is also necessary because strong and corrosion-resistant materials (as the matrix to support the porosities) are usually associated with significantly higher thermal conductivity, hence reducing overall insulation performance. Third, the balance between the allowable heat loss of the tanks and insulation cost needs to be carefully considered because a low heat loss to achieve higher daily round-trip efficiency will certainly be accompanied by a higher up-front cost for more thermal insulation. Balancing multiple design parameters at the same time is challenging and requires compromise. The project team is aware of the compromises that must be made at the beginning of the project, and the main goal is to explore the design space for thermal insulation and tank performance to find the optimal design while acknowledging certain compromises.

The core of the new design for the composite refractory thermal insulation material is the incorporation of closed-cell porosities in a matrix that is resistant to molten salt corrosion and permeation. The closed porosity is achieved by using cenospheres, which are hollow spheres with a particle size range of 10–500 μm (averaging about 50–100 μm), as a byproduct of coal-firing power plants. Cenospheres are known to have an aluminosilicate chemistry as the major constituents (50–60 wt.% of SiO_2 and 20–35 wt.% of Al_2O_3) with various amounts of Fe-oxide, Ti-oxide, Ca-oxide, etc., as the minor constituents. The minor oxide contents depend on the specific operating parameters of the power plants and the sources of the coal. For example, cenospheres from Tarong Power Plant in Australia have one of the lowest Fe_2O_3 content (<1 wt.%) while most other commercial cenospheres have higher Fe_2O_3 content (1–5 wt.%) [9]. Aluminosilicate species are generally more resistant to molten salt. One well-known aluminosilicate is mullite ($3Al_2O_3 \cdot 2SiO_2$), which has been used extensively during molten salt experiments [10–12]. Reference [9] shows that mullite is a major crystalline phase in cenospheres. Hence, cenospheres with a preferred closed spherical form combined with a potentially promising base chemistry that can be resistant to molten salt are considered a major additive to provide the desired closed-cell porosities in the composite refractory insulation.

The first step is to understand the attainable thermal conductivity of the proposed insulation concept. An ideal hypothetical structures are molten-salt-resistant matrix materials (with the lowest possible open porosities) that have closed-cell porosities created by cenosphere additions to achieve thermal insulation. After reviewing several physical models that predict thermal

This report is available at no cost from the National Renewable Energy Laboratory at www.nrel.gov/publications.

conductivity of a porous matrix [13], we chose to use the modified EMT/Maxwell model because it most closely resembles the physics in the proposed insulation material concept. The modified EMT/Maxwell model takes advantage of two basic models and develops an equation that lies between the two models and contains an experimental parameter to fit to specific datasets, as shown in Equation (2) where K is the overall effective thermal conductivity of the n-component composite, k_i and x_i are the thermal conductivity and volume fraction of component i, respectively, and χ is the experimental parameter as described by Gong et al. [13] that varies with the total volume fraction of porosity.

$$\sum_{i=1}^{n} x_i \frac{k_i - K}{k_i + 2\chi K} = 0 \tag{2}$$

The advantage of the modified EMT/Maxwell model is that if χ, the only parameter in the equation, can be determined, then the overall thermal conductivity can be calculated given the thermal conductivity and volume fraction of each component.

Compiled experimental thermal conductivity data K from the literature at various volume fractions of porosities were used to determine the correlation between χ and the porosity for anorthite and mullite (Figure 3), which are two commonly known ceramic materials believed to withstand a molten salt environment. The correlations are mathematically expressed in Equations (3) and (4) for porous anorthite and mullite, respectively, where P is the volume fraction of porosity.

$$\chi = .9989 + 4.61 \cdot 10^{-5} \cdot e^{11.2324 \cdot P} \tag{3}$$

$$\chi = .99956 + 4.4 \cdot 10^{-4} \cdot e^{9.544 \cdot P} \tag{4}$$

This report is available at no cost from the National Renewable Energy Laboratory at www.nrel.gov/publications.

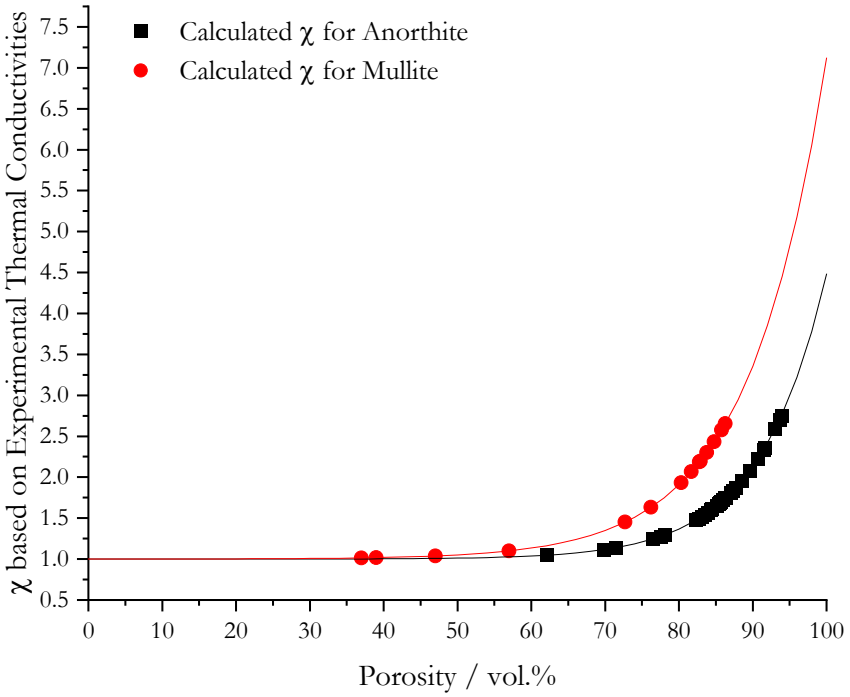

Figure 3. Correlation between the parameter χ used by the EMT/Maxwell-Eucken model and porosity, for porous anorthite and mullite

Although Figure 3 and Equations (3) and (4) show that there is no universal χ correlation for different matrix materials, it is clearly seen that there is little variation of χ in the volume fraction range below 60%. Both anorthite and mullite have a χ value close to 1 in this range. Therefore, although there is no universal χ across the entire volume fraction range, $\chi = 1$ is likely a sufficient approximation in the targeted volume fraction range for cenospheres in the proposed insulation material (e.g., 40%–60% based on the physical space limitation for packing hard-shell spheres as an additive in a matrix). To confirm the hypothesis, a sensitivity analysis was performed to evaluate the errors of the calculated thermal conductivity. The sensitivity analysis was performed between $\chi = 1$ and $\chi = 1.04$. Note that 1.04 was chosen because it was the upper bound of χ at 60% porosity given by Equations (3) and (4), which represents the maximum deviation from our assumption of $\chi = 1$. The results showed that the calculation of effective thermal conductivity using the modified EMT/Maxwell-Eucken model was not very sensitive to a simplification of $\chi = 1$ in the porosity range of 40%–60% for anorthite and mullite. The maximum error was <10%. Therefore, the results suggested that when using the modified EMT/Maxwell-Eucken model to guide the design for the thermal conductivity of the composite refractory materials, there is almost no need to experimentally determine χ, and an assumption of $\chi = 1$ should suffice if the porosity does not exceed 60%. This is the major advantage of using the modified EMT/Maxwell-Eucken model to guide material development.

Next, the attainable thermal conductivity of the composite refractory with cenospheres was estimated using the EMT/Maxwell model. The matrix material was assumed to be anorthite, which represents an average thermal conductivity of 3.67 W/m·K for commonly known matrix materials for refractories. Assuming a reasonable 50 vol.% porosity, the porous composite refractory could achieve a thermal conductivity of ~0.4 W/m·K; with a more aggressive assumption of 60 vol.%

This report is available at no cost from the National Renewable Energy Laboratory at www.nrel.gov/publications.

closed porosity, the thermal conductivity could be reduced to ~0.3 W/m·K. However, compared to a conventional thermal insulation material that could achieve >80 vol.% porosity (but note that these pores are mostly interconnected and open, as shown in Figure 4 [14]) and <0.2 W/m·K thermal conductivity, this is clearly a compromise. For the purpose of guiding early material development and preliminary tank design, a less aggressive thermal conductivity value of 0.4 W/m·K was tentatively adopted.

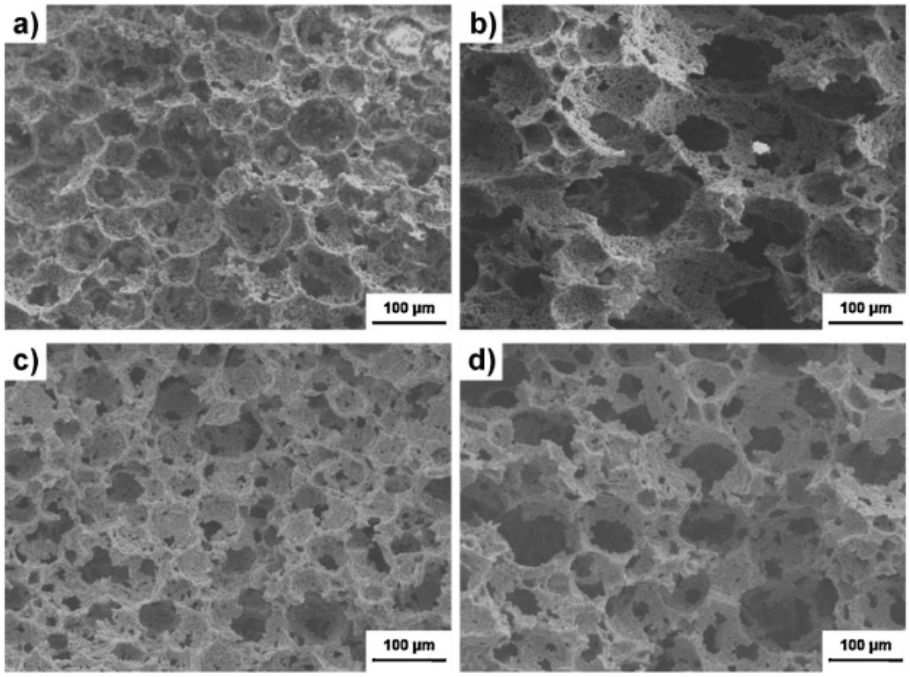

Figure 4. Scanning electron microscope images of the porous structure of traditional refractory fire bricks with interconnected and open porosities

2.1.2 Conceptual Liner Design

As stated in Section 2.1.1, having a frozen salt layer as the self-containment is preferred from the chemical compatibility as well as the containment reliability perspective. However, insulating and containing the molten fraction of the salt inventory by achieving a sufficient temperature drop within a static molten salt layer and freezing the outermost layer of the salt is impractical. In addition, using a traditional two-layer refractory design to contain the molten salt at more than 300°C above its freezing temperature makes it inherently difficult to stop the molten salt permeation in case of a leak, because the temperature of the leaked salt needs to be cooled down by more than 300°C before the salt starts to freeze. Therefore, the project pursues a third design that allows partial molten salt permeation into the composite geopolymer insulation. It could be an acceptable thermal insulation design if the "combination" of partially permeated insulation and molten salt still possesses a decent thermal insulation performance, which echoes the needs for closed porosities such that the gas in the porosities (i.e., the main contributor to thermal insulation) will not be easily displaced by the salt permeation.

It is useful to present the conceptual tank insulation design here before moving to the next sections. Figure 5 shows the conceptual design of the TES tank wall and lists a few key considerations for the internal insulation layers.

This report is available at no cost from the National Renewable Energy Laboratory at www.nrel.gov/publications.

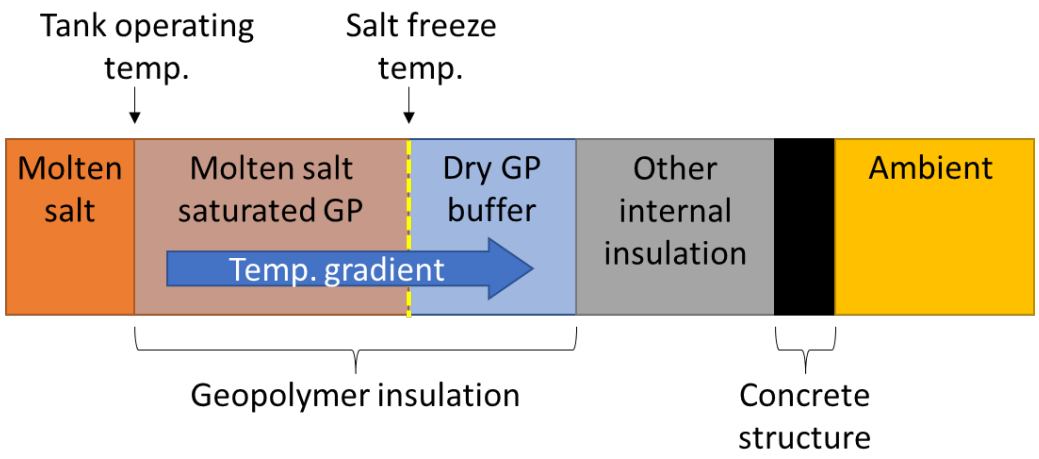

Figure 5. Schematic of the tank wall insulation design. The yellow dashed line indicates the molten salt/solid salt interface

GP = geopolymer

- The "molten salt saturated GP" layer (where GP stands for geopolymer) is designed to be partially saturated by the molten salt where the thermal conductivity is expected to be around 0.5 W/m·K based on theoretical estimation (discussed later). The rest of the geopolymer layer, "dry GP buffer," is designed to be free of molten salt, which has a lower thermal conductivity around 0.4 W/m·K, based on the first-principle estimation given in Section 2.1.1. The dry geopolymer is designed to stay below the salt freeze temperature during normal operation and serves as a buffer zone during excursion events when the heat transfer of the wall changes and the molten salt/solid salt interface (the yellow dashed line in Figure 5) moves. As is apparent, the molten salt/solid salt interface is the most important feature of the design because the frozen solid salt effectively self-contains the molten salt. As long as there is enough physical space and temperature drop in the buffer layer for the molten salt to freeze, molten salt will always be contained by its frozen counterpart with no compatibility issues. The containment will "self-heal" by simply freezing the leaked molten salt if a crack develops, as the temperature beyond the molten salt/solid salt interface is below the freezing temperature by definition of the interface. Equally important, the buffer zone prevents molten salt from permeating into the highly insulating yet fragile "other internal insulation" layer, i.e., traditional highly porous and highly insulating RFBs.
- Around the molten salt/solid salt interface, there are stresses associated with the volume change between the molten and solid salts. For the Gen2 nitrate salt, the volume change is about 4.6% [15]; for the Gen3 chloride salt, the volume change is estimated to be about 20% [16]. This could raise concerns over the mechanical strength of the geopolymer near the interface, especially when the interface moves back and forth over time due to slight changes of heat transfer through the tank walls/floor.
- The entire geopolymer insulation layer is under a temperature gradient of 200°C/m–500°C/m, estimated with Equation (1) assuming an effective thermal conductivity of 0.4 W/m·K, an allowable heat flux range of 100–200 W/m^2, and a temperature drop of 300°C.
- The molten salt saturated section of the geopolymer needs to maintain most of its closed porosity over time and avoids extensive chemical attack from the salt on the closed porosity

This report is available at no cost from the National Renewable Energy Laboratory at www.nrel.gov/publications.

structure, e.g., cenopsheres. The goal is to minimize loss of thermal insulation performance due to permeation of molten salt into the closed porosities as time progresses.

- Even when the molten salt permeates into some porosities of the geopolymer insulation, it is assumed that the geopolymer insulation stills retain a reasonable thermal insulation performance because the salt trapped inside small pores is stagnant and has a relatively low thermal conductivity of 0.4–0.5 W/m·K. Unlike the conventional two-layer insulation design (e.g., used by Gen3 Liquid Pathway CSP technology [2]) where salt permeation through the first layer of dense refractory (most likely through the mortar joints) may introduce a significant heat transfer increase and even chemical/mechanical damage inside the backup insulation layer, this geopolymer-based design is more fail-safe and can sustain more "abuse" when some parts of the geopolymer insulation start to experience more salt permeation than expected.

2.2 Lab-Scale Materials Development and Molten Salt Testing for Geopolymer Insulation

Given the key considerations of the insulation concept presented in the previous section, it is meaningful to discuss the experimental approaches that the project team used to develop and optimize the geopolymer materials below.

2.2.1 Selection of Matrix Material

The preliminary selection of the matrix material must take into account several considerations:

- The matrix needs to be chemically resistant against molten salt to provide the intended protection for the cenospheres.
- The matrix needs to be thermally stable at least to 720°C, i.e., the hot tank temperature for the chloride salt TES.
- The matrix needs to be similar in chemistry to the cenospheres and other additives such that the interface with the matrix is stable in terms of chemical compatibility and mismatch of coefficient of thermal expansion.
- The matrix needs to have a relatively low thermal conductivity to minimize its impact on overall thermal insulation performance.

After extensive literature review, geopolymers appear most attractive for further investigation. Geopolymers are a group of inorganic alkaline aluminosilicate materials with an amorphous structure. They are mostly made from aluminosilicate-rich sources (e.g., metakaolin). The synthesis process is similar to that of cement. The known advantages of geopolymers are summarized as follows:

- The structure of geopolymers is mostly an amorphous aluminosilicate network with alkaline elements and other minor impurities from the source as network formers or modifiers, which means the compatibility to aluminosilicate-based cenospheres is promising.
- Aluminosilicates such as mullite can be chemically resistant to molten chlorides and molten nitrates, as shown in previous work and literature [10,16,17]. Therefore, it is optimistic that geopolymers could show similar compatibility, although geopolymers have an amorphous structure.

This report is available at no cost from the National Renewable Energy Laboratory at www.nrel.gov/publications.

- The amorphous nature of the geopolymers suggests that the thermal conduction through the amorphous network is not as effective as through other solid crystalline materials; thus, geopolymers could have a lower thermal conductivity. It has been found that geopolymers with a 30–35 vol.% open porosity can have a thermal conductivity of 0.17–0.35 W/m·K [18]. When mixed with fly-ash and cenospheres, metakaolin-based geopolymers can reach a low thermal conductivity of 0.173 W/m·K at 40 vol.% of fly-ash/cenosphere addition at room temperature [19]. Both cases show that geopolymers may be able to achieve lower thermal conductivity than that of a porous anorthite or mullite at similar porosity range, thanks to its amorphous structure.
- An additional benefit of geopolymers is the relatively easy synthesis process, similar to cement manufacturing. After mixing the aluminosilicate raw material (e.g., metakaolin) with an aqueous, basic activator (e.g., an aqueous NaOH and Na-silicate solution), geopolymers can be casted into different shapes and cured at a slightly elevated temperature (60°C–80°C) to gain strength [20,21]. This simple synthesis process, in principle, resembles the castable manufacturing in the refractory industry. For example, precasts can be made into different shapes and cured in a factory before installation; castables can be poured and cured on-site. Both highly resemble the standard practices of the refractory installation industry, which may benefit the adoption of geopolymers by the industry.

The disadvantages of geopolymers mostly relate to a lack of extensive knowledge because the material is still relatively new, especially for high-temperature refractory applications. A few disadvantages are summarized below:

- Geopolymers can form open-cell porosity from the dehydration process during curing. Controlling the dehydration process and minimizing the fraction of open porosities is important to avoid extensive salt permeation.
- The high-temperature mechanical strength and chemical resistance of geopolymers are also related to the curing process. Therefore, it needs to be demonstrated that geopolymers can be sufficiently strong and chemically stable with molten salt at up to 720°C.
- Although the raw materials for geopolymers (such as metakaolin, fly-ash, and rice husk ash) are relatively cheap, the basic activators (such as NaOH and Na-silicate) needed to break down these aluminosilicate sources before curing are relatively expensive and can constitute a large fraction of the materials cost.

The ultimate goal is to optimize and tune the geopolymer recipe with proper additives, to better suit the molten salt environment and ensure that the hollow cenospheres can be properly incorporated into the geopolymer matrix to achieve the desired thermal conductivity without extensive damage caused by molten salt.

2.2.2 Selection of Inclusion Materials

As stated in Section 2.1.1, cenospheres are designed to be a major component of the geopolymer-based insulation material. They are hollow aluminosilicate spheres with a particle size distribution between a few micrometers and a few hundred micrometers, with the peak particle size usually in the 50–100 μm range. Figure 6 is the optical microscope image of CenoStar ES500 cenospheres, a commercially available product. The image shows the hollow sphere morphology and the dominating particle size. CenoStar ES500 was selected for the study due to its superior mechanical

This report is available at no cost from the National Renewable Energy Laboratory at www.nrel.gov/publications.

strength (>90% survival at 3,200 psi compression) and high melting point (1,200°C–1,400°C). Other commercial cenospheres may have lower thermal conductivity, but that usually comes with a compromise of significantly lower mechanical strength and chemcial stability with molten salts. For example, SphereOne XOL-200 has one of the lowest bulk densities of about 0.14 g/cc but has one of the lowest compressive strengths as well. Such a trade-off is showcased in Table 1, which lists several properties of CenoStar ES500 and SphereOne XOL-200.

Table 1. Selected Properties of Two Commercial Cenospheres, CenoStar ES500 and SphereOne XOL-200

Properties	CenoStar ES500	SphereOne XOL-200
Compressive strength	3,200 psi	200 psi
Melting temperature	1,200°C–1,400°C	N/A
Deformation temperature	N/A	1,250°C
Bulk density	0.32–0.45 g/cm^3	0.14 g/cm^3
True density	0.85–0.95 g/cm^3	0.25 g/cm^3

Figure 6. Optical microscope image of CenoStar ES500 cenospheres with the hollow sphere morphology

Besides using cenospheres to provide closed porosities and thermal insulation, lightweight aggregates were also selected as another inclusion material to provide stability against excessive shrinkage during curing and firing, as shrinkage cracking has been reported by the literature as the major challenge for geopolymer-based materials [22–24]. Mulcoa 43LW from Imerys was recommended by Morgan Advanced Materials (Morgan) as the aggregates based on (1) its low specific gravity of about 1.7 g/cm^3 and low thermal conductivity of about 1 W/m·K at room temperature to minimize impact on overall thermal conductivity of the geopolymer composite, (2) its low iron content (<1.5 wt.% Fe_2O_3) for better chemical stability when wetted by molten salts,

This report is available at no cost from the National Renewable Energy Laboratory at www.nrel.gov/publications.

and (3) the higher mechanical stability compared to conventional lightweight aggregates of similar density. In fact, the Mulcoa 43LW particles themselves have about 40 vol.% porosity with more than half being closed porosity, which is ideal from the perspective of molten salt permeation resistance.

2.2.3 Lab-Scale Geopolymer Insulation Recipe Development

2.2.3.1 Geopolymer Synthesis Procedures

In general, the main ingredients of the geopolymers evaluated by this project are:

- Metakaolin, a calcinated form of the clay mineral kaolinite, to provide more reactivity of the alumina and silica for geopolymerization
- Cenospheres, to provide closed porosity for thermal insulation performance
- Sodium silicate and sodium hydroxide aqueous solution as an activator for the metakaolin to initiate the geopolymerization process
- Lightweight refractory aggregates to provide dimensional stability against shrinkage and crack propagation during higher-temperature heat treatment and final operation.

Sodium silicate and sodium hydroxide activator solution is usually prepared one day before the geopolymer synthesis. Reagent-grade sodium silicate pentahydrate ($Na_2SiO_3 \cdot 5H_2O$, ≥95% purity, Sigma Aldrich) is used for bench-scale testing at the National Renewable Energy Laboratory (NREL). Commercial-grade sodium silicate (K® Sodium Silicate, PQ Corporation) is used for production trials at Morgan. Note that the SiO_2:Na_2O wt. ratio for the reagent sodium silicate is about 0.97 while that for the K Sodium Silicate is about 2.88. The vastly different composition of the reagent-grade and commercial-grade sodium silicates requires compensation of Si or Na if the same geopolymer composition is to be targeted at NREL and Morgan. The dry ingredients are first mixed in a bench-scale 5-quart mixer for 5–10 minutes and then mixed with the activator solution for another 5–10 minutes before casting into a mold. The mold is then wrapped with plastic film for 1–2 days to avoid excessive dehydration before demolding for additional curing and subsequent high-temperature heat treatment. Curing is used to facilitate geopolymerization, which happens at room temperature or a slightly elevated temperature of 60°C–90°C. Chemically, geopolymerization is a polycondensation process where $Al(OH_4)^-$ and $SiO_2(OH)_2^{2-}$ ions combine to form bridging oxygen bonds and release water molecules. The bridging oxygen bonds then form the backbone of the polymer-like geopolymer structure.

2.2.3.2 Si-to-Al Ratio

Two key parameters for the geopolymer synthesis are the Si-to-Al atomic ratio and Al-to-Na atomic ratio. Because geopolymer is an alkaline aluminosilicate amorphous structure, the former ratio is believed to be correlated with the extent of the geopolymerization process. In a similar amorphous structure like glass, alkaline elements like Na and K are usually considered network modifiers that break down a bridging oxygen bond to compensate the +1 positive charge from the alkaline element [9]. Another way to compensate for the +1 positive charge is to combine it with an Al^{3+} ion to keep the charge neutrality (i.e., equivalent to a species with +4 charge). This is why the Al-to-Na ratio is another important factor, as both Al^{3+} and Na^+ ions can impact structural integrity.

This report is available at no cost from the National Renewable Energy Laboratory at www.nrel.gov/publications.

Figure 7 shows the bulk density vs. thermal conductivity (measured at 100°C) for geopolymer samples made at NREL, after standard curing procedure of 60°C for 7 days without additional higher-temperature treatment. The data point for a reference K-23 firebrick is also given. The results help explain (1) the effects of different ratios and (2) the impact of the ratios on thermal conductivity. Two observations should be noted:

1. There was a general trend of higher bulk density and thermal conductivity for higher Si-to-Al atomic ratio. It agreed with the literature expectation that higher Si-to-Al ratio leads to better geopolymerization and produces a denser geopolymer matrix. Such an argument seems to be corroborated by open porosity measurements with an isopropyl alcohol (IPA) immersion technique that resembles ASTM C830 where the open porosity was 28.41% ± 2.22% for 14 geopolymer samples with a Si-to-Al ratio between 1.16 and 1.24, whereas the open porosity was 21.40% ± 1.69% for five geopolymer samples[4] with a Si-to-Al ratio of around 2.
2. Despite different ratios and cenosphere additions, all data points roughly converged on a relatively straight line, which agrees with literature expectation for geopolymers [25]. This suggested a simple optimization criterion for thermal conductivity—bulk density. Bulk density is of particular interest because it is a macroscopic and easily measurable quantity. It indicates that if the targeting thermal conductivity is ~0.25 W/m·K, the optimal bulk density should be around 1 g/cm^3. Caution should be given here because all data points shown in Figure 7 came from geopolymers without high-temperature treatment. The relationship could shift if the geopolymers had not transitioned into their final phase, residual water was still present, and/or some open porosities had not been closed via high-temperature treatment.

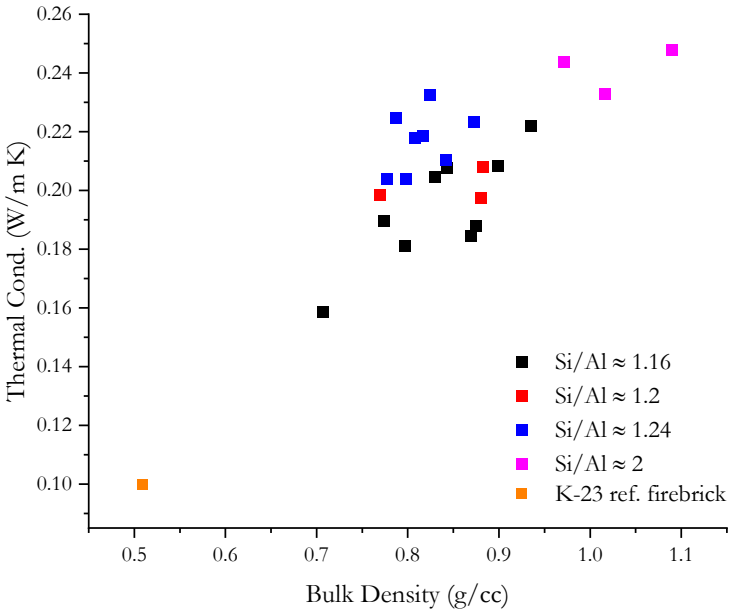

Figure 7. Bulk density vs. thermal conductivity geopolymer samples with different Si/Al atomic ratios

[4] Two samples were produced at NREL and three samples were produced at Morgan.

This report is available at no cost from the National Renewable Energy Laboratory at www.nrel.gov/publications.

2.2.3.3 Cenosphere Content

Several geopolymers at a Si-to-Al atomic ratio around 1.16 were synthesized with four different cenosphere (CS)-to-metakaolin (MK) ratios (0.95, 1.33, 1.74, and 2.24). Figure 8 shows a clear effect of cenosphere addition to reduce both the bulk density and thermal conductivity. The results confirmed the proposed method to tune thermal conductivity by optimizing the cenosphere content. Therefore, Figure 8 formed the basis of NREL's next effort of finding the maximum CS-to-MK ratio to achieve the lowest possible thermal conductivity. Although higher CS-to-MK ratio seems beneficial to thermal insulation, multiple practical factors limit the quantity of cenospheres that can be added:

1. When the cenosphere content is too high, there is not sufficient metakaolin binder and other additives during the mixing step to fill the interparticle spaces formed by the cenospheres. Hence, the interparticle spaces will absorb a significant amount of water, eventually leading to higher open porosity after curing.
2. When there is not enough metakaolin binder (i.e., Figure 6 resembles the most extreme case where no metakaolin binder is used), the structure of the resulting geopolymer will allow easy liquid permeation, and its mechanical strength will be significantly compromised.

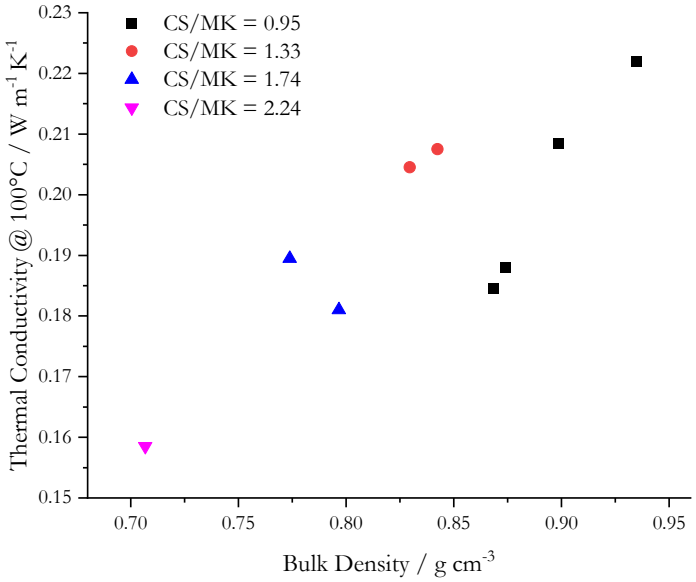

Figure 8. Bulk density vs. thermal conductivity for geopolymers at a Si-to-Al atomic ratio of about 1.16 and with different cenosphere-to-metakaolin ratios

Experimentally, NREL first made a trial in a simple system (with the activator liquid, metakaolin, and cenospheres only). In this case, the CS-to-MK weight ratio was very high at 2.24, and the weight fraction of cenospheres in the total solids was 69.1 wt.%. There were several straightforward observations during the mixing and casting stage: (1) a significant amount of additional water was needed to make the mixture workable, i.e., 0.5 g of additional water was added for each gram of activator solution used; (2) the solid/liquid activator mixture had a very high viscosity, and the mixing action before casting became noticeably more difficult; and (3) the viscous mixture did not flow easily into the mold. After 24 hours of curing at room temperature,

This report is available at no cost from the National Renewable Energy Laboratory at www.nrel.gov/publications.

it was clear that the geopolymer mixture was gritty (i.e., the cenosphere particles easily came off the geopolymer blocks), which was indicative of weak adhesion of the particles to the geopolymer matrix. These observations deemed that 69.1 wt.% of cenospheres in the solid portion was too high. NREL followed up with more recipes and found that in a simple activator-metakaolin-cenosphere system, the maximum CS-to-MK ratio was about 1.92, and the cenosphere wt.% was about 65%.

The next step was to find out if a higher content of cenospheres could be achieved with the help of some other solid additives. The first additive tested was an amorphous silica fume. Amorphous silica fume is believed to have a dual-function: (1) it can significantly increase the Si-to-Al ratio, and (2) it can significantly reduce water usage as shown by other refractory applications in the industry. To achieve a Si-to-Al ratio of 2, roughly 0.46 g of silica fume was needed for each gram of metakaolin. It was very interesting that by adding solid silica fume into the same recipe shown above, no additional water was needed at all. The Massachusetts Institute of Technology (MIT) and NREL both confirmed this function of silica fume by first producing a geopolymer mixture that was almost too dry to mix. Subsequent addition of silica fume particles actually made the dry mixture "wetter," which showed the fascinating nature of silica fume. In other words, adding solid silica fume made a mixture more liquid-like for easier casting. Table 2 shows the selected recipes used to investigate silica fume's effect on water usage. The numbers in the table are normalized to the amount of metakaolin to allow easier comparison. There are a few observations:

1. For Batches 3, 4, and 5, no additional water was needed because silica fume was used.
2. The mixture for Batch 5 was noticeably less viscous compared to Batch 4, which should be solely attributed to additional silica fume (almost 22% more silica fume added).
3. There was a general decrease of liquid-to-solid ratio down the list. The decrease reflected the benefit of silica fume addition to reduce water usage. which should eventually lead to lower open porosity as suggested by the literature.

Table 2. Selected Geopolymer Recipes Used To Investigate Silica Fume Effect on Water Usage Reduction

Batch #	Batch Size (g)	Total Activator	Additional Water	Metakaolin	Cenospheres	Silica Fume	CS-to-MK Ratio	CS wt.%	Liquid-to-Solid Ratio
		Normalized Weight (unitless)							
1	33.5	1.39	0.69	1.00	2.24	0.00	2.24	69.1%	0.641
2	68.1	1.95	0.26	1.00	1.92	0.00	1.92	65.7%	0.756
3	84.8	1.94	0.00	1.00	1.92	0.46	1.92	56.1%	0.575
4	168.3	1.94	0.00	1.00	2.40	0.46	2.4	62.1%	0.502
5	376.2	1.94	0.00	1.00	2.40	0.56	2.4	60.6%	0.490

To be rigorous, Table 2 did suggest a scale effect on water usage (as shown by the column "Batch Size"), i.e., more water was needed for smaller batch sizes, possibly due to higher water evaporation. Hence, the dry-out effect may skew the observation on total water usage. After discovering the potential errors, NREL switched to larger batch sizes for all future studies.

This report is available at no cost from the National Renewable Energy Laboratory at www.nrel.gov/publications.

2.2.3.4 Room-Temperature Curing Effect

Aggressive dehydration during the initial curing process at 25°C and 60°C was a concern, which could lead to cracking, as shown by early testing results. Therefore, geopolymer samples were cured while wrapped in plastic films, which aimed to control the activity of water vapor in the surrounding atmosphere and reduce the speed of dehydration. The downside of such a curing process was the possibility of insufficient curing. Therefore, NREL monitored the total mass of geopolymer samples during the curing process at 60°C for 7 days. Figure 9 shows the data for more than 10 samples. Negative numbers indicate daily weight loss due to water escape. Error bars indicate ±1 standard deviation. It is clear that the daily weight loss of these samples was fairly consistent. Most data points fell inside the range of 0.75–1.5 wt.% of mass loss per day, and there was no noticeable decrease as a function of curing time. The results simply indicated that 7 days of curing at 60°C (wrapped in plastic film) was not sufficient. This was a compromise between avoiding too-aggressive curing and achieving sufficient curing/complete geopolymerization.

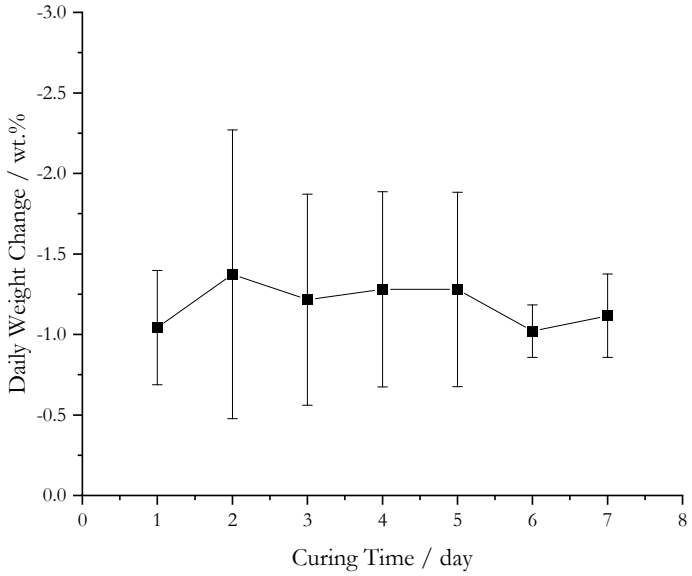

Figure 9. Seven-day daily weight change monitoring for NREL's geopolymer samples curing at 60°C while wrapped in plastic film. Negative numbers indicate daily weight loss due to water escape. Error bars indicate ±1 standard deviation.

Figure 10 shows the weight tracking of more geopolymer samples with different curing methods. All samples were cured for 7 days at 60°C while wrapped in plastic film. The samples were then cured using different methods after the initial 7 days of curing. The goal was to understand (1) the true curing period until the mass loss becomes stable and (2) whether there is a significant difference between different curing methods (e.g., 60°C vs. room temperature, wrapped vs. not wrapped). For almost all samples, the daily weight loss started to drop around Day 7 and Day 8. Around Day 10, the daily weight loss became almost negligible. In addition, the different curing methods used after the initial 7-day curing period did not make a significant impact on the overall curing. All samples followed a similar trend of daily weight loss. Upon closer inspection of Figure 10, we could only observe a slight difference between samples that were wrapped (black and green) and unwrapped (red, blue, and purple). The unwrapped samples were more affected by a few thunderstorms that happened around Day 9 and Day 10 when the daily weight change shifted

This report is available at no cost from the National Renewable Energy Laboratory at www.nrel.gov/publications.

toward slight weight gain as a result of much higher relative humidity in the lab.[5] Given the data in Figure 10, it can be assumed that once the geopolymer bricks are manufactured and cured for 7 days at 60°C while wrapped in plastic film to prevent too-aggressive water release, the bricks may be stored and transported under ambient environment before the next manufacturing process. There is even a possibility to slightly shorten the initial 7-day curing time to reduce the use time of curing ovens, thus increasing production rate and decreasing costs.

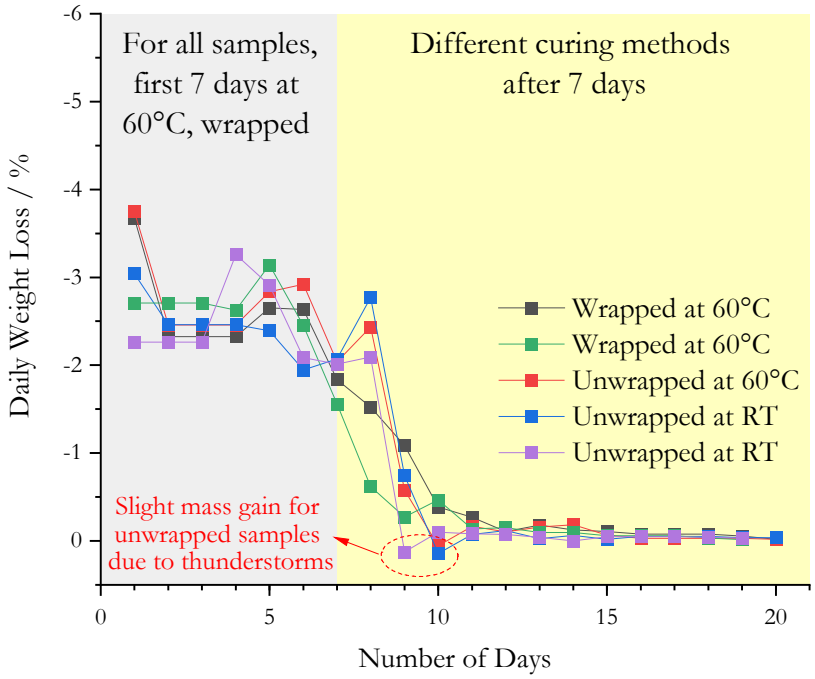

Figure 10. Twenty-day daily weight change monitoring of geopolymer sample curing at 60°C while wrapped in plastic film.

RT = room temperature

2.2.3.5 High-Temperature Firing Effect

NREL next investigated the effect of higher-temperature heat treatment to accelerate removal of residual water that was not driven off during the low-temperature curing process and complete the geopolymerization process to improve the geopolymer's properties such as higher compressive strength and lower open porosity.

Figure 11 shows the results of a comprehensive study on high-temperature treatment effect after the initial curing process on the geopolymers. To compare across samples, the mass, volume, and density data were normalized to the measured values right after curing at 60°C for 7 days. The dashed lines were used to indicate the rough trend for each quantity. Note that there were variations across different geopolymer samples (represented by different data point colors and shapes) because different recipes were used. The overall statistical scatter across all geopolymer groups was the highest for the normalized mass but the scatter was much smaller within individual

[5] Lab records showed an increase of relative humidity from 25% (during a typical dry day in Golden, Colorado) to >50% (during the thunderstorm days).

This report is available at no cost from the National Renewable Energy Laboratory at www.nrel.gov/publications.

geopolymer groups. The scatter for normalized density can be explained by the same reason (density = mass/volume). In general, the observed trends were consistent. First, because bulk density in

Figure 11(c) is proportional to mass and inversely proportional to volume, mass loss and volume shrinkage are competing factors for density calculation. It is necessary to look at mass and volume changes individually to understand what phenomena are responsible for the overall bulk density change. The bulk density change can be broken into three stages: (1) an initial decrease below 200°C, (2) relatively stable density between 200°C and 800°C, and (3) an upward increase above 800°C.

During the first stage (<200°C), a >15 wt.% mass loss dominated the change of bulk density, with a minor dimensional shrinkage of <5 vol.% as shown by the normalized volume in Figure 11(b).

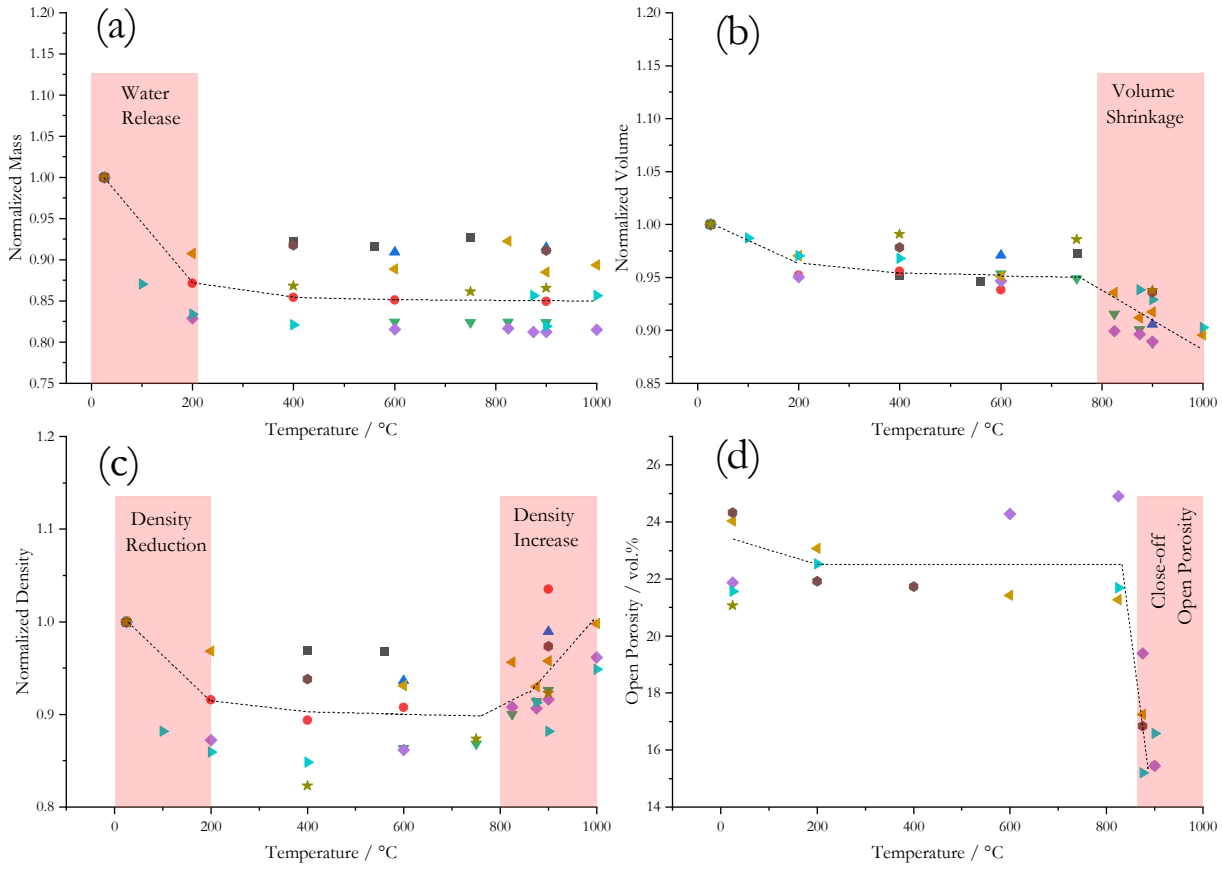

Figure 11. (a) Normalized mass, (b) normalized volume, (c) normalized bulk density, and (d) open porosity as a function of heat treatment temperature after curing at 60°C for 7 days

The initial decrease at up to 200°C is consistent with results in Figure 9, which suggests that there was residual water/moisture in the geopolymer after 7 days if only 60°C was used for curing. Note that open porosity in Figure 11(d) also seemed to decrease slightly (however, the magnitude of the change may be comparable to the measurement errors). The true decrease of open porosity in the geopolymer matrix was likely masked by the fact that NREL's samples had a significant amount of cenospheres added (which were unlikely to contribute to any open porosity decrease). In

This report is available at no cost from the National Renewable Energy Laboratory at www.nrel.gov/publications.

contrast, MIT focused on geopolymer matrix (i.e., without any cenosphere addition). MIT's result in Figure 12(a) shows that even during the first stage with low-temperature heat treatment (at 200°C–300°C), there was a noticeable decrease of open porosity. Figure 12(b), plotted in a different way, confirms that a higher Si-to-Al ratio led to a lower open porosity at any heat treatment temperature.

During the second stage (200°C–800°C), none of the quantities (mass, volume, density, and open porosity) changed significantly, which confirms that, for water removing/drying purposes, a lower-temperature heat treatment in the range of 200°C–300°C may suffice. This is important to know because the lower-temperature heat treatment may be completed during the CSP plant preheating stage (i.e., using the preheating to fully remove moisture).

During the third stage (above ~800°C), there was a noticeable reduction of sample volume (up to 8 vol.%). With almost no change in mass, it led to a noticeable bulk density increase. This is particularly important to the proposed molten salt application. The possible reasons for the shrinkage must be given. In a geopolymer system, there are three major components, metakaolin "binder," cenospheres, and additives/aggregates. At high temperature, cenospheres are known to be stable, which means volume shrinkage is likely not from cenospheres. In these early geopolymer samples, no aggregates were used. The only additive used was silica fume, which is a solid material with a low coefficient of thermal expansion at high temperature (because of its amorphous nature). Therefore, the only possible reason for the observed shrinkage was the closing of porosities in the geopolymer matrix that were initially introduced by dehydration during curing and lower-temperature heat treatment. This is corroborated by the open porosity measurement in

Figure 11(d) where a noticeable drop in open porosity almost coincides with the volume shrinkage above 800°C. The magnitude of the open porosity decrease is around 5–8 vol.%, which is larger than the typical measurement errors. Therefore, it is hypothesized that the decrease was due to true reduction of open porosity instead of inherent measurement error.

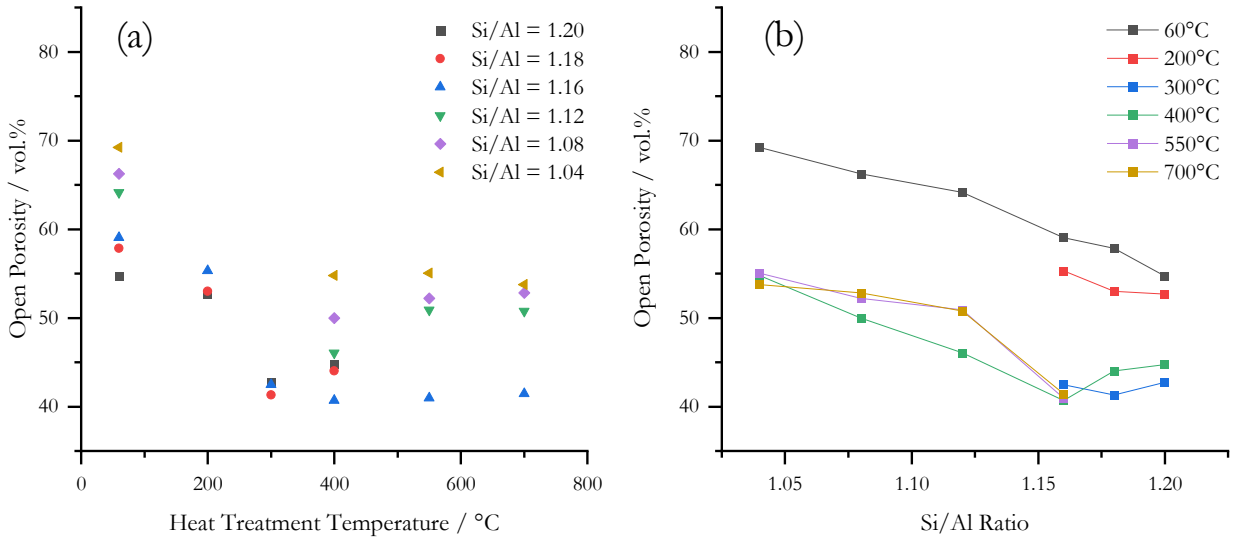

Figure 12. (a) Heat treatment temperature vs. open porosity at different Si-to-Al ratios and (b) Si-to-Al ratio vs. open porosity at different heat treatment temperatures

This report is available at no cost from the National Renewable Energy Laboratory at www.nrel.gov/publications.

The absolute bulk density data also reflected the benefit of cenosphere addition (Figure 13) even after high-temperature heat treatment. Although a direct comparison between cenosphere content and thermal conductivity is not available, the correlation between bulk density and thermal conductivity shown in Figure 7 and Figure 8 suggests that the benefit of using cenospheres to reduce thermal conductivity after heat treatment still holds.

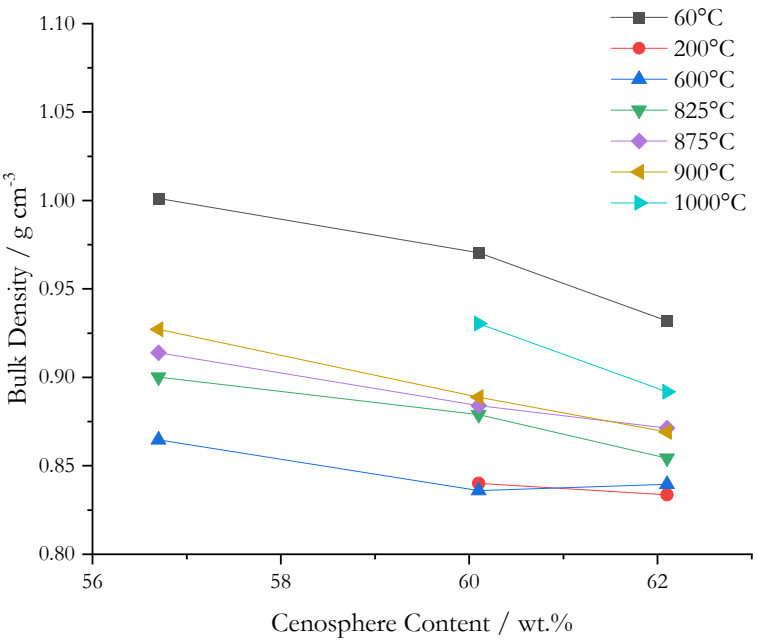

Figure 13. Relationship between cenosphere content and bulk density for various geopolymer samples after different heat treatment

As stated before, Figure 7 shows the bulk density vs. thermal conductivity for geopolymer samples without heat treatment. Here, the same relation in heat treated geopolymers is presented in Figure 14. For a quick comparison, "Line 1" indicates the bulk density vs. thermal conductivity relation in Figure 7. The two data points without any heat treatment fall on this line. However,

Figure 11 suggests that these untreated samples have remaining water. Drying at a low temperature such as 200°C should reduce the bulk density by ~10%. Therefore, it is anticipated that these two samples, after being fully cured, should have a density around 0.8–0.9 g/cm^3 and fall inside the dashed circle in Figure 14. They will serve as the new starting point to understand the high-temperature treatment effect on thermal conductivity, which follows "Line 2." Now, the thermal conductivity behavior of a geopolymer after high-temperature treatment can be roughly predicted. For example, if the goal is to make a geopolymer system with a bulk density ~0.9 g/cm^3 and ~15 vol.% of open porosity,[6] the anticipated thermal conductivity range is ~0.3 W/m·K. Note that the final optimal composition will have extra cenospheres, which should reduce the thermal conductivity while retaining a similar level of open porosity. For comparison, conventional firebricks with a similar 10–20 vol.% porosity (mostly open porosities) usually have a thermal conductivity that is 3–5 times higher than that of geopolymers with cenospheres. For example,

[6] Not including closed porosities which is the fundamental motivation for the geopolymer system, i.e., maximizing closed porosity for thermal insulation while minimizing open porosity for salt permeation resistance.

This report is available at no cost from the National Renewable Energy Laboratory at www.nrel.gov/publications.

Morgan's Kao-tuff CV firebrick has a comparable total porosity of ~21.5 vol.% but with a higher thermal conductivity of 1.3 W/m·K; the SR-90 firebrick has a comparable porosity around 18 vol.% but with an even higher thermal conductivity of >3 W/m·K; the Kaolite 2200 firebrick has a comparable low thermal conductivity around 0.21 W/m·K but with a much higher porosity at 56.8 vol.%. This means that the concept of introducing closed porosities by cenosphere addition in a geopolymer matrix is competitive in terms of thermal insulation performance. The composite geopolymer insulation may be one of the first refractory insulations that can simultaneously achieve (1) 10–20 vol.% open porosity, (2) ~0.3 W/m·K thermal conductivity, (3) a light weight of about 1 g/cm^3 bulk density, and (4) >20 MPa cold crush strength, i.e., >20,000 N·m/kg strength-to-weight ratio.

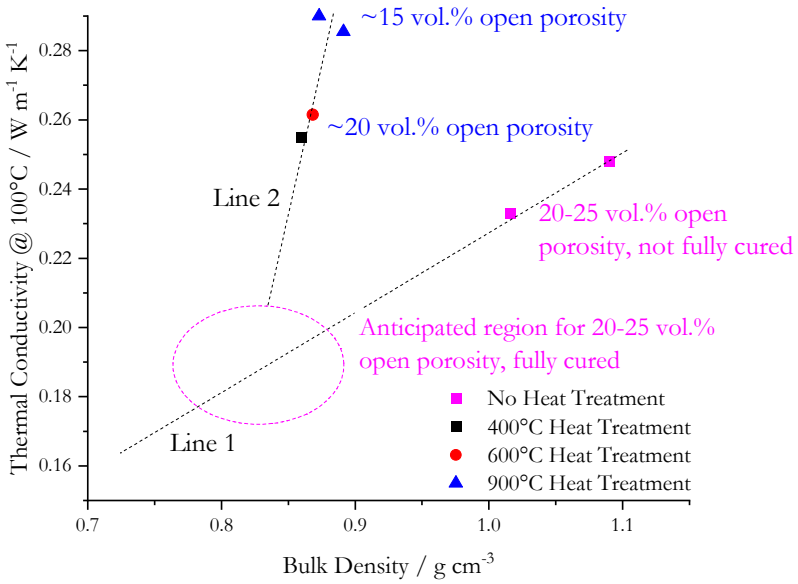

Figure 14. Bulk density vs. thermal conductivity for geopolymer samples showing the effect of higher-temperature treatment

The results in Figure 12 already give a hint on how to minimize open porosity. It is evident that an increase of Si-to-Al ratio from 1.04 to 1.20 reduced the open porosity of the geopolymer samples under all treatment conditions (e.g., 60°C curing without any high-temperature treatment, heat treatment at 400°C, 550°C, and 700°C). More importantly, those samples were the simplest, i.e., only made with metakaolin and activator and without any effects from cenospheres and aggregates. The trend observed could be directly applied because the design strategy was to separately optimize the geopolymer matrix and the aggregate additions.

The effect of cenosphere addition on the reduction of open porosity was also studied. The effect seemed to be twofold. First, the addition of cenospheres displaced the geopolymer matrix; hence, it physically limited the volume where open porosities could reside. This is the simplest mechanism of open porosity reduction as observed experimentally. As a secondary effect, the addition of cenospheres could improve the particle packing and reduce water usage during mixing, which will ultimately lead to lower open porosity. Like Figure 12(a), Figure 15 shows the open porosity in geopolymer samples with and without cenosphere addition. The result confirmed the cenosphere addition effect. It also supported the observed effect of Si-to-Al ratio on open porosity in geopolymer samples with cenosphere addition, similar to results shown in Figure 12(b).

This report is available at no cost from the National Renewable Energy Laboratory at www.nrel.gov/publications.

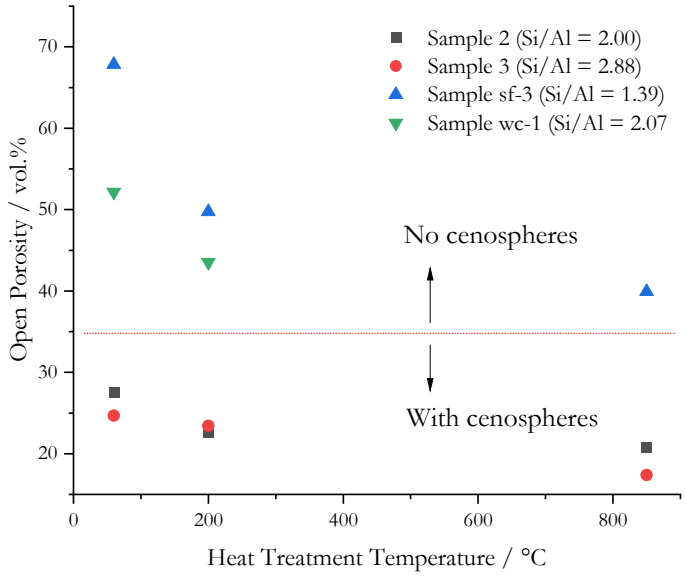

Figure 15. Open porosity for geopolymers with and without cenospheres and at different Si-to-Al ratios

Besides reducing open porosity, cenospheres also improve the mechanical properties of the geopolymers. Figure 16 summarizes the cracking behaviors of different geopolymer samples with (Sample 2 and Sample 3) and without cenosphere addition (Sample sf-3 and Sample wc-1), heat treated at different temperatures. It clearly shows the advantage of using cenospheres because very little cracking was observed for Sample 2 and Sample 3, whereas cracking already occurred at 200°C for Sample sf-3 and Sample wc-1.

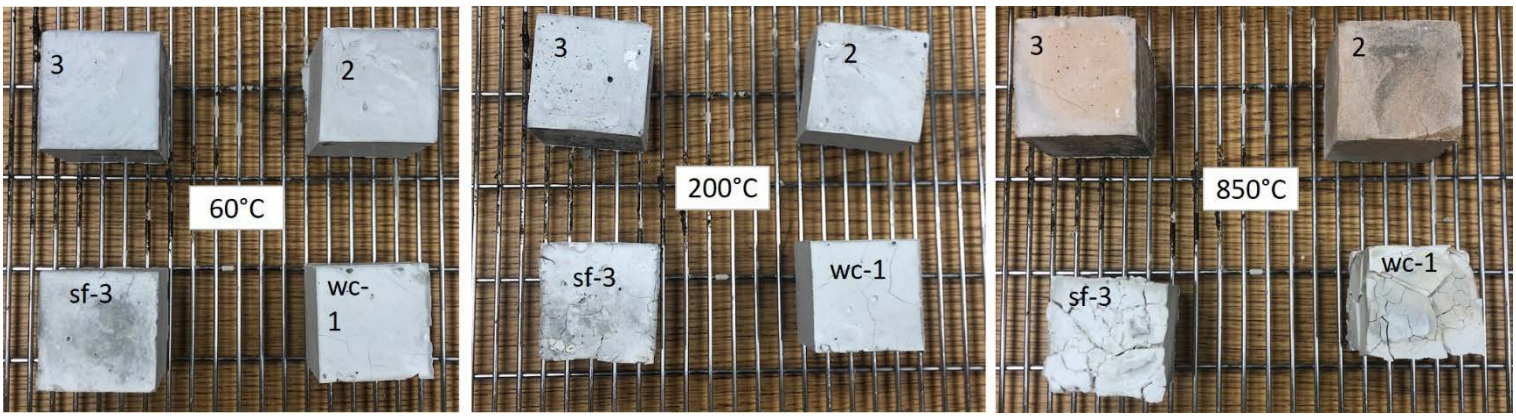

Figure 16. Cracking behaviors at different temperatures for geopolymer compositions with and without cenosphere addition

To summarize, optimal curing and heat treatment is likely a two-step process where the geopolymers will first be fully cured (based on mass change) at a lower temperature of 200°C–400°C and later heat treated at a higher temperature of 800°C–900°C to minimize open porosities. In addition, heat treatment of insulation materials above the anticipated service temperature of an application is a common practice in the refractory industry. It could expose any potential production issues and allow quality assurance measures to prevent premature cracking before

This report is available at no cost from the National Renewable Energy Laboratory at www.nrel.gov/publications.

deploying the insulation to service. The real needs for a high-temperature treatment to reduce open porosity will be determined based on molten salt testing results (discussed later).

2.2.3.6 Geopolymer Recipes

The discovery presented in the previous sections provided a baseline recipe for Morgan to study the effects of aggregates. To summarize, Morgan's study revealed the ideal geopolymer composition with (1) a Si-to-Al atomic ratio of ~2, (2) an Al-to-Na atomic ratio of ~1, (3) CS-to-MK ratio of 2.4, (4) a targeted bulk density of 0.9–1 g/cm^3, and (5) a targeted thermal conductivity of <0.3 W/m·K (when measured at 100°C). Table 3 summarizes 10 geopolymer recipes investigated by Morgan.

Table 3. Summary of Morgan's Geopolymer Study

Ingredients (g)		GP-10	GP-11	GP-12	GP-13	GP-14	GP-15	GP-18	GP-19	GP-20	GP-21
Solid	IMERYS MetaKaolin	20.44	16.10	16.10	16.10	15.33	16.10	15.15	15.15	15.15	15.15
	ES500 RMS Microspheres	35.76	28.18	28.18	28.18	31.59	33.18	36.30	36.30	36.30	36.30
	Mulcoa 43LW Aggregate (4X8)		9.36	9.36		8.91		4.23	4.23	4.23	4.23
	Mulcoa 43LW Aggregate (8X14)		5.58	5.58		5.31		2.63	2.63	2.63	2.63
	Mulcoa 43LW Aggregate (-14M/F)		6.29	6.29		5.99		2.82	2.82	2.82	2.82
	Poraver Expanded Glass (0.25-0.5)				21.23		16.23		1.91		1.91
	A-1000 Silica Fume									5.00	5.00
	Additive 1			0.150							
	Additive 2			0.050							
	Additive 3			0.15							
Liquid	Sodium Silicate (K Brand)	36.43	28.70	28.70	28.70	27.33	28.70	27.00	27.00	27.00	27.00
	Sodium Hydroxide (10M)	7.36	5.80	5.80	5.80	5.52	5.80	5.46	5.46	5.46	5.46
Total Weight		99.99	100.01	100.36	100.01	100.00	100.01	93.59	95.50	98.59	100.50
Key Parameters											
Additional Water (wt.%)		0.00	2.10	1.60	12.40	3.90	11.10	6.50	7.00	0.00	4.10
Al/Na molar ratio		1.00	1.00	1.00	1.00	1.00	1.00	1.00	1.00	1.01	1.01
Si/Al molar ratio		1.96	1.96	1.96	1.96	1.96	1.96	1.96	1.96	2.49	2.49
CS to MK mass ratio		1.75	1.75	1.75	1.75	2.06	2.06	2.40	2.40	2.40	2.40
CS Weight Fraction		0.64	0.43	0.43	0.43	0.47	0.51	0.59	0.58	0.55	0.53
Measured Properties											
Bulk Density after 25°C curing (g/cc)		1.09	1.23	1.25	0.91	1.18	0.93	1.04	1.02	1.14	1.12
Bulk Density after 60°C curing (g/cc)		0.99	1.13	1.09	0.88	1.09	0.83	0.95	0.94	1.09	1.04
Open porosity (vol%) before HT (by Morgan)		15.2	14.4	16.7	21.9	16.3	22	20.3	20.6	10.2	14.4
Open porosity (vol%) before HT (by MIT)		19.65	20.34	21.1	26.23	N/A			N/A		
Compressive strength (MPa) before HT		22.8	22.9	15.5	3.4	24.2	3.9	14.8	12.1	20.3	9.1

The reasoning for these selected recipes and key experimental observations are as follows:

1. GP-10 was selected as the first benchmark with a simple recipe that has metakaolin and cenospheres as the only solid ingredients. This recipe had a desired Si-to-Al ratio of ~2, a desired Al-to-Na ratio of ~1, a cenosphere weight fraction of 64% in the solid ingredients (which was close to the values presented in Table 2), and, most importantly, no need for additional water. The measured properties also fell into the targeted range. The bulk density after 60°C curing was about 0.99 g/cm^3; the open porosity was about 20 vol.%; the compressive strength was 22.8 MPa. Therefore, GP-10 served as a good benchmark.
2. In the second group test, GP-11 to GP-13 were studied to understand the effect of three groups of aggregates: Mulcoa 43LW aggregates, proprietary Additives 1–3, and Poraver expanded glass.

This report is available at no cost from the National Renewable Energy Laboratory at www.nrel.gov/publications.

a. GP-11 incorporated Mulcoa 43LW aggregates at a total weight fraction of 21.2 wt.% without changing any other key parameters. The aggregates did not significantly affect the open porosity or the compressive strength, but they did increase the density by ~10% which is reasonable because the Mulcoa 43LW aggregates were denser at >1.73 g/cm^3. However, the major benefit of Mulcoa 43LW aggregates was not reflected in Table 3. Morgan had shown that having coarse aggregates did improve cracking resistance at high temperatures. Therefore, it was decided to keep the Mulcoa 43LW aggregates, even though the benefits on open porosity and compressive strength were not significant.

b. GP-12 was tested with almost the same composition as GP-11, except that several of Morgan's proprietary Additives 1–3 were added at a very low level of 0.35 wt.%. However, a noticeable decrease of compressive strength from >22 MPa to ~15 MPa was observed. The proprietary additives were very basic (pH > 10), which might have had a negative impact on the geopolymerization process and weakened the geopolymer samples. For this reason, Additives 1–3 were no longer considered.

c. GP-13 was very similar to GP-11, except that all Mulcoa 43LW aggregates were replaced by Poraver expanded glass. This substitution had a major effect on properties: a substantial amount of extra water (12.4 wt.%) was needed to make the mixture workable before casting; the open porosity also increased by ~5 vol.%; the compressive strength was significantly compromised (reduced from >22 MPa to <5 MPa). The only positive effect was the reduction of bulk density to less than 0.88 g/cm^3, one of the lowest values observed, because the Poraver expanded glass had a low bulk density at 0.34 ± 0.03 g/cm^3 (even lower than that of the CenoStar ES500 cenospheres). For these reasons, expanded glass additives were no longer considered.

3. The third group test (GP-14 and GP-15) aimed to increase cenosphere addition by increasing the CS-to-MK ratio from 1.75 to 2.06 and by increasing the cenosphere weight fraction in solids from 43% to 51%.

   a. GP-14, compared to GP-11, required slightly more water usage because more low-density cenospheres were used. It also had a lower bulk density and comparable open porosity and compressive strength. The results of GP-14 suggest that there was likely more room to increase cenosphere content in a metakaolin-cenosphere-aggregate system.

   b. Similar to GP-13, GP-15 required lots of water addition (at 11.1 wt.%) and had a very low compressive strength of 3.9 MPa, even when the total Poraver expanded glass was reduced by more than 25%. The GP-15 result again confirmed that the usage of Poraver expanded glass should not be considered.

4. The last group test (GP-18 to GP-21) aimed to further optimize the composition by (1) reducing Mulcoa 43LW aggregates to <10 wt.%, (2) increasing cenosphere weight fraction to 59% (GP-18), (3) adding a minor amount of Poraver expanded glass at <2 wt.% (GP-19), and (4) adding a small amount of amorphous silica fume at ~5 wt.% to reduce water usage and increase Si-to-Al ratio to ~2.5. It is clear that additional solid silica fume did decrease the water usage significantly (by comparing GP-20 to GP-18, and GP-21 to GP-19).

This report is available at no cost from the National Renewable Energy Laboratory at www.nrel.gov/publications.

5. Morgan also investigated a few geopolymer samples with a CS-to-MK ratio of more than 2.5 and a cenosphere weight fraction of more than 61% (not shown in Table 3). Both samples required a significant amount of water of 9.3 wt.% and 11.5 wt.%, and the final mixtures were still too dry to be suitable for casting. The resulting compressive strength was <5 MPa. The results suggested a limit of cenosphere addition because a small increase of cenosphere weight fraction from 59% (GP-18) to 61% caused substantially different behaviors.

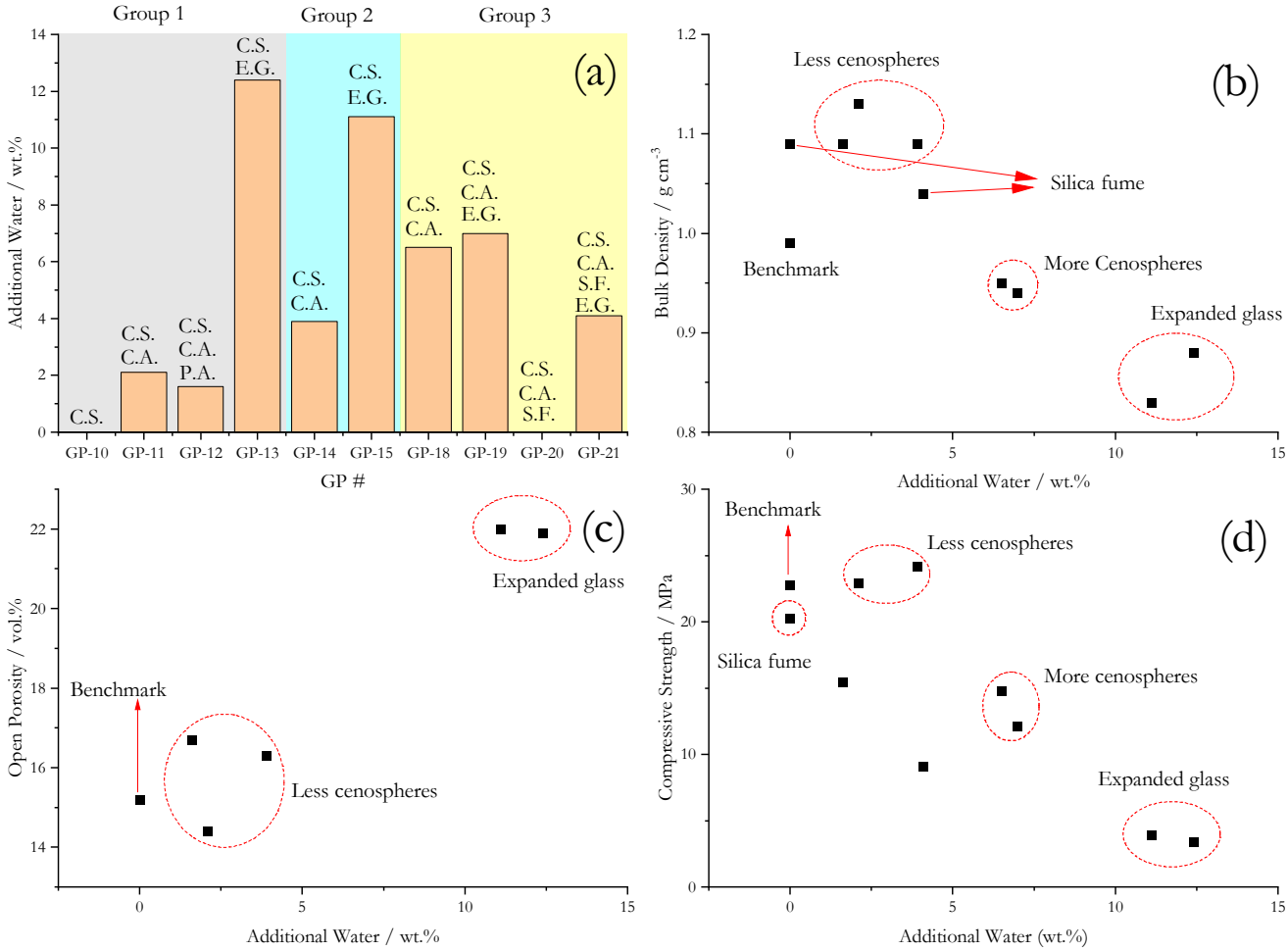

Figure 17. (a) Additional water use for geopolymer samples, (b) bulk density vs. additional water usage, (c) open porosity vs. additional water usage, and (d) compressive strength vs. additional water usage for geopolymer recipes investigated by Morgan.

C.S. = cenospheres; C.A. = coarse aggregates; P.A. = proprietary additives; E.G. = expanded glass; S.F. = silica fume

Figure 17 presents the findings graphically.

Figure 17(a) shows the total additional water usage. Different ingredients/additives are presented as cenospheres (C.S.), coarse aggregates (C.A.), proprietary additives (P.A.), expanded glass (E.G.), and silica fume (S.F.). In groups 1 and 2, coarse aggregates slightly increased water usage, and expanded glass significantly increased water usage. In group 3, comparisons between GP-18

This report is available at no cost from the National Renewable Energy Laboratory at www.nrel.gov/publications.

and GP-19 and between GP-20 and GP-21 showed that expanded glass increased water usage. Comparisons between GP-18 and GP-20 and between GP-19 and GP-21 showed that silica fume significantly decreased water usage.

Figure 17(b)– (d) summarize the effect of additional water usage on bulk density, open porosity, and compressive strength. The major reason for the observed variation from the benchmark (GP-10) behavior is given in each figure. It is very intriguing to see that all three properties had a strong correlation to additional water usage regardless of the types and amounts of additives used. It should be noted that

Figure 17 shows the properties without any high-temperature treatment. Therefore, the potential risk of geopolymer cracking was not reflected, which may be a major reason to include coarse aggregates.

In conclusion, the most promising compositions, based on all testing results, were GP-10 (benchmark) and GP-20. GP-10 had (1) one of the highest cenosphere contents of 64 wt.% to achieve better thermal insulation, (2) one of the highest compressive strength values of 22.8 MPa, (3) one of the lowest open porosity values of 15.2 vol.%, and (4) an average bulk density of 0.99 g/cm^3 (indicating acceptable thermal conductivity). The only drawback for GP-10 is the possibility of sample cracking at high temperature because this composition did not have any coarse aggregates. Morgan showed that coarse aggregates could improve high-temperature (above 1,000°C) cracking resistance. The next best composition is GP-20, which had relatively balanced properties as well: (1) ~55 wt.% of cenospheres to achieve low thermal conductivity in the range of 0.2–0.3 W/m·K (estimated based on thermal conductivity vs. bulk density relation from Figure 14), (2) the lowest open porosity of ~10 vol.%, (3) ~20 MPa of compressive strength, and (4) 1.0–1.1 g/cm^3 bulk density. The compositions of both GP-10 and GP-20 were selected by Morgan for production trials in larger batches. It was decided to investigate the temperature effect on these GP-10 and GP-20 compositions at four temperatures: 400°C, 720°C, 900°C, and 1,050°C. A temperature of 400°C is an intermediate operating temperature of molten salt TES tanks. The results at 400°C will also inform the possibility of using tank preheating and normal operation to achieve sufficient heat treatment. A temperature of 720°C is the upper operating temperature for geopolymer insulation in a Gen3 molten salt TES tank. A temperature of 900°C is the onset of the final stage of property changes (see

Figure 11). A temperature of 1,050°C is close to the upper use limit of the geopolymer recipes based on preliminary firing experiments.

2.2.3.7 Other Additives

A major cost component of the candidate geopolymer compositions is expected to be the labor associated with the long curing process. At lab scale, this curing process involved drying the sample in the mold wrapped in plastic film at room temperature for 24 hours, releasing the sample from the mold and drying at 60°C for 7 days, and heat treating the sample at various temperatures. On an industrial scale, the first room-temperature drying step (usually called setting) takes much

This report is available at no cost from the National Renewable Energy Laboratory at www.nrel.gov/publications.

longer for two reasons. First, the geopolymer bricks are much bigger than lab samples,[7] which usually means that water release during setting takes more time. Second, because of the larger size, the geopolymer bricks need to have ample strength before they can be safely released from the mold without deformation; otherwise, even normal handling will likely damage the bricks before the 60°C curing step, during which the bricks are supposed to gain more mechanical strength. A long setting time also means that a large number of molds will be required, and floor space could become an issue for large-volume production. Both could contribute to a higher final price of the geopolymer insulation.

Based on Morgan's suggestion, an aluminum-phosphate-based additive, FABUTIT 748 from Budenheim, Germany, was investigated to accelerate the initial setting. FABUTIT 748 is known to speed up setting of alkaline silicate refractory bricks. The exact chemical reason of why FABUTIT 748 accelerates setting of alkaline silicates is not well-known to the public. But to a first-order approximation, phosphorus in the form of phosphate has a 5+ valency. It usually means that P may serve as a network former in a silicate system, which should strengthen the silicate backbone. Similarly, in the geopolymer system, which has a similar aluminosilicate backbone, phosphate should also serve as a network former and accelerate the curing process by forcing the dehydration reaction when a bridging oxygen is formed. Therefore, it is hypothesized that the addition of FABUTIT 748 has a dual-function: (1) reducing setting time and (2) improving the mechanical and chemical strength of the geopolymers.

Table 4 summarizes the setting time of standard GP-10 and GP-20 compositions with different levels of the FABUTIT 748 addition. It can be seen that FABUTIT 748 addition between 1.5 wt.% and 3% was effective at reducing setting time for standard GP-10 and GP-20. Although more addition at 6 wt.% could dramatically reduce the setting time to 2 hours (tested for GP-10 only), a major side effect was the excessively aggressive dehydration, which led to warping and cracking. Therefore, the optimal FABUTIT 748 addition was believed to be around 3 wt.%.

Table 4. Setting Time for Standard GP-10 and GP-20 Compositions With Different FABUTIT 748 Additions

Setting Time for Samples With FABUTIT Additions (Hours)					
FABUTIT wt.%	0%	1.5%	1.7%	3%	6%
GP-10	72		72		2
GP-20	48	24-48		18	

2.2.4 Lab-Scale Geopolymer Mortar Recipe Development

A key question for the implementation of geopolymer insulation bricks is the selection of mortar material. Given the unique properties of the geopolymer bricks, NREL and Morgan developed a geopolymer-based mortar material. The mortar had a very similar chemistry compared to the geopolymer bricks, except it did not have the cenospheres, silica fume, and the FABUTIT phosphate. Table 5 shows an example recipe for a geopolymer mortar developed and tested at

[7] Morgan's early production trials made 9-in. × 4.5-in. × 4.5-in. and 9-in. × 2-in. × 2-in. bricks compared NREL's 2-in. × 2-in. × 2-in. samples. For ASTM C201 thermal conductivity tests, Morgan made even larger 18-in. × 18-in. × 4.5-in. samples.

This report is available at no cost from the National Renewable Energy Laboratory at www.nrel.gov/publications.

Morgan. NREL's mortar development and testing used different sodium silicate to match the overall composition.

Table 5. Example Recipe of a Geopolymer Mortar Developed and Tested at Morgan

Ingredients	Weight Percentage
IMERYS Metakaolin	14.99
K® Sodium Silicate	21.42
10 M NaOH Solution	8.03
48 M/F Kyanite	38.89
100 M/F Mulcoa 60	16.67

The main rationale behind the geopolymer-based mortar is the similar composition to the geopolymer bricks for better chemical compatibility and match of thermal expansion behavior to ensure a stable interface. In addition, the geopolymer insulation liner is envisioned to be partially saturated by molten salt. Hence, there is no requirement of the geopolymer mortar to be resistant to molten salt permeation. It is a main design advantage over traditional hot face liner design where a chemically, mechanically and thermally stable mortar with molten salt permeation resistance is required but very challenging to design from the materials perspective.

A similar synthesis method was used to make and apply geopolymer mortars. Figure 18 shows a geopolymer mortar joint during mortar application (left), a few minutes after mortar application (middle), and after 720°C heat treatment (right). The mortar joint was left in an ambient atmosphere without any wrapping during the entire testing period to simulate the field application where the mortared bricks are exposed to ambient atmosphere all the time. Just a few minutes after mortar application, the mortared joint started to gain strength, and it could not be easily bent or twisted by hand. After 7 days of curing in ambient atmosphere and temperature, the mortared joint was heat treated at 720°C to simulate the highest operating temperature of the geopolymer liner in a molten salt TES tank. After the heat treatment, only a few surface cracks were observed, and the mortar joint could not be broken either by bending or twisting. The preliminary results were very encouraging before rigorous mechanical testing.

This report is available at no cost from the National Renewable Energy Laboratory at www.nrel.gov/publications.

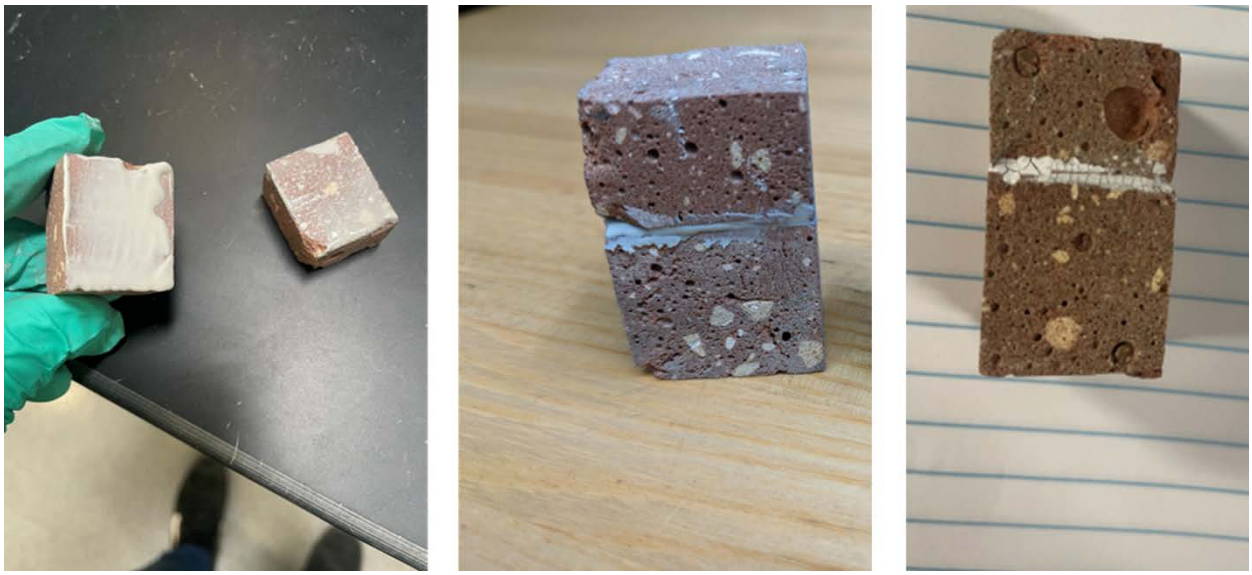

Figure 18. A geopolymer mortar joint during mortar application (left), shortly after mortar application (middle), and after 720°C heat treatment (right)

It is important to understand the working time of the mortar. In the field, workers usually mix mortar raw materials and start to apply mortar to bricks until the mortar mixture dries out. The working time of the mortar determines the time frame. This is an important parameter to know because it will help explain how much mortar material should be prepared for each mortar batch based on how fast the workers can apply mortars.

Table 6 and Figure 19 present the timeline for the geopolymer mortar mixing experiment, which shows the rough working time of the mortar mixture.

Table 6. Mortar Drying Time for the Geopolymer-Based Mortar Developed at NREL

Time After Initial Mixing (min)	Observations	Comments
10	Mortar is workable	
15	Comparable consistency to minute 10	Applied to the first set of bricks
20	Mortar becomes thicker	
50	Mortar becomes thicker and stronger	Applied to the second set of bricks
120	Mortar becomes “frozen”	

This report is available at no cost from the National Renewable Energy Laboratory at www.nrel.gov/publications.

Figure 19. Pictures showing the drying of the mortar as a function of drying time

Based on the information from Table 6 and Figure 19, it was determined that the working time for the mortar was 60–90 minutes. For reference, the shortest working time for a mortar that can be used in the field is significantly lower, at about 10–15 minutes. Hence, the geopolymer mortar should be suitable for field application. In addition, the mortar will be shipped as "dry mortars," meaning the wet and dry components are not premixed before shipping to prevent reactions. The workers will open different containers of raw materials and mix on-site following the recipe. The main reason is that the geopolymer mortar will set slowly after mixing with the activator, so premixed "wet mortars" should be avoided. Additionally, dry mortars are usually easier and cheaper to ship because no chemical reactions occur during shipping.

Figure 20 shows the picture of (a) a mortar joint made of non-heat-treated geopolymer bars, (b) a reference geopolymer bar with heat treatment at 1,050°C, and (c) a mortar joint made of heat treated geopolymer bars at 1,050°C, all made at Morgan's facility. The mortar joints showed similar behaviors compared to NREL's mortar tests above.

This report is available at no cost from the National Renewable Energy Laboratory at www.nrel.gov/publications.

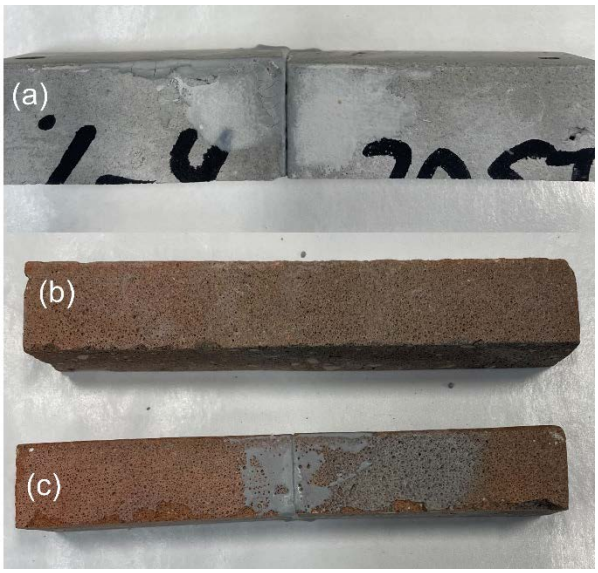

Figure 20. Pictures of (a) a mortar joint made of non-heat-treated geopolymer bars, (b) a reference geopolymer bar with heat treatment at 1,050°C, and (c) a mortar joint made of heat treated geopolymer bars at 1,050°C

Morgan performed quantitative mechanical testing using a four-point bending setup (Figure 21) to measure the modulus of rupture (MOR).

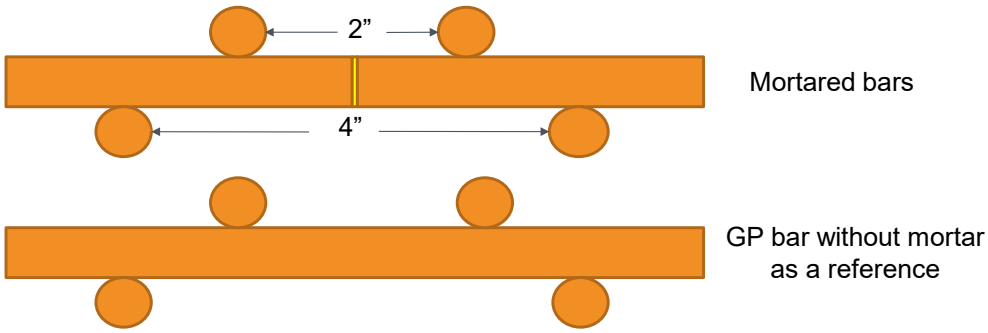

Figure 21. Schematic of the four-point bending test setup to measure the modulus of rupture of a geopolymer (GP) mortar joint

Table 7 shows the summary of the MOR measurements for the mortar joints shown in Figure 20. Figure 22 is a picture summary of the post-bending geopolymer samples without and with a mortar joint. It shows the failure location and failure mode of the tested samples.

Table 7. Summary of the Modulus of Rupture (MOR) Measurements for Reference GP-20-3 Bars and Mortared GP-20-3 Joints

Test Sample	Brick Firing Condition	Heat Treatment on Mortar	MOR Results
Mortared unfired bricks	No firing	No	1.20 MPa
Reference brick (no mortar)	1,050°C	No	1.25 MPa
Mortared fired bricks	1,050°C	No	0.51 MPa

This report is available at no cost from the National Renewable Energy Laboratory at www.nrel.gov/publications.

It should be noted that the mortared geopolymer bricks without 1,050°C firing was almost as strong as the reference brick, which showed great potential for the mortar to be mechanically strong and suitable for holding the geopolymer bricks in TES tanks. More information could be extracted from Figure 22 to confirm such a claim. Note that at the failure interface, a part of the unfired + mortared brick was pulled out by the mortar (see the red dashed circles), which indicated that the mortar and the mortar/geopolymer interface at that portion of the mortar joint was stronger than the geopolymer brick.

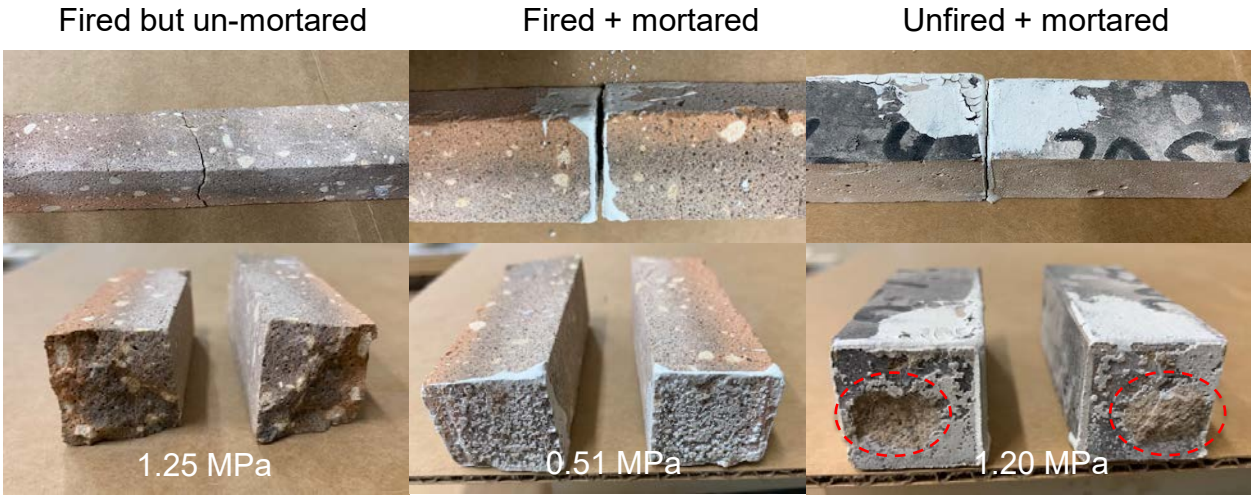

Figure 22. Picture summary of post-bending GP-20-3 samples without and with mortar joint subject to different firing conditions. The red dashed circles show where a part of the unfired + mortared bar was pulled out by the mortar.

As a reference, a recommended mortar for the Gen3 molten chloride TES tank liner, Steuler acid mortar S 50 HF, has a compressive strength of 40 MPa and a flexural strength of 13.5 MPa. The reported flexural strength value is the inherent flexural strength of the acid mortar. No flexural strength is available when the acid mortar is used to join two refractory bricks together for the bending test. Based on early testing of the metakaolin-only geopolymer bricks,[8] geopolymer mortar is expected to have 20–30 MPa compressive strength. In summary, the MOR measurements for the mortar joints suggested promising bonding behavior of the geopolymer mortar to geopolymer bricks. More mechanical testing results are reported in a later section.

2.2.5 Room-Temperature Materials Properties

2.2.5.1 Bulk Density and Mechanical Strength

Table 8 summarizes the physical and mechanical properties for standard GP-20 with FABUTIT 748 and extra water. Measured properties include bulk density, MOR, cold crush strength (CCS), permanent linear change, and open porosity. Extra water was added to some samples to tune the workability for large-volume production. The key observations are given below.

[8] It is reasonable to compare metakaolin-only geopolymer bricks to geopolymer mortars because they have very similar chemistry and recipe.

This report is available at no cost from the National Renewable Energy Laboratory at www.nrel.gov/publications.

Table 8. Summary of Physical and Mechanical Properties for Standard GP-20 With FABUTIT 748 Additive and Extra Water

	GP-20	GP-20 With 2.9% Water	GP-20 With 3% FABUTIT	GP-20 With 3% FABUTIT and 2.7% Water
Sample Preparation Method				
	Tamped	Cast Vibrated	Tamped	Cast Vibrated
Setting Time (hour)				
	48–72	72	18	16–18
Bulk Density (g/cc)				
Air Cured	1.09	1.07	1.14	1.1
60°C (7 days)	0.95	1.01	0.98	0.98
400°C (5 hours)	0.92	0.9	N/A	0.89
MOR (MPa)				
400°C Heat Treatment	1.55	0.96	N/A	2.79
CCS (MPa)				
400°C (Soaps)	N/A	18.74	N/A	23.98
400°C (Cubes)	16.19	N/A	N/A	17.00
Linear Shrinkage (%)				
Ambient to 60°C	-1.2	-0.7	-0.9	-0.4
60°C to 400°C	-0.7	-0.6	N/A	-1.0
Open Porosity by IPA Method (vol.%)				
60°C Curing	12.1	11.4	13.7	N/A
400°C Heat Treatment	10.9	N/A	12.2	16.3

- About 2.7–2.9 wt.% of extra water was needed in GP-20 to allow casting.
- The bulk density decrease due to extra water addition was minimal (i.e., less than 0.03 g/cc from 0.92 g/cc).
- Addition of 3% FABUTIT 748 slightly increased bulk density (by comparing GP-20 with GP-20 with 3% FABUTIT 748), which qualitatively corroborated the hypothesis about phosphate being a network former. The effect of FABUTIT 748 on bulk density seemed minimal when there was already 2.7–2.9 wt.% of extra water added.
- In terms of modulus of rupture, GP-20 with 3% FABUTIT 748 and 2.7% water had the highest value at 2.79 MPa. Although there was no data point for GP-20 with 3% FABUTIT, a higher value was expected.
- For CCS, GP-20 with 3% FABUTIT 748 and 2.7% water had the highest value.
- In terms of open porosity measured by the IPA method, there was also no major compromise due to the addition of FABUTIT and extra water. All values fell into the

This report is available at no cost from the National Renewable Energy Laboratory at www.nrel.gov/publications.

expected range of 10–20 vol.%. Note that the open porosity was likely the property prone to the highest experiment errors.[9]

Based on these observations, GP-20 with ~3% FABUTIT 748 and additional water was selected for further investigation because the additives accelerated setting to reduce labor and equipment costs and improved manufacturability by enabling casting, both of which are preferred by large-scale production.

Table 9 summarizes the physical and mechanical properties of GP-20 with 3% FABUTIT 748 and 2.7%–2.9% extra water when heat treated at different temperatures. The heat treatment temperatures investigated were selected based on the molten salt immersion tests (discussed later). Empty cells indicate that there are no data available.

Table 9. Summary of the Physical and Mechanical Properties of GP-20 with 3% FABUTIT 748 and 2.7%–2.9% Extra Water

Properties	Sample Type or Technique Type	Heat Treatment Temperature						
		400°C	950°C	1,000°C	1,050°C	1,100°C	1,150°C	1,200°C
Bulk Density (g/cc)	Soap Sample	0.89		0.96		0.91		
	Cube Sample			0.95		0.95		
Modulus of Rupture (MPa)		2.79		2.21		1.63		
Cold Crush Strength (MPa)	Soap Sample	23.98						
	Cube Sample	17.00		16.87		16.35		
Porosity (vol.%)	Isopropyl Alcohol (IPA)	15.9 ± 0.5	11.5	5.9 ± 0.7	2.8	1.4	3.4 ± 2.0	3.2
	Mercury Porosimetry	54.9	55.1		47			59.2
	X-ray Computed Tomography (XCT)	44.0				42.0		60.4

The bulk density of these samples at different heat treatment temperatures was around 0.9–1 g/cm^3. The MOR and CCS were measured. Because the TES liner will mostly be under compression by design, it is the CCS that matters the most. For all of the tested samples (as well as original GP-10, GP-20, and all GP-20 variants shown in Table 3 and Table 8), the CCS values all fell into a range of >15 MPa. The >15 MPa CCS far exceeds the required compressive strength of <1 MPa for liner installation (as specified by JT Thorpe). The additional strength will contribute to mechanical integrity of the liner when the liner is undergoing potential salt freeze/thaw cycling (as shown by the design concept in Figure 5).

2.2.5.2 Closed and Open Porosity

The open porosity of geopolymer materials is of particular interest when they are used for molten salt insulation and containment in TES tanks. Based on literature review and characterization results, it is believed that the composite geopolymers with cenospheres have a unique distribution of pore sizes. On the one hand, it is hypothesized that these geopolymers have very large pores in

[9] Errors on the order of plus/minus several volume percent were observed by comparing the measurements from Morgan, NREL, and MIT on samples from the same batch and following the same experimental procedures.

This report is available at no cost from the National Renewable Energy Laboratory at www.nrel.gov/publications.

the 50–300 μm range, which are composed of two major components: closed porosities formed by cenospheres and open porosities formed during the geopolymerization process. On the other hand, Duxson et al. [26] showed that sodium geopolymers also have mesopores (i.e., pores in the 2–50 nm range). The drastically different pore sizes make characterization difficult because there is no single characterization tool that can easily capture the entire pore size range, which is why Table 9 lists porosities measured by different techniques.

Figure 23 shows the open porosity of GP-20 samples with FABUTIT 748 addition as a function of heat treatment temperature, measured by the IPA technique. The vertical bars (if available) indicate ±1 standard deviation. Although the absolute magnitude of the open porosity measured by the IPA technique may not be accurate, it is believed that the IPA technique is self-consistent, and the relative trend of the open porosity as a function of heat treatment temperature is valid. As shown by Figure 23, there was a slow decrease of open porosity between 400°C and 900°C, followed by a steep decrease between 900°C and 1,100°C. These two decreases were consistent with the result in

Figure 11. Beyond 1,100°C, the slight increase was most likely due to thermal instability of the geopolymer matrix and/or its components, which may have created some large pores. The observed dimensional changes of the geopolymer samples above 1,100°C also corroborated with the open porosity increase, as the ends of the geopolymer sample experienced a noticeable volume expansion.

This report is available at no cost from the National Renewable Energy Laboratory at www.nrel.gov/publications.

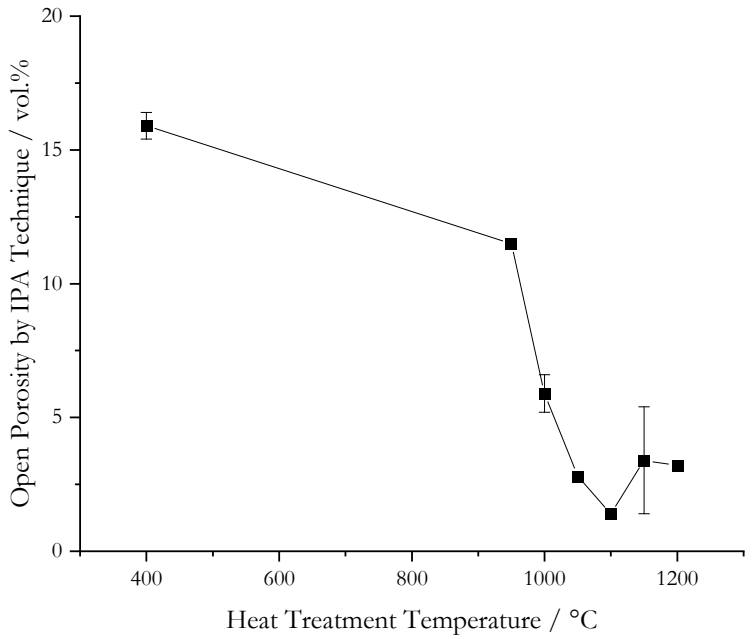

Figure 23. Open porosity of GP-20 samples as a function of heat treatment temperature, measured by IPA technique

The remaining question is which part of the total porosity was measured by the IPA technique. To answer this question, X-ray computed tomography (XCT) was conducted on GP-20 samples (heat treated to 400°C) as a reference. Figure 24(a) shows the XCT scan result where the brightness of the scan corresponds to density (e.g., dark color indicates air or porosity while bright color indicates geopolymer matrix, cenosphere shells, or aggregate additives). Calculation by the XCT instrument suggested a total of ~44.0 vol.% of porosity (including any open porosities and closed porosities but excluding any submicrometer pores inside the geopolymer matrix that are outside of the measurement range). An in situ XCT scan was conducted on another GP-20 sample where a small piece of the sample was first fully immersed in water, then the top of the sample was measured, as shown by the schematic in Figure 25. The XCT scan result is given by Figure 24(b). Because of capillary effect, water easily saturated the entire finger sample in a few minutes before the XCT measurement. The numbers 1–5 in Figure 24(b) show the locations of a few open porosities or cavities that were not formed by cenospheres. Interestingly, none of these open porosities showed any signs of water saturation, because otherwise the locations would appear as bright spots. Experimentally, the finger sample had a substantial mass gain and color change due to water saturation through the capillary effect after only a few minutes of water immersion. This suggested that liquids like water and IPA (both have similar fluid dynamics properties at room temperature to have similar capillary forces) may not be able to permeate certain large porosities. Because the capillary effect is a strong function of the size of the capillary (i.e., the pores in the geopolymer), these liquids have a tendency to reside in the small submicrometer pores whose presence in the geopolymer matrix has been suggested by Duxson et al. [26]. However, with a minimum voxel size of no less than 1 μm^3, the XCT technique was limited in this respect and could not measure submicrometer pores.

This report is available at no cost from the National Renewable Energy Laboratory at www.nrel.gov/publications.

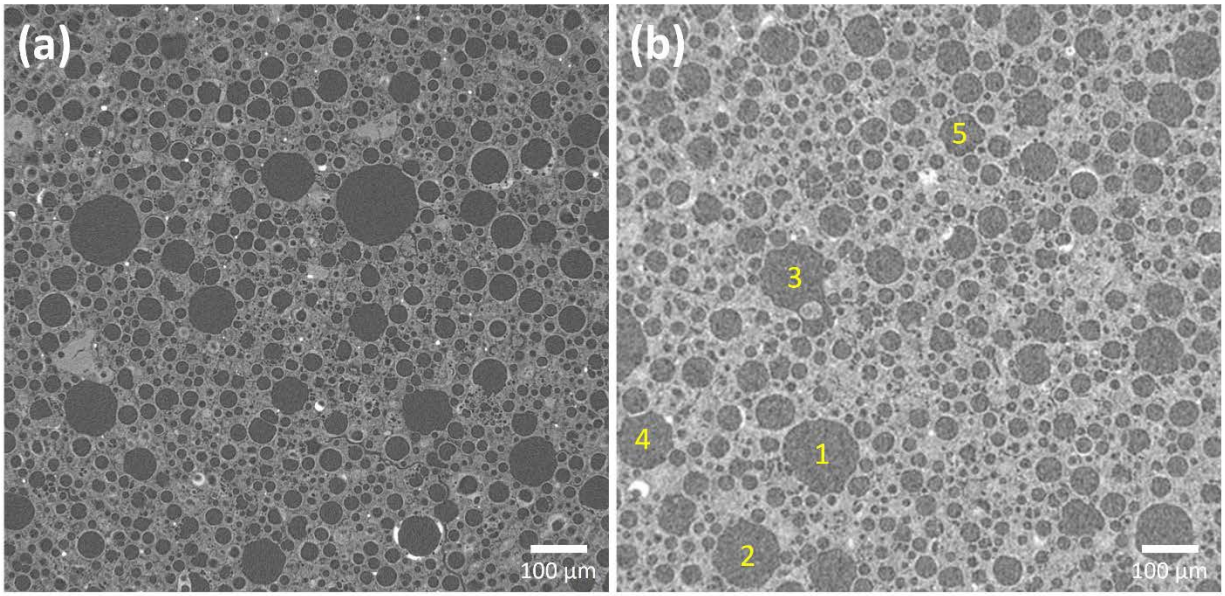

Figure 24. XCT scans on (a) dry GP-20 samples without any liquid immersion and (b) wet GP-20 samples saturated with water at room temperature

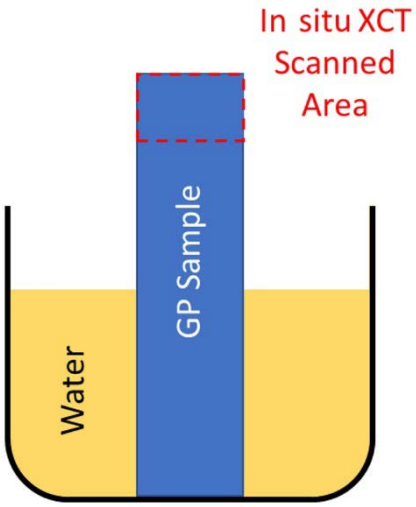

Figure 25. Schematic showing the in situ XCT scan for a geopolymer sample saturated in water

Mass gain due to water saturation was clearly observed, and XCT confirmed that water saturation did not occur within either the open pores or the closed pores formed by cenospheres. Therefore, it was speculated that water saturation only occurred in the submicrometer pores in the geopolymer matrix. Interestingly, molten salt at high temperature has fluid dynamics properties similar to water at room temperature. Hence, if the speculation is true and other factors are ignored for now, there is a chance that some pores in the composite geopolymer may resist molten salt permeation due to the unique pore size distribution and drastically different capillary forces in these pores.

Figure 26 shows the XCT scans for dry geopolymer GP-20 samples with different heat treatment. Upon closer inspection, the morphology of the cenospheres and open cavities started to change

This report is available at no cost from the National Renewable Energy Laboratory at www.nrel.gov/publications.

(i.e., shape change and deformation) at a heat treatment temperature of 1,100°C. At a heat treatment temperature of 1,200°C, the morphology change became even more obvious. This morphology change was likely responsible for the porosity increase above 1,100°C observed in Figure 23 because the deformation of the cenospheres and cavities might have led to more open porosities, which could be measured by the IPA technique.

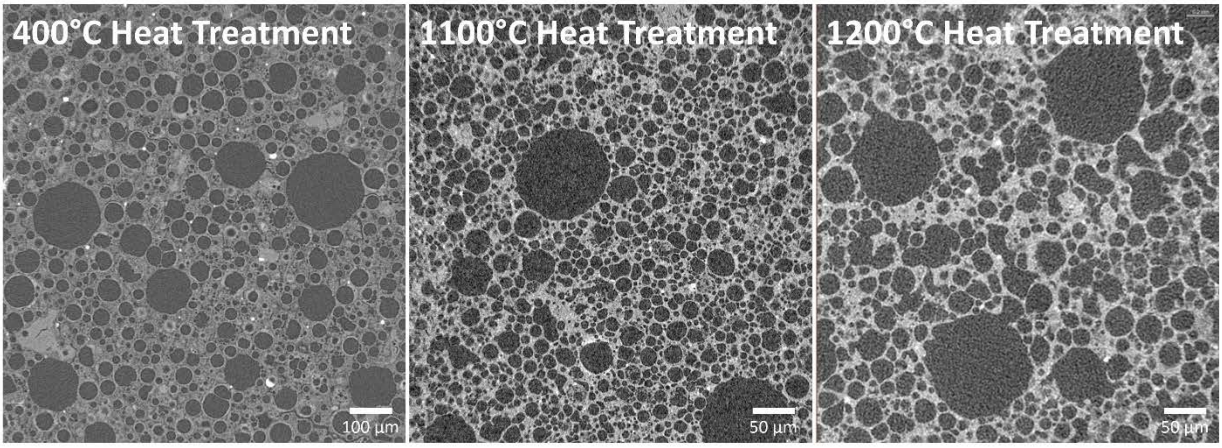

Figure 26. XCT scans for dry geopolymer GP-20 FABUTIT and water with different heat treatment, without any salt immersion

Mercury porosimetry measurements were also performed on GP-20 samples. Figure 27(a) shows the result of differential mercury intrusion, i.e., the total volume of pores at different pore size. There are a few observations:

- For all heat treatment temperatures, the pores had a bimodal distribution. At ≤950°C, pores in the >1 µm range dominated. At higher heat treatment temperatures (1,050°C and 1,200°C), the balance shifted toward smaller pores. In terms of salt permeation behavior, it is hypothesized that larger pores are more prone to salt permeation because trapped gas may impede salt permeation, especially when the pores are in the submicrometer range. Trapped gas that skews porosity measurement is common. A widely adopted practice is to evacuate the material under vacuum or boil the material in water to remove any trapped gas before liquid intrusion. The lower porosity value measured by the IPA technique was likely caused by the lack of such steps to remove trapped gas inside the submicrometer pores.
- The magnitude of pores larger than 1 µm was the lowest in the sample heat treated at 1,050°C, suggesting that 1,050°C heat treated samples may have the best salt permeation resistance. This agreed with the IPA porosity measurements, which suggested that 1,050°C–1,100°C may be the ideal heat treatment temperature to reduce open porosity.
- However, the total pore volume shown in Figure 27(a) was obviously skewed by the volume of larger pores, as the total pore volume scales with the third power of pore diameter. Figure 27(b) shows the differential mercury intrusion normalized by pore size to provide a more representative view of the total number of pores at different pore size. It showed that for all heat treatment temperatures, pores below ~10 nm dominated in number. This confirmed the presence of mesopores, which agreed with the experimental results and the report by Duxson et al. [26].

This report is available at no cost from the National Renewable Energy Laboratory at www.nrel.gov/publications.

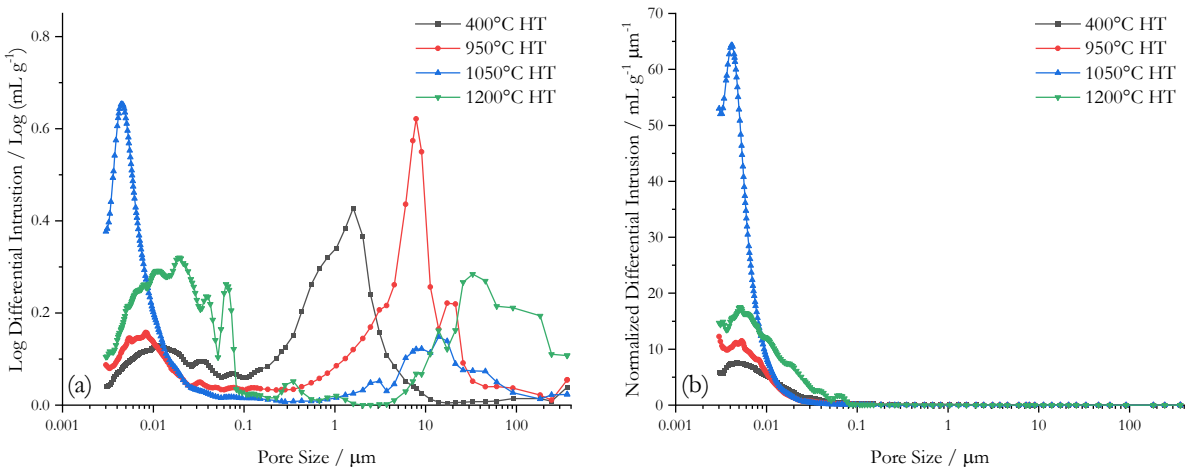

Figure 27. (a) Incremental mercury intrusion at different pore size and (b) differential mercury intrusion at different pore size

The limitations of the mercury intrusion technique for measuring the geopolymer system should be noted. To provide enough mercury intrusion, significant external pressure was used, especially for small pores. This pressure exceeded ambient pressure for any pores below ~12 µm and increased to ~170 psi (or 11.57 atm) for submicrometer pores. It eventually increased to 18,058 psi (or 1,229 atm) for pores smaller than 10 nm. The high pressure may have damaged the cenospheres, which have a compressive strength at about 2,000 psi. To understand whether the cenospheres were damaged, a mercury porosimetry test with repeated intrusions was performed. Figure 28 shows the relationship between measured pore size and cumulative intrusion volume. Note that 2,000 psi intrusion pressure corresponded to about 0.08 µm pore size. It was found that a rapid increase of measured intrusion volume coincided with this pressure range. It suggested that the rapid intrusion volume increase was a result of mercury entering the cenospheres when the mercury pressure was above the strength of the cenospheres. In addition, the extrusion data for Cycle 1 and the intrusion data for Cycle 2 did not trace the intrusion data for Cycle 1. This typically happens when the ratio of the pore diameter to the pore neck is greater than 4. If the cenospheres were broken by the mercury intrusion during the first cycle, then the cenospheres' large ratio of pore diameter to pore neck (certainly larger than 4) would not allow full extrusion of the mercury, leading to the observed disagreement of the data for Cycle 1 and Cycle 2. Therefore, it is possible to distinguish the closed porosities formed by cenospheres from other open porosities. If the rapid increase below 0.08 µm were due to breakage of cenospheres, then most of the cumulative intrusion volume afterward would be attributed to cenospheres because their volume would dominate that from small pores with <0.08 µm diameter. Therefore, it was estimated that the cenospheres were on the order of 35 vol.%, the large open pores (e.g., above 10 µm) were about 7 vol.%, and the midsized open pores (e.g., between 0.08 µm and 10 µm) were about 4 vol.%, all normalized to the total bulk volume of the geopolymer sample.

This report is available at no cost from the National Renewable Energy Laboratory at www.nrel.gov/publications.

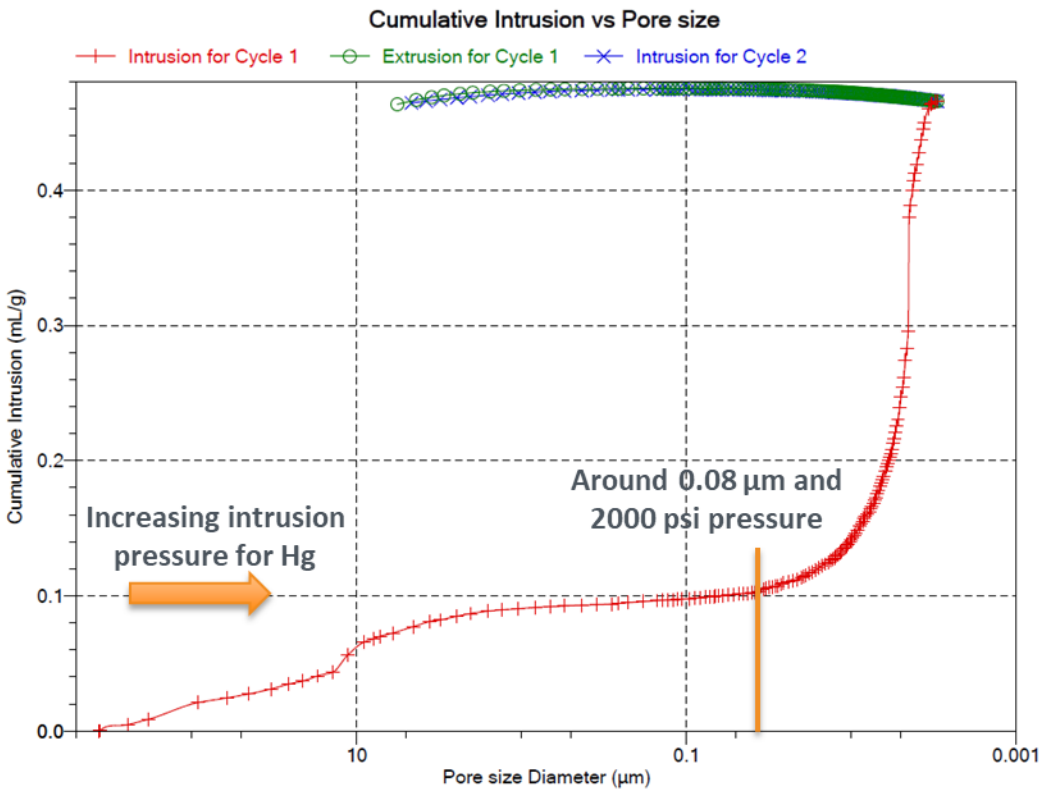

Figure 28. Repeated intrusion of mercury porosimetry on a GP-20 sample after heat treatment at 1,050°C

An additional mercury porosimetry test with repeated intrusions was performed on the same geopolymer recipe with heat treatment at 900°C. The result had significantly higher cumulative intrusion volume for pores between 0.08 µm and 10 µm, which suggested that 1,050°C heat treatment closed off certain midsized pores, agreeing with the significant volume shrinkage when geopolymer samples were treated above 900°C, as shown by

Figure 11. Although there was no quantification, the distribution of ~35% vol.% closed cenospheres, ~7 vol.% large open pores/cavities, and ~4 vol.% of midsized open pores is possible based on the XCT scans of geopolymer samples with various heat treatment (Figure 26).

In short summary, the combined results from the IPA technique, XCT scans, and mercury porosimetry confirmed the presence of both the mesopores (inside the geopolymer matrix) and the macropores (from cavities and cenospheres). This wide size distribution and the locations of these different pores are unique for the composite geopolymer material (when compared to traditional firebricks), which may contribute to different behaviors during molten salt immersion.

2.2.6 High-Temperature Materials Properties

2.2.6.1 Coefficient of Thermal Expansion

Figure 29 shows the coefficient of thermal expansion (CTE) for GP-20 by dilatometry. The CTE of the first heating cycle was slightly higher at 2.90×10^{-6} °C^{-1} than that of the second and third

This report is available at no cost from the National Renewable Energy Laboratory at www.nrel.gov/publications.

cycles at an average of 2.38 × 10^{-6} °C^{-1} for all heating and cooling steps.[10] For comparison, GP-20's CTE is lower than most commercially available refractory firebricks (e.g., 4.5 × 10^{-6} °C^{-1} to 9 × 10^{-6} °C^{-1} for aluminosilicate bricks [27]), suggesting good applicability as thermal insulation materials with lower chances to develop excessive thermal stresses. The low CTE was likely the result of free volume provided by the cenospheres and the open porosities because the local, microscopic thermal expansion of the matrix phase could be "absorbed" by the free volume and hence minimize the overall macroscopic thermal expansion. More free volume could benefit cracking resistance when the molten salt wets the geopolymer and undergoes freeze/thaw cycles (as demonstrated by Majkrzak et al. for cenosphere-filled bricks during water freeze/thaw cycles [28]).

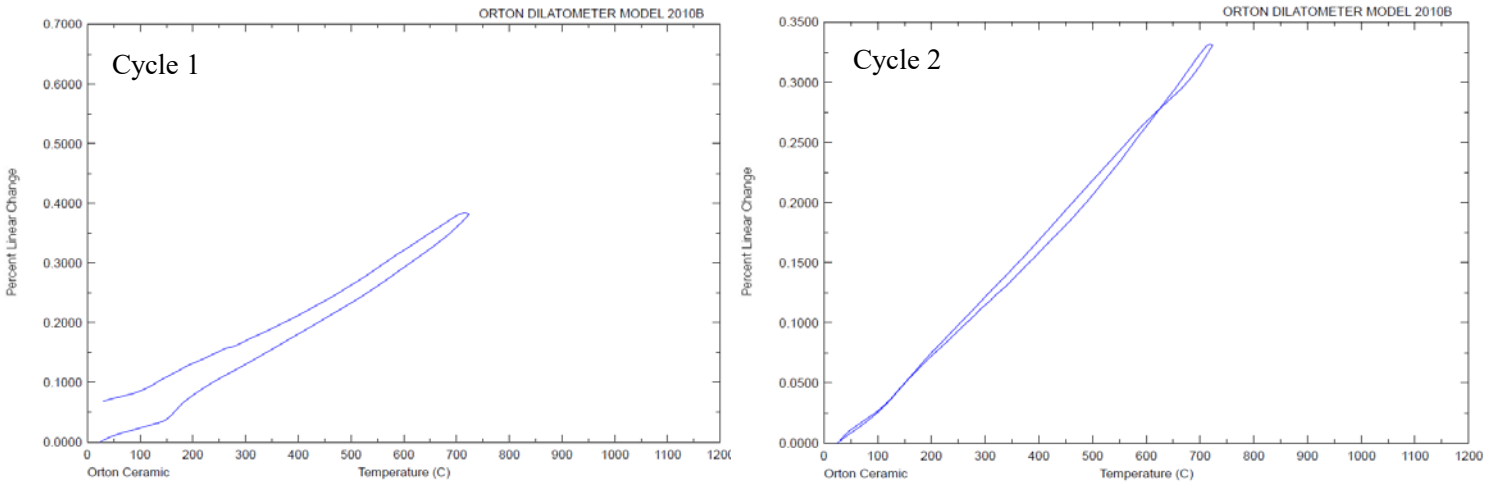

Figure 29. Coefficient of thermal expansion measurements on GP-20 by dilatometry

2.2.6.2 Compressive Strength at High Temperature

Experimental measurements of the strain vs. stress relationship at high temperature is more challenging than measurements at room temperature because the extensometer used for strain measurement is not rated to the temperature of measurement. Only the stress at failure could be accurately measured while the strain can only be approximated by a digital image correlation method.

The mechanical properties of geopolymer at high temperature can be estimated based on literature information. Junaid et al. [29] and Pan and Sanjayan [30] suggested that, compared to room temperature properties, the high-temperature strain of geopolymer could increase 2 times and 10 times, respectively. The difference is likely due to the different raw materials and compositions used by the authors. The strength reduction is less than 40% at about 700°C–850°C. Therefore, it is expected that the geopolymer bricks and mortar joints have about 7–10 MPa of compressive strength and 0.0015–0.01 mm/mm of strain at a measurement temperature of about 720°C. This translates to an elastic modulus of about 0.7–6 GPa.

Experimental measurements of geopolymer bricks and mortar joints at 400°C and 720°C showed that the properties significantly exceed expectation. Table 10 summarizes the compressive strength

[10] The data for the third cycle are not shown but are very similar to the second cycle.

This report is available at no cost from the National Renewable Energy Laboratory at www.nrel.gov/publications.

and ultimate strain of geopolymer bricks and mortar joints at room temperature and high temperatures. A few observations are made:

1. At any measurement temperature, the mortar joints were comparable to the bricks in terms of compressive strength. In some cases, the mortar joints were stronger than the bricks.
2. At high temperatures, both the bricks and the mortar joints had higher compressive strength than their counterparts when measured at room temperature.
3. The ultimate strain of bricks and mortar joints measured at high temperatures was higher than their counterparts when measured at room temperature, within the expected range of 2–10 times increase as reported by [29] and [30].
4. The ratio of strength to strain mostly falls into the range of 2–5 GPa. Although the ratio is not the same as the modulus of elasticity, it provides an order-of-magnitude estimate.

Table 10. Summary of the Compressive Strength and Strain of Geopolymer Bricks and Mortar Joints at Room Temperature and High Temperature

Samples	Measurement Temp. (°C)	Ultimate Strength (MPa)	Ultimate Strain (mm/mm)	Ratio of Strength to Strain (GPa)
Baseline Brick	25	10–20	0.00045	33.3
Mortar Joint		10.6 ± 3.0	0.0026 ± 0.0014	4.1
Baseline Brick	400	19.9	0.00082	18.4
		38.7	0.00264	5.7
Mortar Joint		19.9	0.00480	3.1
		34.4	0.00269	5.6
		25.9	0.00276	5.4
		33.3	0.00671	2.2
Baseline Brick	720	27.0	0.00291	5.2
		41.3	0.00424	3.5
Mortar Joint		27.7	0.00705	2.1
		33.4	0.00311	4.8
		37.3	0.00513	2.9
		40.5	0.00748	2.0

The first observation seemed to suggest that the geopolymer mortar had a positive effect on the mechanical properties of the geopolymer bricks. NREL and Morgan investigated the cracking behavior of geopolymer bricks and found that surface cracking was most likely caused by volume shrinkage. These surface cracks could be the crack initiation sites that eventually lead to brick failure. The geopolymer mortar, on the other hand, did not show any extensive signs of cracking, likely due to the smaller volume needed to form the mortar joint, which was easier for controlling dehydration and limiting shrinkage. Therefore, it was possible that the mortar filled the surface cracks on the bricks and strengthened bricks, i.e., a "repair" effect on surface cracks of the bricks.

This report is available at no cost from the National Renewable Energy Laboratory at www.nrel.gov/publications.

Figure 30 shows the mortar joints before and after room-temperature compression testing. The long, vertical cracks proved that the mortar joints were not necessarily weaker than the bricks. For high-temperature compression testing of the mortar joints, the entire brick/mortar was crushed into smaller pieces, which also suggested that the mortar had comparable strength to the bricks at high temperatures.

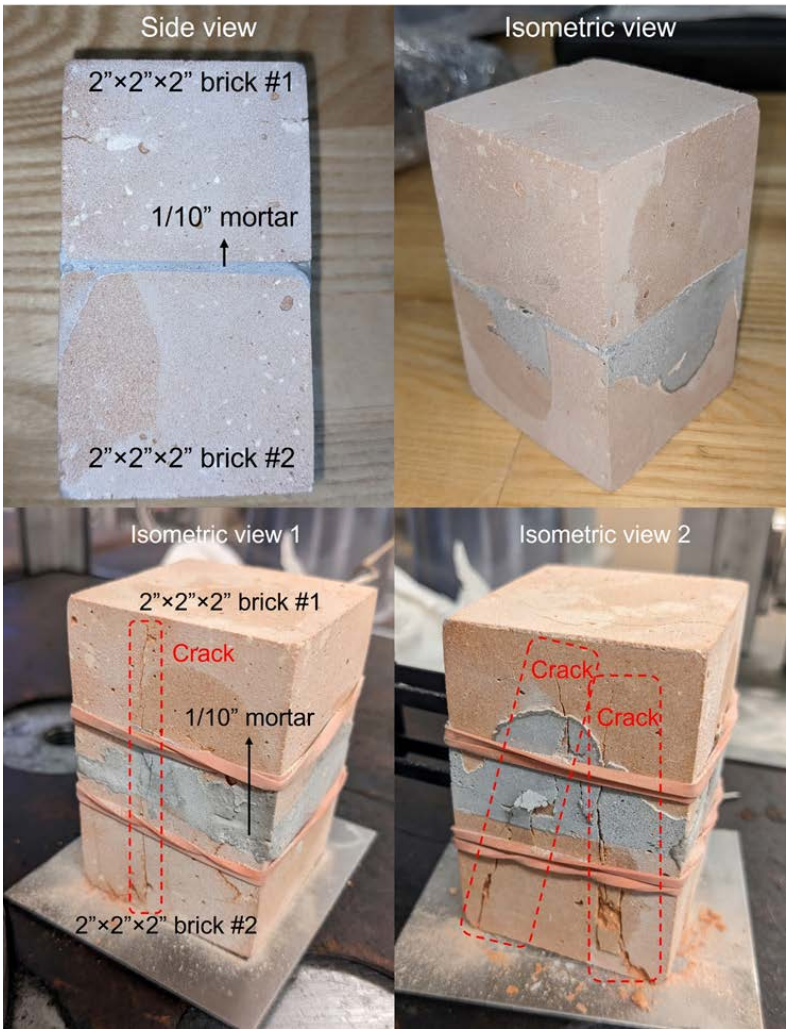

Figure 30. Images of the mortar joints before and after room-temperature compression testing

The second observation was more encouraging. Generally, it is not very common for refractories to have improved strength at high temperatures. Some refractories are stronger at high temperatures because the higher-temperature treatment is part of the manufacturing steps. For example, certain cement becomes stronger at higher temperature because the heat promotes complete curing, thus making the chemical bonds stronger. However, this is likely not the case for geopolymer. All geopolymer bricks had been heat treated up to 1,050°C before any compression testing at room temperature and high temperature. Hence, the bricks should have gone through the complete drying and curing cycle. Therefore, the strength enhancement should not be a result of additional drying and curing during the high-temperature compression testing. The exact reason was unknown. It was hypothesized that certain phases and/or additives in the geopolymer recipe may have an effect of mitigating crack initiation and propagation at high temperatures.

This report is available at no cost from the National Renewable Energy Laboratory at www.nrel.gov/publications.

The third observation indicated that the bricks and mortar joints at high temperatures had more compliance while having comparable or higher strength. This is particularly important. It suggests that the geopolymer material can have more compliance at high temperature. It echoes the second observation that higher temperature has a positive effect on geopolymer material, which makes it capable of sustaining both higher strain and stress.

Figure 31 shows the strain vs. stress relationship[11] for geopolymer bricks and mortar joints measured at high temperatures of 400°C and 720°C. The reference data for geopolymer bricks and mortar joints when measured at room temperature (blue solid and dashed lines) are included for comparison. The noisy strain data are due to the nature of the optical digital image correlation method because the heated air around the sample may negatively impact the quality of the images captured during the compression test. Most bricks and mortar joints measured at high temperautres (pink and red lines) had higher ultimate strain and higher ultimate strength than the reference bricks and mortar joints measured at room temperature (blue lines). This is the ideal case for a refractory liner application because higher strength means the material fails at a higher load while higher strain means the material can sustain more deformation before failure. Another encouraging observation was that the high-temperature moduli of elasticity (approximated by the slope of the strain vs. stress curve near origin) for most bricks and mortar joints were lower than the room-temperature values. This is beneficial from the thermal stress management perspective because thermal stress is proportional to the modulus of elasticity.

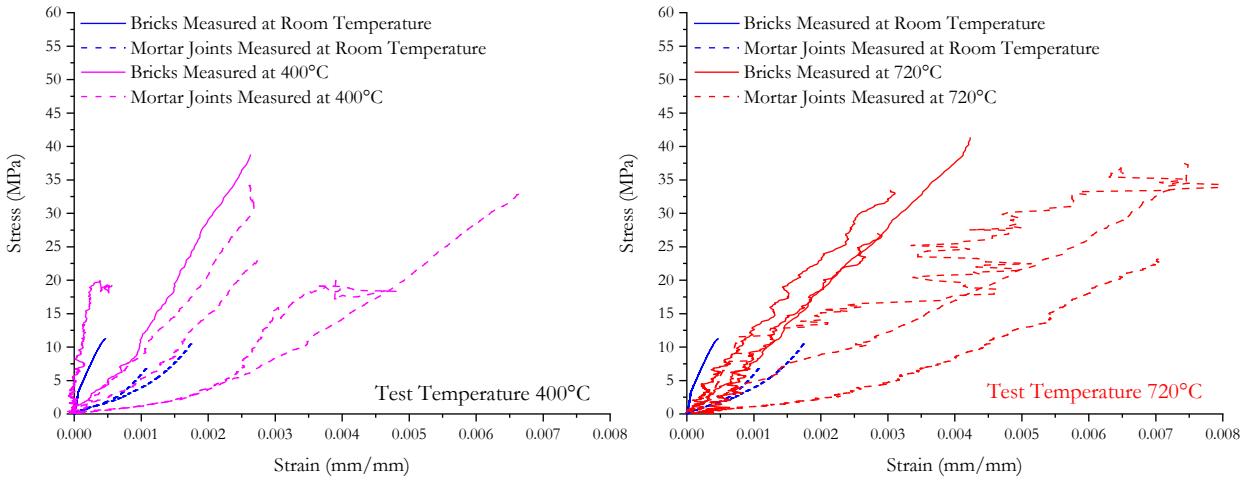

Figure 31. Strain vs. stress relationships for geopolymer bricks and mortar joints measured at 400°C and 720°C

The source of higher ultimate strain was most likely from the mortar joint. Figure 32 shows the in situ distribution of strain for a mortar joint sample when tested at 400°C. It is clear that the mortar joint layer sustained a higher strain than the brick layers during the test. This behavior was expected because the aggregates used for the mortar layer were smaller and finer. Hence, more deformation was expected from such mortar composition. Note that for compression testing of a mortar joint where the brick layers and mortar layer were in series, the failure stress was the

11

This report is available at no cost from the National Renewable Energy Laboratory at www.nrel.gov/publications.

strength of the weakest layer. It confirmed that high temperatures had a strengthening effect on geopolymer bricks and mortar joints.

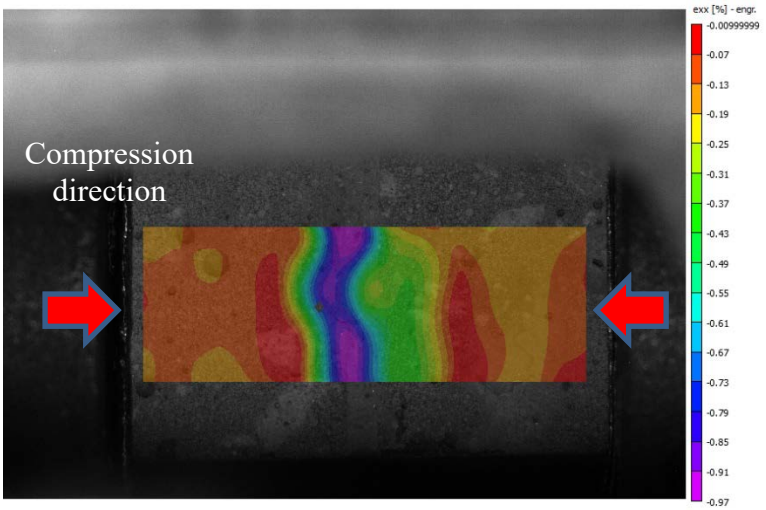

Figure 32. Distribution of strain for a mortar joint sample when tested at 400°C

This is in sharp contrast to traditional mortar materials where a mortar joint is typically significantly weaker than the bricks at high temperatures, as shown by the testing of Duro II brick + Duro mortar by the Gen3 Liquid Pathway project [2]. For example, the Duro II brick + mortar joints had a similar strength of 70–80 MPa compared to that of the Duro II brick when measured at room temperature and 350°C. However, the mortar joints' strength decreased significantly to 20–30 MPa at 720°C while the bricks' strength remained at 70–80 MPa. The post-compression images shown in Figure 33 confirmed the compression data. At room temperature and 350°C, the Duro II bricks in the mortar joints cracked, whereas there was no observation of brick cracking at 720°C because the mortar layer failed at a much lower stress level and bricks remained intact. In contrast, the geopolymer mortar joints all failed by having multiple cracks throughout the bricks and mortar layer, which indicated that the mortar layer was as strong as the bricks (see Figure 30).

This report is available at no cost from the National Renewable Energy Laboratory at www.nrel.gov/publications.

Figure 33. Post-compression images of Duro II mortar joints

2.2.6.3 Mechanical Strength With Molten Salt Permeation

Measuring the mechanical strength of the geopolymer samples at high temperature and with molten salt permeation was even more challenging. Because of the saturated molten salt inside the test samples, it was not recommended to test the samples to failure because it would expose the testing apparatus to corrosive molten salts. Therefore, high-temperature deformation tests were conducted at Morgan. Morgan used a simple hot loading test setup to measure the deformation of geopolymer samples permeated with molten salt. The samples were loaded at about 50 psi (0.35 MPa) and about 150 psi (1 MPa) for a duration of 1.5 hours at 550°C with and without molten salt permeation and at 720°C without molten salt permeation. A pressure of 50 psi corresponded to the estimated sum of the maximum hydrostatic pressure from the salt inventory and the mechanical loading from stacking the bricks to form the liner. A pressure of 150 psi, as recommended by JT Thorpe, corresponded to the estimated CCS needed to safely handle the bricks during installation. A pressure of 150 psi (1 MPa) was also well within the high-temperature compressive strength of the geopolymer materials (see Table 10), so there was no risk of breaking the sample bricks and exposing the test setup to molten salt. Because of the hazardous nature of the molten chloride salt in air atmosphere, which can generate HCl gas if not in an inert atmosphere,[12] the hot loading tests were conducted at 550°C/720°C without molten salt permeation (as benchmarks) and at 550°C only with the molten nitrate salt permeation.[13]

Table 11 summarizes the deformation of geopolymer samples with and without molten salt permeation when measured at 550°C and 720°C. Although there were some confusing results (e.g., a lower deformation of 0.24% was measured when a dry sample was subjected to a higher load of 150 psi at 720°C while a higher deformation was measured under the same conditions but

[12] Atmosphere control was not available for the hot loading test setup.
[13] No testing at 720°C with molten nitrate salt permeation because molten nitrate salt thermally decomposes above 600°C and forms hazardous NO_x gas.

This report is available at no cost from the National Renewable Energy Laboratory at www.nrel.gov/publications.

subjected to a lower load of 50 psi) the overall observation was encouraging. The data suggested that ~15% of mass gain due to salt permeation (which roughly corresponded to molten salt wetting porosities at about 10% of total sample volume) did not introduce a significant change in mechanical properties, regardless of the loads and test temperatures. Overall, less than 0.5% deformation is well within the acceptable values for refractories at high temperatures. Slight deformation may also be beneficial, to some extent, when thermal stress management is considered, which is in line with the argued benefit of having a lower modulus of elasticity to better manage thermal stresses.

Table 11. Summary of High-Temperature Deformation of Geopolymer Samples With and Without Molten Salt Permeation

Salt Permeation	Mass Gain	Permeation Time	Load	Test Temp. (°C)	Deformation
No	N/A	N/A	~50 psi	550	0.06%
Yes	14%	2 hours			0.15%
Yes	15%	28 days			0.59%
No	N/A	N/A		720	0.69%
No	N/A	N/A	~150 psi	550	0.23%
Yes	15%	28 days			0.17%
No	N/A	N/A		720	0.24%

2.2.6.4 Dry Thermal Conductivity vs. Temperature

Figure 34 shows the thermal conductivity of GP-10 and GP-20 at up to 800°C measured by ASTM C201. The test samples were produced by Morgan with a much larger size of 18 in. × 18 in. × 2.5 in. Following common practice in the refractory industry, the descending values (measured during cooling after initial heating) were adopted as the thermal conductivity because ascending values are usually affected by drying of the refractory samples.[14] The observed higher ascending thermal conductivity values (during initial heating to 400°C) were within expectations due to the removal of water.

[14] The preparation of the large thermal conductivity test samples did not follow the standard 7-day, 60°C curing process because ASTM C201 accounts for potential error caused by sample drying/curing.

This report is available at no cost from the National Renewable Energy Laboratory at www.nrel.gov/publications.

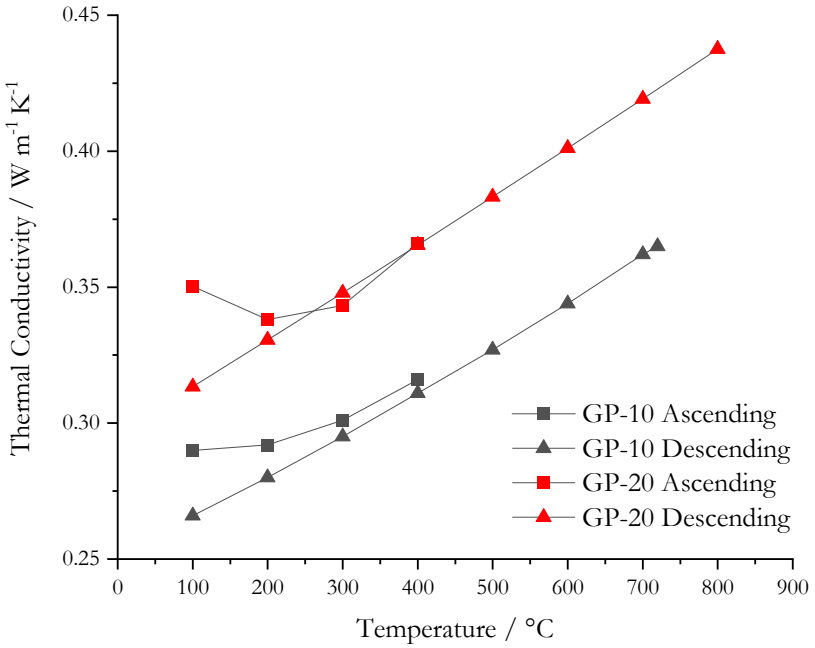

Figure 34. Thermal conductivity of GP-10 and GP-20 measured by ASTM C201

Figure 35 compares the thermal conductivity of GP-10 and GP-20 to other commercially available refractory firebricks offered by Morgan.[15] It shows that the geopolymer bricks are comparable to commercial firebricks in terms of thermal insulation at high temperatures. Their temperature dependence of thermal conductivity is also similar in magnitude at $1.2–1.8\times10^{-4}$ W/m·K^2. It should be noted that GP-10's thermal conductivity of 0.266 W/m·K when measured at 100°C coincided with previous thermal conductivity measurements using a different testing method, as shown in Figure 14 (i.e., 0.255 W/m·K on samples after 400°C heat treatment, and 0.262 W/m·K on samples after 600°C heat treatment, both measured at 100°C). It proves that regardless of the difference in raw materials and measurement equipment, geopolymer properties are reproducible.

[15] Kaolite Super HS Cast and Kaolite Super HS Gun are two commercial refractory materials that are similar to GP-10 and GP-20 in terms of chemical makeup, overall porosity, and bulk density.

This report is available at no cost from the National Renewable Energy Laboratory at www.nrel.gov/publications.

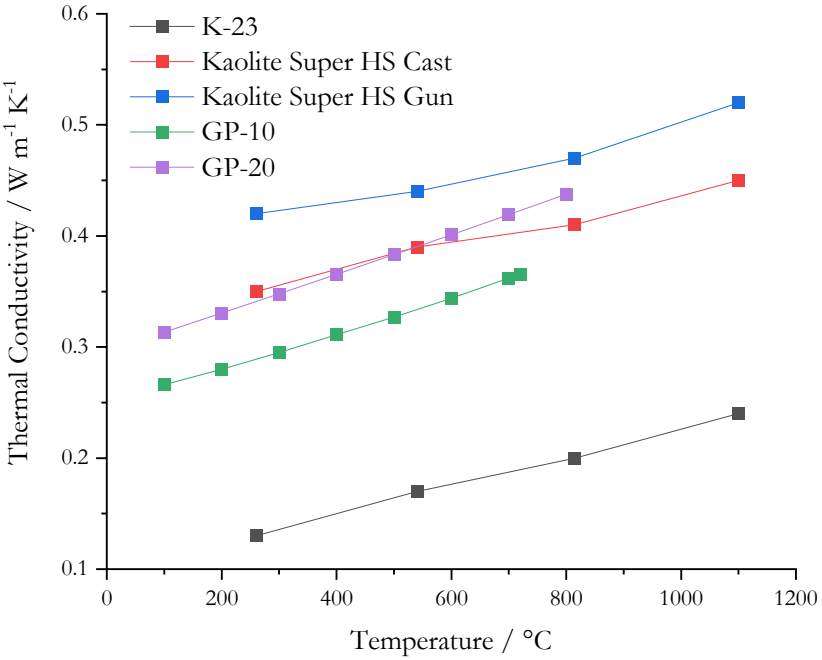

Figure 35. Comparison of thermal conductivities for GP-10, GP-20, and other commercially available insulation firebricks

2.2.6.5 Wet Thermal Conductivity vs. Temperature

As shown in Figure 35, the composite geopolymer insulations with cenosphere and aggregate additions are comparable to traditional refractory materials that have similar overall porosities, in terms of thermal insulation performance at high temperature. The key difference is the increase of thermal conductivity when molten salt permeation occurs. As shown by the schematic in Figure 5, the new molten salt insulation design uses a partially saturated geopolymer layer while achieving thermal insulation of the molten salt. Such a design requires the lowest impact of molten salt permeation on thermal conductivity. Figure 36 compares the experimental dry thermal conductivity and estimated wet thermal conductivity (i.e., when saturated by molten salt) for GP-10 and GP-20. It was estimated based on the EMT/Maxwell model using the high-temperature dry thermal conductivity data from Figure 35 and the average measured open porosity at a heat treatment temperature of 720°C (i.e., about 20 vol.% for GP-10 and 10 vol.% for GP-20). Figure 36 shows that although the dry thermal conductivities of GP-10 and GP-20 were different, their wet thermal conductivities were very similar. On average, GP-10 and GP-20 had similar wet thermal conductivities of ~0.45 W/m·K[16] at the molten salt operating temperature (i.e., 300°C–565°C for molten nitrate and 500°C–720°C for molten chloride). This was partly due to the fact that the thermal conductivity of the molten salt is also about 0.4–0.5 W/m·K [15,31]. This range was close to the effective thermal conductivity of the combined geopolymer matrix and closed

[16] The thermal conductivity assumes no contribution from any thermal convection of the permeated molten salt because the small size of the molten salt droplets inside the open porosities is not able to introduce significant convective heat transfer. Fluid dynamics analysis shows that molten salt droplets below a few millimeters does not have high enough Rayleigh number to introduce significant convective flows.

This report is available at no cost from the National Renewable Energy Laboratory at www.nrel.gov/publications.

porosities (excluding open porosities), which was also around 0.4–0.5 W/m·K.[17] Therefore, the mixing of two similarly conductive phases (i.e., one from molten salt and other one from geopolymer matrix and closed porosity) at any fraction would likely produce a final mixture with an overall effective thermal conductivity in the same range.

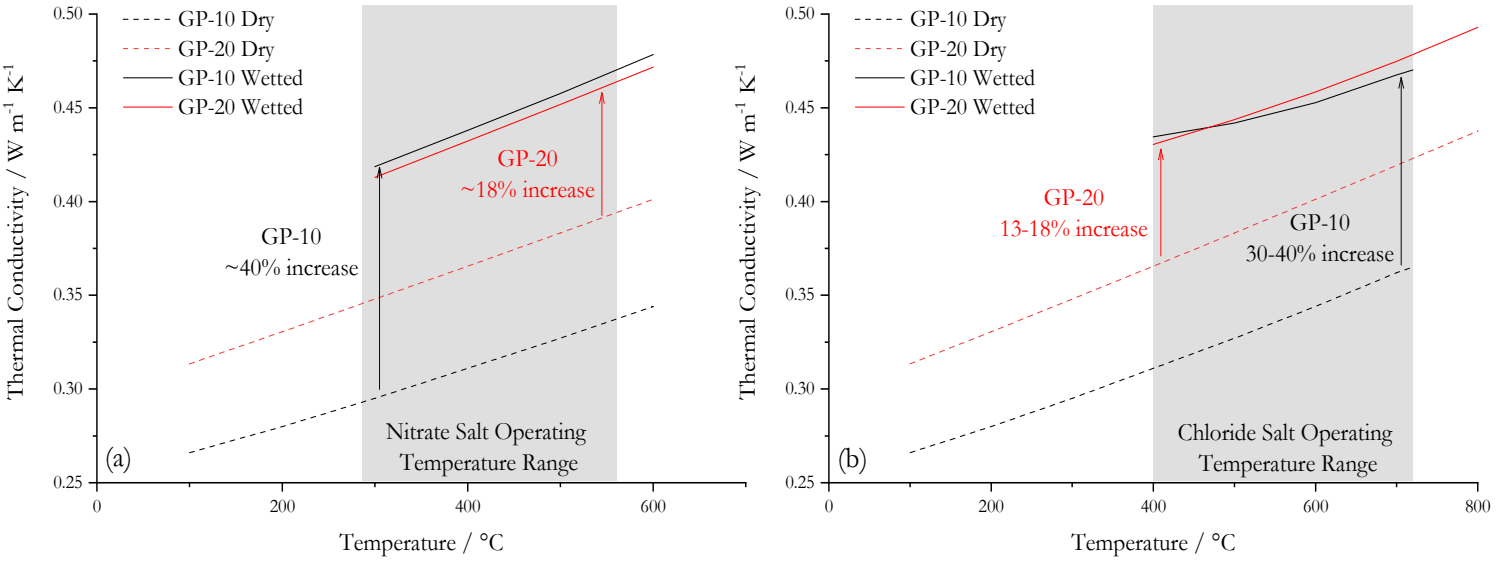

Figure 36. Experimental dry thermal conductivity and estimated wet thermal conductivity for GP-10 and GP-20 in (a) molten nitrate salt and (b) molten chloride salt

To verify the accuracy of the EMT model, Figure 37 compares the experimental wet thermal conductivity at room temperature and modeled wet thermal conductivity. It should be noted that "wet" means saturation of a geopolymer sample by molten salt at high temperature. But the actual experimental thermal conductivity measurement was performed at room temperature when the salt solidified inside the pores. Although this method did not measure wet thermal conductivity at molten salt temperature, it allowed verification of the EMT model at room temperature using the thermal conductivity of frozen salt. As shown by Figure 37, the discrepancy between the modeled values and the experimental values was larger at lower temperature and became smaller at higher temperature. This was expected because the thermal conductivity instrument that measured the dry thermal conductivity usually has larger errors near room temperature, as reflected by the larger standard deviation of multiple measurements on the same sample (not shown).

[17] The effective thermal conductivity was back-calculated with the EMT/Maxwell thermal conductivity model using the data of (1) the experimentally measured dry thermal conductivity of the geopolymer, and (2) the known thermal conductivity for air.

This report is available at no cost from the National Renewable Energy Laboratory at www.nrel.gov/publications.

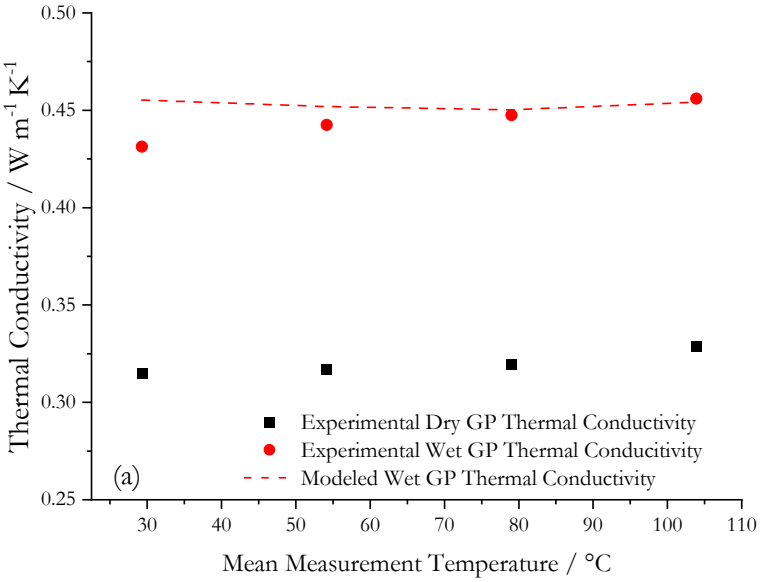

Figure 37. Comparison of experimental wet GP thermal conductivity with modeled wet GP thermal conductivity

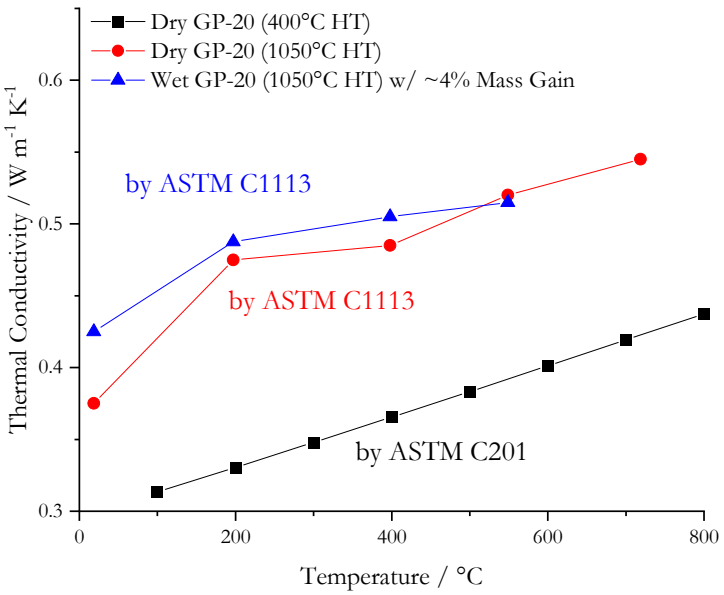

Figure 38. Experimental wet thermal conductivity vs. dry thermal conductivity using different methods

Figure 38 shows the comparison of the experimental dry thermal conductivity and wet thermal conductivity of the GP-20 samples with different high-temperature heat treatment. The dry thermal conductivity from Figure 34 is included again, which used ASTM C201 (parallel plate method). For wet thermal conductivity measurement on samples with molten salt permeation at high temperature, ASTM C1113 (hot wire method) was selected because of the lower risk of damaging the measurement apparatus due to the presence of molten salt. To understand the instrument errors, the dry thermal conductivity of a geopolymer sample was also measured by ASTM C1113. Based

This report is available at no cost from the National Renewable Energy Laboratory at www.nrel.gov/publications.

on Morgan's experience, ASTM C1113 usually produces 10%–20% higher thermal conductivity on the same material. In addition, 1,050°C heat treatment also contributed to higher thermal conductivity. It had to be assumed that the ASTM C1113 method is self-consistent, and hence the difference between the dry and wet thermal conductivity using the same ASTM C1113 method should not be subject to significant instrument errors. As shown by Figure 38, for a GP-20 sample that was immersed in molten salt for about 1 hour, a 4% mass gain due to salt permeation translated to negligible thermal conductivity increase. The relatively low mass gain due to molten salt permeation will be discussed later. If all open porosities (i.e., 10–15 vol.%) were wetted by molten salt, a mass gain of about 20% would be anticipated given GP-20's density of ~1 g/cm^3, molten nitrate salt's density of ~1.73 g/cm^3, and molten chloride salt's density of ~1.55 g/cm^3 (at the maximum TES operating temperature of 560°C and 720°C, respectively) [15,31].

Based on calculations and experimental measurements from Figure 36, Figure 37, and Figure 38, it was estimated that the composite geopolymer's thermal conductivity, when all open porosities were wetted by molten salt, would still be about 0.5 W/m·K at the respective operating temperature of molten nitrate salt TES and molten chloride salt TES. The increase was a relatively modest 10%–20%.

Table 12 summarizes the dry and wet thermal conductivities of commercial insulation materials with various levels of open porosity. The wet thermal conductivity was calculated based on the EMT model using the known dry thermal conductivity and molten salt thermal conductivity. Two groups of commercial insulation materials were presented. First, K-23 and Kaolite 2200 represent the high-porosity materials, which have low dry thermal conductivity to start with, but the percentage increase of thermal conductivity when wetted is excessively high at 700% and 190%. On the other hand, Kao-tuff CV and SR-90 represent the low-porosity materials, which have high dry thermal conductivity, but the percentage increase of thermal conductivity when wetted is low at 13.3% and 5.2%. Neither group is suitable for the molten salt application. The former would introduce a lot of risks of tank overheating or local hot spots if the liners were wetted by molten salt. The latter does not present the overheating issue, but the high thermal conductivity does not appeal from the perspective of thermal insulation performance. Figure 38 and Table 12 certainly showcase the main advantage of using a composite geopolymer as thermal insulation for molten salt. The modest increase of thermal conductivity when salt permeation occurs in the geopolymer liner limits the changes of the temperature profile through the tank walls and floors, hence reducing the risk of tank overheating that may lead to more catastrophic structural failures. And the initial dry thermal conductivity in the range of 0.3–0.4 W/m·K, although not as low as that of high-porosity insulations, is still more attractive as a thermal insulation. Therefore, the composite geopolymer insulation is the most balanced option for molten salt TES applications when both dry and wet insulation performances are important.

This report is available at no cost from the National Renewable Energy Laboratory at www.nrel.gov/publications.

Table 12. Dry and Wet Thermal Conductivity of Commercial Insulation Materials

Commercial Materials With Open Porosity vol.%	Thermal Conductivity (W/m·K)		Percentage Increase of Thermal Conductivity When Wetted
	Dry	Wet (calculated)	
K-23 with 73 vol.%	0.1	0.803	700%
Kaolite 2200 with 57 vol.%	0.2	0.583	190%
Kao-tuff CV with 22 vol.%	1.3	1.473	13.3%
SR-90 with 18 vol.%	3.0	3.156	5.2%

2.2.7 Structure Characterizations

2.2.7.1 X-ray Diffraction Analysis

As shown by Figure 11, noticeable volume shrinkage and porosity reduction occurred after heat treatment above ~850°C. It was hypothesized that these changes were due to a phase transition between a low-temperature amorphous phase to a high-temperature crystalline phase of the geopolymer matrix. Figure 39 shows the X-ray diffraction (XRD) patterns of geopolymer samples made of metakaolin and the basic activator (no other additives) after different heat treatment temperatures. The XRD patterns confirmed such hypothesis where an amorphous hump that was present in all samples with <720°C heat treatment disappeared after 900°C heat treatment while intensive crystalline peaks associated with sodium aluminosilicate appeared.

This report is available at no cost from the National Renewable Energy Laboratory at www.nrel.gov/publications.

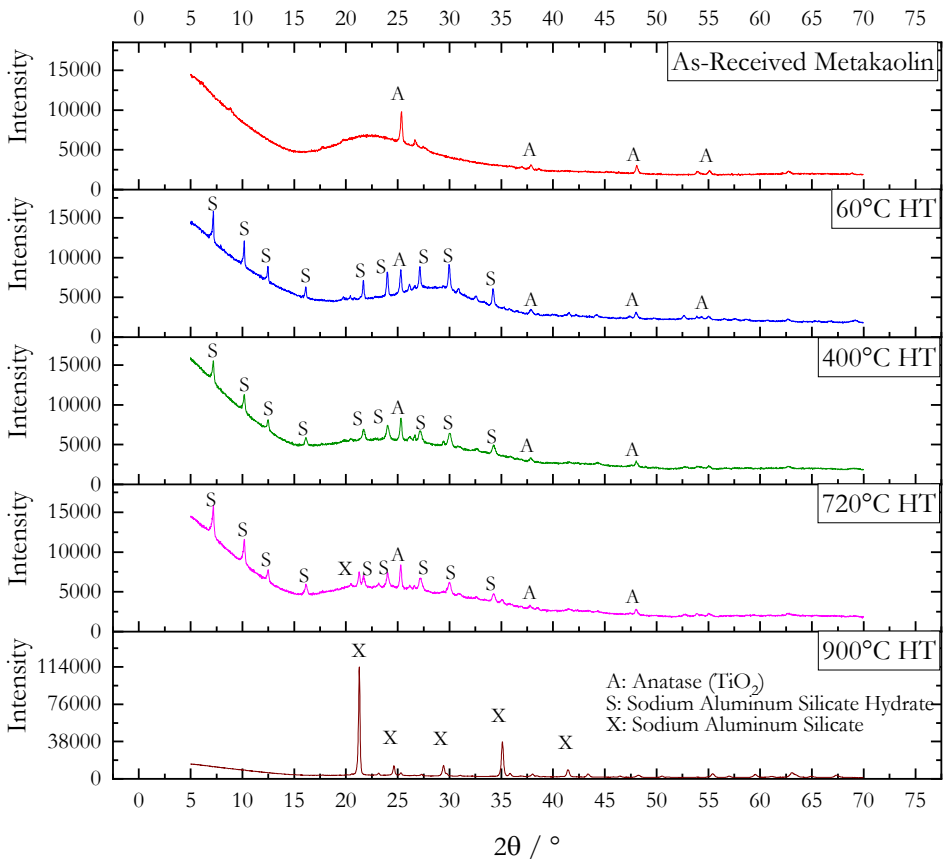

Figure 39. XRD patterns on geopolymer samples with different heat treatment

Additional XRD analysis was performed on the same geopolymer material with a known amount of crystalline corundum (15 wt.%) added to quantify the amounts of amorphous phase and crystalline phase(s) as a function of heat treatment temperature. Figure 40 shows the quantification of different phases (excluding the added 15% reference crystalline corundum phase). At 60°C and 720°C heat treatment temperatures, an amorphous phase dominated at >90% with <10% of crystalline sodium aluminosilicate hydrate phase. At 900°C heat treatment temperature, the crystalline sodium aluminosilicate started to dominate while the amorphous phase dropped to ~13%. The results confirmed the decision to test geopolymer properties and stabilities during molten salt immersion for samples treated below and above ~850°C.

This report is available at no cost from the National Renewable Energy Laboratory at www.nrel.gov/publications.

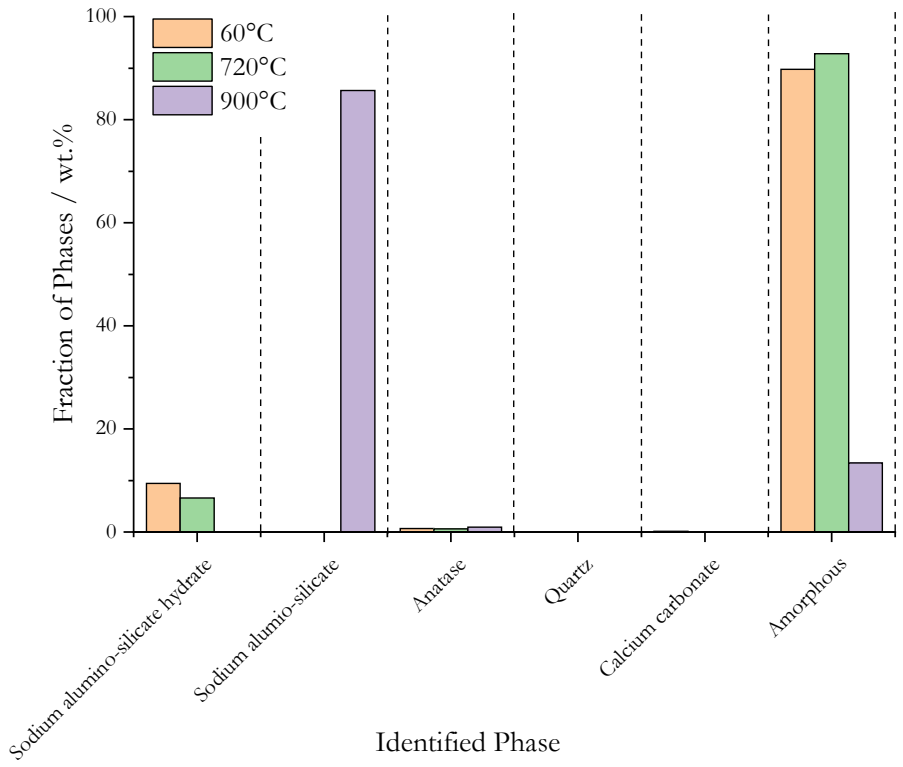

Figure 40. Quantitative XRD results of different phases in geopolymer samples with different heat treatment

2.2.8 Molten Salt Immersion Tests

Open porosity is one of the most important properties for the geopolymer insulation concept, which requires partial saturation of the liner. This concept requires a chemically, mechanically, and thermally robust matrix with a significant amount of closed porosities that aim to provide thermal insulation due to their hollow sphere morphology. To achieve this ideal situation, the matrix needs to protect the cenospheres by limiting the amount of open porosities in itself to avoid extensive interaction between the salt and cenospheres. The schematic in Figure 41 calls out the most ideal post-immersion morphology with (1) a protective geopolymer matrix, (2) intact closed porosities formed by cenospheres, and (3) minimal number of salt-wetted open porosities. To assess the protection provided by the geopolymer matrix to the cenospheres, different molten salt immersion tests were performed and summarized in the following sections.

This report is available at no cost from the National Renewable Energy Laboratory at www.nrel.gov/publications.

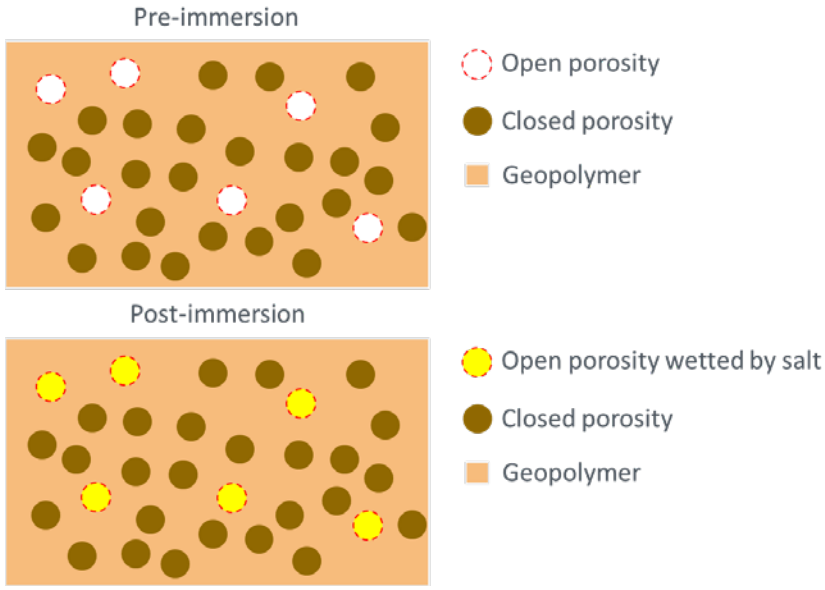

Figure 41. Schematic of the geopolymer insulation's structure before and after salt immersion

Isothermal immersion tests in molten nitrate salt and molten chloride salt were performed at NREL where small "fingers" and large blocks of geopolymer samples were partially immersed in a molten salt bath at an isothermal temperature (Figure 42). Note that these NREL samples did not have coarse aggregates at the time because the purpose was to focus on the protection effect of the geopolymer matrix on the cenospheres.

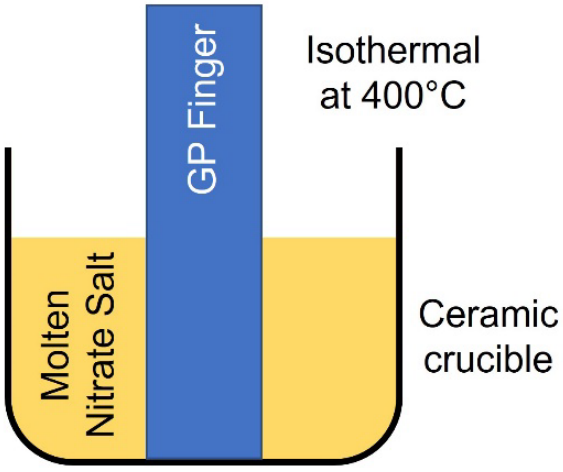

Figure 42. Schematic of the isothermal salt immersion tests for geopolymer samples

A typical finger sample was about 10 g with a dimension of 5 cm × 1.5 cm × 1.5 cm. A typical block sample was about 10 cm × 5 cm × 3 cm. Morgan's immersion tests were at an even larger scale where the block samples were about 23 cm × 11.5 cm × 5 cm. The isothermal testing temperature was between 400°C and 550°C for molten nitrate salt and up to 650°C for molten

This report is available at no cost from the National Renewable Energy Laboratory at www.nrel.gov/publications.

chloride salt. A temperature of 400°C is an intermediate temperature[18] of the geopolymer insulation layer in a nitrate salt TES hot tank while 550°C is about the operating temperature of the hot tank. The geopolymer samples were partially immersed in the salt bath for a few reasons. First, based on preliminary molten salt tests, a strong capillary effect was observed where the open porosities of the geopolymer had a wicking effect on molten salt. Hence, there was little difference between partial immersion and full immersion. Second, a partial immersion would simulate the tank wall insulation at the salt level. Third, full immersion was not easy to achieve because the geopolymer samples with closed porosities (bulk density around 1 g/cm^3) would tend to float in molten salt (density above 1.5 g/cm^3). The immersion samples with permeated salt were retrieved from the molten salt bath with quick cooling in ambient conditions to allow mass measurement, which was an important indicator of salt permeation. Then the samples were put back to the molten salt bath while the bath was still at the same high temperature. The test procedure effectively introduced a fast freeze/thaw cycle every time the sample mass was measured. As a precaution, after each freeze/thaw cycle, the sample was flipped upside down to alternate the end of the sample immersed in molten salt. During multiday immersion (usually 20–40 days), the mass gain of the samples was monitored which was a direct indicator of the extent of salt permeation. In the most ideal case, the immersion samples were expected to have an initial mass gain due to quick saturation of some open porosities, followed by a plateau of mass gain which indicated no more saturation/permeation into the closed porosities formed by cenospheres.

2.2.8.1 Isothermal Immersion Tests in Molten Nitrate Salt

The molten nitrate salt testing plan was primarily divided into three molten salt temperatures, 400°C, 450°C, and 550°C. The first was the average salt temperature of a Gen2 nitrate salt hot tank while the last was close to the operating temperature of the hot tank. Molten nitrate salt testing of the geopolymer insulation was considered a priority over the molten chloride salt testing for the following reasons:

1. The Gen2 molten nitrate salt TES is more relevant to the current market.
2. The nitrate salt test could be conducted in ambient atmosphere, meaning the experimental setup and post-experiment characterizations were more straightforward. The knowledge learned from the nitrate salt testing could then be applied to the more challenging chloride salt testing.

To evaluate the molten salt permeation, a straightforward metric, the percentage mass gain, was used to describe the extent of salt permeation inside the geopolymer samples during isothermal immersion.

2.2.8.1.1 Molten Nitrate Salt Immersion at 400°C

Figure 43 shows the percentage mass gain of three GP-20 samples with 400°C heat treatment. 400°C heat treatment was selected because it was shown that 400°C could provide high enough temperature to thoroughly dry the geopolymer blocks while minimizing the energy consumption and manufacturing cost associated with the heat treatment. Figure 43 suggests that geopolymer samples treated at 400°C, after the initial mass gain, had a stable percentage mass gain over a

[18] Based on our conceptual design, the geopolymer layer will need to (1) be in direct contact with the nitrate salt at 565°C, (2) be partially wetted by the salt, and (3) reduce the temperature to the melting point of the salt at around 235°C.

This report is available at no cost from the National Renewable Energy Laboratory at www.nrel.gov/publications.

prolonged period (between 500 hours and 800 hours for the three samples), even with frequent freeze/thaw cycling. The image inset shows the XCT scan of Sample 1 after 19 days of immersion. Although the mass gain was nearly 30 wt.%, the measured total porosity by XCT was about 43.0 vol.%, which was very similar to the value of 44.0 vol.% of the dry geopolymer sample with the same 400°C heat treatment (see Table 9). The morphology also did not vary significantly from that of the dry sample as shown in Figure 24(a). Hence, it is suggested that the salt saturation only occurred inside the matrix's micropores while the large pores (mostly formed by cenospheres) were intact. Because the percentage mass gain was relatively stable for the entire test period, the morphology of the salt permeation at a much longer immersion time was believed to remain similar, and no more salt saturation occurred. Even if considering the roughly 4.6 vol.% shrinkage of the nitrate salt due to salt freezing,[19] the GP-20 recipe with 400°C heat treatment survived molten nitrate immersion at 400°C for a long period of time without significant salt permeation into the large porosities (i.e., mostly closed porosities from cenospheres).

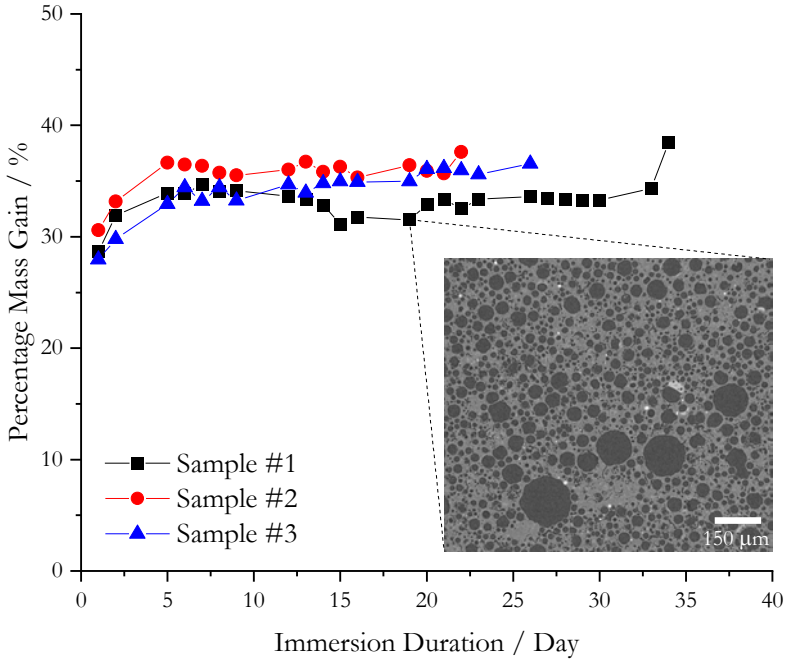

Figure 43. Percentage mass gain of GP-20 FABUTIT and water (heat treated at 400°C for 5 hours) during molten nitrate salt immersion at 400°C. The inset shows the XCT scan for Sample #1 after 19 days of immersion.

To further prove that the larger closed porosities formed by cenospheres were not wetted by molten salt, electron microscopy analysis was performed. Figure 44 shows the scanning electron microscopy images of a geopolymer sample before and after molten nitrate immersion for 40 minutes. The pre-immersion sample had some gaps between the cenospheres and the geopolymer matrix. It should be noted that because the geopolymer sample had to be cut and polished before the scanning electron microscopy analysis, some of the gaps or cracks may be exaggerated by the polishing procedure, but the actual gaps and cracks may be less severe. These gaps were mostly

[19] Salt volume shrinkage means that the porosity measured by XCT was slightly overestimated, and the actual porosity during salt immersion was slightly higher.

This report is available at no cost from the National Renewable Energy Laboratory at www.nrel.gov/publications.

filled by frozen salt in the post-immersion image, which could be seen by the slightly different brightness of areas around the cenosphere particles.

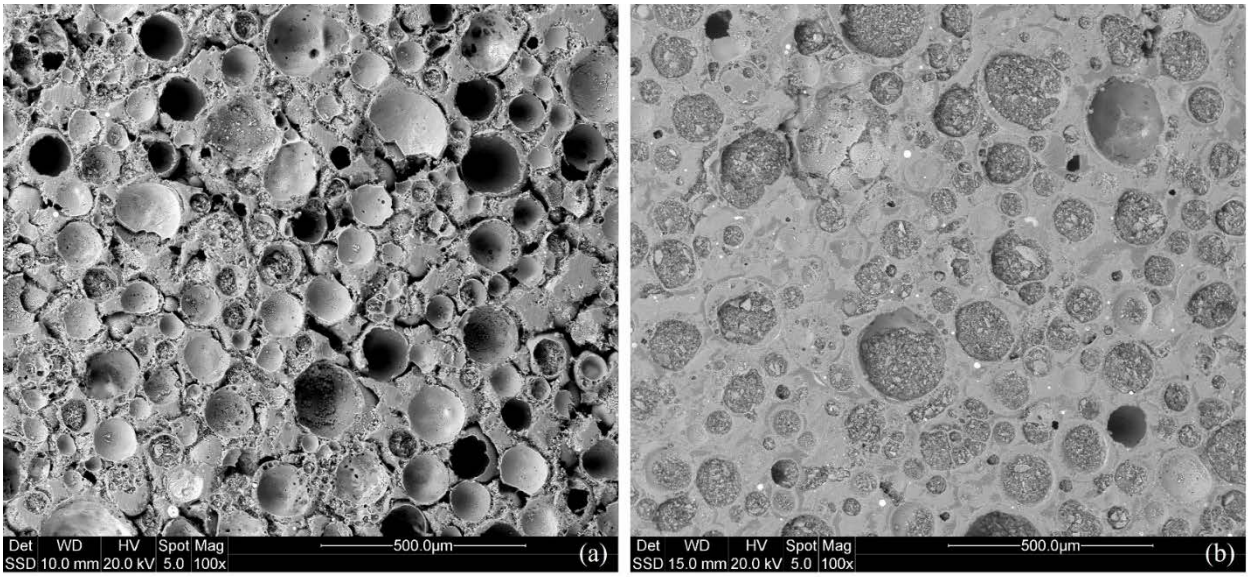

Figure 44. Scanning electron microscopy image of a geopolymer sample without aggregates (a) before molten nitrate immersion and (b) after molten nitrate immersion at 565°C for 40 minutes

Figure 45 shows the energy dispersive spectroscopy elemental mapping of the same geopolymer sample after immersion in molten nitrate salt for 40 minutes. It shows detectable signals for N and K (2% and 5%, respectively),[20] which were not major elements in the pre-immersion geopolymer system because N and K should only be from the $NaNO_3$-KNO_3 salt mixture, i.e., a result of molten nitrate salt immersion. The elemental mapping also shows that wherever there was geopolymer matrix or cenosphere particles (as indicated by strong Al and Si signals because geopolymer and cenospheres are both aluminosilicates), there was little signal for N and K. On the other hand, the locations with strong N and K signals coincided with those where the gaps and cracks were present.

Additionally, there was a noticeable Na signal, because the geopolymer and cenospheres had Na. But the signal was stronger in the gaps and cracks. This suggested that the gaps and cracks were filled with salt during immersion. Therefore, the energy dispersive spectroscopy evidence proved that, for the tested sample immersed in molten nitrate for 40 minutes, salt permeation mostly only occurred in the gaps and cracks between the cenospheres and the geopolymer matrix.

Figure 46 shows the optical microscopy image of a geopolymer brick produced by Morgan without any salt immersion. The key difference in materials was the addition of coarse aggregates. Compared to Figure 44(a), this Morgan sample did not show many gaps/cracks between cenosphere particles and the geopolymer matrix. It was encouraging because fewer gaps/cracks should better protect the cenospheres from the molten salt. Since aggregate addition usually leads to lower shrinkage, it is reasonable to observe fewer gaps/cracks.

[20] Although energy dispersive spectroscopy is not intended to quantify the N and K signals, especially when the measured content is ≤5%, their co-existence with the Na signal indicates that N and K are indeed present.

This report is available at no cost from the National Renewable Energy Laboratory at www.nrel.gov/publications.

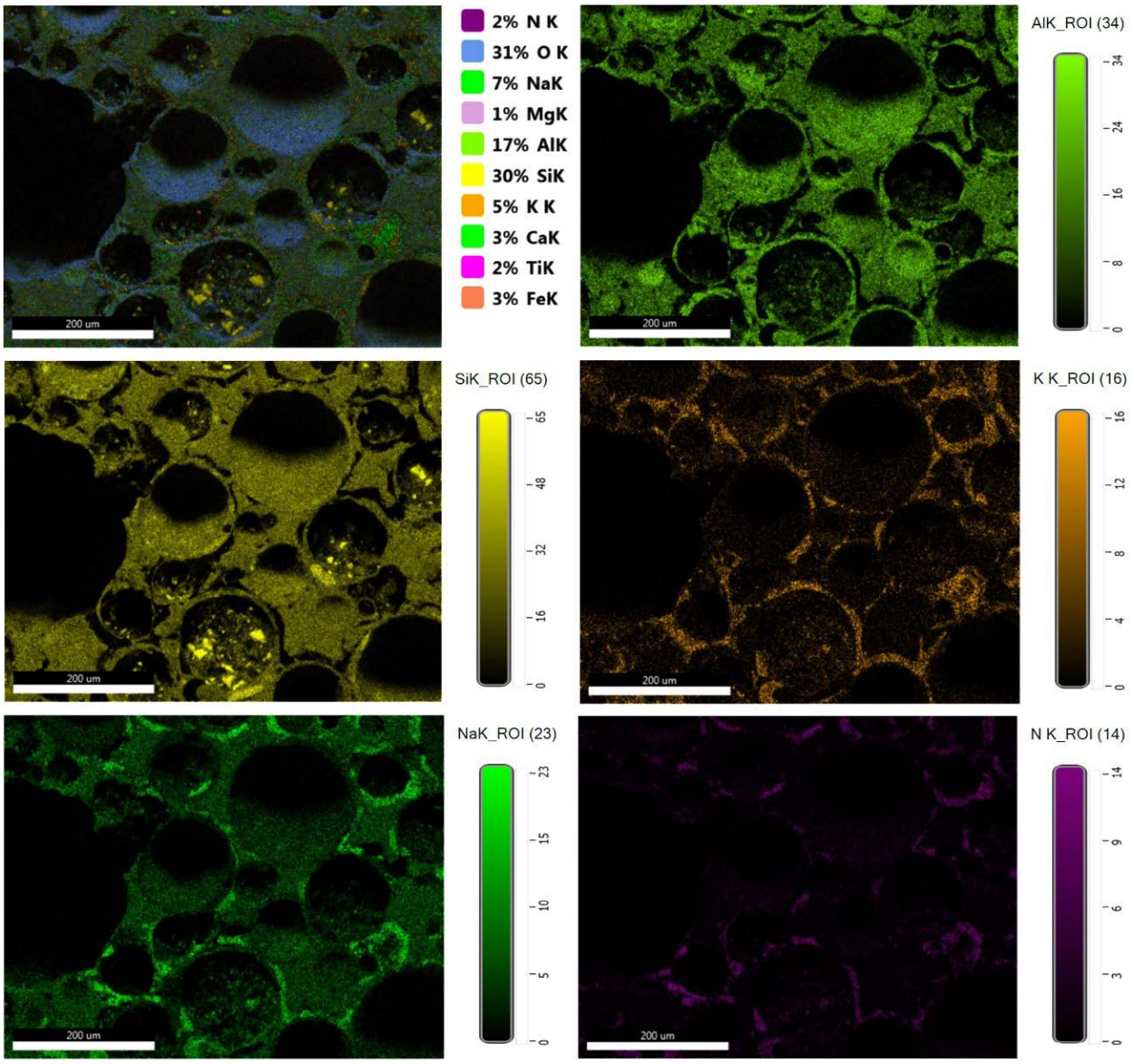

Figure 45. Energy dispersive spectroscopy elemental mapping of a geopolymer sample after 400°C immersion in molten nitrate salt for 40 minutes

This report is available at no cost from the National Renewable Energy Laboratory at www.nrel.gov/publications.

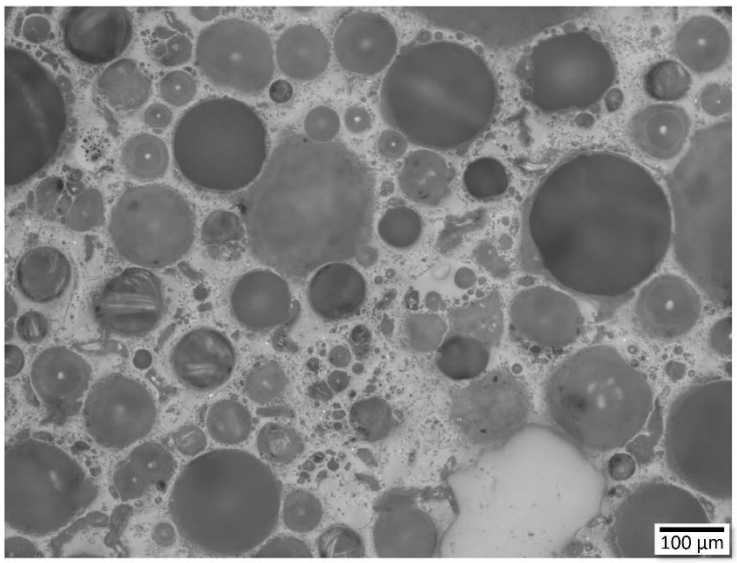

Figure 46. Optical microscopy image of a geopolymer sample with coarse aggregates

2.2.8.1.2 Molten Nitrate Salt Immersion at 450°C

It is useful to find out the maximum salt immersion temperature where the 400°C heat treated geopolymers can survive. Therefore, NREL performed salt immersion at 450°C with geopolymer fingers heat treated at 400°C. Figure 47 shows the XCT scans after 5 days and 19 days of molten nitrate salt immersion at 450°C. The corresponding mass gains were 43.8% and 62.7%, respectively. Surprisingly, at such high mass gains, the XCT scans still revealed a high level of porosity (47.0 vol.% and 37.8 vol.% for 5 days and 19 days of immersion, respectively). Therefore, it is optimistic that 400°C heat treated samples could be used at up to 450°C (but likely not much higher). The implication is that the final insulation may be a cascaded design with a first layer of insulation heat treated at higher temperatures to resist molten salt above 400°C–450°C and a second layer of insulation heat treated at lower temperatures to resist molten salt below 400°C–450°C.

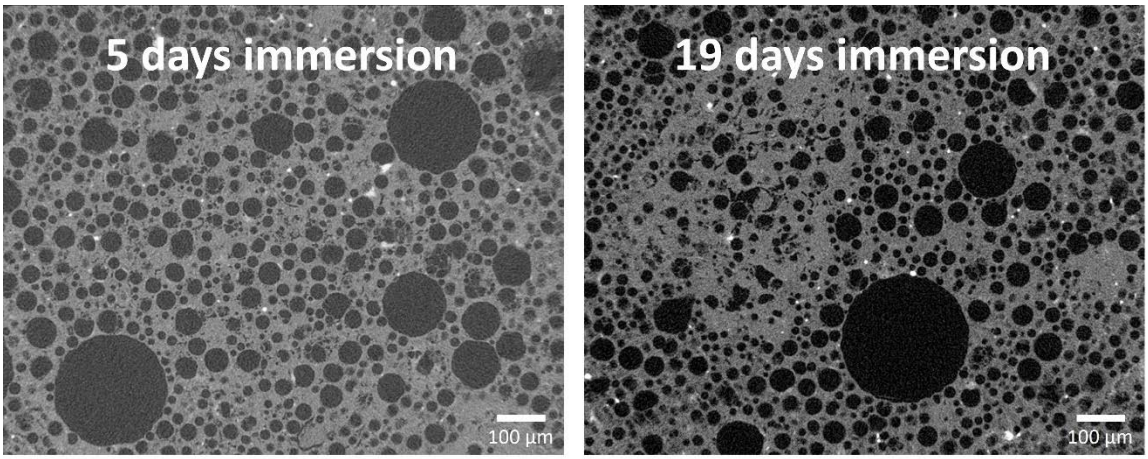

Figure 47. XCT scans for a geopolymer finger sample heat treated at 400°C, after 5days and 19 days of molten nitrate salt immersion at 450°C

This report is available at no cost from the National Renewable Energy Laboratory at www.nrel.gov/publications.

2.2.8.1.3 Molten Nitrate Salt Immersion at 550°C

Figure 48 shows the XCT scan of a geopolymer finger sample heat treatment at 400°C after 1 day of molten nitrate salt immersion at 550°C. Compared to the structure of the sample before any salt immersion shown in Figure 24(a) and after 19 days of molten nitrate salt immersion at a lower temperature of 400°C shown in Figure 43, the XCT scan in Figure 48 clearly shows salt permeation into a significant fraction of the cenospheres and some open cavities. The percentage mass gain was also at a higher level of 85.5 wt.%, which confirmed significant salt permeation from the XCT scan. Both results indicate that 400°C heat treatment to the geopolymer matrix did not provide enough protection for the cenospheres when molten salt permeation happens at 550°C.

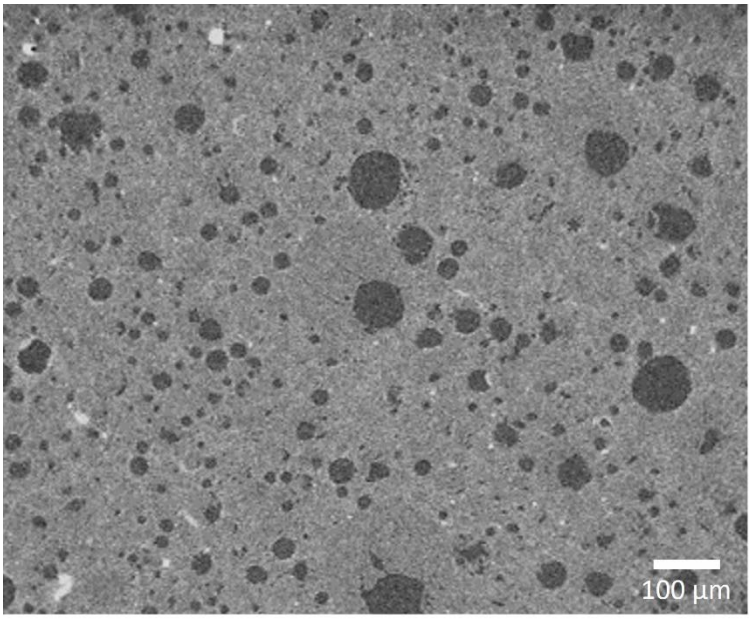

Figure 48. XCT scan of a geopolymer sample heat treated at 400°C, after 1 day of molten nitrate salt immersion at 550°C

Based on results charted in Figure 23 and Figure 27(a), the proposed change to the geopolymer processing was to reduce the open porosities with a heat treatment at a higher temperature of 1,050°C. Figure 49 shows a geopolymer finger sample with a significant dimension distortion after heat treatment at 1,200°C for 5 hours. Other samples after 1,100°C–1150°C heat treatment exhibited similar distortion (less distortion than 1,200°C but still visible). Dimensional distortion usually is an indicator of difficult manufacturing because it requires more attention during heat treatment (e.g., by using a nonstandard mold with a slight curve to account for distortion), or it requires dimension correction after heat treatment (e.g., via cutting and grinding). Both add costs to manufacturing and slow down production speed. Hence, 1,050°C is believed to be the best heat treatment temperature not only from the porosity reduction perspective but also from the manufacturability perspective.

This report is available at no cost from the National Renewable Energy Laboratory at www.nrel.gov/publications.

Figure 49. Geopolymer finger sample (1.5 cm × 1.5 cm × 5 cm) showing a significant dimension distortion after 1,200°C heat treatment for 5 hours

Figure 50 shows the percentage mass gain of geopolymer finger samples heat treated at different temperatures between 720°C and 1,200°C during molten nitrate salt immersion at 550°C. The different shapes of the data points of the same color indicate different samples for the same heat treatment temperature. It is clear that samples with 1,050°C heat treatment had the lowest percentage mass gain at almost any immersion time. It suggested that 1,050°C was the optimal heat treatment temperature, at least based on the criteria of lowest mass gain at a given time, likely due to the lowest open porosity. It should also be noted that each data point indicated a freeze/thaw cycle because the sample needed to be taken out of the furnace and cooled down for mass measurement. NREL noticed that for these samples tested at 550°C molten salt temperature that the freeze/thaw effect was more pronounced compared to that during the 400°C molten salt immersion tests. Some samples showed cracking after 10 days of immersion and freeze/thaw

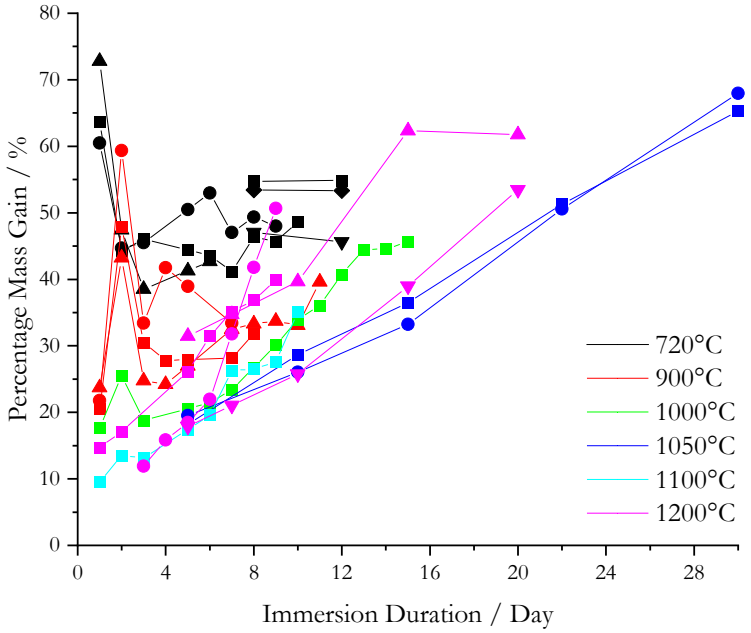

Figure 50. Percentage mass gain of geopolymer finger samples with different heat treatment during molten nitrate salt immersion at 550°C

This report is available at no cost from the National Renewable Energy Laboratory at www.nrel.gov/publications.

cycling. NREL also observed bubbling when some fingers were put directly back to 550°C molten salt bath without preheating. Both might have contributed to the sample fracture behaviors. Coupled with higher molten salt temperature, which usually equals more corrosive environment, the samples immersed at 550°C fractured in a much shorter period compared to the samples immersed at 400°C (Figure 43), which could last over 35 days without any fractures. The conclusion is that the 1,050°C heat treated samples survived at least 30 days in 550°C molten salt without fracture when they only experienced five freeze/thaw cycles.[21]

Figure 51 shows the XCT scans for the geopolymer finger samples in Figure 50, after 7 days of salt immersion at 550°C. The corresponding mass gains were 42.7%, 33.4%, 23.4%, 26.3%, and 31.5% at 720°C, 900°C, 1,000°C, 1,100°C, and 1,200°C heat treatment, respectively. By close inspection of the XCT scans and comparison to the XCT scans of the geopolymer samples treated at similar temperatures without any salt immersion (Figure 26), the samples heat treated at 1,000°C and 1,100°C showed the best behaviors (i.e., they exhibited very little difference when compared to their dry counterparts in Figure 26) with the least amount of salt permeation into the cenospheres and open cavities. The XCT observations were consistent with the mass gain results in Figure 50 where at 7 days, samples treated at ≥1,000°C had significantly lower mass gain compared to samples treated at 720°C and 900°C.

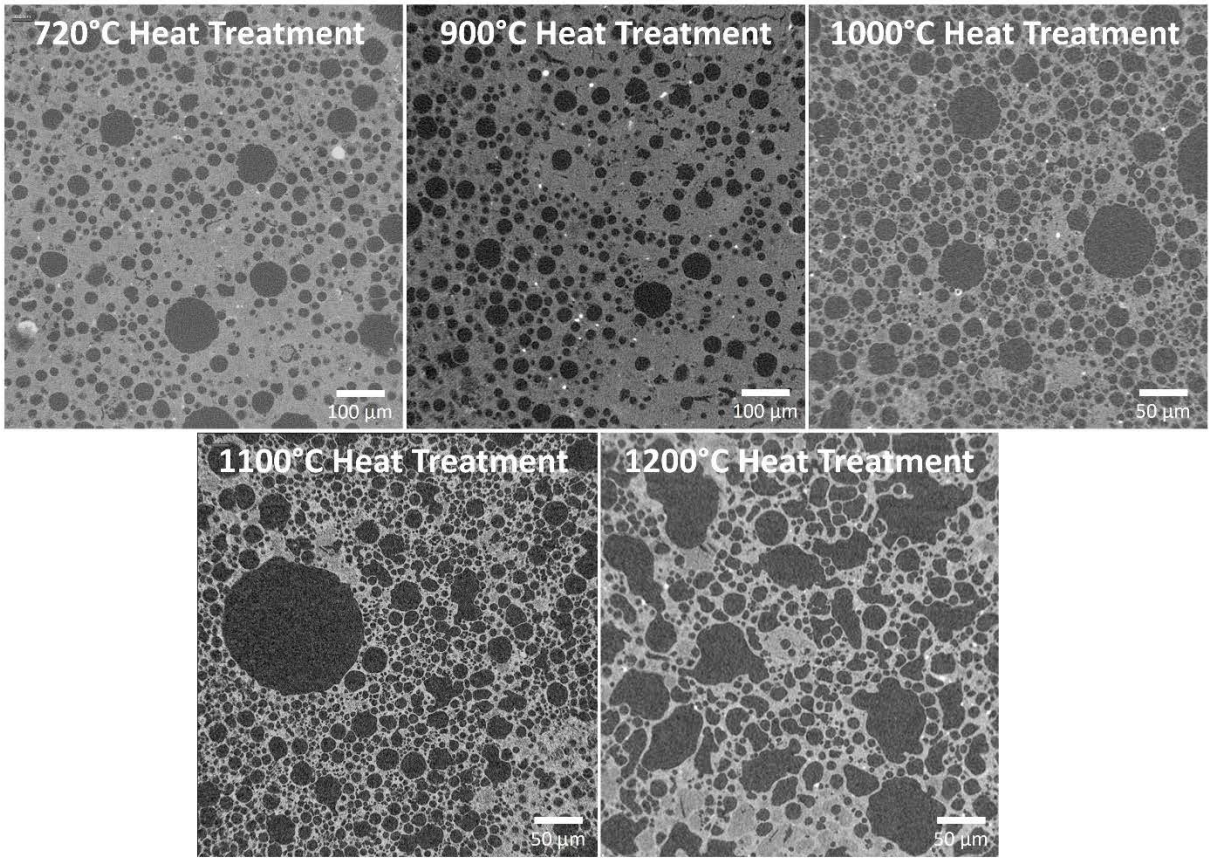

Figure 51. XCT scans for geopolymer finger samples, with different heat treatment, after 7 days of salt immersion at 550°C

[21] The samples did not fracture after 30 days. The tests were stopped because the samples were used for XCT analysis.

This report is available at no cost from the National Renewable Energy Laboratory at www.nrel.gov/publications.

Figure 52 shows the XCT scans for the geopolymer finger samples with heat treatment at 1,000°C and 1,050°C, after 15 days of salt immersion at 550°C. The corresponding mass gains were 45.64% and 33.24%, respectively. Based on the percentage mass gains and the XCT images, the 1,050°C heat treatment was better. In Figure 52, it was observed in the 1,000°C heat treated sample that more cenospheres were permeated by salt around the regions of cracks. The hypothesis was that the long cracks created an easy pathway for molten salt to reach the bulk of the material and started permeation into cenospheres from there. This phenomenon prompted investigation of the salt permeation behaviors in the bulk of the sample vs. near the surface of the sample.

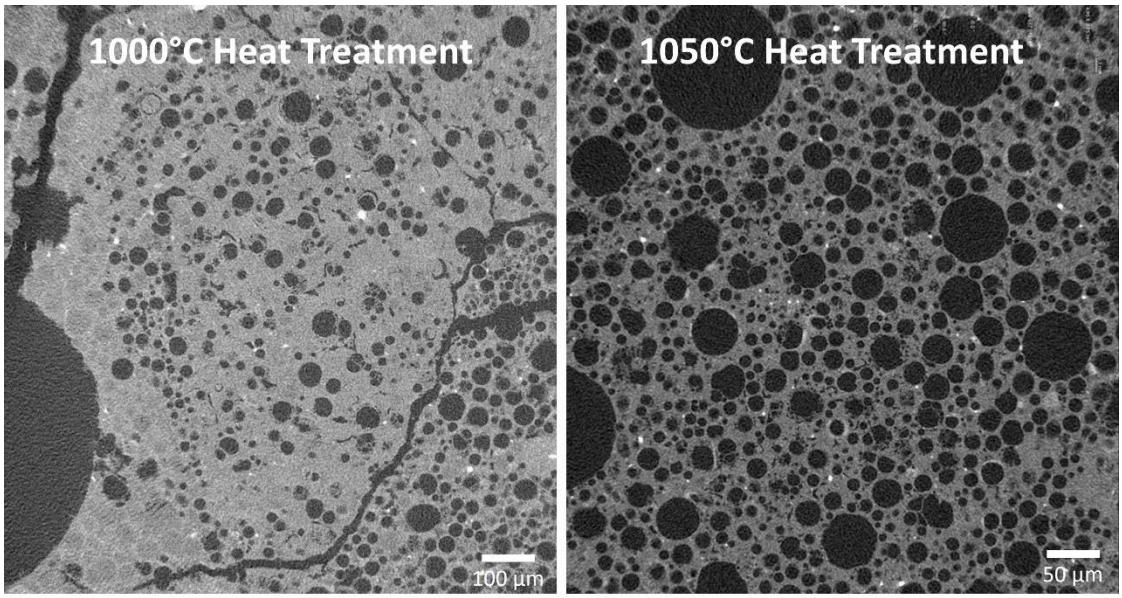

Figure 52. XCT scans for wet geopolymer GP-20 FABUTIT and water with different heat treatment, after 15 days of salt immersion at 550°C

Figure 53 shows the XCT scan of a geopolymer sample with heat treatment at 1,050°C, after 30 days of salt immersion at 550°C. The corresponding mass gain was 67.95%. The most interesting observation was not just the retention of some closed porosities and large open cavities at such a high mass gain, but also which part of the measured sample had the most salt permeation into closed porosities. The sample was oriented in a way that the top and right side of Figure 53 were the surfaces that directly interfaced with the molten salt. It was obvious that these two sides lost more closed porosities to salt permeation. The most important information that can be extracted from such behaviors was that salt permeation was a function of depth from the interface between the molten salt and the geopolymer surface. In other words, salt permeation may be geometry-dependent and less significant for larger samples. This hypothesis was corroborated by the IPA porosity measurement results. The low porosity values by the IPA technique indicated that certain pores with trapped air may impede IPA saturation. The same could happen to molten salt because the fluid dynamic properties of the IPA and molten salt were similar. Without additional external pressure, the molten salt may not be able to intrude into a small pore, or it may take longer time, due to the resistance from the surface tension. This was observed by the mercury intrusion analysis: almost 1 atm external pressure was needed to push mercury into pores at 12 µm size, almost 4 atm external pressure was needed to push mercury into pores at 3.5 µm size, and almost 13 atm external pressure was needed to push mercury into pores at 1 µm size. The external pressure increased

This report is available at no cost from the National Renewable Energy Laboratory at www.nrel.gov/publications.

exponentially with decreasing pore size. More than 120 atm was needed for pores at 0.1 μm size. This effect was usually not observed in traditional porous firebricks because of the larger pore size and more unimodal size distribution. But geopolymers had bimodal or even multimodal distribution of pores, hence the small pores may have a special effect of preventing salt permeation. The deeper into the bulk, the more pronounced this effect could be. This is important because the geopolymer structure suggested that to access the closed porosities formed by the cenospheres, the salt needed to permeate through the matrix with submicrometer pores. The bigger the geopolymer sample, the more matrix needed to be passed through by the salt. Hence, bigger geopolymer blocks may have a superior molten salt permeation resistance.

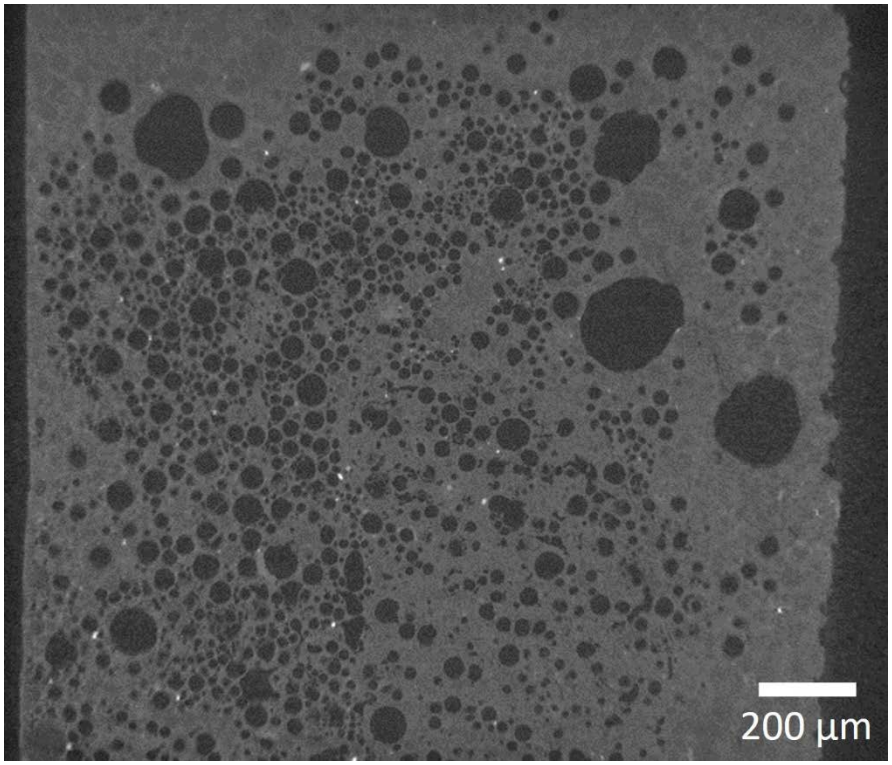

Figure 53. XCT scan for a geopolymer finger sample heat treated at 1,050°C, after 30 days of salt immersion at 550°C

The size effect was observed experimentally. Morgan performed salt immersion tests for a few large 23-cm × 11.5-cm × 5-cm geopolymer block samples heat treated at 1,050°C. After around 30 minutes of immersion, the sample mass gain was only 2%–3%. NREL performed salt immersion tests for a few 10-cm × 5-cm × 3-cm geopolymer block samples heat treated at 720°C and 1,050°C. Figure 54 shows the comparison of percentage mass gains during 550°C salt immersion for small finger samples and large block samples heat treated at 720°C and 1,050°C. The 720°C heat treated samples showed almost no size effect. On the contrary, the sample size effect was much more pronounced for the 1,050°C heat treated samples where the mass gain for large block samples was less than 20% at 30 days, compared to ~60% mass gains for small finger samples after similar durations of salt immersion. This was partly due to a much lower open porosity from a higher heat treatment temperature of 1,050°C, which was shown to close off open pores (see Figure 23). And as shown before, the salt permeation resistance was a function of the depth from the geopolymer surface/molten salt interface (Figure 52 and Figure 53). More

This report is available at no cost from the National Renewable Energy Laboratory at www.nrel.gov/publications.

importantly, the percentage mass gain showed a plateauing behavior around 15–30 days and after about 45 days. Because the large block samples were still measured frequently like the finger samples, the fast freeze/thaw cycling may have negatively affected the performance, as the volume change of the permeated molten salt inside the gaps and cracks of the geopolymer sample during the freeze/thaw cycle could stress the structure and cause more cracks. Without the frequent freeze/thaw cycles, the salt permeation resistance behavior may be improved. Given the observations and experimental results, it is optimistic that the salt permeation resistance for full-sized geopolymer blocks (e.g., on the order of 50 cm × 50 cm × 50 cm based on preliminary insulation liner design) without frequent and fast freeze/thaw cycling will be better. Unfortunately, it requires a much larger experimental apparatus such as a prototype molten salt storage tank to confirm the true performance of full-sized geopolymer insulation.

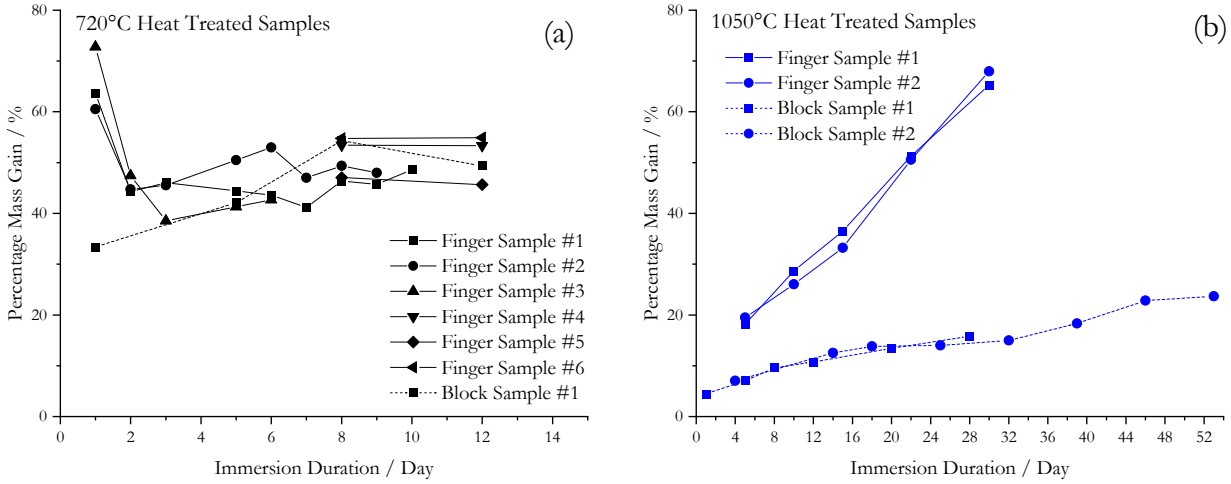

Figure 54. Comparison of percentage mass gains after salt immersion at 550°C for small finger samples and large block samples when (a) heat treated at 720°C and (b) heat treated at 1,050°C

Figure 55 shows the XCT scan images for Block Sample #2 in Figure 54 after 53 days of immersion in molten nitrate salt at 550°C. The left image shows the scan for a piece retrieved from the center of the block sample. The right image shows the scan for a piece retrieved from the corner of the block sample. The total porosities for the center and corner pieces based on the XCT scans were about 45.4% and 34.0%, respectively. For reference, the total porosity for the same geopolymer composition after 15 days of salt immersion at 550°C was about 47.5%. By closer inspection of the images in Figure 55, it seems that the permeation of the closed porosities by the molten salt was slightly more prominent at the corner, which agreed with the hypothesis that salt permeation is dependent on the depth from the geopolymer brick/molten salt interface. For reference, the center piece used for XCT was from a 10-cm × 5-cm × 3-cm brick, so the minimum salt permeation distance to the center piece was ~1.5 cm. In contrast, the corner piece was in direct contact with the salt, which means salt permeation occurred immediately. Regardless, both location showed good resistance to molten salt permeation, especially after 53 days of immersion and frequent freeze/thaw cycling. The results supported the hypothesis that a larger, commercial-scale brick could perform better.

In summary, the results of the isothermal immersion tests of geopolymer blocks in molten nitrate salt were very encouraging. They corroborate the material design that uses the geopolymer matrix

This report is available at no cost from the National Renewable Energy Laboratory at www.nrel.gov/publications.

as protection for the closed porosities formed by cenospheres in a molten nitrate salt environment where the closed porosities retained most of their properties during molten salt immersion up to 53 days.

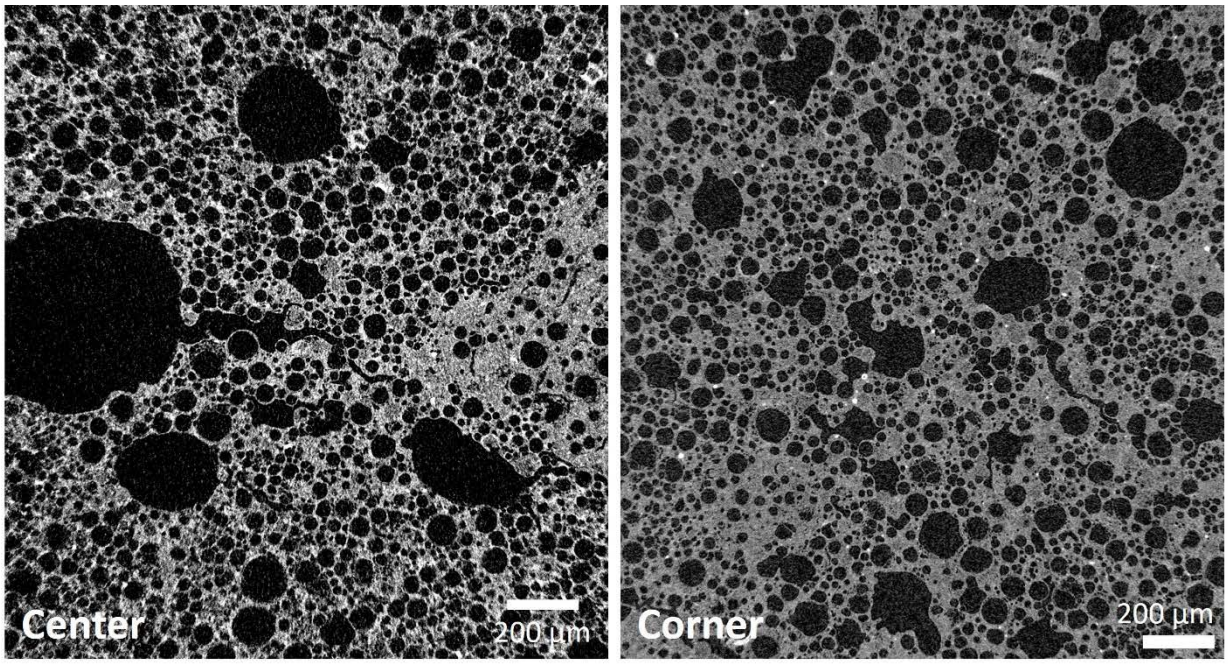

Figure 55. XCT scans of a block geopolymer sample after 53 days of immersion in molten nitrate salt at 550°C

2.2.8.1.4 X-ray Diffraction Analysis

A chemical compatibility check was performed with XRD to confirm that molten salt did not introduce significant chemical changes to the geopolymer matrix. The testing was focused on a metakaolin-only geopolymer with and without heat treatment at 900°C. The purpose was to confirm chemical stability of the matrix material alone in molten nitrate salt. The XRD patterns are given by Figure 56 and Figure 57.

This report is available at no cost from the National Renewable Energy Laboratory at www.nrel.gov/publications.

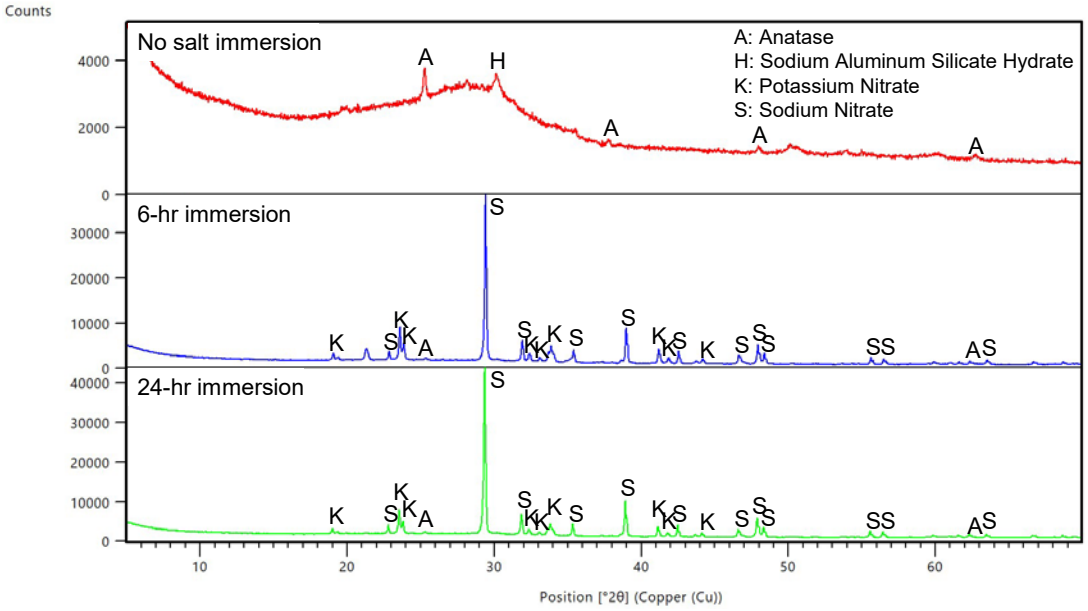

Figure 56. XRD patterns for metakaolin-only geopolymer without heat treatment, pre- and post-immersion in molten nitrate salt

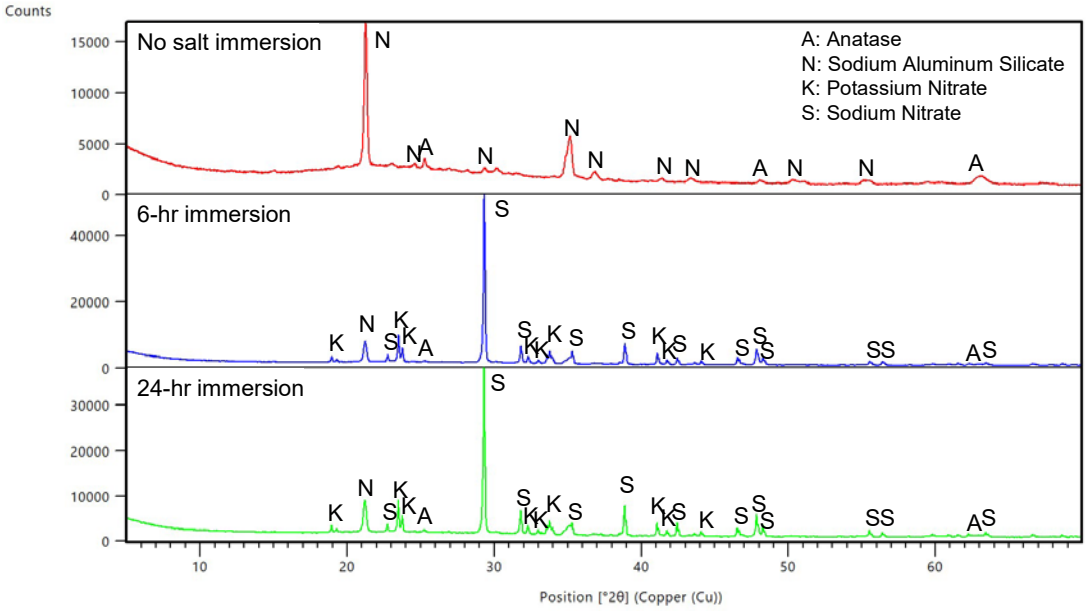

Figure 57. XRD patterns for metakaolin-only geopolymer with heat treatment at 900°C, pre- and post-immersion in molten nitrate salt

For metakaolin-only geopolymers, all major peaks in the XRD patterns were accounted for, including sodium nitrate and potassium nitrate (from salt saturation), sodium aluminum silicate hydrate (the known constituent in geopolymers without heat treatment), sodium aluminum silicate (the known constituent in geopolymers with heat treatment at 900°C), and anatase (from TiO_2 impurity in the raw metakaolin). In the post-immersion samples, no other major peaks were found, indicating minimum chemical reaction between the geopolymer matrix and the molten nitrate salt.

This report is available at no cost from the National Renewable Energy Laboratory at www.nrel.gov/publications.

It should be noted that analysis of a complex XRD patten can be subject to errors. But the XRD patterns should at least serve as qualitative proof that the metakaolin-based geopolymer matrix could be chemically stable in molten nitrate salt at up to 24 hours of immersion. Although longer-term tests might be desired, they might not be required. The ultimate goal of the geopolymer matrix is to protect the cenospheres from being attacked by the salt rather than for the matrix to remain chemically unchanged. Therefore, the XRD analysis was intended as a complementary study to the isothermal immersion tests and the thermal cycling immersion tests (discussed later).

2.2.8.2 Isothermal Immersion Tests in Molten Chloride Salt

Figure 58 shows the mass gain of one geopolymer block sample (7.5 cm × 5 cm × 2.5 cm) during immersion in molten chloride salt at 650°C for 27 days. The immersion results in molten nitrate salt are also included in Figure 58 for comparison. The geopolymer sample was not tested at the full Gen3 CSP operating temperature of 700°C–720°C because significant molten salt vaporization could clog up the test setup, making it difficult to safely remove the geopolymer sample from the molten salt bath for weight measurement. If the geopolymer sample cannot be removed from the molten salt bath before the salt freezes, the mass gain due to salt permeation cannot be measured. Note that for frequent weight measurement and fast freeze/thaw cycling, testing using a normal muffle furnace in ambient atmosphere was selected, which may contribute to more molten salt attack on the geopolymer matrix and closed porosities due to the increased corrosivity of the molten chloride salt.

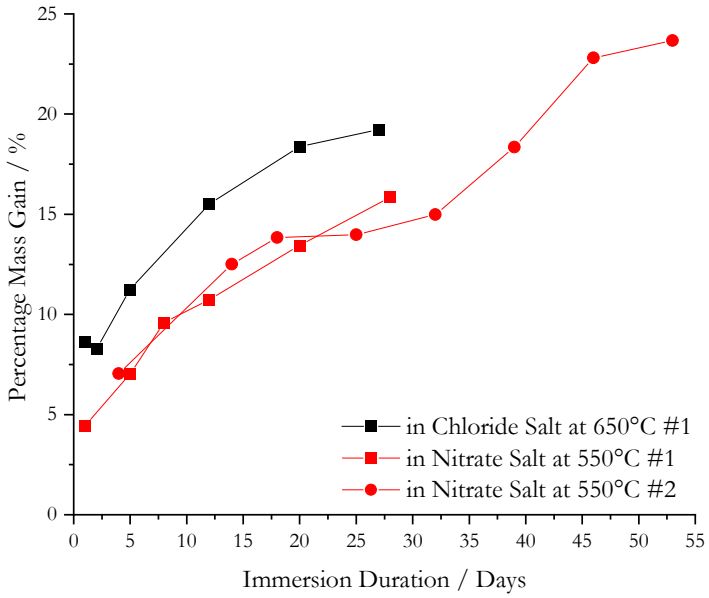

Figure 58. Comparison of the mass gain of geopolymer samples due to molten nitrate salt immersion at 550°C and due to molten chloride salt immersion at 650°C

Usually, molten chloride salt is expected to be more corrosive and cause more damage to the geopolymer insulation (or any other common materials like metals and ceramics) due to its higher operating temperature. But the results showed that the geopolymer performed comparably in the molten nitrate and molten chloride salts, where the difference was less than 5 wt.% of mass gain up to 25 days. Even the trend of mass increase with immersion time was similar between the two molten salts. This was encouraging because it suggested that, similar to when immersed in molten

This report is available at no cost from the National Renewable Energy Laboratory at www.nrel.gov/publications.

nitrate salt, the geopolymer matrix was likely protecting the cenospheres when immersed in molten chloride salt. Based on the similarity of mass gain data, it is postulated that molten salt permeation through the open porosities followed by attack on the cenosphere walls, regardless of the chemistry of the salt, is the dominating mechanism responsible for the loss of the closed porosities and thermal insulation performance. If this were true, then the hypothesis of larger geopolymer bricks used in a commercial-scale TES tank having better resistance to molten salt immersion would apply to not only a molten nitrate salt TES tank but also a molten chloride salt TES tank.

Figure 59 shows the XCT scan of the geopolymer block sample in Figure 58 after 27 days of immersion in molten chloride salt at 650°C. The specimen was retrieved from the center of the block sample. The total porosity was about 50% based on XCT calculation. The result looked very promising, either based on the appearance of the intact closed porosities or based on the estimated total porosity.

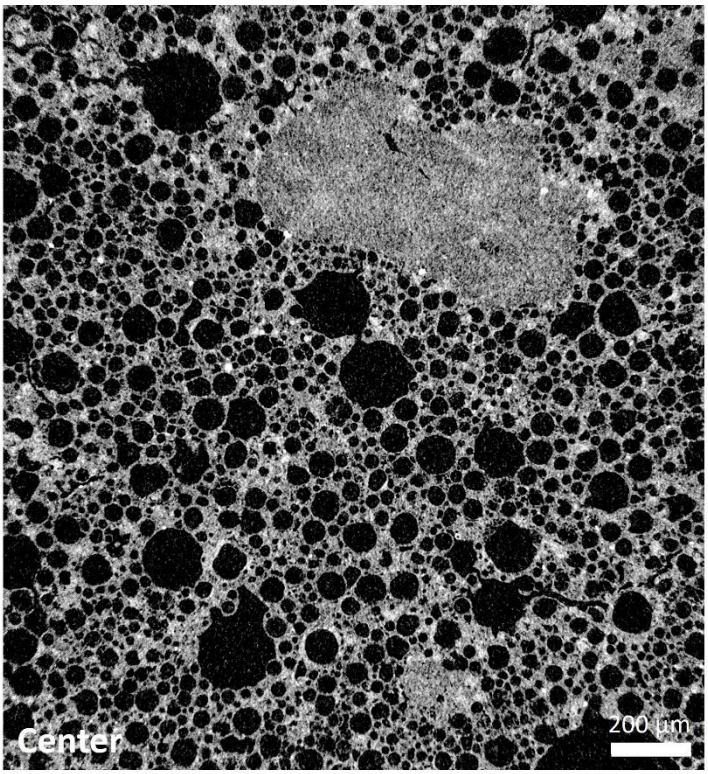

Figure 59. XCT scan of a geopolymer sample after 27 days of immersion in molten chloride salt at 650°C

Figure 60 shows the appearance of the geopolymer block sample in Figure 58 after 27 days of molten chloride salt immersion at 650°C. There was a clear color change, which is usually observed on ceramics and refractories when in contact with the corrosive molten chloride salt. For example, high alumina tubes (e.g., >95% alumina) used for molten chloride salt purification have a permanent color change in the section close to the molten chloride salt (either below the liquid surface or above in the vapor phase). Hence, it was not surprising to see a similar phenomenon. The more encouraging observation was that the brick retained its shape (including sharp corners and other local features with distinct geometry) and was not severely damaged by corrosion after 27 days (~650 hours) at 650°C.

This report is available at no cost from the National Renewable Energy Laboratory at www.nrel.gov/publications.

Figure 60. Appearance of a geopolymer block sample after 27 days of molten chloride salt immersion at 650°C

2.2.8.3 Thermal Cycling Immersion Tests in Molten Nitrate Salt

In addition to isothermal immersion tests, thermal cycling immersion tests with a temperature gradient were also performed. Figure 61 shows the schematic for the test setup, which is different from the isothermal immersion test setup (Figure 42) in a few ways:

- Instead of finger samples, much larger bar samples were used for thermal cycling immersion tests at 22.9 cm × 5.1 cm × 5.1 cm (9 in. × 2 in. × 2 in.). Larger dimensions were used to allow one end of the sample to be exposed to ambient conditions outside the furnace hot zone while the other end was immersed in molten salt.
- There was a significant temperature gradient within the geopolymer bar. When the furnace was heating up, the bottom of the bar could reach as high as 530°C while the top could be as low as 30°C–40°C. When the furnace was cooling down, the bottom of the bar (which was the hottest part at any time) was cooled to below the melting point of the salt to allow freezing of permeated salt inside the sample.
- Temperatures along the length of the bar samples were continuously monitored with thermocouples, as shown in Figure 61.

This thermal cycling immersion test setup purposely introduced not only a significant temperature gradient but also a salt freeze/thaw event for every heating/cooling thermal cycle. The maximum temperature gradient inside the bar was >2,000°C/m, which was much greater than the expected temperature gradient of 200°C/m–500°C/m in a molten salt TES tank. The purpose of the thermal cycling immersion tests was to simulate the geopolymer insulation layer in the direction of tank temperature drop (e.g., radially through the tank walls). The furnace heating and cooling changed the temperature profile inside the geopolymer bar samples and effectively moved the salt freeze plane up and down. The goal was to observe any changes or failures that might occur during the test. Since there was also salt freeze/thaw in each heating/cooling cycle, the geopolymer bar sample would experience a similar or even more complex stress test compared to the isothermal immersion test due to the presence of the temperature gradient at the same time. It was believed that this

This report is available at no cost from the National Renewable Energy Laboratory at www.nrel.gov/publications.

thermal cycling immersion test was the best representation of what could happen in the geopolymer insulation liner in a molten salt TES tank, especially at the liquid/solid salt interface.

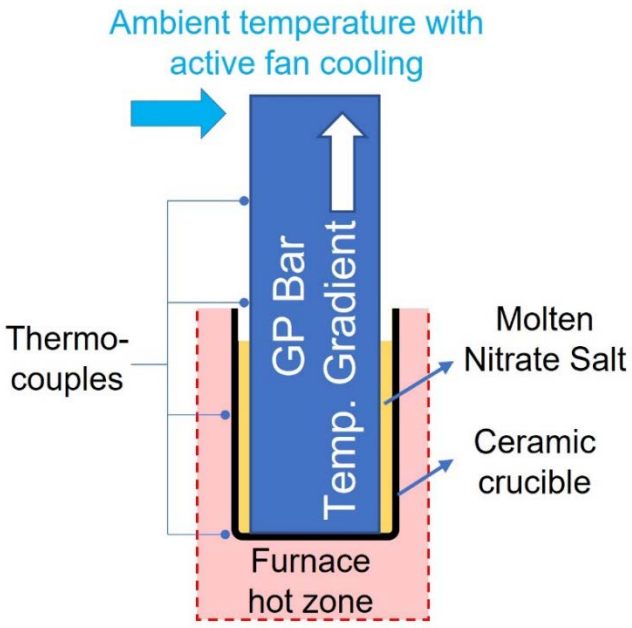

Figure 61. Schematic of the thermal cycling salt immersion tests

2.2.8.3.1 Standard Geopolymer Recipe

Figure 62 shows a picture of an early geopolymer bar sample without high-temperature heat treatment at 1,050°C after the thermal cycling immersion test in molten nitrate salt. Some cracks occurred in the molten-salt-saturated region of the sample. These cracks were found on three long faces of the bar as well as the bottom face that was immersed in molten salt. Because the sample was one of the first larger 9-in. × 2-in. × 2-in. bar samples produced, the cracking behavior might be associated with imperfect handling that led to preexisting cracks prior to thermal cycling. However, regardless of the crack formation, the bar survived over 10 cycles (i.e., no complete fracture of the bar after removed from the setup) with a temperature difference as large as 450°C during each heating/cooling cycle.

This report is available at no cost from the National Renewable Energy Laboratory at www.nrel.gov/publications.

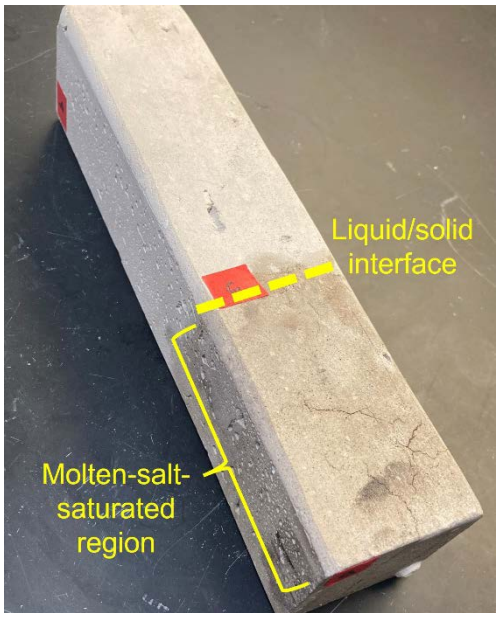

Figure 62. A geopolymer bar sample after a 10-cycle thermal cycling immersion test

Another geopolymer bar sample without high-temperature heat treatment at 1,050°C (without preexisting cracks) was tested for 20 cycles. The bottom 3 in. of the bar was cut off after the thermal cycling immersion test. Its post-immersion density was measured to be ~1.76 g/cc. The next 2 in. of the bar was measured to be ~1.46 g/cc, and the rest of the bar remained ~0.92 g/cc (i.e., similar to the pre-immersion bulk density because the top did not any have salt saturation). Given the pre-immersion bulk density of 0.92 g/cc and an open porosity of 10.9%, the calculated post-immersion bulk density should be 1.13 g/cc, assuming that the salt was frozen at 230°C with a density of 1.944 g/cc and it only saturated the open porosity. Clearly, the calculated post-immersion bulk density did not match the measured post-immersion bulk density. The most likely reason was that the assumption of molten salt only wetting the open porosity was not accurate because the bar samples were not heat treated at 1,050°C to close off some open porosities. A very rough calculation is given below.

For the bottom 3 in. of the bar to have a post-immersion bulk density of 1.76 g/cc, the total volume wetted by salt should be about 43 vol.%. For the next 2 in. of the bar to have a post-immersion bulk density of 1.46 g/cc, the total volume wetted by salt should be about 27%. Given the porosity measurement results by different methods (Table 9), it was reasonable to assume that some closed porosities were attacked and wetted by the molten salt in these geopolymer bar samples without high-temperature heat treatment. It corroborated the findings from the isothermal immersion tests, i.e., geopolymer samples must be heat treated at high temperatures around 1,050°C for the matrix to provide enough protection to the closed porosities formed by cenospheres.

2.2.8.3.2 Standard Geopolymer Recipe With Hardeners

Figure 63 shows the pictures of the four long faces of a post-experiment geopolymer bar sample with 3% of an aluminum phosphate hardener (FABUTIT 748 from Budenheim, Germany). The yellow rounded rectangle indicated a preexisting crack, most likely due to delamination during production. The red rounded rectangles indicated the cracks formed during the 20-cycle thermal cycling immersion test. Based on the connection of the cracks, it was hypothesized that the crack

This report is available at no cost from the National Renewable Energy Laboratory at www.nrel.gov/publications.

was initiated around the preexisting crack on Face d. The crack then propagated to Face a, Face b and Face c. Some other minor cracks were also formed around the propagation.

Figure 63. Four long faces of a geopolymer bar sample with 3% FABUTIT 748 addition after 20 cycles of thermal cycling immersion test

It was difficult to attribute these cracks to the sample's chemistry vs. the preexisting crack. But the result at least highlighted the importance of minimizing preexisting cracks, which suggested that handling during casting and curing is critical, and a geopolymer recipe with a potential to cause delamination must be avoided if possible. Both could be a weakness of the recipe with the hardener because this recipe could not be easily cast into the mold, which may be prone to formation of unwanted cracks and later delamination due to its high viscosity. Accelerated setting without additional water could also lead to shrinkage cracks.

As shown on the right side of Figure 63, the bar sample was cut into three pieces after the experiment. The post-immersion bulk density of the two bottom pieces, where full salt saturation occurred, were measured to be 1.240 and 1.276 g/cc. Given the pre-immersion bulk density of 0.953 g/cc and open porosity around 15.3%, the calculated post-immersion bulk density should be around 1.250 g/cc, assuming that the salt was frozen at 230°C with a density of 1.944 g/cc and it only saturated the open porosity. The relatively close match of the measured post-immersion bulk density and the calculated post-immersion bulk density suggested that most closed porosities were intact, in contrast to the results for the bar samples without the hardener. So the hardener seemed to benefit the molten salt permeation resistance.

The bottom two pieces of the bar sample saturated by frozen salt were sent for compression tests. The compression results of the two blocks were 27.3 MPa (middle block) and 32.7 MPa (bottom block with a long crack), both higher than any of the geopolymer samples that had been tested before. Note that the frozen salt would most likely act like a "glue." Therefore, the increase of the compressive strength did not necessarily reflect an enhancement of the mechanical properties of the geopolymer while it was saturated by molten salt at high temperature. But the intent was to roughly understand the effect of the molten salt on the mechanical properties of the post-immersion geopolymers. The tested geopolymer samples were in drastic contrast to other highly porous

This report is available at no cost from the National Renewable Energy Laboratory at www.nrel.gov/publications.

commercial refractory materials, which crumbled after salt immersion and had negligible compressive strength.

2.2.8.3.3 Standard Geopolymer Recipe With Hardeners and Additional Water

Additional water was added to reduce the viscosity of the recipe in the previous section. The goal was to resolve the preexisting crack issues due to possible delamination. One bar sample of this composition was tested extensively during the thermal cycling immersion test.

Before discussing the performance, it is necessary to compare the types of preexisting cracks of the tested bar samples to illustrate the effect of extra water, as shown by Figure 64. The surface appearances were different in the two recipes. The sample surface with 3% FABUTIT 748 hardener looked less smooth, or "grainier." This behavior was consistent with a trial recipe that used much lower water during mixing where the mixture felt "sandy." The cracks were also distinct. The sample with 3% FABUTIT had a long crack (indicated by the yellow rounded rectangle) while sample with 3% FABUTIT and 2.7% water had multiple cracks that radiated from a few surface features. Although without any quantitative evidence, the former seemed to warrant more attention. The fact that this was a single long crack likely due to delamination was more concerning. It suggested that the constituents in the recipe were not able to arrest a major crack initiation and subsequent propagation, which would eventually lead to macroscopic delamination. This was possibly a result of not having enough water that, in combination with NaOH and Na2SiO3, served as the binder during the geopolymerization process.

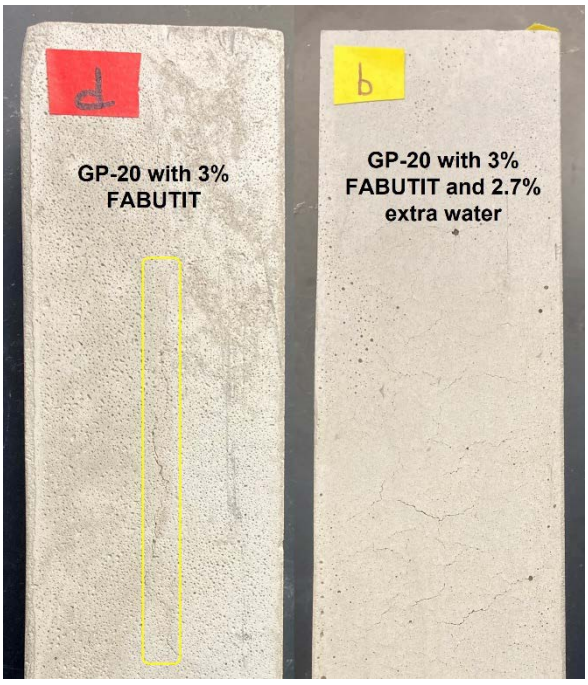

Figure 64. Comparison of cracking of a geopolymer bar sample with 3% FABUTIT and a geopolymer bar sample with 3% FABUTIT and 2.7% extra water

In contrast, the distribution and length of the cracks in the bar sample with 2.7% additional water were more uniform, suggesting that the cracks were a result of a more homogeneous event, e.g., shrinkage cracking that had more equal chance to occur throughout the sample surface. This

This report is available at no cost from the National Renewable Energy Laboratory at www.nrel.gov/publications.

phenomenon is commonly seen in the production of conventional firebrick materials too. It usually happens when the fine particulates float more easily with the liquid binder to the surface of the cast mixture. Therefore, there are higher chances of having the surface cracking due to the lack of coarse aggregates. Most likely, these smaller cracks are a surface phenomenon and the bulk of the geopolymer should not have similar cracks.

In total, the bar sample with 3% FABUTIT 748 and 2.7% water was subject to a 50-cycle thermal cycling immersion test. Figure 65 shows the pictures of the pre- and post-immersion sample after 35 thermal cycles.

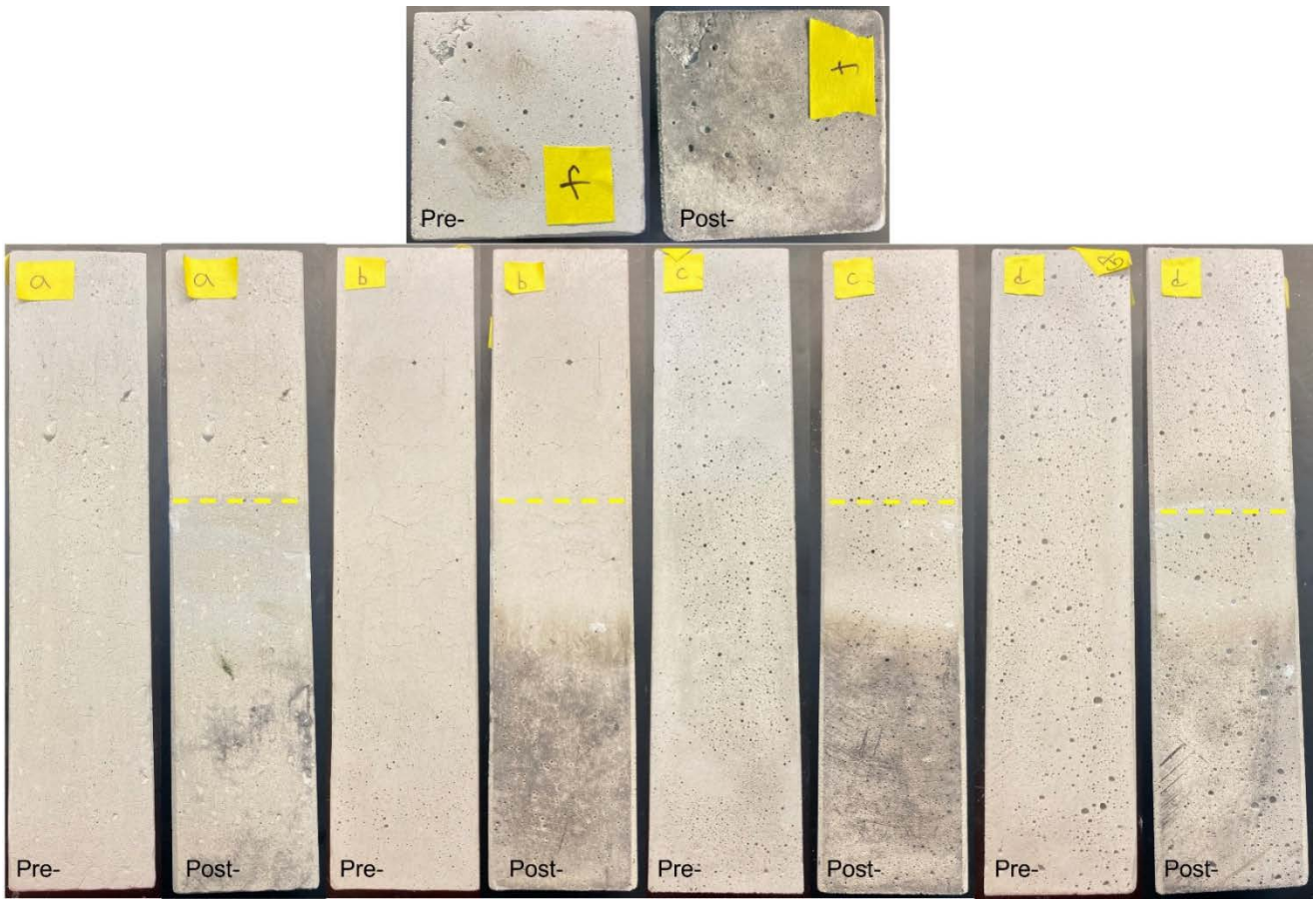

Figure 65. Pictures of pre- and post-immersion geopolymer bar sample with 3% FABUTIT 748 and 2.7% extra water after 35 cycles of thermal cycling immersion test

Face a to Face d were the sides that were partially immersed in molten salt, and Face f was the bottom side that was fully immersed in salt. The yellow dashed lines indicated the highest level of salt saturation in the post-immersion pictures. After comparing the pre- and post-immersion images for each face, it was concluded that the sample with 3% FABUTIT 748 and 2.7% water behaved well for 35 cycles. There was no obvious evidence of crack formation and delamination. The sample appeared to be very similar after 50 thermal cycles. NREL measured the bulk density of the geopolymer sections that were immersed in molten salt, using a similar method as described before. The measured bulk densities were 1.693 g/cc, 1.561 g/cc, and 1.537 g/cc for the bottom ~1 in., the next ~1 in., and the next ~3/4 in., respectively. The decreasing trend was similar to the observations before.

This report is available at no cost from the National Renewable Energy Laboratory at www.nrel.gov/publications.

In summary, the thermal cycling immersion tests were designed to stress-test the geopolymer samples to beyond the TES tanks' service conditions due to the frequent freeze/thaw cycling and high temperature gradient. It was not surprising to observe molten salt permeation into closed porosities. Under the normal service conditions, it is believed that the geopolymer liners at commercial scale would perform better, as shown by the isothermal immersion test results.

2.3 Scaling Up for Industrial-Scale Geopolymer Insulation Bricks

2.3.1 Conceptual Liner Design for a Prototype Tank Test

A prototype molten salt TES tank designed by an ongoing U.S. Department of Energy project was used as a basis to specify the size and shape of geopolymer insulation bricks for production trials. Figure 66 shows the liner drawing, designed by Morgan, for the prototype TES tank.

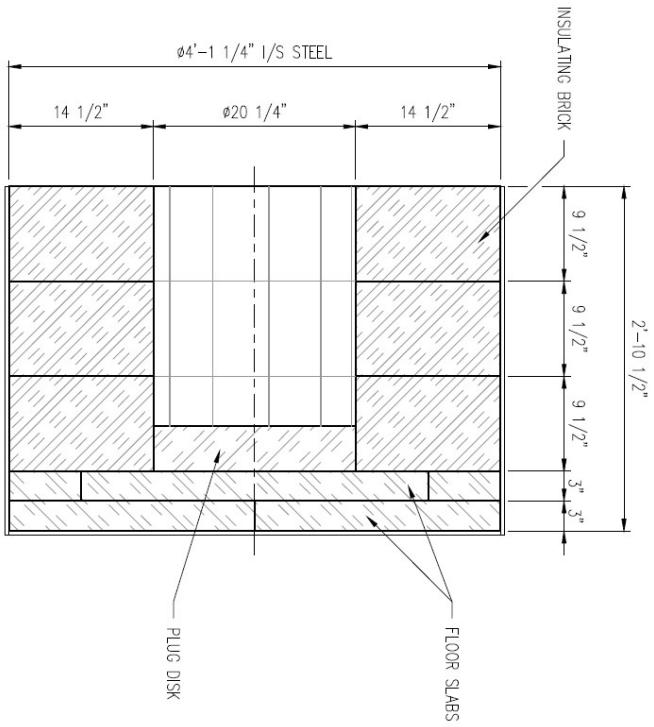

Figure 66. Insulation liner drawing of a geopolymer-lined prototype molten salt storage tank

The drawing features a one-layer design in the radial direction without any other insulation materials. The interface between the insulating bricks is parallel to the direction of salt permeation. In the axial direction, the drawing has a three-layer design with a plug-disk and floor slabs. This design features a zigzag interface between the floor slags and insulating bricks where salt permeation is more complex than in the radial direction. All interfaces between geopolymer bricks are envisioned to be joined by the geopolymer-based mortar (Section 2.2.4). The variety of mortar joint geometry not only provides the opportunity to test the mechanical integrity of mortars but also allows the measurement of the salt permeation behaviors as a function of permeation path.

Given the liner design, Morgan produced large molds as shown in Figure 67, which were used to demonstrate the manufacturability of the geopolymer materials in a production plant. The thermal insulation thickness of the insulating wall bricks in the radial direction of the prototype TES tank

This report is available at no cost from the National Renewable Energy Laboratory at www.nrel.gov/publications.

was about 14.5 in. or 368 mm. Each brick weighed about 50 lbs or 22.7 kg. For reference, the thermal insulation thickness of a commercial TES tank with geopolymer liner was estimated to be 1–2 times of the prototype-scale brick thickness. Hence, testing 14.5-in. bricks was believed to have direct impact on understanding the scaling of the geopolymer insulation.

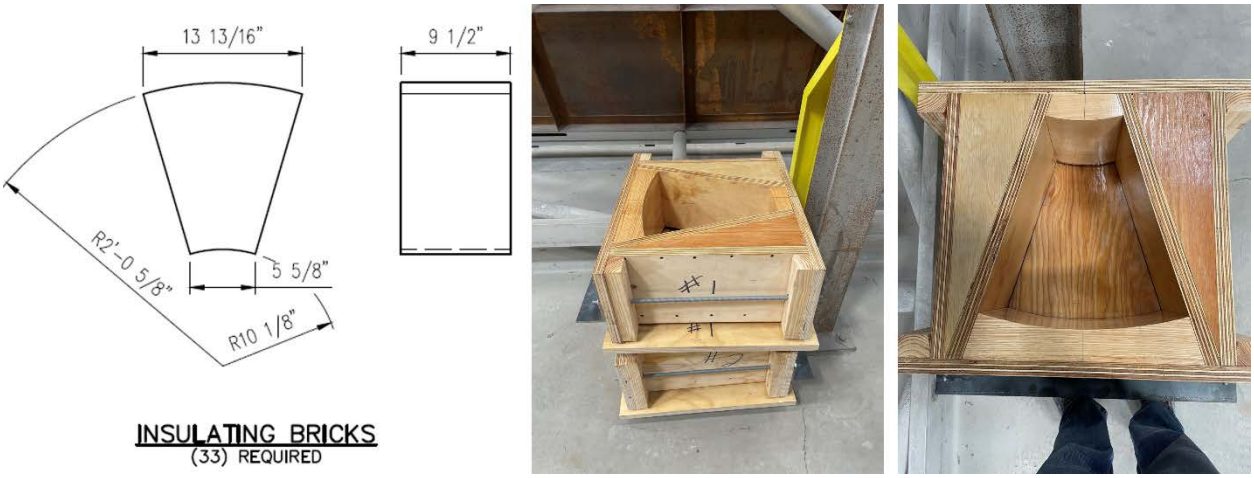

Figure 67. Schematic of geopolymer bricks showing the brick dimensions that fit the prototype tank and wooden molds made by Morgan to produce such geopolymer bricks

Figure 68 shows the pictures of the geopolymer insulation after casting inside a mold (left) and after 7 days of curing at 60°C (right). The material was cast easily into the mold and cured nicely to form sharp edges after curing.

Figure 68. Pictures showing the geopolymer insulation after casting inside a mold (left) and after 7 days of curing at 60°C (right)

Morgan and NREL performed thermal simulation of the geopolymer liner in the prototype molten TES tank (assuming molten chloride salts were used). The goal was to understand whether the liner in such a prototype salt storage tank could achieve the expected temperature profile and what heat loss would be expected. The key question was whether the conceptual liner design as shown in Figure 5, which has a salt freeze plane in the middle of the geopolymer liner, can be achieved.

This report is available at no cost from the National Renewable Energy Laboratory at www.nrel.gov/publications.

Table 13 summarizes the boundary conditions and simulation results. The key difference between Morgan's and NREL's simulations was that Morgan used a more complex three-dimensional (3D) heat transfer model and NREL estimated it with a simplified 1D heat transfer model.

Table 13. Summary of the Boundary Conditions and Simulation Results for the Geopolymer-Lined Prototype Storage Tank

	Morgan	NREL
Boundary Conditions and Constraints		
Salt temperature (°C)	720	720
Ambient temperature (°C)	22	22
Radiation emissivity of the tank shell	0.6	0.9
Ambient wind speed (m/s)	0	0.1
Total GP layer thickness (mm)	368	368
Results		
Wet GP thickness (mm)	194	195.1
Buffer GP thickness (mm)	174	172.9
Wet/buffer GP interface temperature (°C)	399.91	399.85
Tank shell temperature (°C)	70	69.52
Heat flux (W/m^2)	769.88	860.04

Regardless of the difference in heat transfer model used by Morgan and NREL, the temperature profiles obtained were very similar. In both cases, salt freezing occurred well within the geopolymer layer. Figure 69 is a schematic showing the location of the salt freeze plane (red lines) inside the geopolymer liner based on the tank geometry. In comparing to the liner schematic in Figure 66, the salt freeze plan was roughly in the midpoint of the wall liner in the radial direction and was roughly between the horizontal floor slab liners in the axial direction. Such a heat transfer profile would allow testing of the salt freezing not only within a geopolymer layer but also in between two geopolymer layers, i.e., around the mortar joint. The only noticeable difference between the simulations performed at Morgan and NREL was the total heat flux through the geopolymer liner due to the discrepancy between the 3D model and 1D model. It was expected that to achieve a freeze plane inside the geopolymer liner for a small prototype tank, more heat flux must be allowed. The heat fluxes of 770 W/m^2 and 860 W/m^2 were significantly higher than a commercial tank system if aiming for 98% daily round-trip efficiency (RTE) (i.e., <140 W/m^2 for the hot tank). However, the conceptual liner design was not primarily focused on achieving a high daily RTE; instead, its focus was to verify the partial saturation design of the geopolymer liner and its durability during operation. Morgan also performed similar simulations for the same prototype TES tank with a geopolymer liner assuming nitrate salts were used. The results suggested similar conclusions that a freeze plane could be achieved at about 258 mm into the liner with about 110 mm of dry geopolymer as the buffer. Simulation results for both types of salts indicated that size and shape of the bricks chosen by Morgan were closely relevant to the needs for future prototype tank testing.

This report is available at no cost from the National Renewable Energy Laboratory at www.nrel.gov/publications.

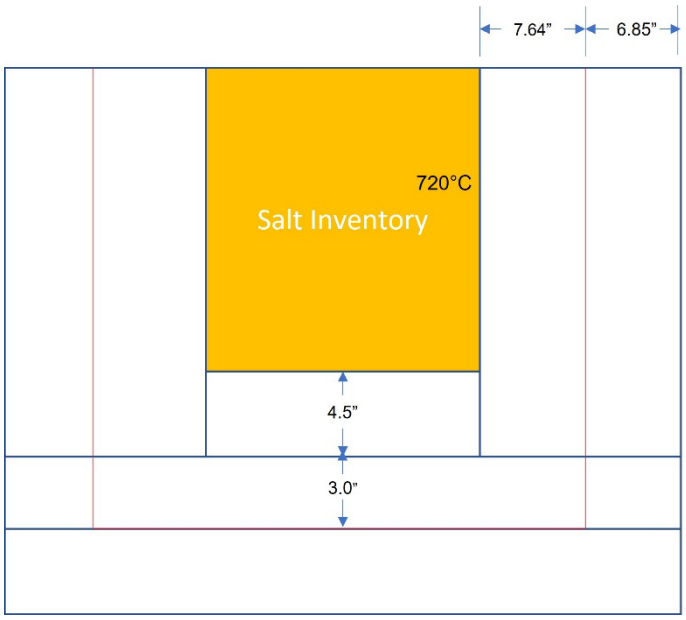

Figure 69. Schematic showing the location of the salt freeze plane inside the geopolymer liner in a prototype tank

2.3.2 Plant Demonstration and Diagnosis

2.3.2.1 Early Production Trials

Morgan produced several geopolymer bricks with heat treatment at 1,050°C as defined by the lab-scale studies. The composition has about 3 wt.% FABUTIT 748 and 3 wt.% additional water, as it showed promising performance based on the molten salt testing results. Figure 70 shows the comparison of one side face of the geopolymer brick before (left) and after (right) firing at 1,050°C. Some surface cracking was observed in both cases. Surface cracking is not a major concern for salt permeation resistance as long as the surface cracks do not propagate and cause more cracks.

This report is available at no cost from the National Renewable Energy Laboratory at www.nrel.gov/publications.

Figure 70. Comparison of one side face of a geopolymer brick before (left) and after (right) firing at 1,050°C

However, a bigger concern is the mottled surface after firing, as shown in Figure 71, which compares the top face of the geopolymer brick before (left) and after (right) firing at 1,050°C. Such mottled behavior only occurred at the top surface, which may be a result of fine particles in the wet mixture before casting migrating to the top surface of the sample. These fines had a lower melting point, thus giving the surface this appearance if slightly overfired. It could be avoided by minimizing vibration during casting and minimizing troweling of the surface when finishing. Another possibility was that the firing temperature was too high due to nonuniform distribution of the firing furnace. NREL had observed similar results a few times in the past when firing the geopolymer samples to above 1,050°C.

Figure 71. Comparison of the top face of a geopolymer brick before (left) and after (right) firing at 1,050°C

Figure 72 shows the bottom of the geopolymer brick after firing at 1,050°C. Cracking was observed, which was rarely observed before for small, lab-scale samples. The primary suspect was the wooden mold. Although the mold was applied a layer of shellac for water proofing, added water from the wet geopolymer mix could still escape and be absorbed by the wooden mold,

This report is available at no cost from the National Renewable Energy Laboratory at www.nrel.gov/publications.

causing improper dehydration. Retrospectively, a wooden mold was not the best choice. For later production trials, plastic molds, as used in previous lab-scale studies, were used.

Figure 72. Bottom face of a geopolymer brick after firing at 1,050°C

The first production of scaled-up geopolymer bricks had run into several manufacturing-related issues. But they were not outside the expectations. Morgan identified a few areas for improvement, including (1) how to properly cure the wet mix by controlling the dehydration procedure and (2) how to fire the cured pieces without introducing cracks and other mechanical/chemical defects.

Morgan produced a few more 50-lb geopolymer bricks with ~3 wt.% FABUTIT 748 and ~3 wt.% water. Some surface cracking was still observed. Figure 73 shows the interior cracks after cutting open the sample after 1,050°C firing. Neither NREL nor Morgan observed such serious internal cracking with smaller, lab-scale samples. It was hypothesized that the cracking was primarily correlated to scaling up the brick size. Larger brick volume may retain more moisture/water during the same 7-day 60°C curing process. If the moisture/water during the dehydration process could not be removed sufficiently, its buildup may lead to sudden volume changes during high-temperature firing, or at least the amount of moisture/water that needs to be removed during firing could potentially damage the bricks. Such issues are common in refractory firing. In addition, the large brick was thermally insulating with a thermal conductivity around 0.3–0.4 W/m·K. The low thermal conductivity may lead to slow thermal diffusion from the furnace to the bulk of the brick during firing where a large temperature gradient could be developed, causing thermal stresses and cracking.

This report is available at no cost from the National Renewable Energy Laboratory at www.nrel.gov/publications.

Figure 73. Interior cracks of the 50-lb geopolymer sample after 1,050°C firing

2.3.2.2 X-ray Diffraction Analysis

An alternative hypothesis for the cracking behaviors was that the added amorphous silica fume or other minor silica-bearing ingredients transitioned into quartz or cristobalite during firing—both are polymorphs of SiO_2. Quartz has a known phenomenon called quartz inversion at about 573°C, where the α-β phase transition occurs with a sudden volume change of about 0.45%. Similarly, cristobalite experiences an α-β phase transition at about 225°C where the phase transition is also accompanied by a sudden volume change.

Quartz inversion and cristobalite inversion during heating and cooling could cause some microscopic cracking which may later lead to macroscopic cracking. XRD performed previously on geopolymer samples made from metakaolin and the alkaline activator (see Figure 39) did not show any peaks associated with quartz or cristobalite. However, the XRD results on the geopolymer samples with other additives like silica fume, FABUTIT 748 hardener, and coarse aggregates did show peaks of cristobalite post-firing at 1,025°C and 1,050°C (Figure 74). According to Zhang et al. [32], silica fume conversion to cristobalite can happen at above 800°C and is fully completed at 1,100°C. Alkaline impurities in the silica fume could further promote such conversion. It should be noted that not all silica fume in the tested sample's recipe was expected to be fully converted. Silica fume was added partly as a reactive ingredient to tune the Si-to-Al ratio and Si-to-Na ratio because silica fume was anticipated to participate in the geopolymerization process to form the aluminosilicate structure. Theoretically, only the unreacted silica fume could be converted to cristobalite during the high-temperature firing. Therefore, if silica fume conversion to cristobalite was indeed the culprit of internal cracking, it would certainly suggest necessary improvement over raw material mixing as well as full utilization of the activator solution to enhance the reactivity of the silica fume. If needed, the amount of silica fume should also be reduced to ensure that no silica fume remains unreacted after 60°C curing and before firing.

This report is available at no cost from the National Renewable Energy Laboratory at www.nrel.gov/publications.

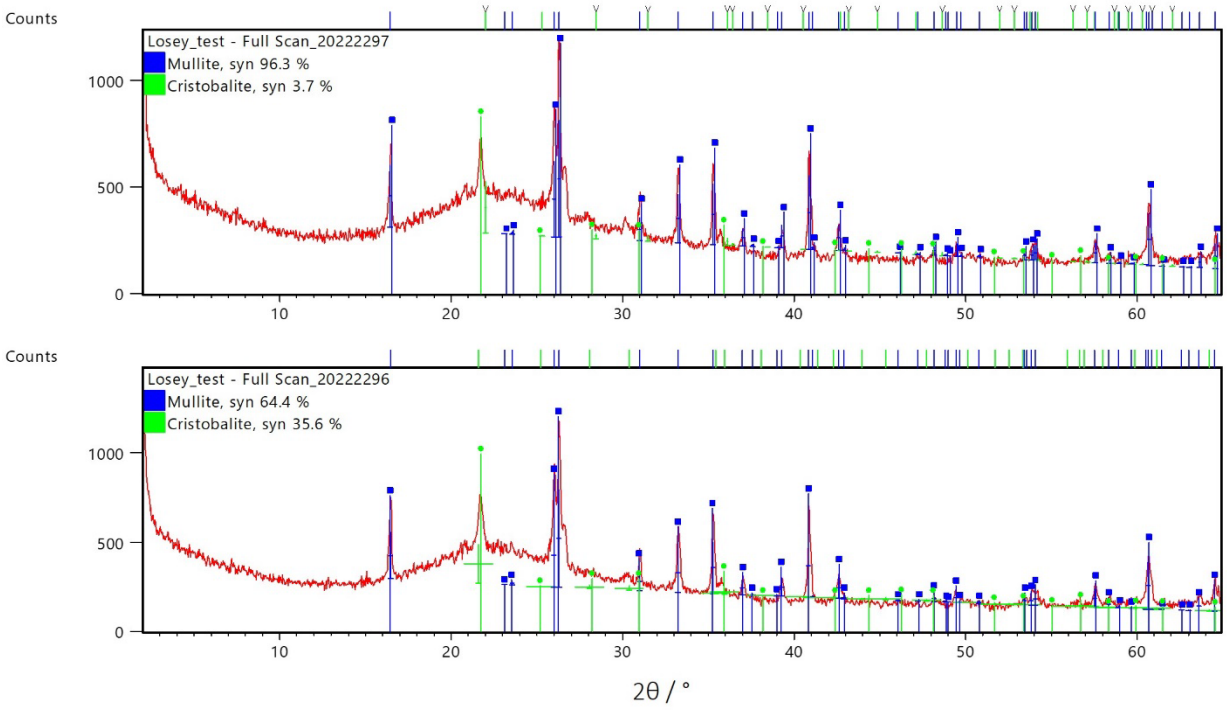

Figure 74. XRD patterns on geopolymer samples with silica fume, after 1,025°C firing (top) and 1,050°C firing (bottom)

2.3.2.3 Optimization of Firing Schedule

To understand the size effect, Morgan performed a round of firing experiments with thermocouples embedded inside the 50-lb geopolymer brick. The brick turned out to be similar to the brick shown before in Figure 73 in terms of cracking. The embedded thermocouples provided a better understanding of what happened inside the brick. Figure 75 shows the temperature monitoring of the ambient condition, the firing kiln, and two locations on the interior of the brick. The interior temperatures of the brick (i.e., TC Left and TC Right in the figure) lagged significantly behind the kiln temperature during heating and cooling. The maximum temperature difference happened around hour 40 during heating and around hour 65 during cooling. The magnitude of the maximum temperature difference was 310°C–320°C. Given the maximum temperature difference, an order-of-magnitude estimation of the thermal stresses during firing was performed. For a general material with a modulus of elasticity E and CTE α, the thermal stress is given by the following equation $\sigma_T = E\alpha\Delta T$, where ΔT is the temperature difference experienced within the material.

This report is available at no cost from the National Renewable Energy Laboratory at www.nrel.gov/publications.

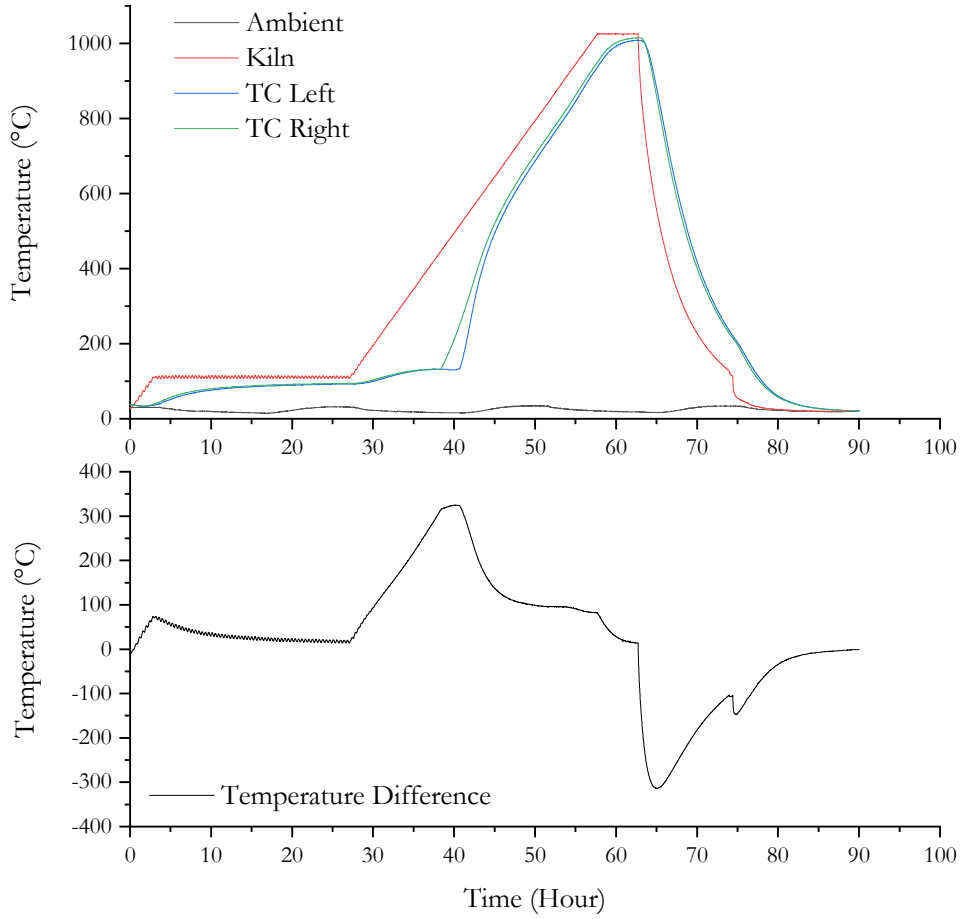

Figure 75. Temperature monitoring of the original geopolymer firing process

Based on Figure 29, the CTE of a typical geopolymer sample was around 2.5 × 10^{-6}/°C. The modulus of elasticity was estimated to be about 5 GPa given a compilation of strength vs. modulus by Lee and Lee [33] where 5 GPa was the lowest observed value for a similar group of alkaline-activated fly-ash/slag geopolymers in the literature. Table 10 also showed that the estimated modulus of elasticity, as approximated by the ratio of ultimate strength to ultimate strain, agreed with the estimated range. If using 5 GPa as an average, the thermal stress is estimated to be about 3.75 MPa. Note that this is a rough estimation of thermal stress. Full finite element analysis (FEA) and more accurate stress-strain relation for the geopolymer brick are needed to perform more meaningful thermal stress analysis during steady state as well as during transient state. But the order-of-magnitude calculation suggests that the large temperature difference during firing might be the reason why cracking was more extensive in large bricks. If the geopolymer did not gain full strength before firing, a few megapascals of thermal stresses (or even stress depending on the actual material properties, geometry, heat transfer scenarios, etc.) would crack the interior.[22] This

[22] The geopolymer's compressive strength is about 20–30 MPa based on experimental measurements. However, the tensile strength in a refractory is significantly lower than its compressive strength. Hence, if the internal thermal stresses are tensile in nature, the geopolymer could crack more easily.

This report is available at no cost from the National Renewable Energy Laboratory at www.nrel.gov/publications.

issue was more relevant for large bricks because the large brick size made it harder for heat to diffuse into the interior, which eventually led to large temperature difference.

Another attribute, other than slow heat diffusion, was that the geopolymer was experiencing a dehydration process during curing which, as an endothermic reaction, prevented the interior from heating up. It was observed that the interior temperature plateaued around 130°C between hour 35 and hour 40 while the furnace was heating up at a constant rate of about 30°C/hour or 0.5°C/min. The fact that the interior temperature could not keep up with such a slow 30°C/hour heating rate was indicative of a certain endothermic phenomenon. After this temperature plateau, the geopolymer interior temperature increased at a significantly faster rate and eventually approached the furnace temperature. Note that after around hour 45, the heating rate of the geopolymer interior was almost the same as the furnace heating rate where the temperature difference was stabilized around 90°C–95°C.

In conclusion, the firing process should be modified to minimize thermal stresses and to reach the target firing temperature in the large 50-lb bricks. The right firing process may control the cracking behavior in large bricks. Morgan was able to successfully make medium-sized bricks with 9-in. × 4.5-in. × 2-in. dimensions where the maximum thermal diffusion length during firing was only about 1 in. (vs. >5 in. in the large 50-lb bricks). No other changes were made during the scaling-up effort. Therefore, it is believed that the cracking was correlated to the large brick size and the thermal stresses. To address these issues, a few modifications to the production process were proposed:

- The wrapping of the large bricks needed to be more thorough. If the exterior of the bricks was not wrapped carefully, the drying process at 60°C may lead to faster dehydration process at the surface of the brick while leaving the interior drying at a relatively slower pace. This differential drying could cause issues later during firing.
- A much slower firing schedule needed to be used with a heating ramp rate of about 0.5°C/min. Previous firing followed a common ramping speed of about 2.5°C/min, which could be too fast for large geopolymer bricks with partially cured interior.
- The furnace needed to be held at a lower temperature, e.g., 130°C–150°C, to allow the geopolymer to cure and gain strength before proceeding to the next stage of higher-temperature firing.
- The cooling rate should be better controlled as well. From Figure 75, the cooling rate was clearly faster than the heating rate which resulted in a large temperature difference of around 310°C at around hour 65.

Figure 76 shows the temperature measurements inside a 50-lb geopolymer brick (TC 1 and TC 2) under the revised firing schedule with additional low-temperature holding steps to minimize temperature gradient and thermal stresses. The additional holding steps were set at about 110°C, 160°C, and 250°C. A temperature of 110°C was intended to completely drive off physical water, and 160°C was intended to complete the geopolymerization process that was believed to have caused the temperature holding at about 130°C in the previous firing experiment. The goal was to minimize the effect of the potential endothermic reaction at around 130°C. In the worst-case scenario, the maximum temperature gradient even with the residual endothermic reaction at 130°C would have been around only 30°C (i.e., 160°C furnace temperature minus the 130°C endothermic reaction temperature). The 250°C temperature was a precaution that ensured completion of the

This report is available at no cost from the National Renewable Energy Laboratory at www.nrel.gov/publications.

geopolymerization process before going to the high-temperature firing step at greater than 1,000°C. It is very likely that this 250°C holding can be removed in the future for more efficient production.

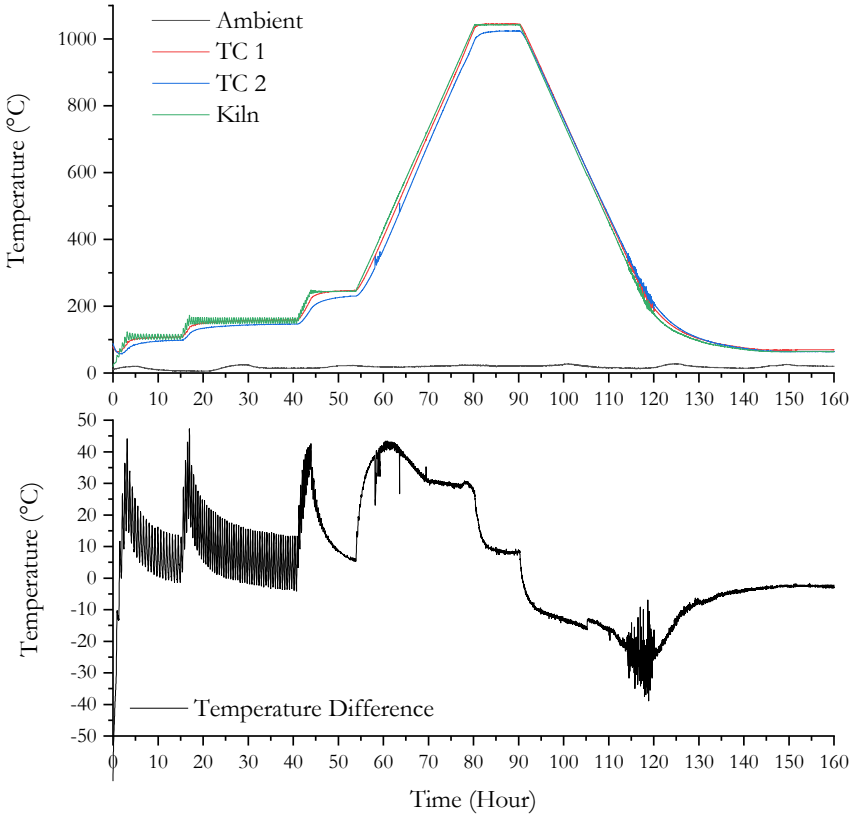

Figure 76. Temperature monitoring of the revised geopolymer firing process

The results in Figure 76 were expected. There was a significant difference in the temperature measurements after the brick was heated at 110°C. Previously, the difference between the intended heating schedule (i.e., the kiln temperature) and the geopolymer interior temperatures increased rapidly from less than 50°C to more than 330°C in about 10 hours. In Figure 76, the geopolymer interior temperatures caught up with the heating schedule in a much shorter time frame and the temperature difference was never more than 50°C, which was a significant improvement. The behavior after the 160°C holding step was also improved. The interior temperatures caught up with the heating schedule during the 250°C holding step in a similar fashion without a large temperature gradient (less than 45°C). More interestingly, once the heating schedule switched to the ramping step towards 1,050°C for final firing, the geopolymer interior temperatures almost followed the heating rate immediately with a maximum temperature gradient of less than 45°C (vs. 330°C with the original firing schedule) and an average temperature gradient of about 30°C (vs. about 100°C with the original firing schedule). Note that the first firing experiment followed most of the revised firing schedule but mistakenly used a higher heating rate of 50°C/hour. Even with the higher heating rate, the temperature gradient was substantially reduced. Hence, it confirmed that an additional holding step at around 160°C was likely able to prevent a significant buildup of temperature gradient during firing. The duration of this holding step could be as short as 5 hours because the sample interior temperatures caught up with kiln temperature in that time frame.

This report is available at no cost from the National Renewable Energy Laboratory at www.nrel.gov/publications.

Figure 77 compares the cross sections of the geopolymer bricks fired with the original and revised schedules. The cracking behavior was greatly reduced due to the added holding steps, even though the revised schedule had a faster heating rate of 50°C/hour. The spiderweb cracking, typically indicative of shrinkage cracking, completely disappeared.

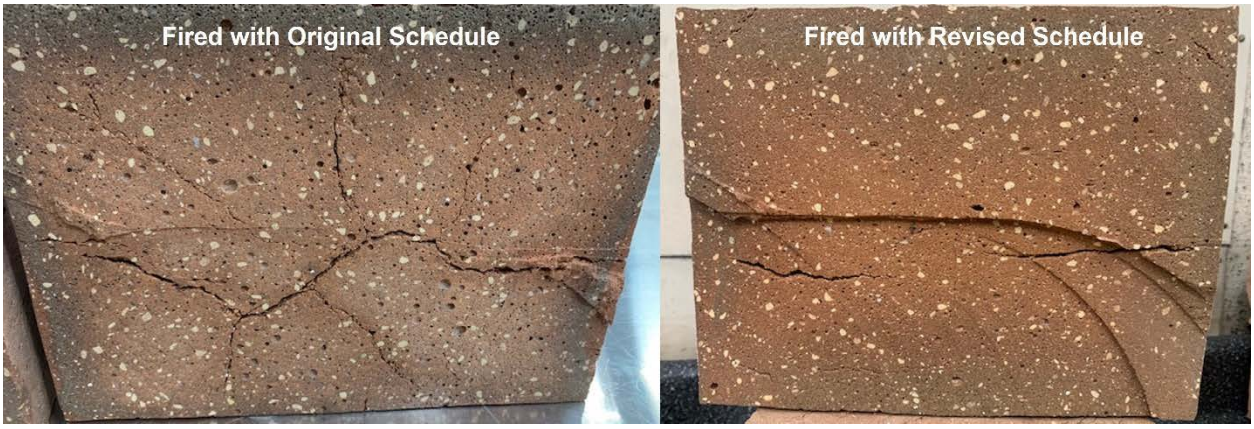

Figure 77. Cross-section comparison of geopolymer bricks fired with original and revised firing schedules

The two horizontal cracks on the right of Figure 77 were suspected to be due to lamination, which was caused by lamination of wet mixture during casting because of less water was added for this sample. In addition, the brick was fired in a vertical orientation where the brick was rotated 90° during firing compared to the orientation during casting. This mistake likely caused some "pulling" stresses on the brick during firing, as illustrated by Figure 78. If lamination occurred during casting, this pulling stress could exaggerate the cracking behaviors. Retrospectively, this was not the most ideal brick orientation during firing. Therefore, Morgan returned to a horizontal firing orientation for future production trials.

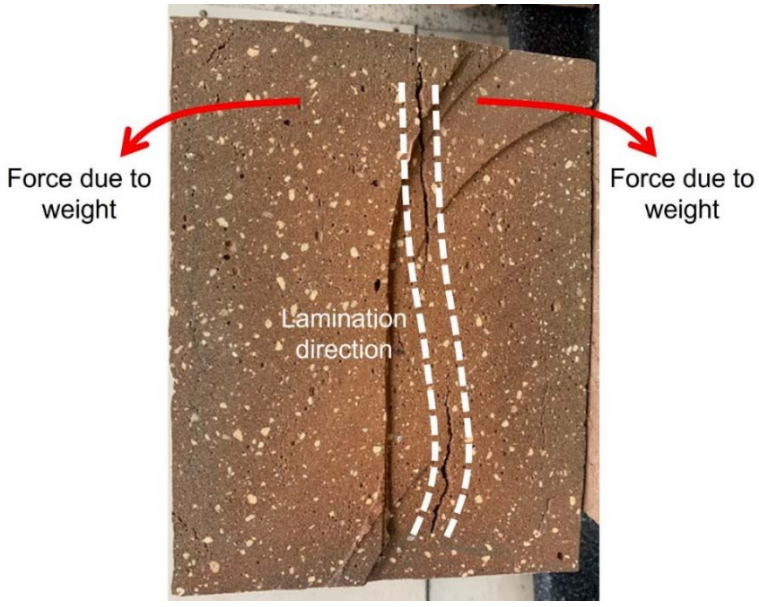

Figure 78. Schematic of geopolymer firing orientation and potential lamination direction

This report is available at no cost from the National Renewable Energy Laboratory at www.nrel.gov/publications.

Another firing experiment was conducted by Morgan. The cross section of the fired brick is shown in Figure 79. It was confirmed that the internal crack was controlled well by the revised firing schedule. Given the results of these two rounds of firing experiments with the revised heating schedule, it indicated that the internal spiderweb cracking was most likely caused by high thermal stresses arising from large temperature differences. There were still some cracks close to the surface as observed in the cross section in Figure 79. But they might be related to too-aggressive dehydration that was likely caused by too much water added to this batch of mixture. Given NREL's lab-scale experience, controlling the dehydration speed was the key to lowering surface cracking. Two batches of geopolymer samples made at NREL for mortar testing confirmed that good wrapping of the bricks during curing was critical to avoid surface cracking.

Figure 79. Cross section of a firing trial with the revised heating schedule showing minimum internal cracking

In conclusion, the firing process was modified to minimize thermal stresses and to reach the target firing temperature in large 50-lb bricks. With the revised firing process, most of the cracking behaviors in large bricks were controlled. Morgan was able to successfully make medium-sized bricks with 9-in. × 4.5-in. × 2-in. and 9-in. × 2-in. × 2-in. dimensions without any cracking issues. Therefore, the cracking must be related to the large brick size. The production challenges were related to properly curing bricks of this size without (1) a too-aggressive dehydration process during low-temperature curing, and (2) too-high thermal stresses during high-temperature firing. The thermal stresses had been regulated using an appropriate firing schedule with multiple holding steps. The remaining cracking was hypothesized to be related to shrinkage of the geopolymer materials in general (e.g., due to dehydration, phase transitions, etc.).

2.3.2.4 Effect of FABUTIT 748 Hardener on Large Bricks

Given the persistence of interior cracking in large geopolymer bricks, NREL and Morgan suspected that the hardening agent, FABUTIT 748, might not be beneficial. According to the FABUTIT 748 manufacturer (Budenheim Germany), FABUTIT 748 was designed to accelerate

This report is available at no cost from the National Renewable Energy Laboratory at www.nrel.gov/publications.

curing of silicates by allowing the active ingredients to react in ambient environment.[23] This suggests that the hardening effect would very likely only happen at the surface if gas diffusion/permeation through the geopolymer surface were the limiting factor. Hence a hard shell is expected to form on the geopolymer brick much earlier than when the interior of the brick starts to harden. This could have a negative impact when the interior starts to shrink due to the geopolymerization process because the hard shell does not have much compliance and hence can stress the interior. In addition, the escape of water may also stress the rigid shell if the shell does not have enough permeability for water vapor.

One small geopolymer sample was made at NREL with 1.7 wt.% of FABUTIT 748 (i.e., similar to the recipe used by Morgan in their plant demonstration), fired immediately after overnight curing at room temperature. The results shown in Figure 80 revealed that addition of FABUTIT 748 had a detrimental effect on cracking. This further corroborated the hypothesis about the negative effect of the FABUTIT 748. In principle, sodium geopolymer is synthesized by activating a mild-pH metakaolin with a basic NaOH and Na-silicate activator solution. The activator breaks down the metakaolin to form the $Al(OH)_4^-$ and $SiO_2(OH)_2^{2-}$ species, which are later polymerized to form the geopolymer structure. FABUTIT 748 is an acidic compound made of aluminum phosphates which is more acidic than metakaolin. It means FABUTIT 748 may have the chance to interfere with the function of NaOH and Na-silicate to break down metakaolin. NaOH with a high pH is intended to break down the less acidic metakaolin to release Al and Si for the geopolymerization process. But the more acidic FABUTIT 748 could neutralize part of the NaOH leading to less effective breakdown of the metakaolin. This is the primary suspected reason why FABUTIT 748 seems to cause cracking.

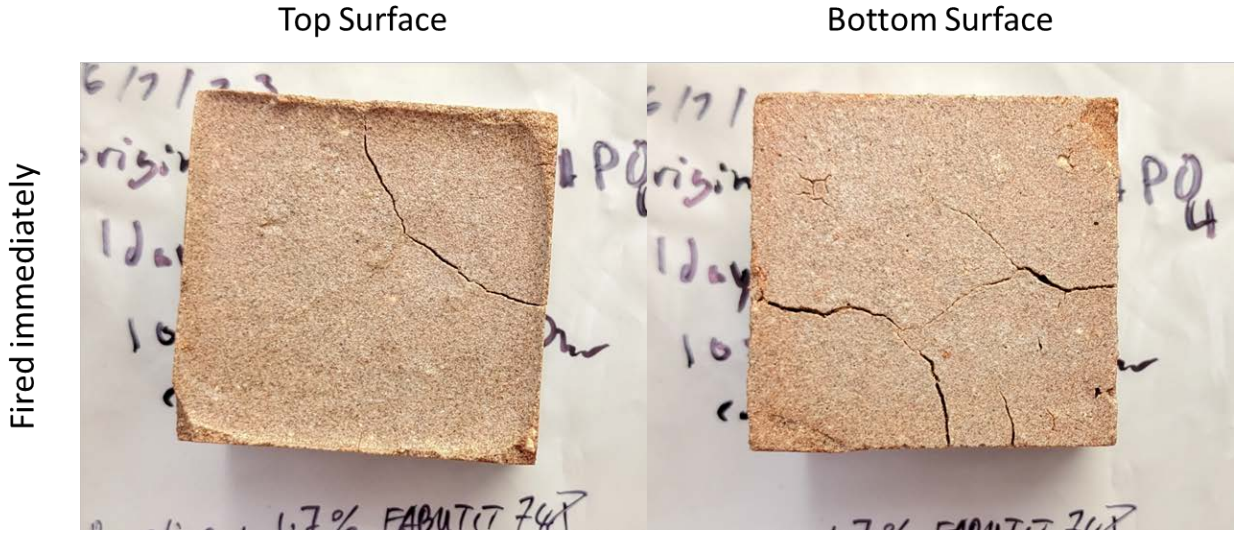

Figure 80. Cracking behavior of a geopolymer brick with 1.7 wt.% of FABUTIT 748 addition after firing

[23] CO_2 is believed to be the active gas that participates in the reaction. The exact mechanism of the reaction was not disclosed by Budenheim.

This report is available at no cost from the National Renewable Energy Laboratory at www.nrel.gov/publications.

2.3.2.5 Reduction of Shrinkage With Additional Aggregates

Figure 81 shows the interior of a series of lab-scale geopolymer samples with different amounts of additional large aggregates (all without the FABUTIT 748 hardener). The linear shrinkage for each sample is given in Figure 81[24] and summarized in Figure 82. The goal was to demonstrate the effectiveness of coarse aggregates on mitigating internal cracking. The name "Baseline" referred to the previous geopolymer recipe with about 10% of coarse aggregates. Three different curing schedules were tested: (1) without 60°C curing and fired immediately after de-molding, (2) fired after 3–5 days in ambient temperature and ambient relative humidity, and (3) fired after 3–5 days in ambient temperature and >95% relative humidity. Regardless of curing schedule, extensive internal cracking was observed for all bricks with less than 20% additional coarse aggregates. By comparing the cracking behaviors of bricks with the same coarse aggregate content but different curing schedules, the best overall behaviors were observed on the bricks fired after 3–5 days of curing, which corroborated with earlier results. As shown before, the curing of the interior prior to firing was critical. Without proper curing, the sample's interior temperature would be kept low while the exterior temperature (roughly equal to the furnace temperature) increased. The temperature difference could lead to large thermal stresses and internal cracking.

In addition to thermal stresses, the effect of stresses due to linear shrinkage was also reflected by the results in Figure 81. The extent of internal cracking was correlated with linear shrinkage within the same group of samples with the same curing schedule. It was clearly demonstrated that large coarse aggregates had a positive impact on the samples' resistance to internal cracking. It agreed with the best industrial practice as well, i.e., the use of additional large aggregates is the one of the most likely solutions for the refractory industry to mitigate cracking risks. NREL and Morgan have been avoiding increasing the coarse aggregate content during lab-scale development because it would compromise the thermal insulation properties. But at this point, large aggregates may be the most viable solution after many attempts on other methods.

[24] An entry with two shrinkage numbers means that two samples were produced and measured.

This report is available at no cost from the National Renewable Energy Laboratory at www.nrel.gov/publications.

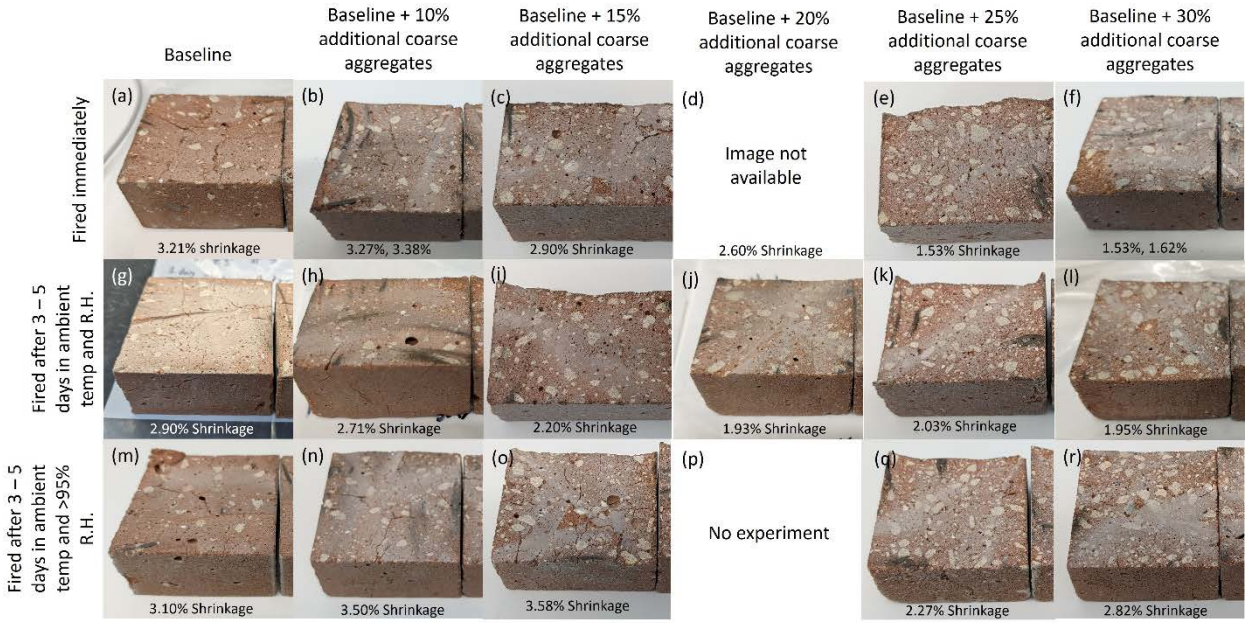

Figure 81. Interior of various geopolymer brick recipes that have additional large aggregates, fired after different curing schedules

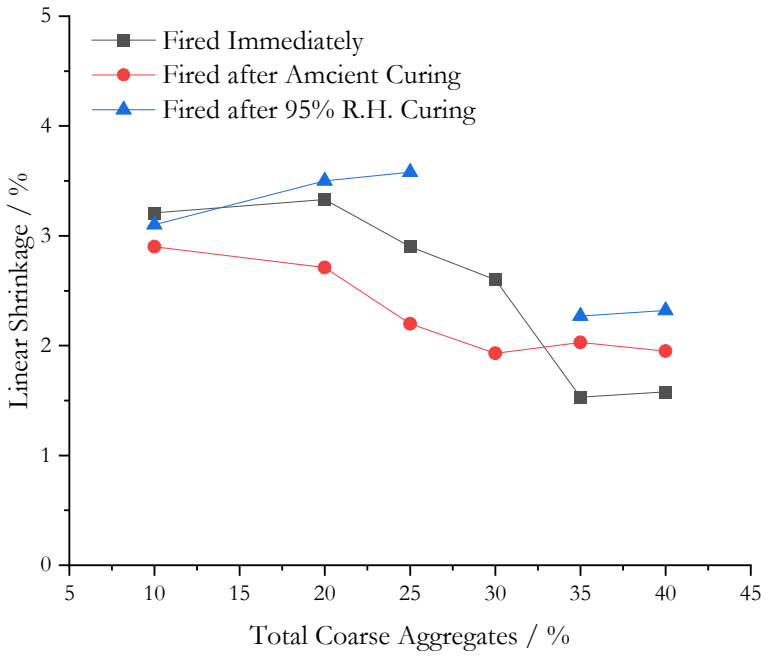

Figure 82. Linear shrinkage vs. total coarse aggregate content for geopolymer samples fired after different curing conditions

Figure 81(a)–(f) show the interior of a series of baseline bricks with 0%–30% additional coarse aggregates which were fired immediately after overnight curing in the mold at ambient temperature. The direct comparison showed that more coarse aggregates, correlated with lower linear shrinkage values, reduced the extent of internal cracking. However, the internal cracking was not completely eliminated. The results in Figure 81(g)–(l) show the effect of a few days of

This report is available at no cost from the National Renewable Energy Laboratory at www.nrel.gov/publications.

curing at room temperature and ambient relative humidity (i.e., no wrapping), coupled with additional coarse aggregates. Note that the samples in Figure 81(i)–(l) behaved the best in terms of internal cracking, which corresponded to the lowest shrinkage values. There was also a trend of reduced external cracking as the content of large aggregates increased. The observation corroborated with previous understanding that some curing, even only at room temperature, with slow firing should improve the resistance to cracking. The same applied to baseline bricks with 10–30 wt.% additional coarse aggregates fired after 3–5 days of curing in ambient temperature and ~95% relative humidity, as shown in Figure 81(m)–(r). The internal cracking was reduced by more large aggregates but was not completely eliminated, possibly due to higher shrinkage.

In short summary, although the persistent internal cracking on the baseline recipe was disappointing after an extensive investigation, the findings on coarse aggregates were still considered positive for geopolymer production. Eventually, it would most likely be a decision based on the compromise between (1) aiming for better thermal insulation properties by keeping the original baseline recipe with a lower amount of coarse aggregates and (2) aiming for a lower risk of cracking by allowing more large aggregates. As shown later in Section 2.3.2.6, curing cost is expected to be a major contributor to the price of geopolymer insulation. The high cost is largely due to the lengthy curing process at 60°C, which not only requires more labor for handling but also needs more materials for molds and more plant space for curing. Therefore, if trial production can demonstrate the technical feasibility of using more large aggregates to improve cracking resistance, which allows a shorter curing time, the trade-off with reduced thermal properties for the final bricks might be economically appealing.

2.3.2.6 Effect of Firing Temperature on Shrinkage and Cracking Behaviors

Figure 11(b) showed the effect of heat treatment temperature on volume of early geopolymer samples that were cured at 60°C for at least 7 days. Since the long 60°C curing turned out to be costly, alternative curing at room temperature without labor-intensive wrapping was preferred. As suggested by the results in Figure 81, room temperature curing at ambient conditions may also be viable. A series of geopolymer samples with 25% additional coarse aggregates were then tested with ambient curing prior to firing at different temperatures of 350°C, 550°C, 750°C, and 1,050°C, with the hope to identify the correlation between firing temperature, linear shrinkage and cracking behaviors. A volume of 25% additional coarse aggregates were selected because this content showed a borderline behavior where ≥25% seemed to guarantee no internal cracking.

Figure 83 shows the interior pictures and the linear shrinkage of the geopolymer samples with 25% additional coarse aggregates fired to 350°C, 550°C, 750°C, and 1,050°C, after 6 days of ambient curing without any wrapping. Internal cracking was not observed thanks to the addition of 25% coarse aggregates. Even the 1,050°C sample did not show any internal cracking, likely because the final linear shrinkage was controlled to be less than 2%. Note that a color change from plain gray to red was observed when the firing temperature increased. It was unknown whether the color change was correlated to distinct phase formations. It was possible that the Fe content in the cenospheres (1–5 wt.% based on suppliers' specifications) may have contributed to the color change when the Fe species was oxidized. The results showed a fast increase of linear shrinkage above a firing temperature of 750°C. The correlation between a fast-increasing linear shrinkage above 750°C and the observed cracking after 1,050°C firing strongly suggested that shrinkage, triggered at high firing temperature possibly due to a phase change of the geopolymer matrix or other active ingredients, may be a contributor to the overall cracking behaviors. Even with

This report is available at no cost from the National Renewable Energy Laboratory at www.nrel.gov/publications.

controlled thermal stresses (as part of the stresses experienced by the material during firing) using the optimized firing schedule as shown in Section 2.3.2.3, stresses developed due to shrinkage may still damage the geopolymer structure. Therefore, managing overall linear/volumetric shrinkage of geopolymer bricks is the key to future success in large-scale production.

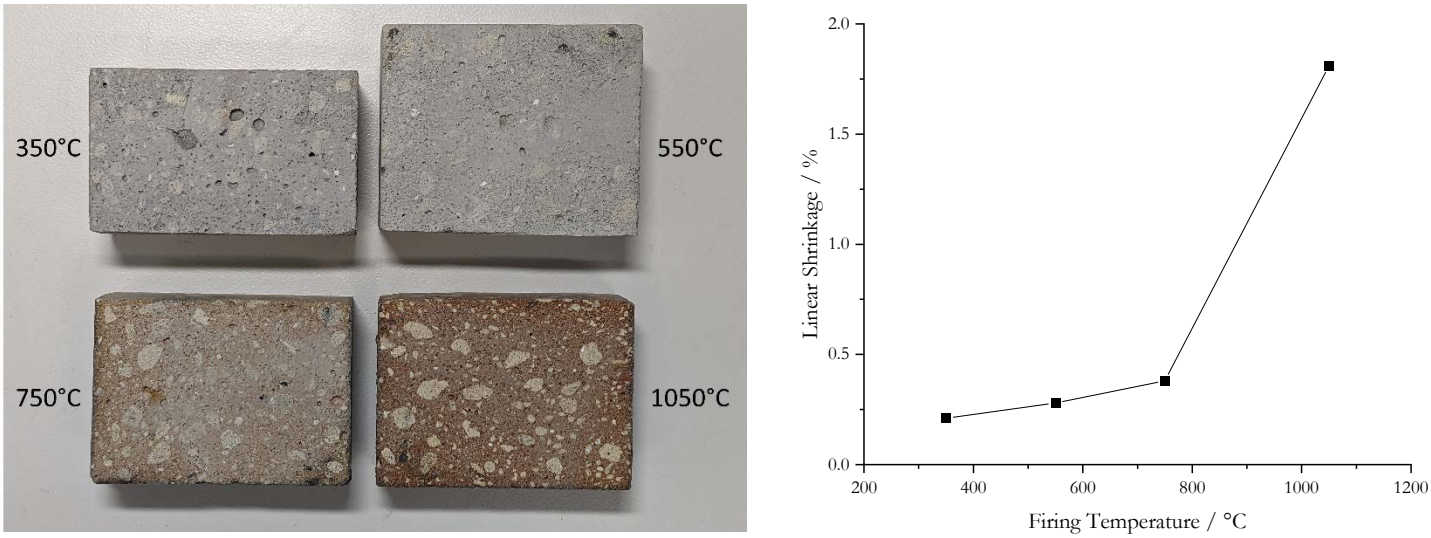

Figure 83. Interior pictures and the linear shrinkage of geopolymer samples with 25% additional coarse aggregates, fired to different temperatures after ambient condition curing

2.3.3 Cost Estimation for Geopolymer Bricks at Prototype Tank Scale

A rough estimate of the geopolymer's selling price was given by Morgan for constructing a prototype molten salt TES tank, as shown in Section 2.3.1. It should be noted that raw materials cost had increased in a wide range of percentages since the start of the project due to the impact of the pandemic. Table 14 summarizes the percentage increase in bulk selling price of the major ingredients for geopolymer insulation. The highest increases were from FABUTIT 748, cenospheres, Mulcoa LW 43 aggregates, and NaOH solution. The FABUTIT 748 price increase was due to costly shipping from Europe and the small-quantity order required for prototype tank-scale production. This price is expected to decrease for a large-quantity order. The cenosphere price increase was due to the soaring shipping cost from Asia where most cenospheres were produced (e.g., China, India). Mulcoa LW 43 aggregates have been taken off the market by the supplier, Imerys. In the long term, it is unknown whether Mulcoa LW 43 will be replaced by another product from Imerys. An alternative coarse aggregate needs to be procured elsewhere or produced in-house by Morgan.

This report is available at no cost from the National Renewable Energy Laboratory at www.nrel.gov/publications.

Table 14. Summary of the Percentage Increase in Bulk Selling Price of the Major Ingredients for Geopolymer Insulation

Raw Material	Percentage Increase in Selling Price
Metakaolin	10%
Cenospheres	73%
Mulcoa LW 43	60%
Silica fume	10%
Sodium silicate	20%
NaOH solution	38%
FABUTIT 748	270%

The significant cost increase of raw materials had a dramatic impact on the total raw materials cost, which increased by more than 130% compared to early estimates. Some of these impacts may be short-term. However, it is unknown whether all the prices will come down to a comparable level as before.

Table 15 shows the estimated selling price and rough breakdown for geopolymer bricks and mortar. The estimated price is not in favor of the geopolymer materials. At $14.73/kg, the geopolymer bricks are hardly affordable to build a commercial-scale TES system with geopolymer internal insulation. Hence, the cost structure was analyzed to identify potential cost-saving routes.

Table 15. Price Summary of Geopolymer Bricks and Mortar at LIMOSA Scale

	Cost Categories	$/kg
Bricks	Materials (including waste) and labor for mixing before casting	2.30
	Casting cost (labor + materials), overhead, and price premium	12.44
	Selling price at prototype tank scale	14.73
Mortar	Selling price at prototype tank scale	2.62

- First, Morgan is not well-known for cast products, and their overall processing cost is not the lowest. As an alternative, Morgan is willing to consider selling the geopolymer mixtures to another specialist for casting. With a premium, Morgan's selling price of the mixture is likely in the $4–$4.5/kg range. To beat the original selling price at $14.73/kg, the rest of the processing cost needs to stay below ~$10.4/kg. Given the lower manufacturing cost by a casting specialist with lower overhead on research and operation and an overall lower premium, it is possible to reduce the cost of the cast product.
- Second, other manufacturing methods such as cold pressing could produce geopolymer with similar properties. If cold pressing were to be shown effective, and a low-cost cold pressing specialist could procure the formulated mix from Morgan, the overall processing

This report is available at no cost from the National Renewable Energy Laboratory at www.nrel.gov/publications.

cost could be further reduced. For reference, even with Morgan's more expensive pricing structure, the cold pressed product was estimated to have a selling price around $11/kg, which is already 25% lower than the cast product.

- Since FABUTIT 748 was shown not suitable for production of large bricks, its elimination would make it possible to reduce another 8%–10% of the materials cost for the mixture.

In summary, the estimated selling price for geopolymer insulation translates to an insulation cost of $10–$15 million for each TES tank. Other than the higher unit cost for a new insulation product (which may be lowered in the future as the technology matures and more manufacturers can compete in the market to help reduce the selling price), there is another reason that impacts the insulation cost. The project aims to design a safer insulation liner by relying on salt freezing inside this insulation layer as salt containment. As pointed out before, such design requires a significantly larger temperature difference across the geopolymer liner (e.g., about 300°C for both the nitrate and chloride salt TES) compared to a traditional hot-face liner (e.g., 10°C–20°C or even less). If the geopolymer liner also needs to achieve other required properties such as mechanical integrity and chemical compatibility, which usually requires durable (usually equivalent to heavier and more thermally conductive) ingredients, it is unlikely for geopolymer to significantly outperform the traditional hot-face liner in terms of thermal insulation. Currently the geopolymer is only 2–3x better in terms of thermal conductivity. At the same time, the much larger temperature differential means a significantly thicker geopolymer liner is needed. Therefore, the overall volume of the geopolymer insulation will be 2–3x compared to a traditional hot-face liner. Coupled with a 3–4x unit price, it explains why the geopolymer liner is not very affordable for large scale structures. As shown by tank costing later, geopolymer is likely only financially viable for a nitrate salt hot tank where the higher energy density of the nitrate salt requires a one-pair design and only the hot tank needs to be internally insulated, as opposed to a two-pair design for the chloride salt TES tanks where two pairs of hot and cold tanks (four tanks) need to be internally insulated.

2.3.4 Recommendations

The project was not successful in consistently producing 50-lb geopolymer bricks without any internal or external cracks at the end of the project timeline. The best sample was shown in Figure 79. However, given the additional research on coarse aggregates and curing/firing schedules, the following can be recommended to minimize the chance of cracking:

1. The most straightforward pathway toward minimizing cracking is to limit the brick size, as early lab-scale bricks and bars showed nearly no cracking. It is believed that the size effect is related to the thickness of the brick that must be cured properly to gain strength prior to firing. The thicker the brick, the more likely a fraction of the brick cannot be cured properly.
2. A coarse aggregate content of 30%–35% seems necessary to prevent substantial linear shrinkage and shrinkage cracking. Early lab-scale bricks with only 10% coarse aggregates did not reflect the real needs because of their small brick size. For production of much larger bricks, the stress due to shrinkage is likely amplified by the much larger dimensions. For the refractory industry, 30%–35% coarse aggregate is a common practice to minimize shrinkage. The actual coarse aggregate content may need to be adjusted given the final size of the bricks, which is an area that needs additional investigation and understanding.

This report is available at no cost from the National Renewable Energy Laboratory at www.nrel.gov/publications.

3. In real-world production, it is common that the bricks need to follow a different a curing schedule because the batch nature of insulation brick production means that some bricks may have to wait for a longer time in the production line until the firing kiln is ready. Some may wait for a shorter time. Technically speaking, longer wait time (i.e., longer curing time) is likely beneficial, as it contributes to more complete curing and better properties prior to firing. Therefore, for high-volume production, it is recommended to make a few test batches with much longer curing time (e.g., 2–4 weeks) and understand if there is any variation of firing behaviors.
4. The molten salt immersion testing results showed that 1,050°C is the optimal firing temperature due to its effect on closing off some open porosities. However, given the other recommendations, flexibility in firing temperature may be available. If a slightly lower firing temperature were able to have comparable performances in terms of molten salt permeation resistance due to the use of more coarse aggregates, a lower linear shrinkage and lower chance of shrinkage cracking may be achievable.

2.4 Installation Design for Geopolymer Thermal Insulation

2.4.1 Heat Transfer and Tank Wall Temperature Profile Calculations

As stated in Section 2.3.3, geopolymer insulation is very costly given the estimated pricing structure. Hence, if the geopolymer layer become too thick, it is not only technically difficult to install the liner but also financially prohibitive to construct the TES tanks. One of the straightforward routes to reduce insulation thickness is to allow a lower daily RTE of the TES tanks. Using the System Advisor Model (SAM), NREL analyzed the potential trade-offs between having a lower daily RTE and its long-term impact. NREL used the built-in, default model for Gen2 nitrate TES systems and the Gen3 chloride TES model developed by the "CSP Gen3: Liquid-Phase Pathway to Sunshot" project [2]. For the calculation, NREL only changed the heat loss value for each scenario to roughly understand the impact on the final levelized cost of electricity (LCOE). The key parameters of the tanks (such as the total thermal storage capacity, duration of storage at full load, and estimated daily RTE) and the resulting LCOE are given in Table 16.

Table 16. SAM Parameters and Simulation Results for Gen2 Nitrate and an Example Gen3 Chloride TES Tanks Showing the Impact of Daily Round-Trip Efficiency (RTE)

	Gen2 Nitrate TES				**Example Gen3 Chloride TES**			
TES thermal capacity (MWh-t)	2,791.3				3,047.1			
Duration of storage at full load (hour)	10				14			
Storage tank volume (m^3)	14,166				31,029			
Parallel tank pairs	1				1			
Estimated heat loss (MW-t)	1.16	2.31	3.47	4.63	2.26	3.39	4.52	5.65
Estimated daily RTE	99%	98%	97%	96%	98.2%	97.3%	96.4%	95.5%
Levelized cost of electricity (¢/kWh)	7.81	7.86	7.92	7.99	6.35	6.39	6.43	6.47

This report is available at no cost from the National Renewable Energy Laboratory at www.nrel.gov/publications.

It must be clarified that the analysis in Table 16 did not intend to represent the final LCOE of the geopolymer-lined tanks, because the actual tank costing was not included. Instead, it was a simplified practice to understand the sole impact of the heat loss and daily RTE of the tanks on long-term cost of electricity, assuming everything else remained the same. Based on the results, each percentage of daily RTE decrease led to about ¢0.05–0.07/kWh of LCOE increase for the nitrate TES system and about ¢0.04/kWh of LCOE increase for the chloride TES system. Therefore, it likely makes sense to reduce the daily RTE by 2%–3% in exchange for a tank design with much thinner insulation liner thickness, because decreasing the daily RTE substantially reduces the initial construction costs for the internal insulation liners, e.g., a RTE decrease from 98% to 96% would reduce the tank liner thickness by roughly 50%.

Next, NREL used a simple 1D heat transfer model to estimate the thicknesses of the internal insulation liners (including geopolymer, backup insulation and concrete tank shell) and the resulting temperature profiles. The goal was to verify the relationship between insulation thicknesses and heat loss/daily RTE. The assumptions used for the simulation are listed below.

- Simulations were performed on both the hot and cold tanks for the chloride and only the hot tank for the nitrate. No simulation was performed on nitrate cold tank because the current nitrate cold tank design did not encounter major technical issues during operation.
- Ambient conditions were assumed to be 17°C with 2.2 m/s average wind speed.
- The thickness of the "Dry GP Buffer" layer, as shown in Figure 5, was 10% of the thickness of the "Molten Salt Saturated GP" layer.
- The thickness of the concrete structure was about 610 mm in all tanks based on conceptual design (discussed later in Section 2.5.1). The thermal conductivity used for the concrete structure was higher than that of normal Portland cement concrete, at about 4.4 W/m·K to reflect the post-tensioned concrete.
- The temperature-dependent thermal conductivity value used for each liner material was simplified by the average value at the mean temperature across the liner.

Figure 84 shows the calculated temperature profile for a geopolymer-lined chloride salt hot tank, based on the conceptual design of Figure 5, at the industrial standard 98% daily RTE. It represented one example of all the simulation results at different daily RTEs.

This report is available at no cost from the National Renewable Energy Laboratory at www.nrel.gov/publications.

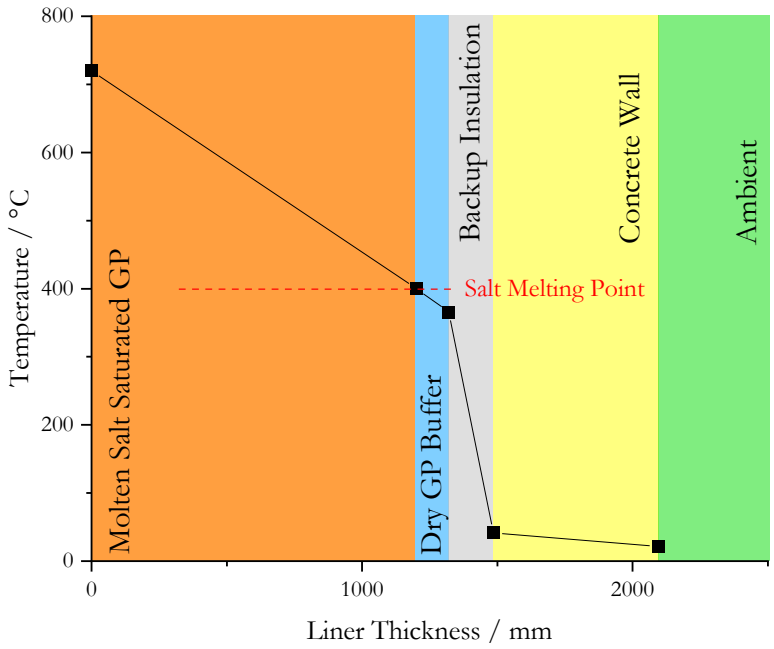

Figure 84. Temperature profile for a geopolymer (GP)-lined chloride salt hot tank at 98% daily RTE

It can be seen that the simulated result met all design criteria:

- The molten salt freeze plane was located right at the interface between the "Molten Salt Saturated GP" layer and "Dry GP Buffer" layer, with the temperature being about 400°C, the melting point of the chloride salt.
- The "Dry GP Buffer" and "Backup Insulation" stayed dry without any molten salt permeation.
- The temperature at the interface between "Backup Insulation" and "Concrete Wall" was only at 41.6°C. This was the maximum temperature within the concrete wall during normal operation. The temperature fell well within the safe temperature of concrete structure use (i.e., below 90°C) and should not impact the mechanical properties of the concrete tank shell.

Apparently, the biggest caveat for this temperature profile was the ~1,300-mm total thickness of the geopolymer insulation (saturated and dry), which was neither technically nor financially viable. Hence, the simulation result confirmed that aiming at 98% daily RTE for the chloride salt hot tank is challenging. The same conclusion was also applicable to the chloride salt cold tank and the nitrate salt hot tank.

Table 17 shows the detailed calculation results of the temperature profiles and liner thicknesses for TES tanks designed at different daily RTEs. All liner thicknesses shown in Table 17 satisfied the conceptual design criteria mentioned above. The green cells indicated acceptable total geopolymer liner thickness from the installation perspective (i.e., below 600 mm total). The red cells indicated too high of a temperature on the concrete tank shell (i.e., above 90°C) under certain conditions.

This report is available at no cost from the National Renewable Energy Laboratory at www.nrel.gov/publications.

Table 17. Summary of Calculated Temperature Profiles and Liner Thicknesses for TES Tanks Designed at Different Daily RTEs

	Chloride Hot Tank				Chloride Cold Tank			Nitrate Hot Tank		
Daily Round-Trip Efficiency	98%	97%	96%	95%	98%	97%	96%	98%	97%	96%
Total GP Thickness (mm)	1,320.0	881.1	660.0	528.8	706.2	470.8	352.6	884.4	588.2	454.3
Backup Insulation (mm)	165.0	105.0	76.0	58.3	318.0	209.0	153.0	46.9	27.0	18.0
Total Insulation (mm)	1,485.0	986.1	736.0	587.1	1,024.2	679.8	505.6	931.3	615.2	472.3
Concrete Temperature Under Normal Operation (°C)	41.6	54.0	66.2	78.4	31.1	38.0	45.1	53.9	72.4	88.8
Maximum Fail Factor	20.5%	21.5%	20.9%	21%	13.7%	13.1%	13.3%	33.7%	33.7%	33.8%
Concrete Temperature Under Maximum Fail Condition (°C)	44.0	57.7	71.1	84.6	31.5	38.6	45.9	61.8	84.4	104.3

All results shown in Table 17 were under normal operating conditions, i.e., assuming there was no excursion event. NREL also performed simulation for scenarios outside normal operations.

1. When there is rain or snow (which should reduce the ambient temperature and increase the heat transfer coefficient at the tank shell), the impact turns out to be negligible. For example, when the ambient temperature was reduced to 0°C and the heat transfer coefficient was increased 1,000 times from 26.7 W/m^2·°C to 26,700 W/m^2·°C for the chloride salt hot tank design that was shown in Figure 84, the overall heat flux only increased slightly from ~140 W/m^2 to ~144 W/m^2, and the salt freeze plane moved inward toward the salt inventory by only 25 mm.
2. It is important to know what must happen before the salt permeates and completely saturates the entire geopolymer liner, i.e., the salt freeze plane moves toward the outside the of the tank and wets the entire geopolymer buffer layer. For this to happen, the thermal conductivity of the wetted geopolymer insulation in the entire liner needs to increase 13%–34% compared to the experimentally measured wetted geopolymer thermal conductivity. The percentage increase here is defined as the "Maximum Fail Factor" in Table 17. For example, the measured thermal conductivity of the wetted geopolymer is about 0.52 W/m·K (see Section 2.2.6.5). For the liner design and salt containment to fail (i.e., molten salt permeating throughout the geopolymer layer and leaking into the porous backup insulation) in the chloride hot tank at 98% RTE, this number needs to increase 20.5% to about 0.63 W/m·K for both the already wetted geopolymer and the dry geopolymer buffer. It is believed that this is an unlikely event because the salt thermal conductivity is lower than the 0.63 W/m·K value, and it is not very likely to increase the thermal conductivity of a material by permeating it with a liquid with lower thermal conductivity. As shown by all the Maximum Fail Factors, the safety margin is substantial.
3. For Nitrate Hot Tank at 96% daily RTE, the maximum concrete tank temperature could be up to 104°C. However, this only happens under the Maximum Fail conditions. Even if this happened, only about 20% of the concrete wall would experience a temperature above 90°C. Most of the concrete wall would still be under 90°C.

This report is available at no cost from the National Renewable Energy Laboratory at www.nrel.gov/publications.

As discussed previously, the geopolymer liner bricks were designed to be about 14.5 in. or 368.3 mm for a prototype molten salt TES tank. If Morgan can manufacture these bricks, producing a geopolymer layer for the commercial TES tanks is technically feasible. Therefore, the five tank design scenarios that have a green "Total GP Thickness" in Table 17 were down-selected for further tank design and costing.

2.4.2 Insulation Liner Design for Full-Scale Thermal Energy Storage Systems

The salt tank internal liner concept mostly consists of geopolymer bricks that are mortared together to form a refractory lining structure within the tank walls. The geopolymer tank internal liner as a system must be capable of:

- Withstanding high temperature of the molten salts without deforming or degrading
- Being able to contain molten salt by allowing salt freezing inside the liners during start-ups, normal operations, and upset events
- Thermally insulating the tank structure shell to prevent overheating the walls, roof, and floor
- Remaining structurally stable during high and low liquid levels.

JT Thorpe provided refractory liner drawings for three tank temperature profile designs in Table 17: a chloride salt cold tank at 96% RTE (Figure 85–Figure 87), a chloride salt hot tank at 95% RTE (Figure 88–Figure 90), and a nitrate salt hot tank at 96% RTE (Figure 91–Figure 93). These designs resemble the Gen3 Liquid Pathway tank liner design with similar key features. The major difference is the thickness of the hot face (i.e., the first layer that is in direct contact with the molten salt) where the geopolymer liner effectively serves as the hot face and is much thicker, within which salt freezes for self-containment.

It should be noted that important real-world phenomena such as the transient behavior of tank liners during start-up, shutdown, salt addition, and daily operation with changing temperatures were not analyzed with high-fidelity FEA during the liner design effort, because there was a lack of accurate materials properties of the liner materials, mortars, expansion joints, mortar joints, etc. Lab-scale materials properties were measured, but properties at commercial scale are also needed for meaningful FEA. The scope of the liner design effort only allowed conceptual designs. The final liner drawings presented several simplified concepts that aim to address relevant concerns from past design experience, including floor corners (i.e., joint between wall and floor) and ceiling corners (i.e., joint between wall and ceiling). Without better materials properties at commercial scale, refinement of the detailed design by FEA is not believed to be meaningful. The conclusion is that at a high level, the geopolymer liner design largely resembles that from the Gen3 Liquid Pathway tank project which has performed steady-state FEA with similar design considerations.

This report is available at no cost from the National Renewable Energy Laboratory at www.nrel.gov/publications.

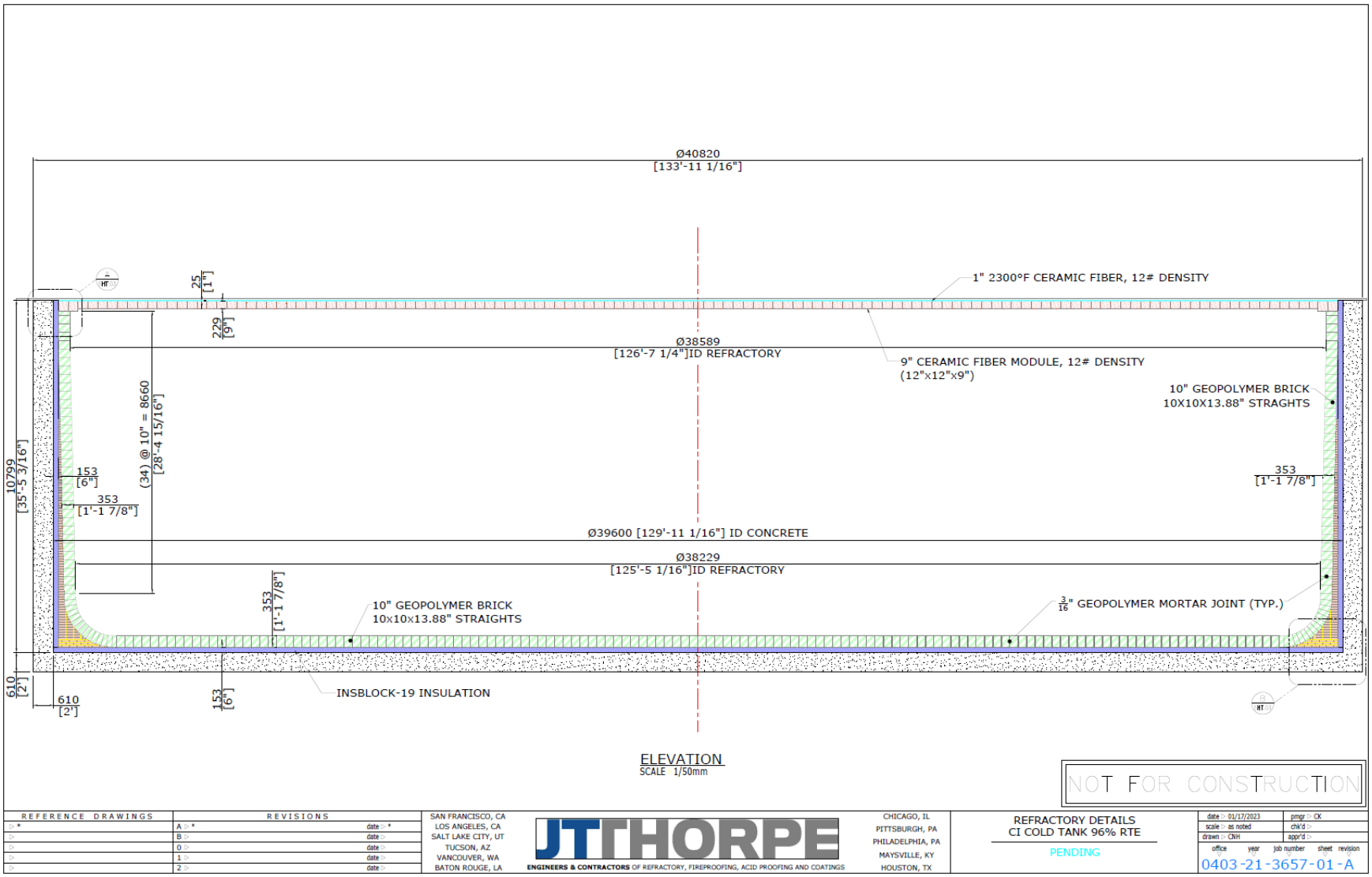

Figure 85. Conceptual one-layer refractory liner design drawing (I) for a chloride salt cold tank operating at 96% daily RTE

This report is available at no cost from the National Renewable Energy Laboratory at www.nrel.gov/publications.

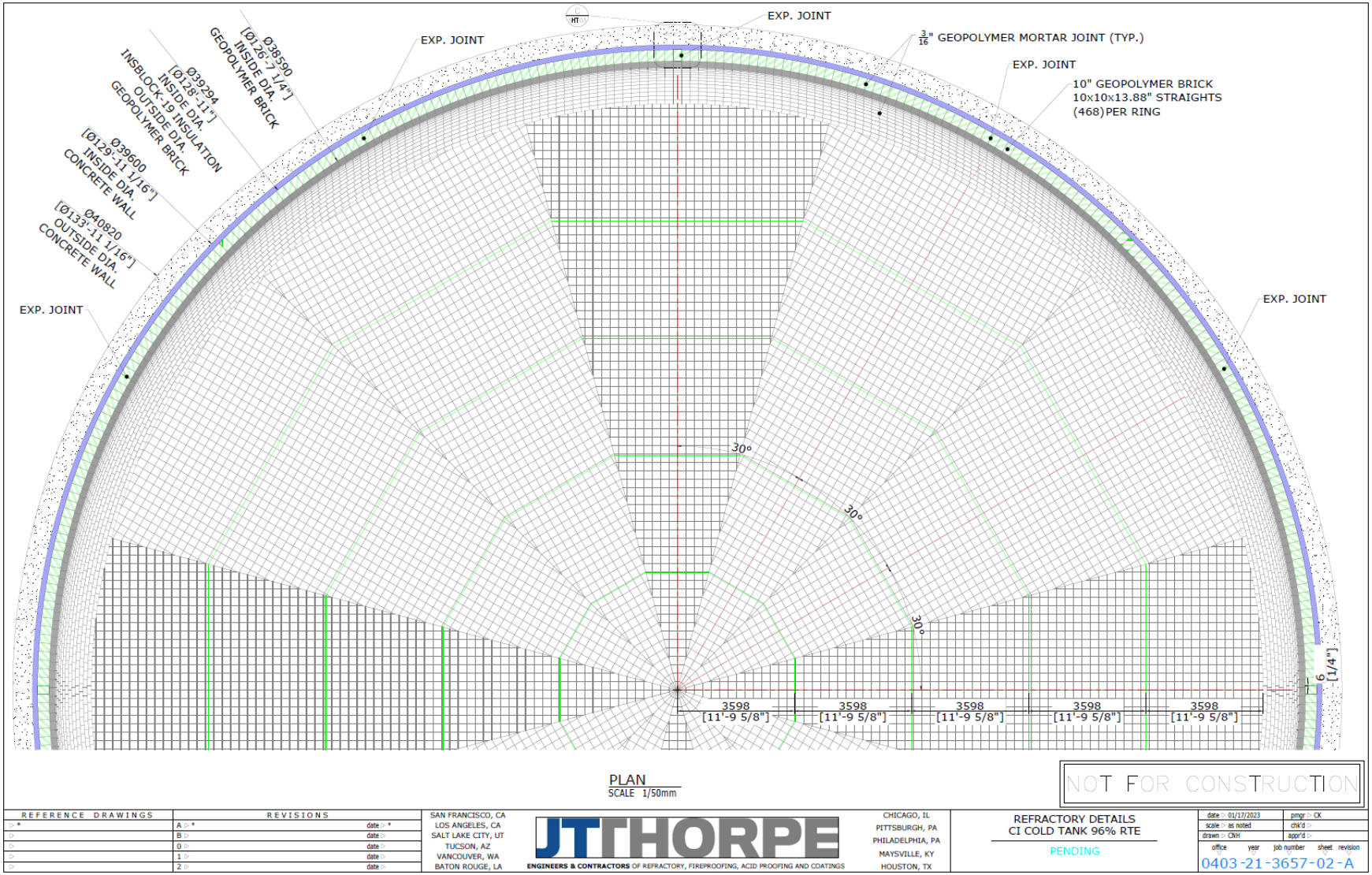

Figure 86. Conceptual one-layer refractory liner design drawing (II) for a chloride salt cold tank operating at 96% daily RTE

This report is available at no cost from the National Renewable Energy Laboratory at www.nrel.gov/publications.

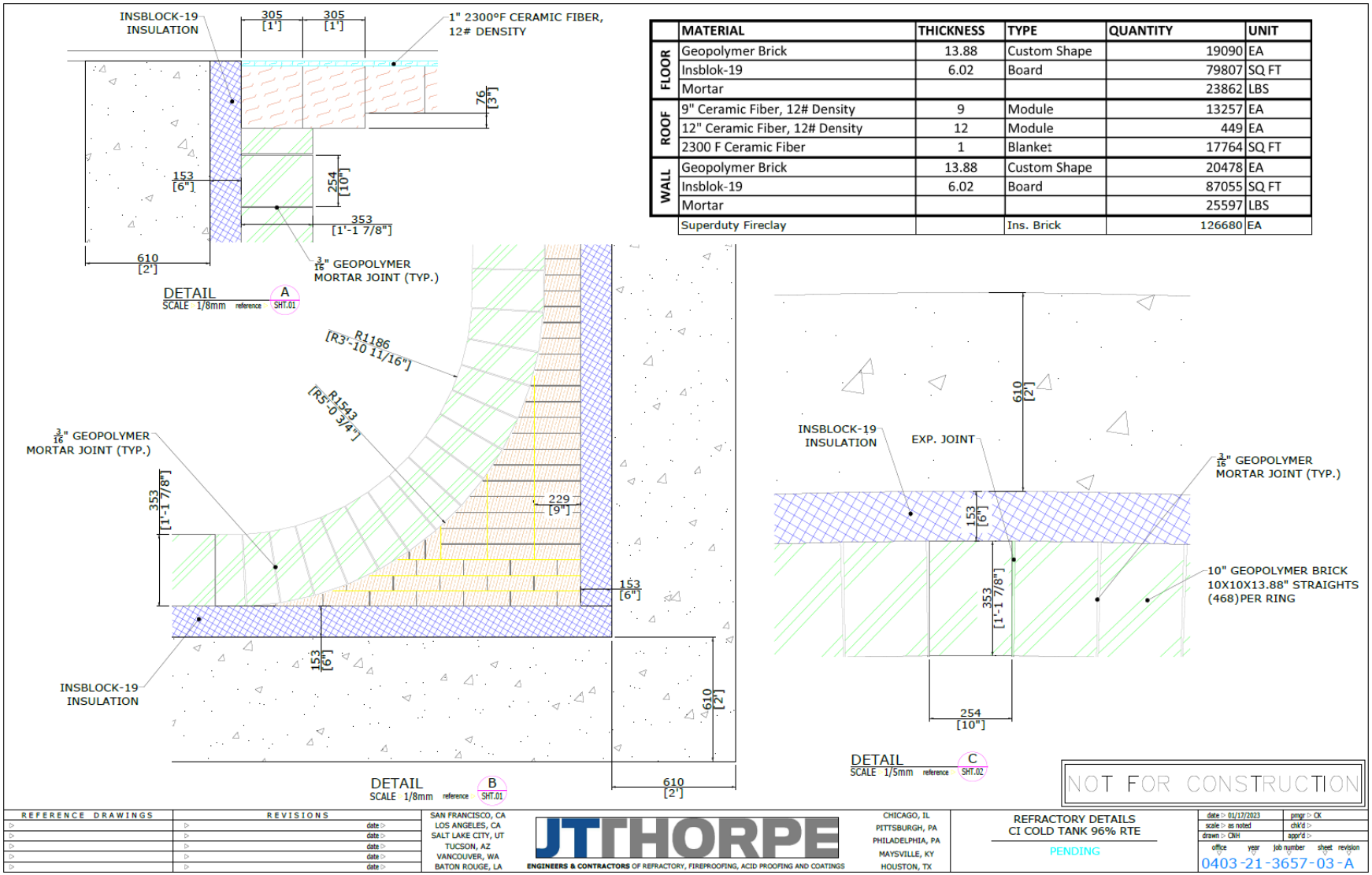

	MATERIAL	THICKNESS	TYPE	QUANTITY	UNIT
FLOOR	Geopolymer Brick	13.88	Custom Shape	19090	EA
	Insblok-19	6.02	Board	79807	SQ FT
	Mortar			23862	LBS
ROOF	9" Ceramic Fiber, 12# Density	9	Module	13257	EA
	12" Ceramic Fiber, 12# Density	12	Module	449	EA
	2300 F Ceramic Fiber	1	Blanket	17764	SQ FT
WALL	Geopolymer Brick	13.88	Custom Shape	20478	EA
	Insblok-19	6.02	Board	87055	SQ FT
	Mortar			25597	LBS
	Superduty Fireclay		Ins. Brick	126680	EA

Figure 87. Conceptual one-layer refractory liner design drawing (III) for a chloride salt cold tank operating at 96% daily RTE

This report is available at no cost from the National Renewable Energy Laboratory at www.nrel.gov/publications.

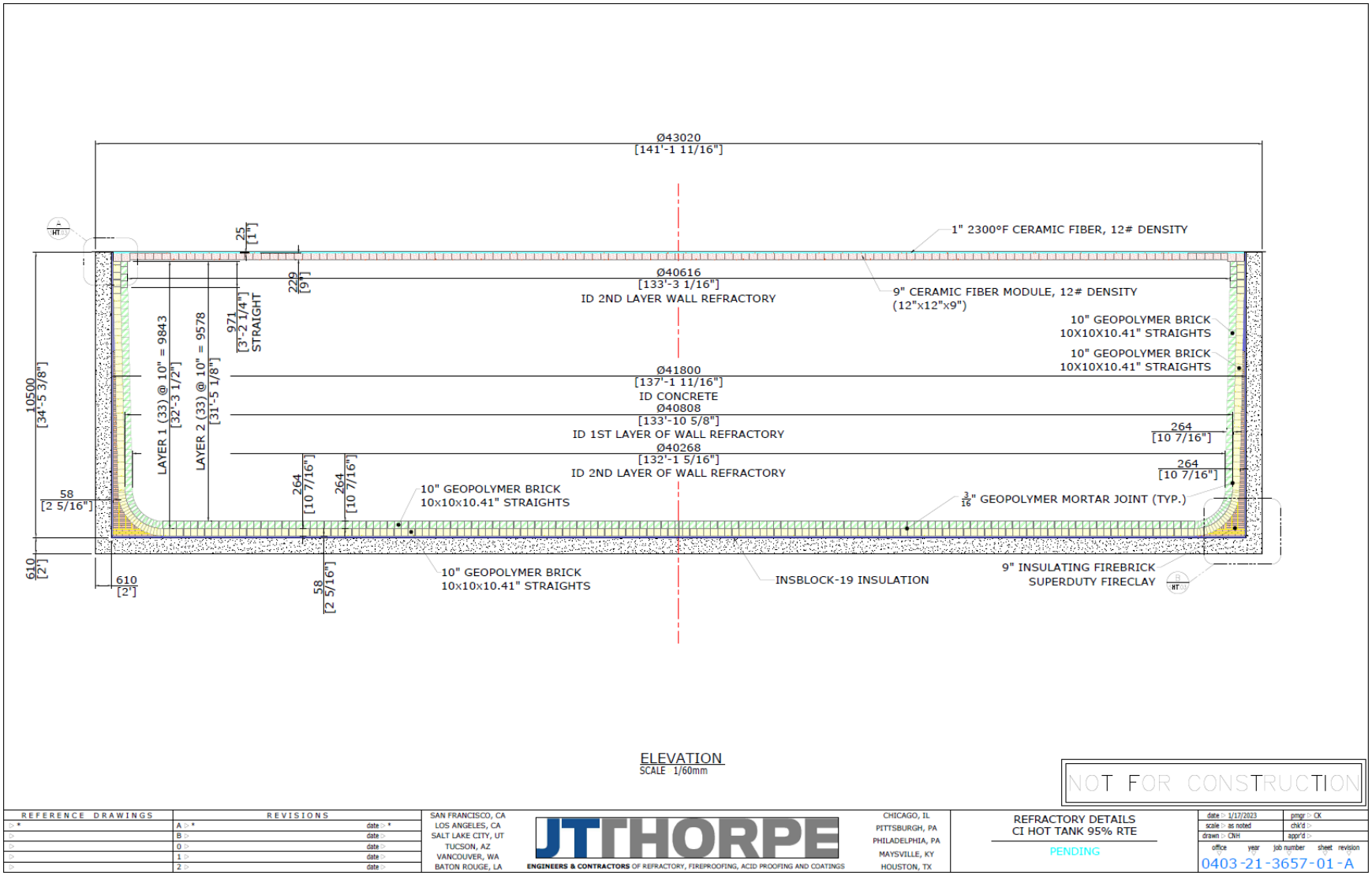

Figure 88. Conceptual two-layer refractory liner design drawing (I) for a chloride salt hot tank operating at 95% daily RTE

This report is available at no cost from the National Renewable Energy Laboratory at www.nrel.gov/publications.

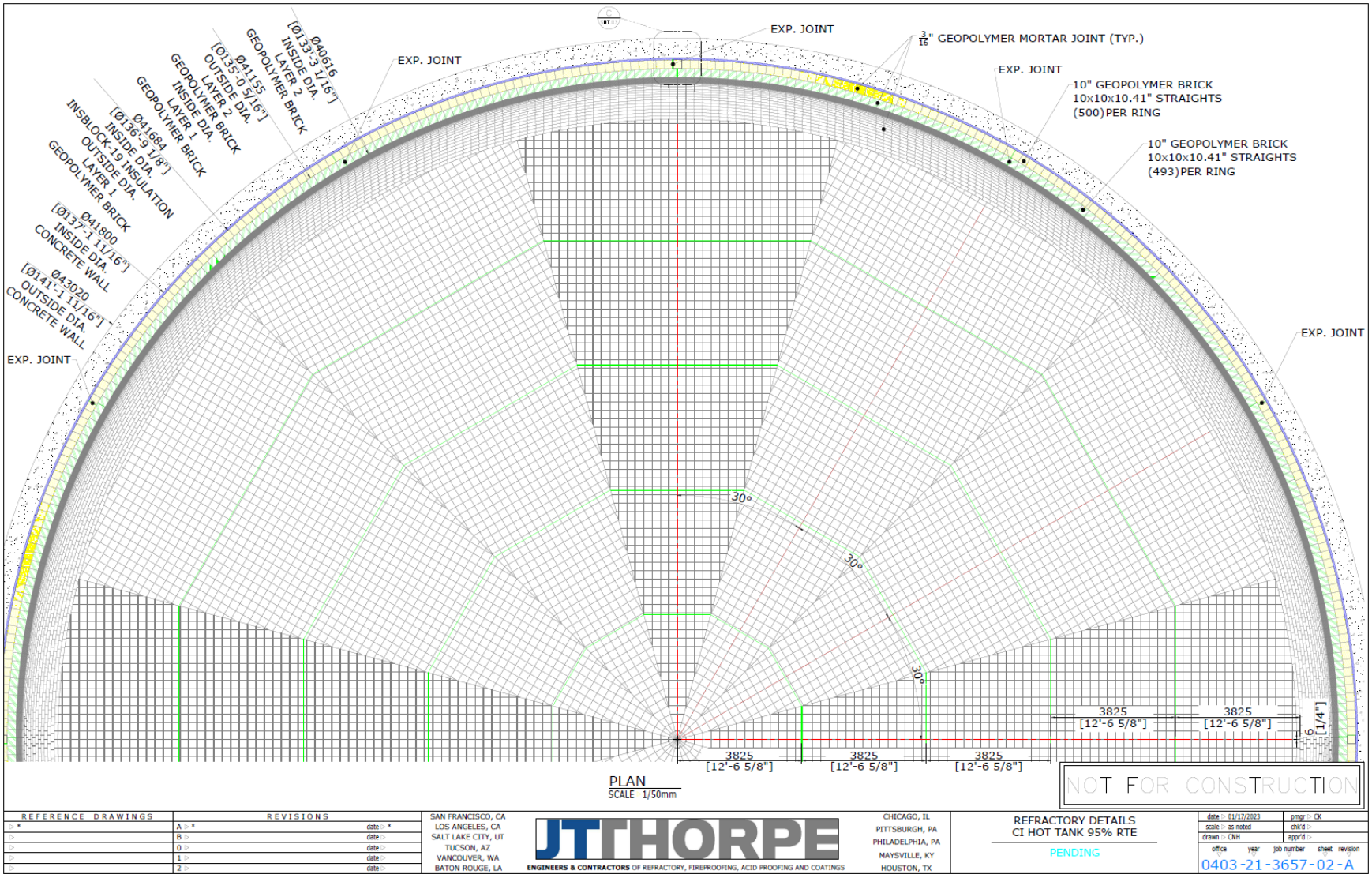

Figure 89. Conceptual two-layer refractory liner design drawing (II) for a chloride salt hot tank operating at 95% daily RTE

This report is available at no cost from the National Renewable Energy Laboratory at www.nrel.gov/publications.

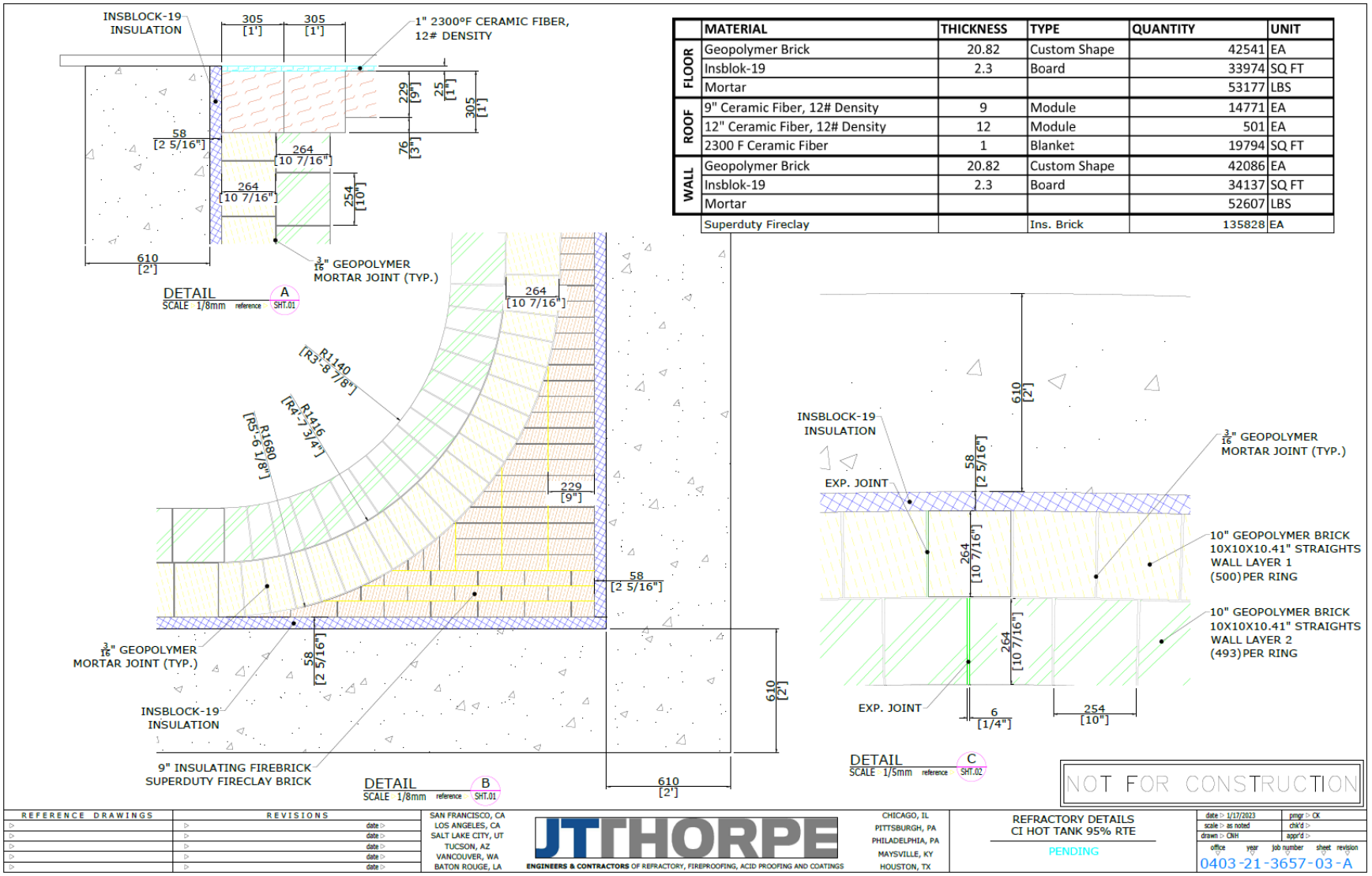

	MATERIAL	THICKNESS	TYPE	QUANTITY	UNIT
FLOOR	Geopolymer Brick	20.82	Custom Shape	42541	EA
	Insblok-19	2.3	Board	33974	SQ FT
	Mortar			53177	LBS
ROOF	9" Ceramic Fiber, 12# Density	9	Module	14771	EA
	12" Ceramic Fiber, 12# Density	12	Module	501	EA
	2300 F Ceramic Fiber	1	Blanket	19794	SQ FT
WALL	Geopolymer Brick	20.82	Custom Shape	42086	EA
	Insblok-19	2.3	Board	34137	SQ FT
	Mortar			52607	LBS
	Superduty Fireclay		Ins. Brick	135828	EA

Figure 90. Conceptual two-layer refractory liner design drawing (III) for a chloride salt hot tank operating at 95% daily RTE

This report is available at no cost from the National Renewable Energy Laboratory at www.nrel.gov/publications.

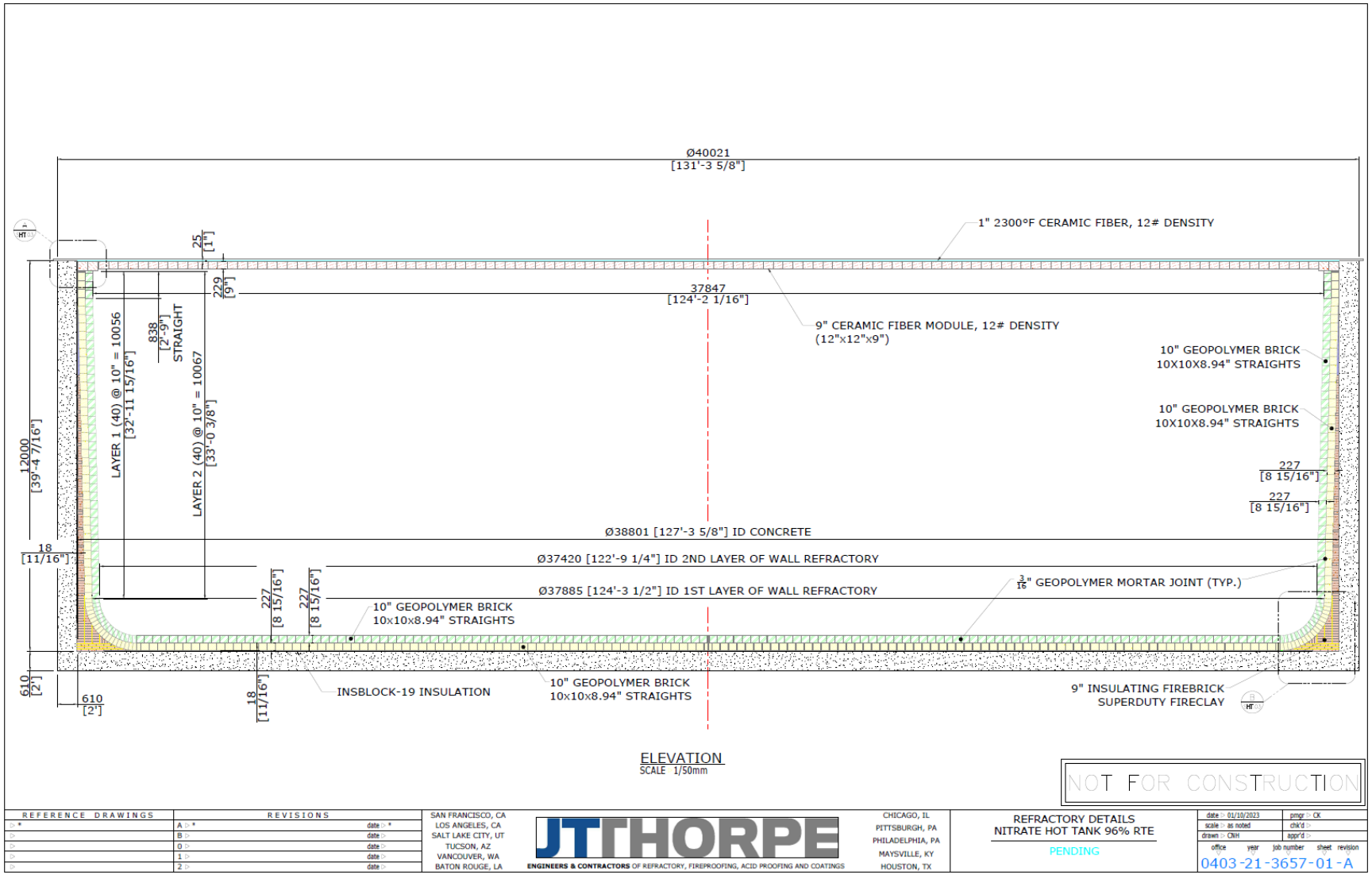

Figure 91. Conceptual two-layer refractory liner design drawing (I) for a nitrate salt hot tank operating at 96% daily RTE

This report is available at no cost from the National Renewable Energy Laboratory at www.nrel.gov/publications.

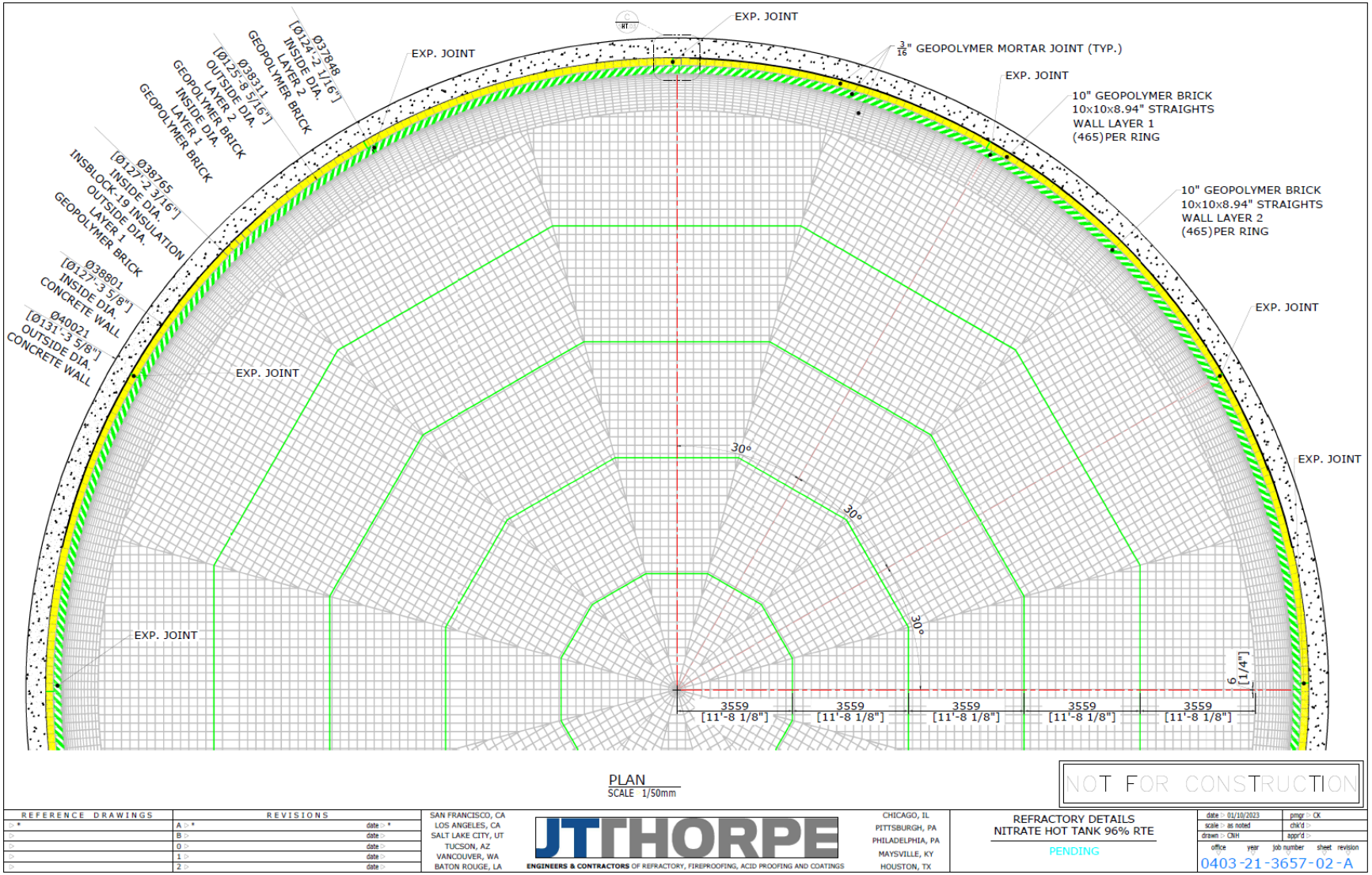

Figure 92. Conceptual two-layer refractory liner design drawing (II) for a nitrate salt hot tank operating at 96% daily RTE

This report is available at no cost from the National Renewable Energy Laboratory at www.nrel.gov/publications.

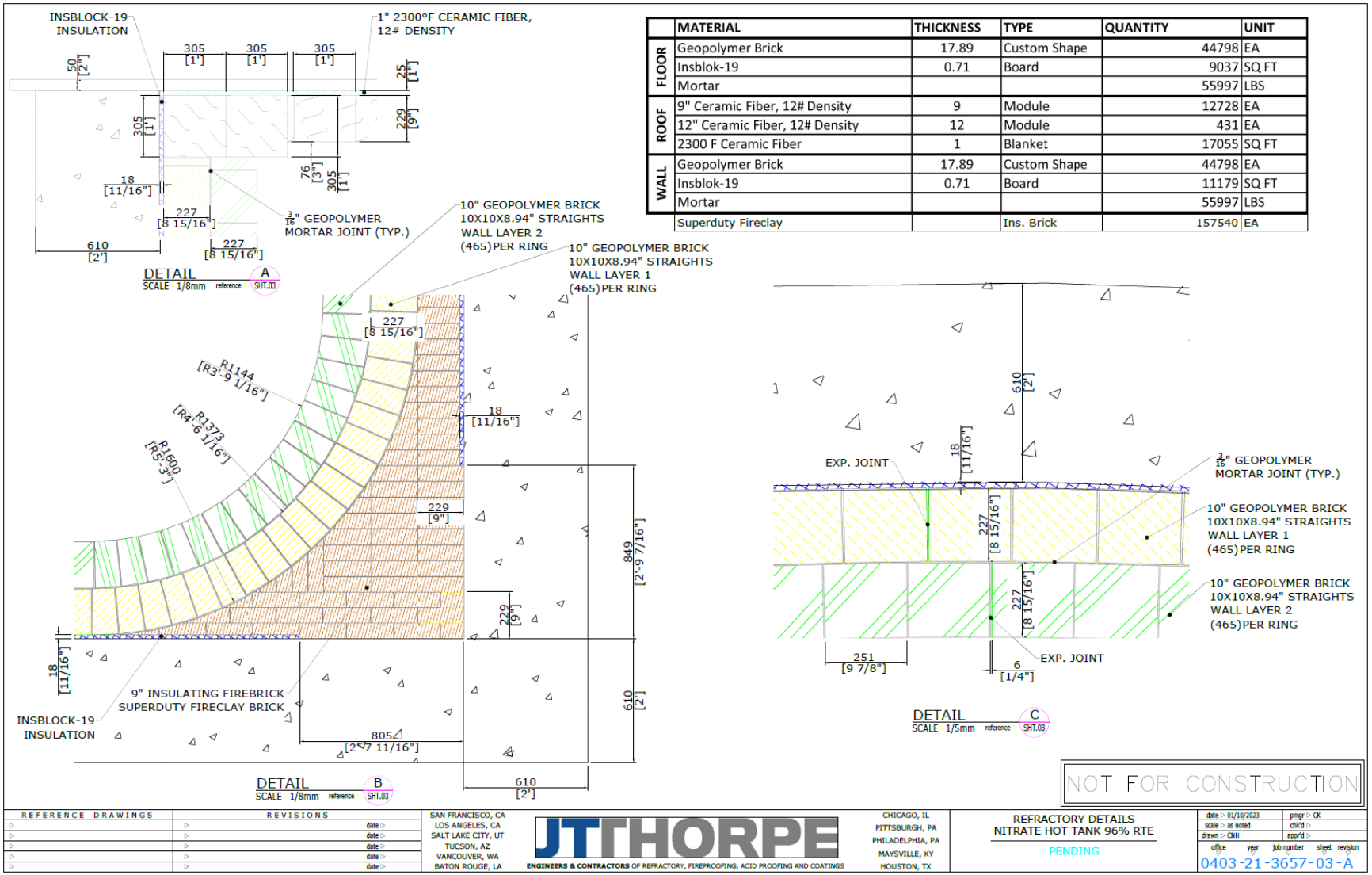

	MATERIAL	THICKNESS	TYPE	QUANTITY	UNIT
FLOOR	Geopolymer Brick	17.89	Custom Shape	44798	EA
	Insblok-19	0.71	Board	9037	SQ FT
	Mortar			55997	LBS
ROOF	9" Ceramic Fiber, 12# Density	9	Module	12728	EA
	12" Ceramic Fiber, 12# Density	12	Module	431	EA
	2300 F Ceramic Fiber	1	Blanket	17055	SQ FT
WALL	Geopolymer Brick	17.89	Custom Shape	44798	EA
	Insblok-19	0.71	Board	11179	SQ FT
	Mortar			55997	LBS
	Superduty Fireclay		Ins. Brick	157540	EA

Figure 93. Conceptual two-layer refractory liner design drawing (III) for a nitrate salt hot tank operating at 96% daily RTE

This report is available at no cost from the National Renewable Energy Laboratory at www.nrel.gov/publications.

2.4.3 Insulation Liner Costing for Full-Scale Thermal Energy Storage Systems

Morgan provided the unit cost of the geopolymer insulation bricks (see Table 15 in Section 2.3.3) for JT Thorpe to estimate the total cost of the five down-selected geopolymer-lined molten salt TES tank systems in Table 17. Table 18 summarizes the estimated tank insulation costs at two sites. The listed cost is for one tank. Due to uncertainties, the costing excludes the following: (1) mobilization/demobilization to site, (2) material freight to site, (3) material sales tax, (4) crew member travel and subsistence, (5) third-party rental equipment, (6) scaffolding, (7) cranes and/or hoists with operators, (8) mechanical work, (9) utilities (i.e., water, air, power, break rooms, sanitation, etc.), and (10) take-offs based on high-level conceptual design.

Table 18. Summary of Estimated Tank Insulation Cost for Different Daily RTEs and Site Locations

	Daily RTE	Site Location	Total Cost ($)	Total Cost ($/kWh-t)
Chloride Hot Tank	95%	Daggett, CA	$ 23,606,239.69	$ 9.84
		Phoenix, AZ	$ 23,287,992.69	$ 9.70
Chloride Cold Tank	97%	Daggett, CA	$ 21,139,898.44	$ 8.81
		Phoenix, AZ	$ 20,681,406.22	$ 8.62
	96%	Daggett, CA	$ 15,948,560.83	$ 6.65
		Phoenix, AZ	$ 15,617,800.34	$ 6.51
Nitrate Hot Tank	97%	Daggett, CA	$ 24,590,828.09	$ 8.81
		Phoenix, AZ	$ 24,316,847.07	$ 8.71
	96%	Daggett, CA	$ 19,384,154.96	$ 6.95
		Phoenix, AZ	$ 19,131,301.10	$ 6.85

Apparently, the geopolymer-based insulation was costly, as each tank cost more than $15 million (materials and labor). In addition, the costs were similar regardless of the site locations, which have substantially different labor costs.[25] The results suggested that the material cost was the dominant factor. This was expected because the geopolymer was significantly more expensive than conventional refractory materials, as shown in Table 15. To further understand the cost structure, the overall cost was broken into different cost categories. Table 19 shows the cost breakdown by cost categories and insulation materials for the most affordable tank in Table 18 (i.e., chloride cold tank at 96% RTE at Phoenix, Arizona). There were some important observations:

- The materials cost was almost 10 times higher than the labor cost, which confirmed that materials cost was the dominant cost category.
- The materials cost for geopolymer was between 90% and 95% of the total materials cost. This was due to a much higher price for geopolymer insulation and a much higher geopolymer thickness compared to other insulations (see Table 17).

Both observations suggest that reducing the geopolymer unit cost is the single most important pathway toward materializing the geopolymer insulation concept. Without a significant cost

[25] Labor rate used for Daggett, CA is about 60% higher than that for Phoenix, AZ.

This report is available at no cost from the National Renewable Energy Laboratory at www.nrel.gov/publications.

reduction, geopolymer insulation for molten salt TES applications will not be financially viable (to be discussed in Section 2.5.2).

Table 19. Cost Breakdown by Cost Categories and Insulation Materials at Different Locations of the Tank for Chloride Salt Cold Tank at 96% Daily RTE

	Insulation Materials	Chloride Salt Cold Tank 96% RTE		
		Cost Category		
		Materials Cost	Labor Cost in Daggett, CA	Labor Cost in Phoenix, AZ
Floor	Geopolymer	$6,360,610.35	$190,899.33	$146,845.64
	Backup Insulation	$295,284.14	$345,828.27	$266,021.75
Roof	Ceramic Fiber	$714,307.71	$314,553.98	$241,964.60
Walls	Geopolymer	$6,822,959.83	$204,775.70	$157,519.77
	Backup Insulation	$322,103.36	$377,238.17	$290,183.21
Subtotal		$14,515,265.38	$1,433,295.44	$1,102,534.96

2.5 Conceptual Concrete Tank Design and Costing

2.5.1 Conceptual Design for Full-Scale Concrete-Based TES Systems

2.5.1.1 Design Criteria

Worley/Advisian performed conceptual concrete tank design. Table 20 summarizes the key design parameters for the geopolymer-lined concrete TES tanks.

This report is available at no cost from the National Renewable Energy Laboratory at www.nrel.gov/publications.

Table 20. Key Design Parameters for the Geopolymer-Lined Concrete TES Tanks

Key Design Parameters	Nitrate Hot Tank	Chloride Hot Tank	Chloride Cold Tank
Site location	Phoenix, Arizona		
Design life	≥30 years		
Daily RTE	≥96%	≥95.5%	
TES size[26]	2,791 MWh-t	2,400 MWh-t	
Max. hours of storage	10	14	
TES configuration[27]	1 hot and 1 cold tank	2 hot and 2 cold tanks	
Design temperature	574°C	720°C	500°C
Salt density [15,16,31]	1,725 kg/m^3	1,550 kg/m^3	1,680 kg/m^3
Salt specific heat [15,16,31]	1.54 kJ/kg·K	1.0 kJ/kg·K	1.06 kJ/kg·K
Salt energy density	2,656.5 kJ/m^3·K	1,550.0 kJ/m^3·K	1,780.8 kJ/m^3·K
Useable salt mass/volume	23,330 Mt/13,525 m^3	19,560 Mt/12,610 m^3	19,560 Mt/11,700 m^3
Tank heel mass/volume	2,138 Mt/1,240 m^3	2,130 Mt/1370 m^3	2,070 Mt/1230 m^3
Tank wall height[28]	13.25 m	11.7 m	11.7 m
Max. liquid static height[29]	11.9 m	10.2 m	10.4 m
Internal liquid diameter	39.73 m	41.8 m	39.7 m
Estimated heat loss	420 W/m^2	290 W/m^2	230 W/m^2
Internal insulation thickness	472 mm	587 mm	506 mm

In addition to the design parameters listed in Table 20, there are several more design considerations:

- Foundation cooling air pipes are provided in the lower base slab to achieve optimal tank floor concrete temperature and soil temperature yet adhere to allowable overall heat flux limitations.
- Ambient conditions outside the tank shell are based on an assumption of an average temperature of 17.3°C and wind speed of 2.2 m/s.
- No external tank insulation is employed, which will increase concrete and rebar strength.
- The roof design concept is a self-supported carbon steel dome roof, all internally insulated with a suspended deck insulation system.

The concrete tank's initial design was arrived at with analytical methods for 1D steady-state heat transfer for predicting thermal gradient through the tank primary sections and stress analysis "hand" calculations for preliminary structural sizing. The stress analysis of the reinforced tank

[26] TES sizing is based on the default SAM molten salt power tower TES input for the nitrate TES and the Gen3 Liquid Pathway TES tank sizing basis for the chloride TES.
[27] The scope of the concrete tank design and analysis only covers the hot tank for the nitrate TES, as there is currently no urgent need to redesign the cold tank.
[28] Including salt heel height, freeboard (0.3 m), suspended deck insulation, and bottom insulation, but excluding concrete base/floor underneath insulation layer).
[29] Including salt heel height.

This report is available at no cost from the National Renewable Energy Laboratory at www.nrel.gov/publications.

wall due to differential thermal expansion raised the potential for the exceedance of concrete tensile strength. To provide more accurate predictions for the state of stress and overall structural integrity, a simplified axis-symmetric finite element (FE) model was constructed by Worley/Advisian. The FE model was first verified with basic checkout cases and then utilized to confirm preliminary structural sizing and design improvements, optimization, and cost reductions.

One of the basic checkout cases for the FE model also served to provide guidance for design directions. The FE model confirmed the theoretical case that a linear thermal gradient through a simply supported wall results in thermal strains that bend the wall without associated thermal stresses. This is because a linear thermal gradient results in a linear distribution of thermal strains that simply supported boundary conditions do not provide constraints against, resulting in no thermal stresses. Note that this is an idealized situation since the wall boundary conditions are not simply supported, and the thermal gradient through a nonhomogeneous wall is not linear. However, this idealized situation did provide important guidance for design direction/evolution.

The preliminary FE model was exercised under a variety of load cases. Sensitivity analyses were performed to meet the project objective of designing a reliable and cost-effective structure. The FE model confirmed the concern over the exceedance of concrete tensile strength identified in the preliminary stress analysis. However, design changes involving both materials (e.g., higher conductivity concrete mix) and boundary conditions (e.g., introducing a radial deadband at the wall-to-floor interface) proved to be highly effective means for mitigating thermal stresses.

The following are a few important findings in Worley/Advisian's preliminary design:

- The original design featuring a concrete roof proved to be impractical under thermal loads—the radial expansion toward the wall combined with the necessary continuous (airtight) junction generates excessive stresses at this interface.
- Post-tensioning of the hoop tendons as initially planned proved to be excessive and could be reduced, especially in conjunction with the original dovetail design into the base, which can cause significant local bending due to restraint as well as radial expansion of the base.
- In general, the temperature drop across the tank floor is less concerning than the wall. This is due to the self-weight and frictional confinement, which tend to mitigate the formation of tensile stresses. The exception is at the section of the base nearing and external to the wall, which sees a rather large drop toward ambient temperature. Significant tensile circumferential/hoop stresses develop in this region.
- The original temperature drop across the wall was confirmed to be problematic despite improvements to the flexibility at the base and roof junctions. There remain sufficient constraints within the system that such a temperature swing across the wall can still generate considerable bending stresses (notably tensile stresses on the outside face). Given the magnitudes involved, this was considered unlikely to be mitigated successfully (i.e., low-cost mitigation solutions) by structural means alone (e.g., added reinforcement/thickness).
- Utilizing steel-fiber-reinforced concrete features both higher conductivity and higher tensile capacity, resulting in a revised temperature drop across the wall, which proved to be effective in mitigating the thermal stresses.
- Vertical post-tensioned tendons can be effectively used to mitigate the thermally generated tensile stresses that develop on the outside face of the tank, if necessary.

This report is available at no cost from the National Renewable Energy Laboratory at www.nrel.gov/publications.

- The combination of steel-fiber-reinforced concrete and vertical post-tensioned tendons features higher tensile stress capacity. These could also be used to significantly reduce or even replace more costly rebar reinforcement.
- Preliminary impact of earthquake dynamic loads [30] was treated as equivalent peak accelerations and applied on the concrete tank and fluid mass as static loads. Response spectra of the N-S, E-W, and vertical components of the El Centro, California, earthquake accelerated time-histories were computed to determine these peak accelerations. Mechanical stresses due to earthquake loading are an important factor and must be considered to accurately compute the state of stress in concrete under combined loading.

From the mechanical/thermal design perspective, Worley/Advisian made the following commentary, which may help achieve potential cost reduction on the concrete tanks and foundations in the final design:

- Significant cost reductions can be realized by reducing the tensile stresses in concrete due to the thermal gradients across the wall. As mentioned in the findings after initial design, Worley/Advisian can show both theoretically as well as numerically (via FE analysis) that a simply supported wall with a linear thermal gradient will not provide internal constraints to the thermal strains resulting in "numerical zero" state for thermal stresses.
- Although neither a simply supported boundary condition nor a perfectly linear thermal gradient is achievable in real applications, this idealized case provides strong direction toward the design evolution that Worley/Advisian can take advantage of in future phases of the project. For example, the introduction of the radial deadband at the wall/floor interface is a step toward a more simply supported boundary condition, which directly translates into thermal stress reductions and therefore cost savings potential.
- The design change from a concrete to steel roof not only resulted in direct cost savings from a material change but also additional cost savings due to (a) increased flexibility at the wall/roof interface (another step toward a more simply supported boundary condition), (b) a reduction in the normal force at the wall/floor interface thereby promoting the transition from stick to slip at that interface at a lower shear load level (again, a step toward a more simply supported boundary condition), and (c) less complex roof penetrations/nozzles.
- The introduction of steel fibers into the concrete matrix is a material enhancement that increases thermal conductivity of concrete, thereby reducing the thermal gradient across concrete surfaces, leading to further reductions in thermal stresses. Intelligent design/spacing of the reinforcement toward a more linear thermal gradient distribution is another important "dial" in reducing thermal stresses. The combination of all these effects can result in a reduction in concrete, reinforcement requirements, and preloads and result in a more cost-effective and robust design.
- The use of steel-fiber-reinforced concrete increases its tensile strength, thereby allowing for a reduction of the amount of rebar, which is primarily used to take tensile loads in

[30] Although the final site location is Phoenix, Arizona, in

Table 20, initial conceptual design did include seismic activities as regions such as certain parts of California (e.g., Daggett) are also desirable locations for concentrating solar power with molten salt TES.

This report is available at no cost from the National Renewable Energy Laboratory at www.nrel.gov/publications.

concrete. If these steel fibers can be procured from cheap/recycled/repurposed sources, this will reduce costs as well.
- Optimized tendon arrangement, based on reduced thermal loads and the use of steel-fiber-reinforced concrete, should result in reduced tendon quantities.
- There is an opportunity to reduce the tank floor concrete thickness, provided the high-fidelity seismic and settlement analyses allow. The thickness from preliminary design is mostly assumed, based on typical practice.
- If the theoretical site/tank can be moved to a lower seismic zone (e.g., Phoenix, Arizona), it would allow for a significant load reduction and therefore lower concrete/rebar quantities.
- Optimization of construction techniques can be investigated, including analyzing slip-form wall pour, or precast walls, which is a function of field labor cost (i.e., site-specific).
- Use of cooling water for the foundation cooling piping systems vs. air-cooled (forced) piping will result in significantly less piping being used in the foundation, although the heat must be rejected via a heat exchanger (likely by increasing the "existing" auxiliary cooling water heat exchanger size).

Based on these preliminary findings, Worley/Advisian made a few recommendations for final tank design:

- A steel panel roof with rafters achieved considerably improved compliance while imparting less load and would also be a lower-cost option. This is already partially accounted for in the rough-order-of-magnitude cost estimates provided in the next section.
- Introducing radial deadband (increasing the rebate width) at the base/wall interface and reducing the friction in this area (steel plate footer) significantly mitigate local stresses by decoupling the radial expansion/contraction movements between the base and wall.
- The arrangement and number of hoop tendons can likely be reduced and repositioned to establish a state of prestress, which more effectively counters the thermal stresses that tend to develop in the opposite direction.
- Additional insulation on the external section of the tank floor external perimeter may be required.
- Further investigation of the benefits of steel-fiber-reinforced concrete and vertical post-tensioning via higher-fidelity FE analysis is required.
- A more thorough transient dynamic analysis to better discern the dynamic behavior of the impact of the tank's higher modes of vibration on stresses (i.e., "whipping loads") is required.
- Conduct a more detailed FE-based heat transfer analysis to include the effects of nonhomogeneous cross sections in the resulting nonlinear thermal gradients.

2.5.1.2 Codes and Standards

Worley/Advisian's design was conducted in accordance with the requirements from American standards detailed below:

- ACI 318 – Building code requirements for structural concrete
- ACI 350 – Code requirements for environmental engineering of concrete structures
- ACI 315 – Details and detailing of concrete reinforcement

This report is available at no cost from the National Renewable Energy Laboratory at www.nrel.gov/publications.

- ACI SP66 – ACI Detailing Manual
- ASTM C512 – Standard Test Method for Creep of Concrete in Compression
- ASCE 7-16 – Minimum Design Loads for Buildings and Other Structures.

Currently, there is no single design code that covers the design of concrete tanks of this type, although analogies have been drawn to liquefied natural gas/liquefied petroleum gas storage tanks. In the United States, ACI 376 ("Code Requirements for Design and Construction of Concrete Structures for Containment of Refrigerated Liquid Gases") may be a useful reference, along with other standards detailed below:

- ACI 376 – Code Requirements for Design and Construction of Concrete Structures for Containment of Refrigerated Liquid Gases
- API 620 – Design and Construction of Large, Welded, Low Pressure Storage Tanks
- API 625 – Tank Systems for Refrigerated Liquefied Gas Storage.

2.5.1.3 Materials

The construction materials, properties and other considerations can be found in Appendix A.

2.5.1.4 Design Drawings

Figure 94 to Figure 96 show the design drawings of the concrete tank structure and foundation for the nitrate salt hot tank, chloride salt hot tank, and chloride salt cold tank, respectively.

This report is available at no cost from the National Renewable Energy Laboratory at www.nrel.gov/publications.

Hot Nitrate Salt Tank Arrangement
Advisian
Mar 23, 2023

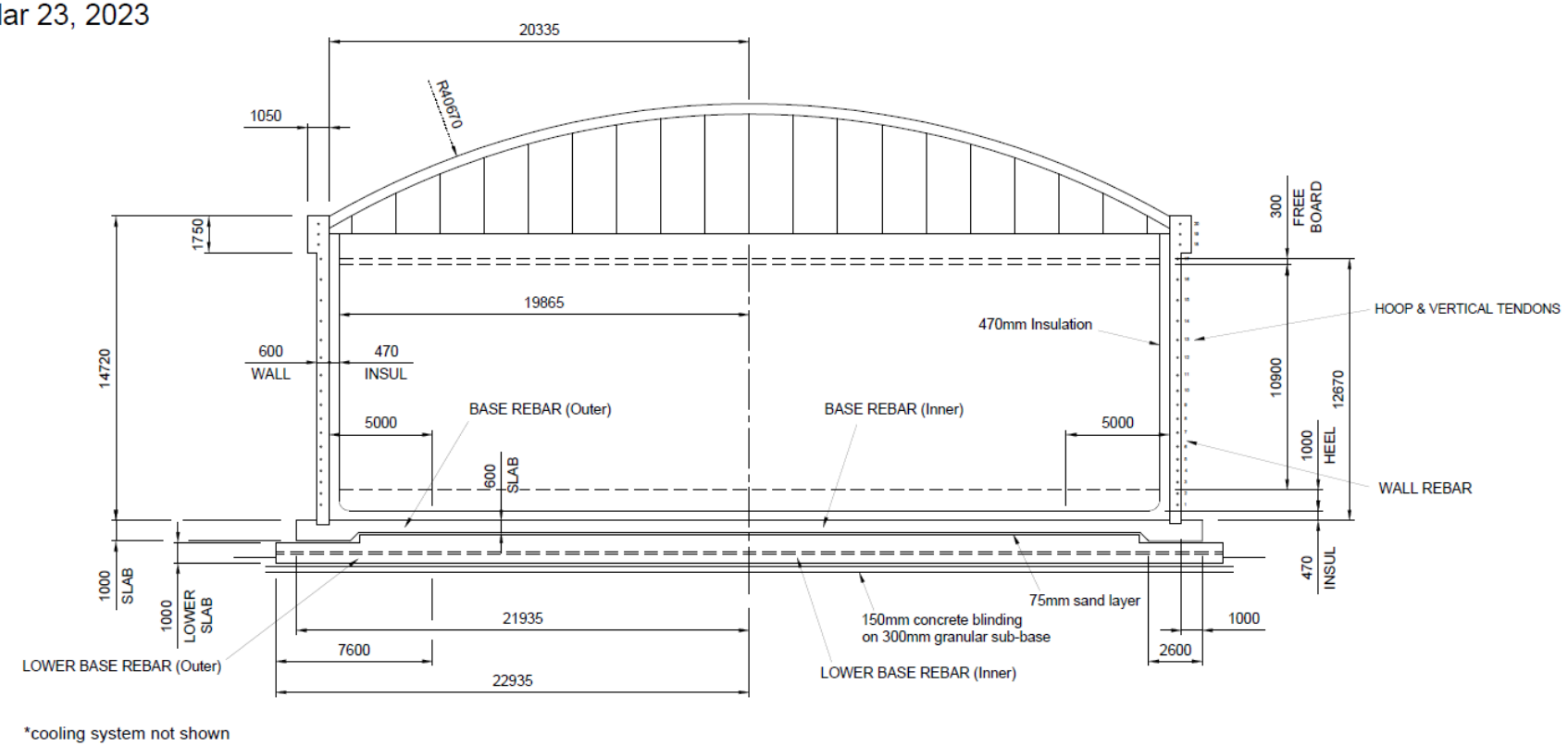

*cooling system not shown

Figure 94. Design drawings of the concrete tank and foundation for the hot nitrate salt tank at 96% daily RTE

This report is available at no cost from the National Renewable Energy Laboratory at www.nrel.gov/publications.

Hot Chloride Salt Tank Arrangement
Advisian
June 22, 2023

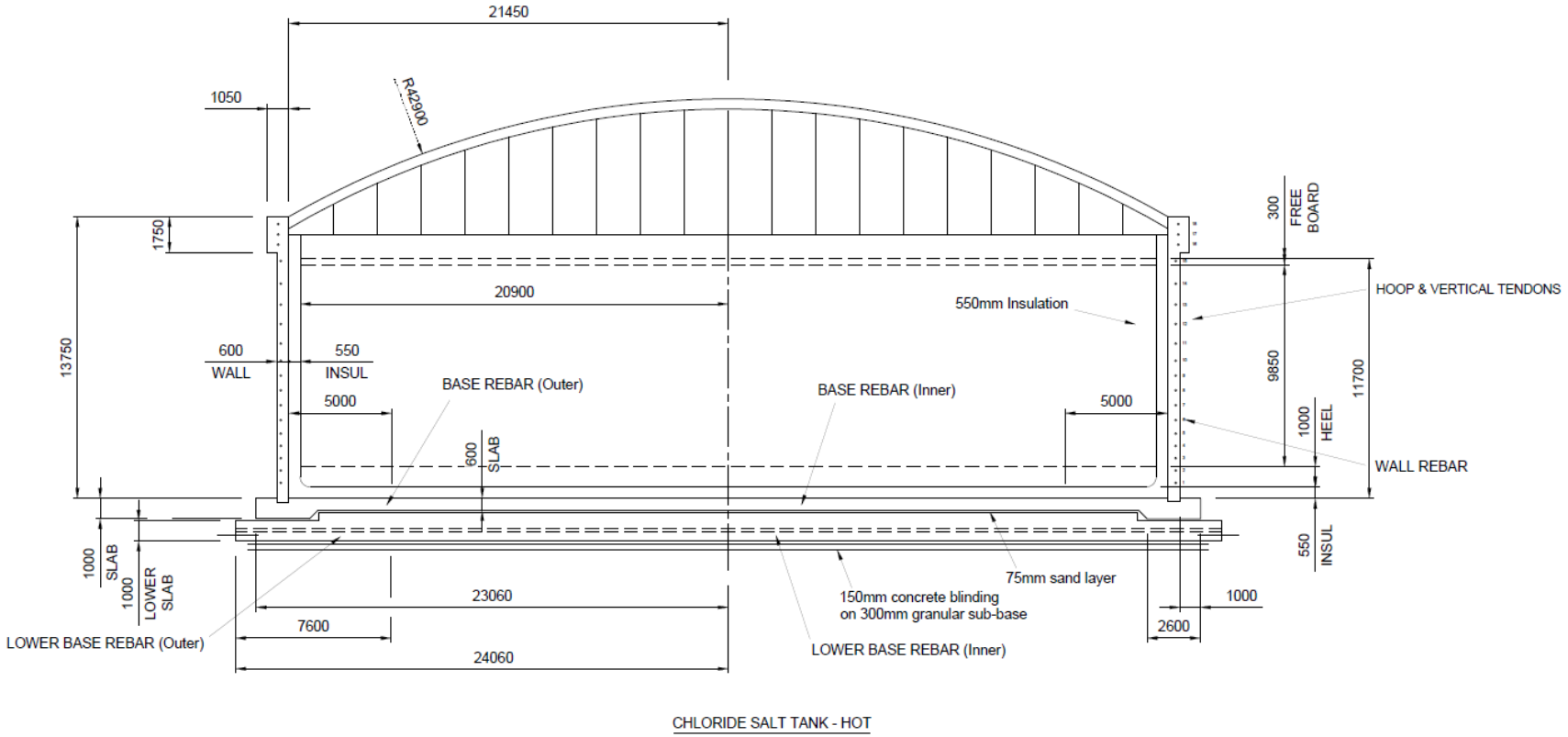

Figure 95. Design drawings of the concrete tank and foundation for the hot chloride salt tank at 95% daily RTE

This report is available at no cost from the National Renewable Energy Laboratory at www.nrel.gov/publications.

Cold Chloride Salt Tank Arrangement
Advisian
June 16, 2023

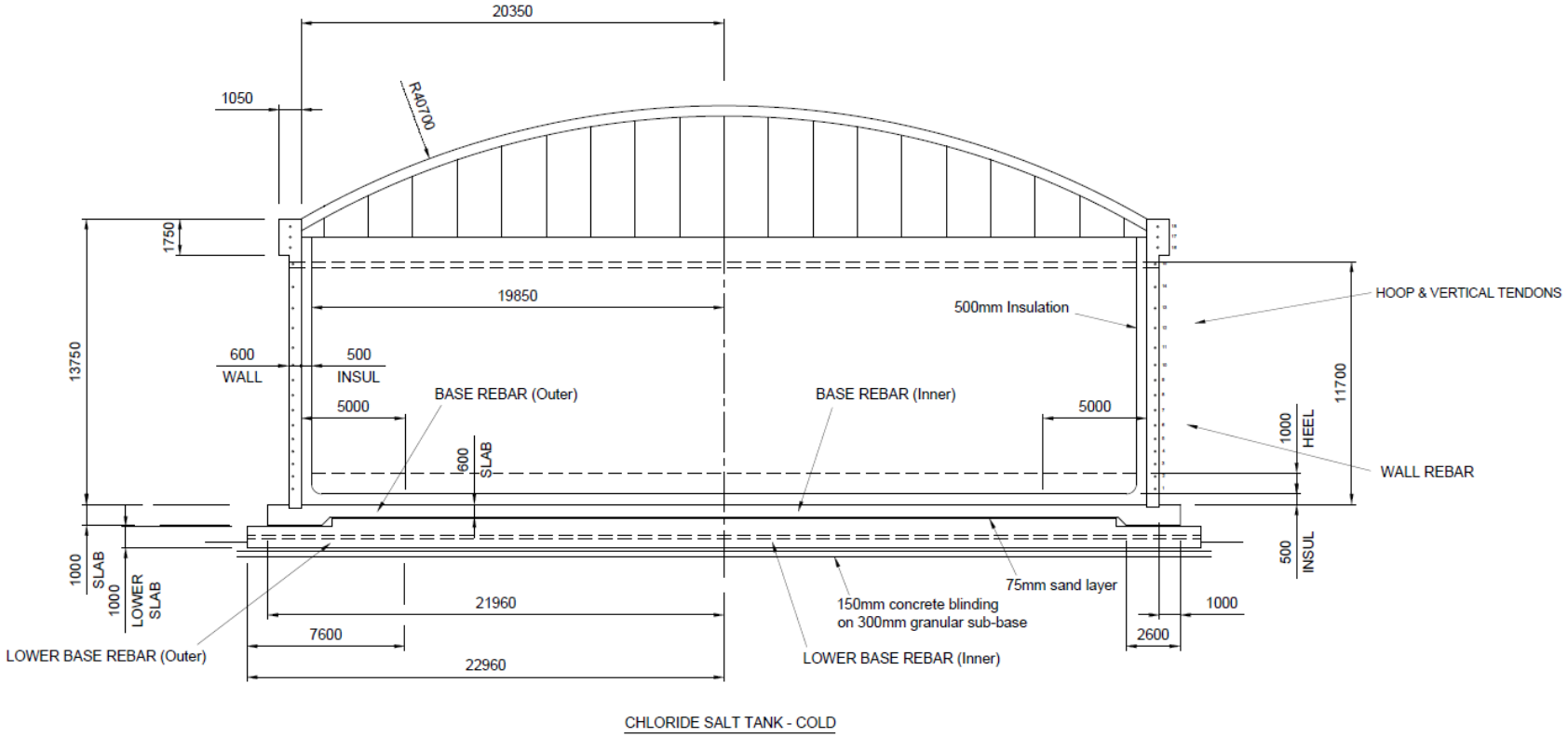

Figure 96. Design drawings of the concrete tank and foundation for the hot chloride salt tank at 96% daily RTE

This report is available at no cost from the National Renewable Energy Laboratory at www.nrel.gov/publications.

2.5.2 Costing for Full-Scale Concrete-Based TES Systems

2.5.2.1 Concrete-Based Molten Nitrate Salt TES Cost

The final capital cost for one concrete-based nitrate salt hot tank was estimated by Worley/Advisian. The total estimated cost to design, construct, and commission the facilities described in this study with a 35% contingency is $24.94 million with a site location of Phoenix, Arizona, excluding the cost of the salt inventory and insulation materials. Based on the overall nitrate salt storage system capacity of 2,791 MWh-t, the hot tank unit cost is $8.94/kWh-t. The capital expenditures (CapEx) estimate is classified as AACEI Class 4 with an accuracy of –20% to +30% and is presented in Q2 2023 U.S. dollars. A summary of the capital cost estimate is shown in Table 21. The details of the concrete tank costing are given in Appendix B.

Table 21. CapEx Estimate Summary for the Concrete Tank Structure, Foundation, and Roof for One Nitrate Salt Hot Tank

Cost Categories	Category Total
Direct Cost	$15,718,524
Indirect Cost	$2,753,764
Contingency	$6,465,301
Total	**$24,937,588**

As shown by Table 18, the insulation cost for one geopolymer-insulated nitrate salt hot tank at 96% daily RTE is $6.85/kWh-t, which makes the total cost of the hot tank about $15.79/kWh-t, with about 56% and 44% split between tank structure (i.e., foundation, walls, floor, and roof) and internal geopolymer insulation.

As a reference, Worley/Advisian performed design and costing for a pair of reference conventional molten nitrate salt storage tanks, consisting of one stainless steel 347H hot tank and one carbon steel cold tank, both without any internal insulation but with external insulation [6]. The study estimated a total TES cost of $26.37/kWh-t (in 2020 U.S. dollars). Figure 97 shows the cost breakdown of one SS 347H hot tank at $9.49/kWh-t, one carbon steel cold tank at $4.77/kWh-t, and the salt inventory $12.11/kWh-t.

This report is available at no cost from the National Renewable Energy Laboratory at www.nrel.gov/publications.

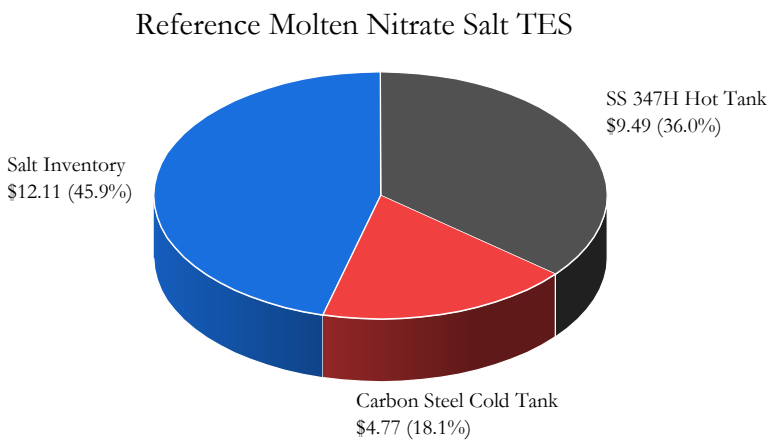

Figure 97. Cost breakdown in $/kWh-t of a reference conventional metal-based molten nitrate salt TES

Using data from the current study and previous study, one can estimate that for a molten nitrate salt TES system that (1) consists of one concrete-based geopolymer-insulated hot tank and a conventional carbon steel externally insulated cold tank and (2) operates at about 97% daily RTE,[31] the total TES cost is about $32.67/kWh-t, assuming the same cost for the cold tank and salt inventory,[32] as shown by the cost breakdown in Figure 98.

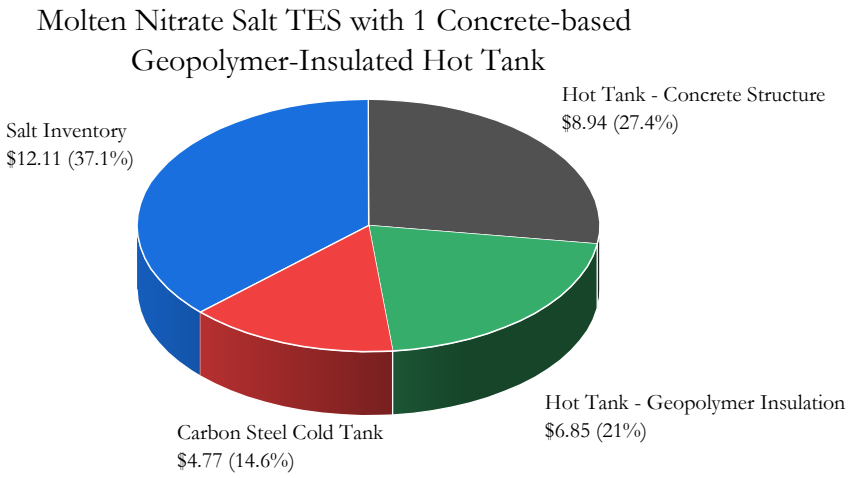

Figure 98. Cost breakdown in $/kWh-t of a molten nitrate salt TES with one concrete-based geopolymer-insulated hot tank and one conventional metal-based cold tank

The difference in total TES cost between Figure 97 and Figure 98 (i.e., about $6.5/kWh-t) is mostly from the geopolymer insulation liner. Given the current design challenges with the SS 347H material as tank structure and the observed tank failures, the CapEx investment on geopolymer insulation liner has the potential to improve tank reliability (as demonstrated by the extensive

[31] The overall 97% daily RTE is approximated by the average of the 98% daily RTE of the conventional cold tank and the 96% daily RTE of the geopolymer-insulated concrete-based hot tank.
[32] Note that the cold tank cost and salt inventory cost were both estimated in 2020 US dollars.

This report is available at no cost from the National Renewable Energy Laboratory at www.nrel.gov/publications.

testing results of geopolymer materials in molten nitrate salt at bench scale). The additional cost may be justified if the geopolymer concept can be scaled up with its effectiveness demonstrated at a larger scale.

2.5.2.2 Concrete-Based Molten Chloride Salt TES Cost

The final capital cost for a chloride salt storage system—consisting of two concrete-based hot tanks and two cold tanks—was estimated by Worley/Advisian. The total estimated cost to design, construct, and commission the facilities described in this study with a 35% contingency is $94.66 million at a site location of Phoenix, Arizona, excluding the cost of the salt inventory and insulation materials. Based on the overall chloride salt storage system capacity of 2,400 MWh-t, the tank system's unit cost is $39.44/kWh-t. The CapEx estimate is classified as AACEI Class 4 with an accuracy of −20% to +30% and is presented in Q2 2023 U.S. dollars. A summary of the capital cost estimate is shown in Table 22. The details of the tank costing are given in Appendix C.

Table 22. CapEx Estimate Summary for the Concrete Tank Structure, Foundation, and Roof for Two Chloride Salt Hot Tanks and Two Chloride Salt Cold Tanks

Cost Categories	Category Total
Direct Cost	$62,303,364
Indirect Cost	$7,813,480
Contingency	$24,540,896
Total	**$94,657,740**

The high cost of the concrete structure and foundation for the molten chloride salt TES, at $39.44/kWh-t, is mostly due to the lower energy density of the chloride salt, as shown in Table 20. With about 60% of molten nitrate salt's energy density, the molten chloride salt requires significantly more salt inventory to achieve similar thermal energy storage capacity, which explains the "2 hot tanks and 2 cold tanks" design if the unit tank size stays comparable. On the other hand, the cost at about $10/kWh-t for each tank is comparable to that for one nitrate salt hot tank. Therefore, it shows that the dominant factor for the chloride concrete structure cost is indeed the need for a larger number of tanks due to chloride salt's lower thermal energy storage capacity.

The total TES cost, including internal insulation and salt inventory, is further exacerbated by the "2 hot tanks and 2 cold tanks" design. The requirement for the expensive geopolymer internal insulation is quadrupled compared to the nitrate salt TES design in the previous section, as all four chloride salt tanks are designed with geopolymer internal insulation liners. Table 23 shows the cost breakdown comparison for the nitrate salt TES and chloride salt TES. At ~$86/kWh-t, the concrete-structured and geopolymer-insulated molten chloride TES is cost-prohibitive. It showcases the challenges associated with designing a TES system using a medium that has substantially lower TES capacity compared to the state-of-the-art molten nitrate salt.

This report is available at no cost from the National Renewable Energy Laboratory at www.nrel.gov/publications.

Table 23. Cost Breakdown Comparison for the Nitrate Salt TES and Chloride Salt TES

	Nitrate TES		**Chloride TES**	
Configuration	**1 Hot Tank**	**1 Cold Tank**	**2 Hot Tanks**	**2 Cold Tanks**
Tank type	Concrete tank + geopolymer insulation	Conventional metal tank	Concrete tank + geopolymer insulation	
Tank cost	$8.94/kWh-t	$4.77/kWh-t*	$20.95/kWh-t	$18.49/kWh-t
Insulation cost	$6.85/kWh-t		$19.41/kWh-t	$13.01/kWh-t
Salt cost	$12.11/kWh-t* [6]		$13.43/kWh-t [2]	
TES cost	$32.67/kWh-t		$85.29/kWh-t	

* Cost estimation in 2020 U.S. dollars

This report is available at no cost from the National Renewable Energy Laboratory at www.nrel.gov/publications.

3 Conclusions

This study conceptually designed a concrete-based TES tank system (for both molten nitrate salt TES and molten chloride salt TES). The tank was designed with concrete walls and foundation with a steel roof, which is believed to be feasible for the scale of commercial molten salt TES. The costing analysis showed that a concrete-based TES tank structure and foundation (excluding thermal insulation) is comparable to a conventional metal-based TES system, on a per-tank basis. It indicates that concrete may be an economically feasible alternative tank structure material for molten-salt-based TES systems.

In order to implement a design with concrete walls and foundation, which cannot be subject to high temperatures, internal insulation to reduce the tank structure's temperature is required. Hence, an internal insulation concept based on partial salt permeation was presented. The partial salt permeation design addresses the challenges of salt containment by relying on a frozen salt layer inside the insulation liner as self-containment. The designed temperature profile inside the insulation liner allows self-healing of frozen salt containment, which addresses the risk of salt leaking. The "self-containment" and "self-healing" design addresses the material challenges associated with developing a liquid-tight mortar (which is regarded as the "weakest link" in the state-of-the-art tank liner design), as the molten salt containment is no longer a relevant requirement for the mortars.

To achieve the conceptual insulation design, a new geopolymer-based composite refractory material with cenospheres and coarse aggregates was developed with extensive testing of materials properties and performance in molten salts. For the geopolymer material to insulate and contain the molten salt, cenosphere inclusion is key to achieving closed porosities, proper high-temperature heat treatment should be used to control open porosities, and proper addition of coarse aggregates is crucial to avoiding cracking after high-temperature heat treatment. The geopolymer insulation was extensively tested in molten nitrate salt and molten chloride salt at lab scale for up to 1,200 hours, isothermally and with thermal cycling. The result shows that the geopolymer insulation has the potential to achieve the "self-containment" and "self-healing" insulation liner design concept.

To realize the materials at commercial scale, production trials of the geopolymer bricks were performed. The scaling effort turned out to be challenging because the large brick dimensions lead to complex stresses during firing, and the phase transitions of the geopolymer matrix and/or additive may have led to shrinkage cracking. Therefore, additional investigation is needed before reliable production of the geopolymer bricks without cracking can be achieved.

Costing analysis of the geopolymer insulation material showed that processing cost due to the labor-intensive manufacturing procedures is the dominating factor in the geopolymer's high overall cost. Cost reduction routes should be explored to make the geopolymer more economically appealing.

Costing analysis of the molten salt TES systems with geopolymer internal insulation and concrete structure/foundation showed that a molten nitrate TES with one metal cold tank and one geopolymer-insulated concrete hot tank is the most economical option at about $33/kWh-t. However, due to the higher cost of geopolymer material and the "two-pair" tank design as a result

This report is available at no cost from the National Renewable Energy Laboratory at www.nrel.gov/publications.

of the lower energy density of the chloride salt, a molten chloride TES with two geopolymer-insulated concrete cold tanks and two geopolymer-insulated concrete hot tanks is cost-prohibitive at >$85/kWh-t.

This report is available at no cost from the National Renewable Energy Laboratory at www.nrel.gov/publications.

4 Recommendations

Although the results from this project suggest a path toward an alternative TES design using concrete as the structure and foundation material and using geopolymer as internal insulation to achieve self-containment of the molten salt, there are a few areas for improvement that have the potential to further de-risk the technology and reduce cost:

- More scientific understanding of the geopolymer's cracking behavior at commercial scale is needed. Specifically, the relationship at the microscopic level between phase transitions and shrinkage should be focused on, which is the leading suspect of cracking based on the results from production trials. The cracking mechanism(s) at the macroscopic level should then be investigated to understand the relationship between proper manufacturing measures and mitigation of cracking.
- Once the cracking behavior of the geopolymer bricks at commercial scale can be resolved, the production method(s) should be revisited to reduce the processing cost. Less labor-intensive and more automated technique(s) such as cold pressing, and easier and more efficient curing and firing processes should be reconsidered.
- If the production issues can be resolved, testing of the geopolymer insulation concept at a larger scale, preferably in a prototype molten salt storage tank, will be valuable. The goals are (1) to verify the size effect of the geopolymer bricks on salt permeation resistance and long-term stability, (2) to verify the salt freezing phenomenon to confirm the self-containment and self-healing features, and (3) to stress-test the geopolymer and mortar, especially at the salt freeze interface to confirm the robustness of the liner and mortar joints when the interface moves in a real-world environment.

This report is available at no cost from the National Renewable Energy Laboratory at www.nrel.gov/publications.

References

[1] Mehos, M., C. Turchi, J. Vidal, M. Wagner, and Z. Ma. 2017. *Concentrating Solar Power Gen3 Demonstration Roadmap.* Golden, CO: National Renewable Energy Laboratory. NREL/TP-5500-67464. https://www.nrel.gov/docs/fy17osti/67464.pdf.

[2] Turchi, C., S. Gage, J. Martinek, S. Jape, K. Armijo, J. Coventry, J. Pye, et al. 2021. *CSP Gen3: Liquid-Phase Pathway to SunShot*. Golden, CO: National Renewable Energy Laboratory. NREL/TP-5700-79323. https://www.nrel.gov/docs/fy21osti/79323.pdf.

[3] Drewes, K., B. Leslie, D. Cubel, B. Kelly, L. Imponenti, S. Bell, R. Clegg, G. Will, and T. Steinberg. 2022. "High Temperature Salt Tank Buckling Failure." Presented at SolarPACES, 2022. Vast Solar. https://www.solarpaces.org/wp-content/uploads/High-Temperature-Salt-Tank-Buckling-Failure.pdf.

[4] Osorio, J. 2023. "Modeling of Stress Distribution in Molten Salt Thermal Energy Storage Tanks for In-Service Central Receiver Power Plants." Presented at 5th Thermal-Mechanical-Chemical Energy Storage Workshop. Aug. 2, 2023. National Renewable Energy Laboratory. NREL/PR-5700-87158. https://www.nrel.gov/docs/fy23osti/87158.pdf.

[5] C.S. Turchi, N. Conmy, Y. Zhao, J. Netter, and P. Davenport. 2023. "Design of an Internally Insulated Tank for Molten Chloride Salt at 720°C." Presented at SolarPACES, Oct. 13, 2023, Sydney, Australia.

[6] Zhao, Y., and R. Bowers. 2023. *Re-Designing the CSP Thermal Energy Storage System to Enable Higher Temperature Performance at Reduced Cost: Final Technical Report*. Golden, CO: National Renewable Energy Laboratory. NREL/TP-5700-84409. https://www.nrel.gov/docs/fy23osti/84409.pdf.

[7] Hong, Y., T. Pickle, J. Vidal, C. Augustine, and Z. Yu. 2023. "Impact of Plate Thickness and Joint Geometry on Residual Stresses in 347H Stainless Steel Welds." *Welding Journal* supplement: 279-s–291-s. https://doi.org/10.29391/2023.102.021.

[8] Foster Jr., P. A. 1960. "Determination of the Cryolite-Alumina Phase Diagram by Quenching Methods." *Journal of the American Ceramic Society* 43(2): 66–68. https://doi.org/10.1111/j.1151-2916.1960.tb13642.x.

[9] Zhao, Y., E. Wagstaff, S. Gage, D. Payne, and C. Turchi. 2022. "Chemical Compatibility of Hollow Ceramic Cenospheres as Thermal Insulation for High-Temperature Thermal Energy Storage Applications With Molten Nitrate Salt." *Solar Energy Materials and Solar Cells* 238: 111597. https://doi.org/10.1016/j.solmat.2022.111597.

[10] Jacobson, N. S., and K. N. Lee. 1996. "Corrosion of Mullite by Molten Salts." *Journal of the American Ceramic Society* 79(8): 2161–2167. https://doi.org/10.1111/j.1151-2916.1996.tb08951.x.

This report is available at no cost from the National Renewable Energy Laboratory at www.nrel.gov/publications.

[11] Jacobson, N. S., J. L. Smialek, and D. S. Fox. 1994. "Molten Salt Corrosion of Ceramics." In *Corrosion of Advanced Ceramics,* NATO Science Series E: (closed), vol. 267. Edited by K. G. Nickel, 205–222. Dordrecht: Springer.

[12] Gage, S. H., J. J. Bailey, D. P. Finegan, D. J. L. Brett, P. R. Shearing, and C. S. Turchi. 2021. "Internal Insulation and Corrosion Control of Molten Chloride Thermal Energy Storage Tanks." *Solar Energy Materials and Solar Cells* 225: 111048. https://doi.org/10.1016/j.solmat.2021.111048.

[13] Gong, L., Y. Wang, X. Cheng, R. Zhang, and H. Zhang. 2013. "Thermal Conductivity of Highly Porous Mullite Materials." *International Journal of Heat and Mass Transfer* 67(December): 253–259. https://doi.org/10.1016/j.ijheatmasstransfer.2013.08.008.

[14] Han, Y., C. Li, C. Bian, S. Li, and C.-A. Wang. 2013. "Porous Anorthite Ceramics With Ultra-Low Thermal Conductivity." *Journal of the European Ceramic Society* 33(13–14): 2573–2578. https://doi.org/10.1016/j.jeurceramsoc.2013.04.006.

[15] SQM. No date. "Thermo-Solar Salts." SQM.com. https://www.sqm.com/en/producto/sales-termo-solares/.

[16] Zhao, Y. 2020. *Molten Chloride Thermophysical Properties, Chemical Optimization, and Purification*. Golden, CO: National Renewable Energy Laboratory. NREL/TP-5500-78047. https://www.nrel.gov/docs/fy21osti/78047.pdf.

[17] Tortorelli, P. F., P. S. Bishop, and J. R. DiStefano. 1989. *Selection of Corrosion Resistant Materials for Use in Molten Nitrate Salts*. Oak Ridge, TN: Oak Ridge National Laboratory. ORNL/TM-11162.

[18] Villaquiran-Caicedo, M. A., R. Mejia de Gutierrez, S. Sulekar, C. Davis, and Juan C. Nino. 2015. "Thermal Properties of Novel Binary Geopolymers Based on Metakaolin and Alternative Silica Sources." *Applied Clay Science* 118(December): 276–282. https://doi.org/10.1016/j.clay.2015.10.005.

[19] Wang, M.-R., D.-C. Jia, P.-G. He, and Y. Zhou. 2011. "Microstructural and Mechanical Characterization of Fly Ash Cenosphere, Metakaolin-Based Geopolymeric Composites." *Ceramics International* 37(5): 1661–1666. https://doi.org/10.1016/j.ceramint.2011.02.010.

[20] Sore, S. O., A. Messan, E. Prud'Homme, G. Escadeillas, and F. Tsobnang. 2020. "Comparative Study on Geopolymer Binders Based on Two Alkaline Solutions (NaOH and KOH)." *Journal of Minerals and Materials Characterization and Engineering* 8(6): 407–420. https://doi.org/10.4236/jmmce.2020.86026.

[21] Rovnaník, P. 2010. "Effect of Curing Temperature on the Development of Hard Structure of Metakaolin-Based Geopolymer." *Construction and Building Materials* 24(7): 1176–1183. https://doi.org/10.1016/j.conbuildmat.2009.12.023.

This report is available at no cost from the National Renewable Energy Laboratory at www.nrel.gov/publications.

[22] Castel, A., S. J. Foster, T. Ng, J. G. Sanjayan, and R. I. Gilbert. 2016. "Creep and Drying Shrinkage of a Blended Slag and Low Calcium Fly Ash Geopolymer Concrete." *Materials and Structures* 49: 1619–1628. https://doi.org/10.1617/s11527-015-0599-1.

[23] Khan, I., T. Xu, A. Castel, R. I. Gilbert, and M. Babaee. 2019. "Risk of Early Age Cracking in Geopolymer Concrete due to Restrained Shrinkage." *Construction and Building Materials* 229(December): 116840. https://doi.org/10.1016/j.conbuildmat.2019.116840.

[24] Eisa, M. S., M. E. Basiouny, and E. A. Fahmy. 2022. "Drying Shrinkage and Thermal Expansion of Metakaolin-Based Geopolymer Concrete Pavement Reinforced With Biaxial Geogrid." *Case Studies in Construction Materials* 17(December): e01415. https://doi.org/10.1016/j.cscm.2022.e01415.

[25] Huiskes, D. M. A., A. Keulen, Q. L. Yu, and H. J. H. Brouwers. 2016. "Design and Performance Evaluation of Ultra-Lightweight Geopolymer Concrete." *Materials & Design* 89(January): 516–526. https://doi.org/10.1016/j.matdes.2015.09.167.

[26] Duxson, P., J. L. Provis, G. C. Lukey, S. W. Mallicoat, W. M. Kriven, and J. S. J. van Deventer. 2005. "Understanding the Relationship Between Geopolymer Composition, Microstructure and Mechanical Properties." *Colloids and Surfaces A: Physicochemical and Engineering Aspects* 269(1–3): 47–58. https://doi.org/10.1016/j.colsurfa.2005.06.060.

[27] Chen, K. J., H. Y Chang, Y. C. Ko, and T. F. Lee. 1982. "Thermal Expansion of Aluminosilicate Refractory Brick." *American Ceramic Society Bulletin*. 61(8). https://www.osti.gov/biblio/5863670.

[28] Majkrzak II, G. L., J. P. Watson, M. M. Bryant, and K. Clayton. 2007. "Effect of Cenospheres on Flyash Brick Properties." Presented at 2007 World of Coal Ash (WOCA), May 7–10, 2007, Convington, KY.

[29] Junaid, M. T., A. Khennane, O. Kayali, A. Sadaoui, D. Picard, and M Fafard. 2014. "Aspects of the Deformational Behaviour of Alkali Activated Fly Ash Concrete at Elevated Temperatures." *Cement and Concrete Research* 60(June): 24–29. https://doi.org/10.1016/j.cemconres.2014.01.026.

[30] Pan, Z., and J. G. Sanjayan. 2010. "Stress-Strain Behaviour and Abrupt Loss of Stiffness of Geopolymer at Elevated Temperatures." *Cement and Concrete Composites* 32(9): 657–664. https://doi.org/10.1016/j.cemconcomp.2010.07.010.

[31] Wang, X., J. Del Rincon, P. Li, Y. Zhao, and J. Vidal. 2021. "Thermophysical Properties Experimentally Tested for NaCl-KCl-MgCl2 Eutectic Molten Salt as a Next-Generation High-Temperature Heat Transfer Fluids in Concentrated Solar Power Systems." *Journal of Solar Energy Engineering* 143(4): 041005. https://doi.org/10.1115/1.4049253.

[32] Zhang, S., S. Tie, and F. Zhang. 2018. "Cristobalite Formation From the Thermal Treatment of Amorphous Silica Fume Recovered From the Metallurgical Silicon Industry." *Micro & Nano Letters* 13(10): 1465–1468. https://doi.org/10.1049/mnl.2018.5167.

This report is available at no cost from the National Renewable Energy Laboratory at www.nrel.gov/publications.

[33] Lee, N. K., and H. K. Lee. 2013. “Setting and Mechanical Properties of Alkali-Activated Fly Ash/Slag Concrete Manufactured at Room Temperature.” *Construction and Building Materials* 47(October): 1201–1209. https://doi.org/10.1016/j.conbuildmat.2013.05.107.

This report is available at no cost from the National Renewable Energy Laboratory at www.nrel.gov/publications.

Appendix A. Materials

A.1 Concrete

The minimum compressive strength at 28 days (cylinder test) is as shown in Table A-1:

Table A-1. Minimum Compressive Strength at 28 Days (Cylinder Test)

Structure	Characteristic Cylinder Strength	Special Requirements
Blinding	25 N/mm²	None
Reinforced Base	40 N/mm²	Cement Replacement Other Additives TBA
Post-tensioned Walls	40 N/mm²	Cement Replacement Other Additives TBA
Post-tensioned Ringbeam	40 N/mm²	Cement Replacement Other Additives TBA
Reinforced Roof	40 N/mm²	Cement Replacement Other Additives TBA

Concrete Density

For analysis purposes, concrete densities listed in Table A-2 are assumed.

Table A-2. Concrete Densities

	Density (kN/m^3)	Density (kg/m^3)
Post-tensioned Concrete (tank wall)	25	2,550
Reinforced Concrete (tank floor)	24	2,450
Plain Concrete (limestone based)	22.5	2,290
Steel-fiber Siliceous Concrete (no rebar)	22.9	2,330

Response of Concrete to Design Temperatures

The behavior of concrete at warm temperatures may be different from that at ambient temperature and hence should be considered in the determination of the performance of the structure. It is permissible to incorporate temperature-dependent properties into any structural analysis models. For initial design, the strengths to be used in design should not take account of enhanced properties that may be present at such temperatures.

This report is available at no cost from the National Renewable Energy Laboratory at www.nrel.gov/publications.

Thermal Deformation

The value for coefficient of thermal expansion of concrete for use in design should be the value that is appropriate for the temperature range and moisture content range to be expected in service. Depending on aggregate type, coefficients of thermal expansion may vary from 4–12 × 10^{-6}/°C.

The coefficient of expansion of the concrete is sensitive to the aggregate type, concrete moisture content, and temperature. The coefficient of expansion of a dry to moderately moist concrete mix at ambient and warm temperatures is usually within the range 4–12 × 10^{-6}/°C (Figure A-1).

Coef of Thermal Expansion =

Temp. °C	α /deg C
-200	0.000008
-150	0.000009
-100	0.000009
-50	0.000010
-20	0.000010
0	0.000010
20	0.000010
50	0.000010
100	0.000010
200	0.000010
300	0.000012
400	0.000013
500	0.000016
600	0.000019

Assign a constant value of 10 x 10^{-6}/°C

Figure A-1. Variation of coefficient of thermal expansion with temperature

Stress-Strain Relationship

A design stress strain relationship is required to calculate the stress distribution in the concrete compression zone under the various load conditions (Figure A-2).

This report is available at no cost from the National Renewable Energy Laboratory at www.nrel.gov/publications.

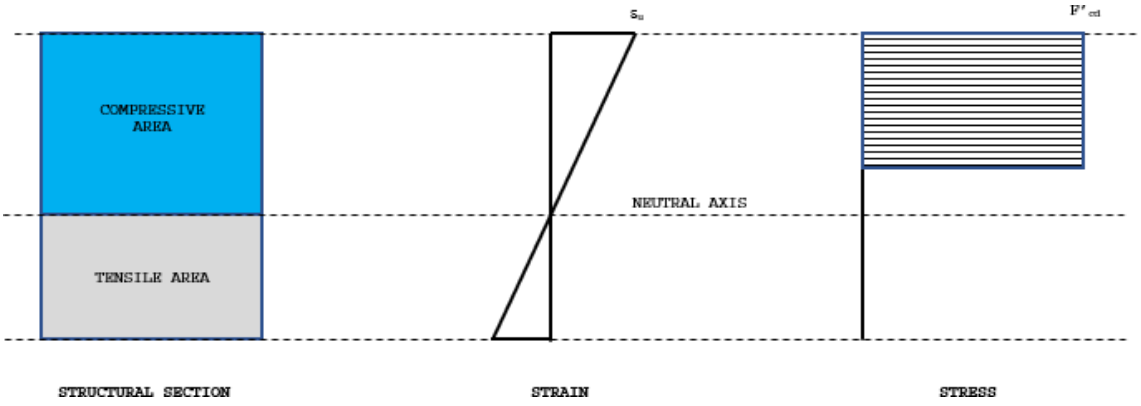

Figure A-2. Stress-strain diagram for concrete

Variation in compressive strength with temperature shall follow guidance given in ACI216.1, which depends upon aggregate type as shown in Figure A-3 (a, b, c).

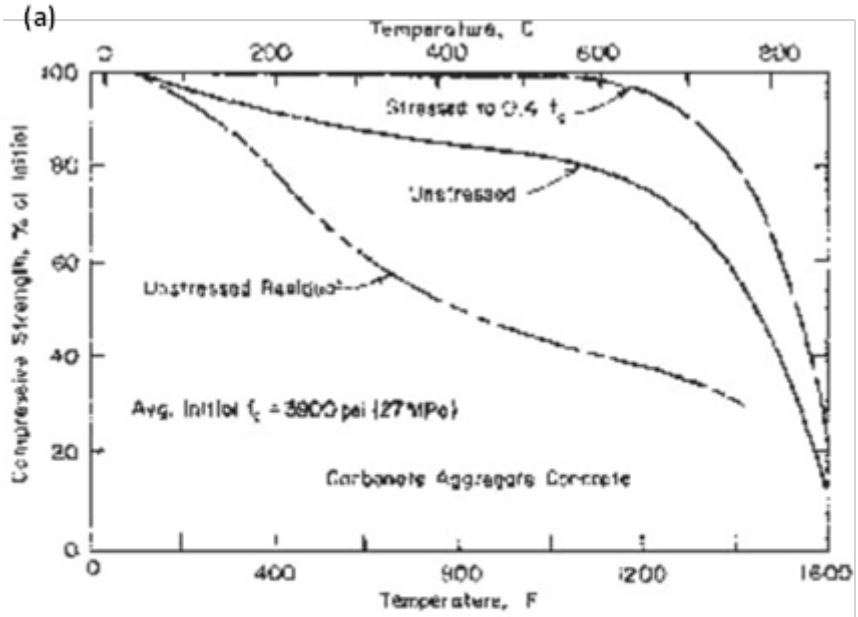

Fig. 4.4.2.2.1c(a)—Compressive strength of carbonate aggregate concrete at high temperatures and unstressed residual after cooling.

This report is available at no cost from the National Renewable Energy Laboratory at www.nrel.gov/publications.

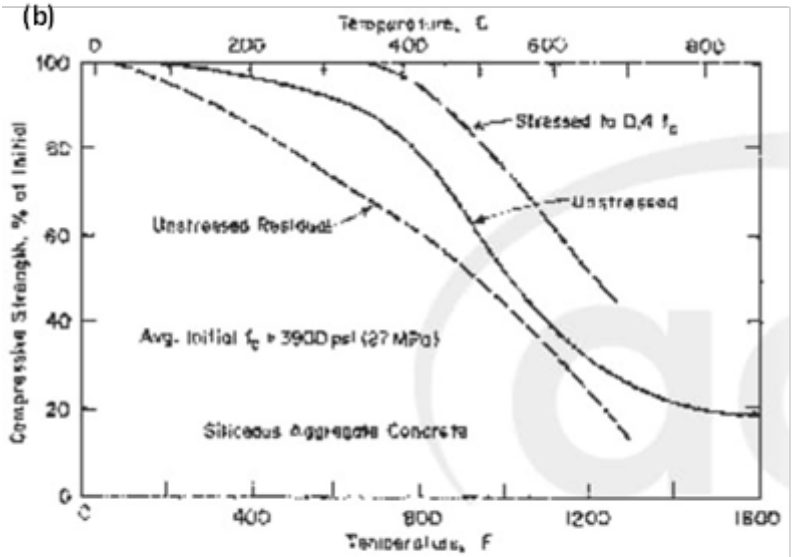

Fig. 4.4.2.2.1c(b)—Compressive strength of siliceous aggregate concrete at high temperatures and unstressed residual after cooling.

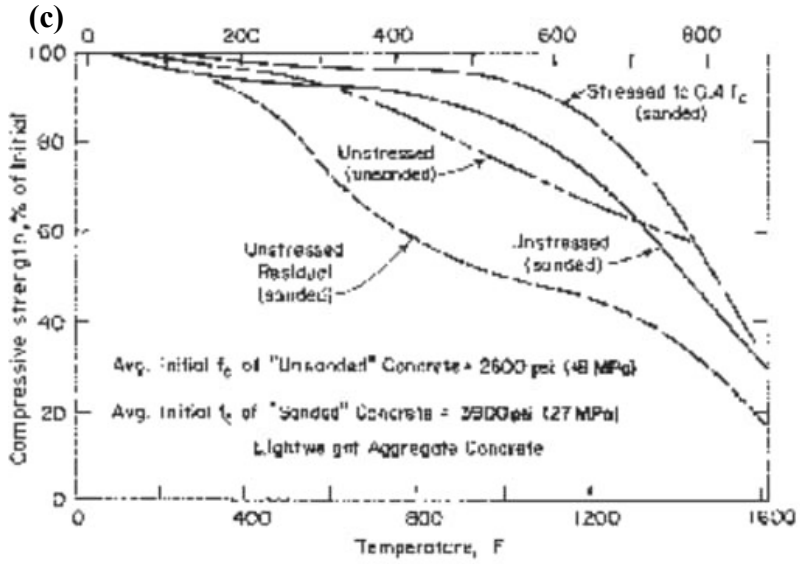

Fig. 4.4.2.2.1c(c)—Compressive strength of semi-lightweight concrete at high temperatures and unstressed residual after cooling.

Figure A-3. Variation in strength of concrete with temperature (from ACI216.1, Fig. 4.4.2.2.1c)

This report is available at no cost from the National Renewable Energy Laboratory at www.nrel.gov/publications.

Poisson Ratio, v

The Poisson Ratio for uncracked post tensioned and reinforced concrete is taken as constant at 0.2.

Modulus of Elasticity, E_c

The modulus of elasticity will be calculated per ACI 318, §19.2.2.

Thermal Properties

The coefficient of thermal expansion is sensitive to the concrete moisture content, aggregate type and temperature. For the purposes of finite element thermal analysis, the concrete will be assigned a value of 10×10^{-6}/°C.

The thermal conductivity of concrete varies as function of aggregate, moisture content, rebar content, temperature, as well as incorporation of any steel-fiber additives. Table A-3 provides a summary of various thermal conductivities used to be used in the tank design1.

Table A-3. Concrete Tank Conductivity Values

	Limestone-based Conductivity, W/m-°K	Siliceous-based w/Steel-Fiber Conductivity, W/m-°K
Post-tensioned Concrete (tank wall)	2.5	4.4
Reinforced Concrete (tank floor)	2.1	3.8
Plain Concrete	1.6	2.9

Steel Reinforcement

The rebar design characteristics at ambient temperature are:

- The yield strength of all reinforcing steel is taken as 66,000 psi (460 N/mm^2).
- The modulus of elasticity of the reinforcing steel is taken as 29,000,000 psi (200,000 N/mm^2), per ACI 318M, Section 8.5.2.
- Thermal expansion coefficient: $\alpha = 10 \times 10^{-6}$/°C.

The reinforcement is assumed elastic-plastic with no strain hardening, as shown in Figure A-4.

This report is available at no cost from the National Renewable Energy Laboratory at www.nrel.gov/publications.

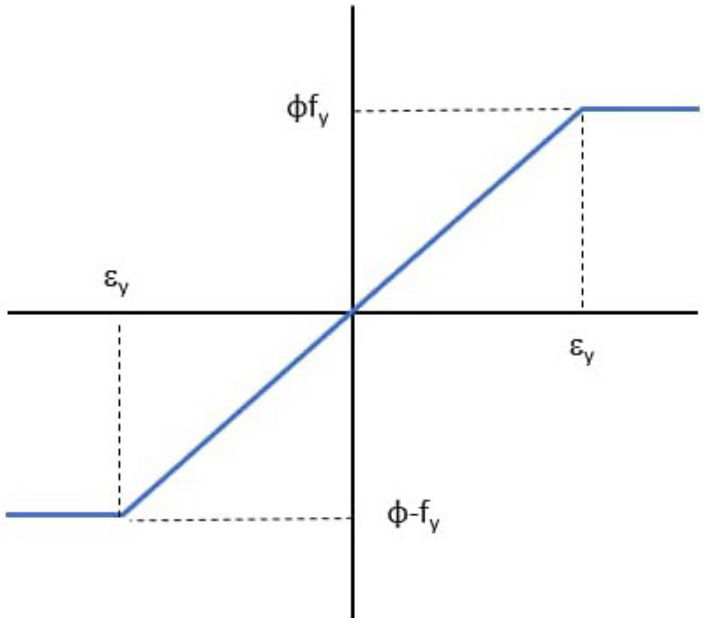

Figure A-4. Stress-strain curve for reinforcement

Post-Tensioning Steel

Post-tensioning of the structure is achieved by using pre-stressing strands conforming to ASTM A416. The strands are formed into tendons and installed in ducts, which have been cast into the concrete. After tensioning, the strands the ducts are filled with grout.

Tendons are formed of stress-relieved very low relaxation 7-wires super strands. The strands are

15.7-mm strands Grade 1860 N/mm^2, with the following mechanical characteristics at ambient temperature:

- Nominal section: S = 150 mm²
- Characteristic tensile strength: fpu = 1,860 N/mm^2
- Modulus of elasticity: EP = 195 GPa
- Thermal expansion coefficient: $\alpha = 10 \times 10^{-6}$/°C.

The following data will be used for the calculations of the prestress losses due to friction and relaxation along the tendons:

- Wobble friction factor: k = 0.001 per m
- Angular friction coefficient: $\mu = 0.14$ per radian
- Wedge draw-in at anchorage: $\delta = 6.0$ mm.

Low relaxation strand:

- Relaxation at 1,000 hours under 70% of the tensile strength shall be ≤2.5%
- The reinforcement is assumed elastic-plastic with no strain hardening, as shown in Figure A-5.

This report is available at no cost from the National Renewable Energy Laboratory at www.nrel.gov/publications.

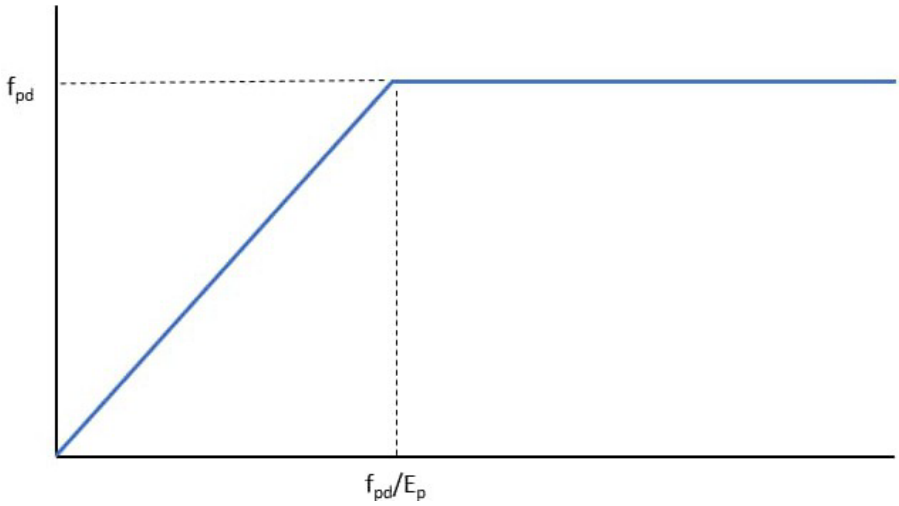

Figure A-5. Stress-strain curve for post-tensioning

Variation in strength with temperature shall follow guidance given in ACI216.1 as shown in Figure A-6.

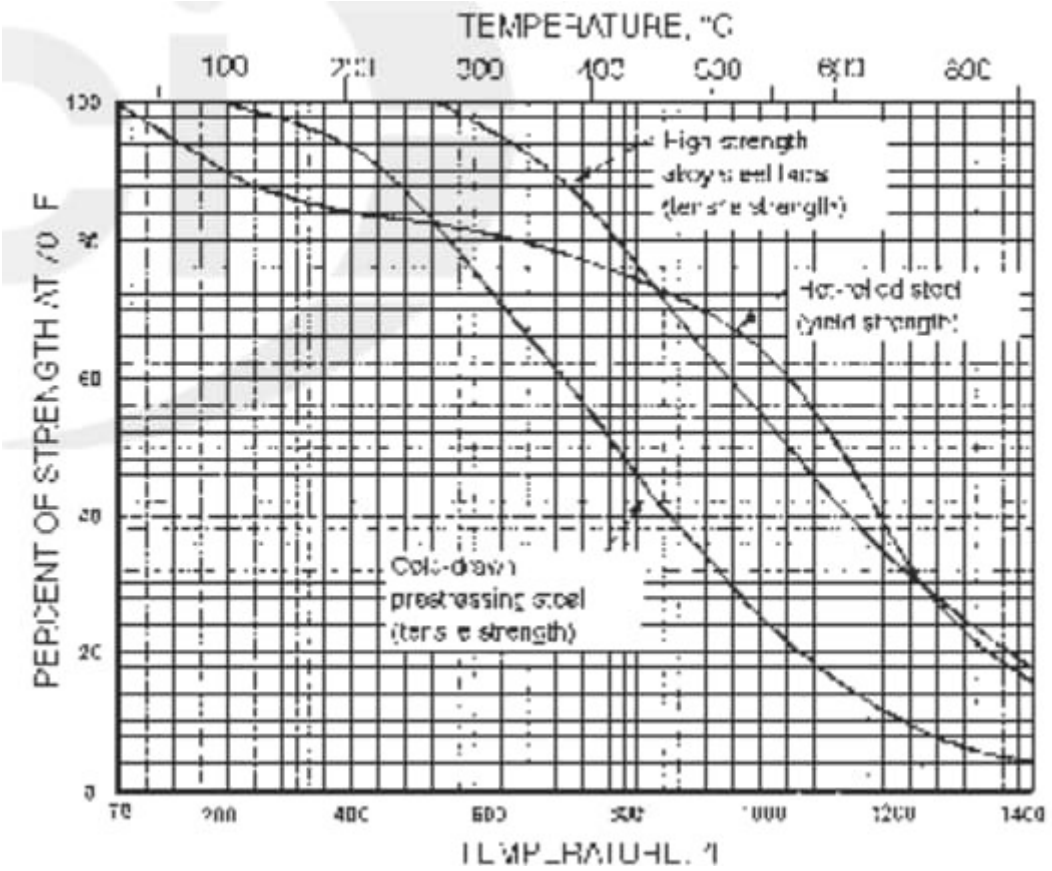

Figure A-6. Variation in strength of flexural reinforcement and strand with temperature (from ACI216.1, Fig. 4.4.2.2.1b)

This report is available at no cost from the National Renewable Energy Laboratory at www.nrel.gov/publications.

A.2 Ultimate Limit State (ULS)

The concrete elements shall meet ULS strength criteria for bending moment, axial load, and shear in accordance with ACI376 and ACI318 for all ULS load combinations, using the material strength reduction factors described within this section.

Partial Load Factors

Partial load factors shall be in accordance with ACI376 and ACI318.

Partial Material Factors (Strength Reduction Factors)

The material strength reduction factors to be used for the Ultimate Limit State (ULS) design evaluation of the concrete outer containment structure are listed in Table A-4.

Table A-4. ULS Strength Reduction Factors

Stress Type	Strength Reduction Factor (ϕ)
Tension Controlled Section	0.90
Compression Controlled Section (With spiral reinforcement)	0.70
Compression Controlled Section (With other reinforcement)	0.65
Shear and torsion	0.75
Bearing on concrete	0.65

A.3 Serviceability Limit State (SLS)

The concrete elements shall meet SLS acceptance criteria for SLS for crack width, reinforcement, and concrete stresses in accordance with ACI376 and ACI318 for all SLS load combinations, using the material strength reduction factors described within this section.

Partial Load Factors

Partial load factors shall be in accordance with ACI376 and ACI318.

Partial Material Factors (Strength Reduction Factors)

The material strength reduction factors used for Serviceability Limit State (SLS) design evaluation are taken as 1.0.

A.4 Concrete Materials

Cement

Cement shall be Portland Cement, in combination with other additives, which may include:

- Pulverised Fuel Ash (PFA)
- Ground Granulated Blast furnace Slag (GGBS)

This report is available at no cost from the National Renewable Energy Laboratory at www.nrel.gov/publications.

- Other approved material.

Blended Hydraulic Cements shall conform to ASTM C-595. Portland cement shall conform to:

- ASTM C-150 Type I (for all applications where not specifically noted otherwise)
- ASTM C-150 Type II or Type V (where needed for sulphate resistance)
- ASTM C-150 Type III (where high strength is required at an early age).

Aggregates

All concrete shall be normal weight concrete with aggregates conforming to ASTM C33 with a maximum nominal size of coarse aggregate of 20 mm. Siliceous aggregate shall be utilized to increase concrete thermal conductivity.

Water

Water used for the following shall be fresh, clean, and free from oil, acid, alkaline, and organic matter or deleterious substances, and shall comply with the recommendations of ASTM C94.

Admixtures

The use of admixtures to promote workability, improve strength, control setting time, or for any other purpose, shall comply with ASTM C-260 and ASTM C-494.

Steel-Fiber

The use of discontinuous discrete steel fibers can be used to enhance concrete tensile strength, reduce cracking, and improve resistance to material deterioration due to fatigue and thermal stresses. Adding steel fibers significantly increases thermal conductivity. Fifty (50)-mm (2-in.) ASTM A820 carbon steel fibers will be utilized with an aspect ratio of 44, similar to Sunny Metal's XOREX concrete fibers.

Polymer Modified Concrete

Polymer Modified Concrete (PMC) uses synthetic polymer-based products in addition to Portland cements. Polymer Modified Concrete is commonly used for applications such as the repair of concrete structures, floor slabs, precast components, concrete drainage products and bridge decks.

Consideration relating to PMC include:

- High compressive and tensile strength
- Improved durability and resistance to chemicals
- Low permeability
- Good freeze/thaw resistance
- High impact resistance
- Plastic shrinkage can be increased
- Modulus of elasticity can be lower than conventional concrete
- Surface discoloration can occur when exposed to UV light
- Polymers may increase lubrication properties of the mix, so less water is required for a workable mix. i.e. high viscosity (making it ideal for injection into cracks)

This report is available at no cost from the National Renewable Energy Laboratory at www.nrel.gov/publications.

- Can be highly influenced by environmental conditions during curing and in service
- Can be more susceptible to higher temperatures than ordinary cement concrete. For example, creep increases with temperature to a greater extent than in ordinary cement concrete, whereas flexural strength, flexural modulus, and modulus of elasticity decrease.

A disadvantage of PMC products can be their relatively high cost, making them more suitable for small-scale repair work than large-scale new construction. However, recycled polyethylene terephthalate (PET) plastic waste has been successfully used to prepare polymer concrete, the use of recycled PET can help in reducing the cost of the material. Additionally, the polymers tend to reduce the thermal conductivity of the concrete—which offers better insulating properties of the concrete but is a disadvantage from a thermal stress perspective (e.g., higher differential temperature across concrete surfaces). This may likely outweigh the benefits (based on Advisian's high-level initial FEA work).

Curing of polymer cement concrete can be different from that of conventional concrete because the polymer forms a film on the surface of the product retaining some of the internal moisture needed for continuous cement hydration. While curing of small patch repairs, or even pours of ground slabs can be carefully controlled and monitored, similar control over large-scale in situ pours, exposed to the elements, may not be so easy to achieve. This is an area that needs to be investigated in future phases/tasks.

Polymer impregnation of precast hardened concrete is a process where low viscosity monomers in liquid or gaseous form are converted to solid polymer, i.e., the open pore structure of the concrete is filled with polymer. This would be applicable to precast elements only.

Forming the tank walls from precast panels may be an area worthy of investigation in future phases/tasks, especially for a location that has high field labor costs.

This report is available at no cost from the National Renewable Energy Laboratory at www.nrel.gov/publications.

Appendix B. Basis of Estimate and Capital Expenditures Summary for Hot Nitrite Salt Tank

B.1 Summary

Capital Cost Estimate

The total estimated cost to design, construct, and commission the facilities described in this study with a 35% contingency is $24.9 million. Based on the overall nitrate salt storage system capacity of 2,791 MWt-h, the hot tank unit cost is $8.94 kWt-h. The CapEx estimate is classified as AACEI Class 4 with an accuracy of −20% to +30% and is presented in Q2 2023 U.S. dollars.

A summary of the capital cost estimate is shown in the table below.

Table B-1. CapEx Estimate Summary for Hot Nitrite Salt Tank

Area	Total
Direct Cost	$15,718,524
Indirect Cost	$2,753,764
Contingency	$6,465,301
Total	**$24,937,588**

Project Job Data

Job data are summarized below.

Owner	NREL
Project Name	Hot Nitrite Tank
Project Type	Reinforced concrete chemical tank
Project Execution Conditions	Greenfield/non-turnaround
Project Execution Type	GC (general contractor), design-build
Build Location	Arizona, USA
Type of Estimate	Worley AACEI Class 4 Capital Cost Estimate
Assessed Accuracy Range	+30% / −20%, after inclusion of contingency at a P_{50} confidence level

B.2 References

1. Design Criteria and Properties – Nitrate, RevA, 1/4/20-23
2. Conceptual Design & Cost Estimate Scope Identification, RevB, 6/30/2020 [Note, internal tank wall and floor insulation system costs by others.]
3. Nitrite Hot Tank Design drawing, 3/23/2023
4. Hot Nitrate Tank civil and structural detailed MTOs (internal Advisian documents)

This report is available at no cost from the National Renewable Energy Laboratory at www.nrel.gov/publications.

5. Hot Nitrate Tank Capital Cost Expenditure (CAPEX) Class 4, RevA4 (internal Advisian document)

B.3 Basis of Estimate

Estimate Classification and Accuracy

The estimate is a Class 4 estimate prepared in accordance with the AACE International estimate classification system. The P50 accuracy range is +30%/−20%, after application of contingency.

The estimate was prepared with a base date of May 2023. The prices and unit rates were used in this estimate were obtained in 2022/2023.

Responsibilities

Advisian has prepared the Capital Cost Estimate based upon material take-offs prepared by discipline engineering leads. The Advisian lead estimator verified the take-offs, analyzed indirect costs, and compiled the estimate, which was approved by the project manager.

Estimate Structure

The Estimate is assembled and coded with Work Breakdown Structure (WBS), and Code of Account (CoA) numbers.

The **WBS** areas are shown in Table B-2 below.

Table B-2. Work Breakdown Structure

WBS	Description	4x Chloride Tanks
1000	Hot Nitrite Tank	$15,718,524
	Total Direct Cost	**$15,718,524**
7000	**Construction Indirect Costs (Support Services)**	
7100	Tank GC's EPCM Costs[a]	$1,100,297
7400	Plant & Equipment	$628,741
7500	Freight/Traffic Warehouse Services & Logistics	$317,392
7900	Commissioning Indirect Costs	$235,778
8000	**Project Delivery Services**	
8100	Owner's Team	$471,556
9000	**Escalation, Allowances & Contingency**	
9900	Contingencies	$6,456,301
	Total Indirect Cost	**$9,219,064**
	Total	**$24,937,588**

[a] Excludes prime EPC/EPCM contractor markups and associated costs.

Duties and Taxes

Duties and taxes are excluded in the estimate.

This report is available at no cost from the National Renewable Energy Laboratory at www.nrel.gov/publications.

Measurement System

The SI (metric) measurement system is used in the estimate.

Pricing

Prices for equipment, construction and miscellaneous materials were based on supplier quotations and in-house data from recent projects and reference databases. Pricing from historical sources was escalated to Q2 2023 based on appropriate PPI indices.

All equipment and material costs are included as FCA Free Carrier manufacturer plant Incoterms 2000. Other costs such as spares, taxes, duties, freight and packaging are covered in the indirect section of the estimate.

Labor Rates and Costs

Labor rates for each construction discipline were developed by Advisian, based on Arizona Construction Industry Workers Agreements and are used throughout the estimate. Hourly labor rate build-ups were reviewed with regional contractors.

The labor rates include:

- Base pay including overtime premiums.
- Vacation and statutory holiday pay
- Fringe benefits and payroll burdens
- Small tools
- Consumables
- Personal protection equipment
- Safety Training
- Supervision

Mobilization, demobilization, and temporary facilities are included in the contractor distributables costs.

Labor crews were assigned to each activity in the estimate, including; site preparation, concrete, reinforcing steel, formwork, post-tensioning, suspended deck insulators, embedded piping, structural.

Man-Hours & Work Schedule

Worley has estimated labor costs based on a man-hours/work week schedule of 10 hours a day, 6 days a week, based on the availability of local contractors capable of executing the project.

Productivity factors were applied to direct field labor hours in order to compensate for labor productivity loss on the job site.

The specific factors considered in this productivity assessment are as follows:

- Site isolation
- Site altitude
- Weather conditions

This report is available at no cost from the National Renewable Energy Laboratory at www.nrel.gov/publications.

- Safety conditions (hazardous materials, confined space, working at heights)
- Work hours and schedule
- Local workforce age, skill, and availability
- Site work congestion (plant conditions)
- Project scale and complexity
- Tools and construction equipment quality
- Local construction techniques
- Local work practices
- Supervision and construction management team.

Contractor Distributables

The contractor distributables cost includes provisions for the following common construction costs:

- Mobilization and demobilization of contractor personnel, equipment, and facilities;
- Contractors' temporary site facilities;
- Contractors' general equipment;
- Maintenance of contractors' temporary facilities and equipment;
- Contractors' on-site execution team;
- Contractors' QA/QC; and
- Contractors' site office operation cost (furniture, IT, cell phones, printers).
- Contractors' overhead and profit.

The contractor distributables cost is estimated based on an analysis of these costs, and applied in the estimate as 26.0% of the estimated labor cost.

B.4 Elements of Cost

The capital cost estimate consists of two main parts (Cost Types in the WBS):

- Direct Costs
- Indirect Costs, including:
    - Project indirect costs
    - Owner's costs
    - Contingency.

Direct Costs

Quantities were developed by discipline engineering leads from drawings and design specifications.

Details on the respective discipline quantities are provided in the MTO documents. The basis of pricing for each discipline is described in the following sections.

Concrete

The unit rates for formwork, reinforcing steel, embedded metals, and concrete placement / finishing are derived from in-house data from similar projects and information from regional

This report is available at no cost from the National Renewable Energy Laboratory at www.nrel.gov/publications.

contractors. Aggregate is assumed to be sourced and supplied locally for use with on-site batch plants. This price is included with the concrete unit prices.

Structural Steel

Steel quantities are calculated from structural design drawings. Insulation is included in the structural MTO.

Prices for supply and installation of fabricated steel sections, grating, plates, handrail, ladders, connections, bolts, and insulation are based on Worley in-house data from recent projects.

Piping

Piping quantities were developed based on a calculation of cooling pipe length and fittings to be embedded into the tank lower slab.

Piping costs are based on unit rates developed from unit cost analysis incorporating crew productivity and material wastage. Fittings (elbows) are estimated separately. Prices are based on current market data published by regional suppliers and from recent projects.

Mechanical Equipment, Electrical, Instrumentation & Controls

No mechanical or electrical equipment is included in the scope. Instrumentation and monitoring systems are not included in the scope.

Indirect Costs & Contingency

Indirect Costs include project indirect costs, Owner's Costs, and contingency.

Project Indirect Costs

EPCM

The tank general contractor's EPCM costs are estimated as a percentage of the total direct cost. Percentage factors were selected for engineering, procurement (EP) and construction management (CM) based on tank construction experience. The total EPCM cost is 7% of the direct cost.

The engineering cost includes all stages of engineering design and covers personnel salaries, burdens, and travel costs (engineering manager, discipline lead, engineers, junior engineers and drafting specialists), IT services, central office costs and support during construction.

Procurement includes personnel salaries (procurement lead, purchasing, expediting, traffic and logistics, material control, inspection and assistant) central office costs and support during construction.

General contractor's CM team will be responsible for management of all tank-related construction activities on the job site.

This report is available at no cost from the National Renewable Energy Laboratory at www.nrel.gov/publications.

Freight and Logistics

The freight and logistics allowance is calculated on a percentage basis based on recent experience and input from suppliers. Supply within the country is assumed for all materials.

The total freight allowance is 4% of the materials cost.

Heavy Equipment

An allowance of 4% of the direct cost is included for large cranes and other heavy equipment.

Owner's Costs

Owner's Project Management

An allowance of 3% of the direct cost is included to cover the Owner's team (project management, supervision, safety, procurement, and project controls), including salaries, travel, accommodation, office costs etc.

Pre-production Operations & Start-up Costs

An allowance of 1.5% of the total direct cost is included to cover all commissioning activities.

Escalation

There is no provision in the estimate for escalation beyond May 2023.

Contingency

In preparing a capital cost estimate, it is a rare occasion when everything is known, specified and measurable. To complete a capital cost estimate for a project, one must provide for that which is not fully known, specified or measurable as well as that not foreseen in order to attain a complete cost figure.

Contingency is applied to this estimate as 35% of direct and indirect costs. The contingency to be added to the base estimate is defined as:

"An allowance for goods and services which at the current state of project definition cannot be accurately quantified, but which history and experience show will be necessary to achieve the given project scope."

The assessment of potential cost and schedule overrun, and the estimation of appropriate contingency levels is an important element of capital cost estimates as it typically addresses some of the major risks to a project.

These key risks relate to items such as:

- Level of detail of scope
- The level of engineering completed at the time of the study

This report is available at no cost from the National Renewable Energy Laboratory at www.nrel.gov/publications.

- Technical risks for untried or “out of ordinary” process items
- Geotechnical and survey issues
- Weather
- Quantity take-off detail
- Availability of materials
- Availability of cranes (heavy lifts, etc.)
- Pricing details for bulk materials and equipment
- Labor cost and labor productivity
- Constructability
- Freight and logistics
- Construction schedule issues
- Permitting constraints.

B.5 Qualifications and Exclusions

Qualifications

The Capital Cost Estimate assumed that:

- Construction activities will be continuous
- Bulk materials such as cement, reinforcing steel, structural steel and plates, and piping will be available when they are required.

Exclusions

Refer to Reference document #2 above. In addition, the internal tank wall and floor insulation system costs are out of scope (by JT Thorpe).

The following items were excluded from the estimate:

- Site infrastructure
- Ancillary buildings
- Mechanical equipment
- Electrical equipment and services
- Instrumentation and controls
- Cost escalation during construction
- Major scope changes
- Interest during construction
- Schedule delays and associated costs, such as those caused by the following:
    - Unexpected ground conditions
    - Extraordinary climate events
    - Labor disputes
    - Receipt of information beyond the control of EPCM contractors
    - Schedule recovery or acceleration.
- Financing costs

This report is available at no cost from the National Renewable Energy Laboratory at www.nrel.gov/publications.

- Costs outside Worley's battery limits
- Sustaining capital costs
- Sunk costs
- Salvage values
- Force majeure
- Currency fluctuations.

This report is available at no cost from the National Renewable Energy Laboratory at www.nrel.gov/publications.

Appendix C. Basis of Estimate and Capital Expenditures Summary for Chloride Salt Tanks

C.1 Summary

Capital Cost Estimate

The total estimated cost to design, construct, and commission the facilities described in this study with a 35% contingency is $94.6 million. Based on the overall chloride salt storage system capacity of 2,400 MWt-h, the chloride tanks—consisting of two hot and two cold tanks—unit cost is $39.4/kWt-h. The CapEx estimate is classified as AACEI Class 4 with an accuracy of −20% to +30% and is presented in Q2 2023 U.S. dollars.

A summary of the capital cost estimate is shown in the Table C-1 below.

Table C-1. CapEx Estimate Summary for Chloride Salt Tanks

Area	Total
Direct Cost	$62,303,364
Indirect Cost	$7,813,480
Contingency	$24,540,896
Total	**$94,657,740**

Project Job Data

Job data are summarized below.

Owner	NREL
Project Name	Chloride salt tanks
Project Type	Reinforced concrete chemical tanks; two hot and two cold tanks
Project Execution Conditions	Greenfield/non-turnaround
Project Execution Type	GC (general contractor), design
Build Location	Arizona, USA
Type of Estimate	Worley AACEI Class 4 Capital Cost Estimate
Assessed Accuracy Range	+30% / −20%, after inclusion of contingency at a P_{50} confidence level

C.2 References

1. Design Criteria and Properties – Chloride Salt, RevC, 6/8/2023
2. Conceptual Design & Cost Estimate Scope Identification, RevB, 6/30/2020 [Note, internal tank wall and floor insulation system costs by others.]

This report is available at no cost from the National Renewable Energy Laboratory at www.nrel.gov/publications.

3. Hot Chloride Tank Design drawing, 6/22/2023
4. Cold Chloride Tank Design drawing, 6/16/2023
5. Civil and structural detailed MTOs - Cold Chloride Tanks (internal Advisian documents)
6. Civil and structural detailed MTOs - Hot Chloride Tanks (internal Advisian documents)
7. Hot and Cold Chloride Tank Capital Cost Expenditure (CAPEX) Class 4, RevA7 (internal Advisian document)

C.3 Basis of Estimate

Estimate Classification and Accuracy

The estimate is a Class 4 estimate prepared in accordance with the AACE International estimate classification system. The P_{50} accuracy range is +30% / −20%, after application of contingency.

The estimate was prepared with a base date of May 2023. The prices and unit rates used in this estimate were obtained in 2022/2023.

Responsibilities

Advisian has prepared the Capital Cost Estimate based upon material take-offs prepared by discipline engineering leads. The Advisian lead estimator verified the take-offs, analyzed indirect costs, and compiled the estimate, which was approved by the project manager.

Estimate Structure

The Estimate is assembled and coded with Work Breakdown Structure (WBS), and Code of Account (CoA) numbers.

The **WBS** areas are shown in Table C-2 below.

Table C-2. Work Breakdown Structure

WBS	Description	4x Chloride Tanks
2000	Cold Chloride Tank #1	$14,603,115
3000	Cold Chloride Tank #2	$14,603,115
4000	Hot Chloride Tank #1	$16,548,568
5000	Hot Chloride Tank #2	$16,548,568
	Total Direct Cost	**$62,303,364**
7000	**Construction Indirect Costs (Support Services)**	
7100	EPCM Costs	$2,492,135
7400	Plant & Equipment	$2,180,618
7500	Freight/Traffic Warehouse Services & Logistics	$1,271,627
7900	Commissioning Indirect Costs	$623,034
8000	**Project Delivery Services**	
8100	Owner's Team	$1,246,067

This report is available at no cost from the National Renewable Energy Laboratory at www.nrel.gov/publications.

WBS	Description	4x Chloride Tanks
9000	**Escalation, Allowances & Contingency**	
9900	Contingencies	$24,540,896
	Total Indirect Cost	**$32,354,376**
	Total	**$94,657,740**

Duties and Taxes

Duties and taxes are excluded in the estimate.

Measurement System

The SI (metric) measurement system is used in the estimate.

Pricing

Prices for equipment, construction and miscellaneous materials were based on supplier quotations and in-house data from recent projects and reference databases. Pricing from historical sources was escalated to Q2 2023 based on appropriate PPI indices.

All equipment and material costs are included as FCA Free Carrier manufacturer plant Incoterms 2000. Other costs such as spares, taxes, duties, freight and packaging are covered in the indirect section of the estimate.

Labor Rates and Costs

Labor rates for each construction discipline were developed by Advisian, based on Arizona Construction Industry Workers Agreements and are used throughout the estimate. Hourly labor rate build-ups were reviewed with regional contractors.

The labor rates include:

- Base pay including overtime premiums.
- Vacation and statutory holiday pay
- Fringe benefits and payroll burdens
- Small tools
- Consumables
- Personal protection equipment
- Safety Training
- Supervision.

Mobilization, demobilization, and temporary facilities are included in the contractor distributables costs.

Labor crews were assigned to each activity in the estimate, including; site preparation, concrete, reinforcing steel, formwork, post-tensioning, suspended deck insulators, embedded piping, structural.

This report is available at no cost from the National Renewable Energy Laboratory at www.nrel.gov/publications.

Man-Hours & Work Schedule

Worley has estimated labor costs based on a man-hours/work week schedule of 10 hours a day, 6 days a week, based on the availability of local contractors capable of executing the project.

Productivity factors were applied to direct field labor hours in order to compensate for labor productivity loss on the job site.

The specific factors considered in this productivity assessment are as follows:

- Site isolation
- Site altitude
- Weather conditions
- Safety conditions (hazardous materials, confined space, working at heights)
- Work hours and schedule
- Local workforce age, skill, and availability
- Site work congestion (plant conditions)
- Project scale and complexity
- Tools and construction equipment quality
- Local construction techniques
- Local work practices
- Supervision and construction management team.

Contractor Distributables

The contractor distributables cost includes provisions for the following common construction costs:

- Mobilization and demobilization of contractor personnel, equipment, and facilities
- Contractors' temporary site facilities
- Contractors' general equipment
- Maintenance of contractors' temporary facilities and equipment
- Contractors' on-site execution team
- Contractors' QA/QC
- Contractors' site office operation cost (furniture, IT, cell phones, printers)
- Contractors' overhead and profit.

The contractor distributables cost is estimated based on an analysis of these costs, and applied in the estimate as 26.0% of the estimated labor cost.

C.4 Elements of Cost

The capital cost estimate consists of two main parts (Cost Types in the WBS):

- Direct Costs
- Indirect Costs, including:
    - Project indirect costs
    - Owner's costs
    - Contingency.

This report is available at no cost from the National Renewable Energy Laboratory at www.nrel.gov/publications.

Direct Costs

Quantities were developed by discipline engineering leads from drawings and design specifications.

Details on the respective discipline quantities are provided in the MTO documents. The basis of pricing for each discipline is described in the following sections.

Concrete

The unit rates for formwork, reinforcing steel, embedded metals, and concrete placement / finishing are derived from in-house data from similar projects and information from regional contractors. Aggregate is assumed to be sourced and supplied locally for use with on-site batch plants. This price is included with the concrete unit prices.

Structural Steel

Steel quantities are calculated from structural design drawings. Insulation is included in the structural MTO.

Prices for supply and installation of fabricated steel sections, grating, plates, handrail, ladders, connections, bolts, and insulation are based on Worley in-house data from recent projects.

Piping

Piping quantities were developed based on a calculation of cooling pipe length and fittings to be embedded into the tank lower slab.

Piping costs are based on unit rates developed from unit cost analysis incorporating crew productivity and material wastage. Fittings (elbows) are estimated separately. Prices are based on current market data published by regional suppliers and from recent projects.

Mechanical Equipment, Electrical, Instrumentation & Controls

No mechanical or electrical equipment is included in the scope. Instrumentation and monitoring systems are not included in the scope.

Indirect Costs & Contingency

Indirect Costs include project indirect costs, Owner's Costs, and contingency.

Project Indirect Costs

EPCM

The tank general contractor's EPCM costs are estimated as a percentage of the total direct cost. Percentage factors were selected for engineering, procurement (EP) and construction management (CM) based on tank construction experience. The total EPCM cost is 4% of the direct cost.

This report is available at no cost from the National Renewable Energy Laboratory at www.nrel.gov/publications.

The engineering cost includes all stages of engineering design and covers personnel salaries, burdens, and travel costs (engineering manager, discipline lead, engineers, junior engineers and drafting specialists), IT services, central office costs and support during construction.

Procurement includes personnel salaries (procurement lead, purchasing, expediting, traffic & logistics, material control, inspection and assistant) central office costs and support during construction.

General contractor's CM team will be responsible for management of all tank-related construction activities on the job site.

Freight and Logistics

The freight and logistics allowance is calculated on a percentage basis based on recent experience and input from suppliers. Supply within the country is assumed for all materials.

The total freight allowance is 4% of the materials cost.

Heavy Equipment

An allowance of 3.5% of the direct cost is included for large cranes and other heavy equipment.

Owner's Costs

Owner's Project Management

An allowance of 2% of the direct cost is included to cover the Owner's team (project management, supervision, safety, procurement, and project controls), including salaries, travel, accommodation, office costs etc.

Pre-production Operations & Start-up Costs

An allowance of 1% of the total direct cost is included to cover all commissioning activities.

Escalation

There is no provision in the estimate for escalation beyond May 2023.

Contingency

In preparing a capital cost estimate, it is a rare occasion when everything is known, specified and measurable. To complete a capital cost estimate for a project, one must provide for that which is not fully known, specified or measurable as well as that not foreseen in order to attain a complete cost figure.

Contingency is applied to this estimate as 35% of direct and indirect costs. The contingency to be added to the base estimate is defined as:

This report is available at no cost from the National Renewable Energy Laboratory at www.nrel.gov/publications.

"An allowance for goods and services which at the current state of project definition cannot be accurately quantified, but which history and experience show will be necessary to achieve the given project scope."

The assessment of potential cost and schedule overrun, and the estimation of appropriate contingency levels is an important element of capital cost estimates as it typically addresses some of the major risks to a project.

These key risks relate to items such as:

- Level of detail of scope
- The level of engineering completed at the time of the study
- Technical risks for untried or "out of ordinary" process items
- Geotechnical and survey issues
- Weather
- Quantity take-off detail
- Availability of materials
- Availability of cranes (heavy lifts, etc.)
- Pricing details for bulk materials and equipment
- Labor cost and labor productivity
- Constructability
- Freight and logistics
- Construction schedule issues
- Permitting constraints.

C.5 Qualifications and Exclusions

Qualifications

The Capital Cost Estimate assumed that:

- Construction activities will be continuous
- Bulk materials such as cement, reinforcing steel, structural steel and plates, and piping will be available when they are required.

Exclusions

Refer to Reference document #2 above. In addition, the internal tank wall and floor insulation system costs are out of scope (by JT Thorpe).

The following items were excluded from the estimate:

- Site infrastructure
- Ancillary buildings
- Mechanical equipment
- Electrical equipment and services
- Instrumentation and controls
- Cost escalation during construction

This report is available at no cost from the National Renewable Energy Laboratory at www.nrel.gov/publications.

- Major scope changes
- Interest during construction
- Schedule delays and associated costs, such as those caused by the following:
    - Unexpected ground conditions
    - Extraordinary climate events
    - Labor disputes
    - Receipt of information beyond the control of EPCM contractors
    - Schedule recovery or acceleration.
- Financing costs
- Costs outside Worley's battery limits
- Sustaining capital costs
- Sunk costs
- Salvage values
- Force majeure
- Currency fluctuations.

This report is available at no cost from the National Renewable Energy Laboratory at www.nrel.gov/publications.